Diagnostics and Control of Transverse Coupled-Bunch Instabilities in Third Generation Electron Storage Rings

David Peake

Submitted in total fulfilment of the requirements of the degree of
Doctor of Philosophy

School of Physics,
The University of Melbourne

March 2012

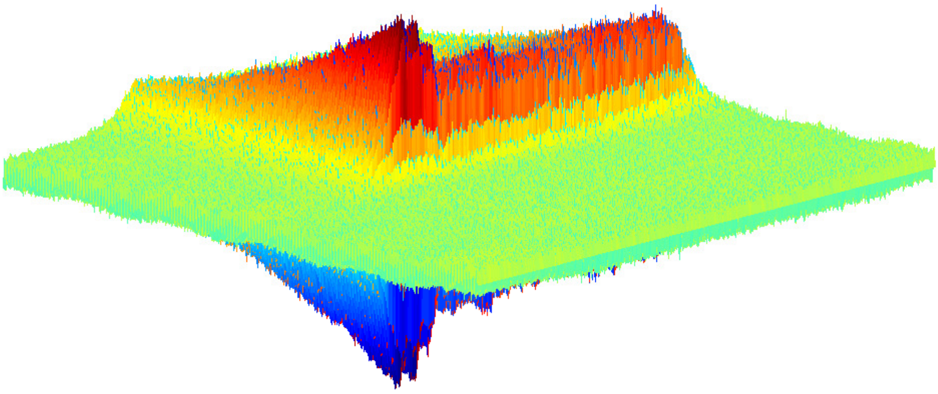

Declaration

This is to certify that

- the thesis comprises of only my original work towards the PhD except where indicated,
- due acknowledgement has been made in the text to all other material used,
- and the thesis is less than 100,000 words in length, exclusive of tables, maps, bibliographies and appendices.

David Joseph Peake

Abstract

The Australian Synchrotron is a newly commissioned third-generation light source situated in Melbourne, Australia. Synchrotron radiation is produced from the 216 metre circumference storage ring where 3 GeV electrons are trapped within a lattice formed by dipole bending magnets and multipole focussing magnets.

The appearance of coupled-bunch instabilities form the primary limitation of modern storage rings. Instabilities enforce an upper limit on stored current and can reduce the utility of radiation production by increasing the effective emittance of the ring.

Stored current limitations due to beam instabilities were discovered early in the commissioning phase of the Australian Synchrotron storage ring and were initially controlled by substantially increasing the chromaticity of the lattice from $(\xi_x, \xi_y) = (2, 2)$ to $(\xi_x, \xi_y) = (3.5, 13)$. Subsequent additions to the ring have resulted in an increase of the strength of destructive instabilities to the point where detrimental side-effects from chromatic corrections reduce the ability of the ring to damp instabilities. This increase in instability strength has lead to the shift from purely passive methods of instability control to the design and construction of an active transverse feedback system.

This thesis describes the commissioning of a bunch-by-bunch transverse feedback system designed to combat coupled-bunch instabilities, allowing for the reduction of chromaticity within the storage ring lattice back to the initial design values $(\xi_x, \xi_y) = (2, 2)$. Reducing the chromaticity also removes detrimental effects such as the reduction of the dynamic aperture and an increase in the lifetime of the beam. Novel methods for tuning the system and maximising the damping rate of the beam are introduced. Using these methods, the feedback system was successfully commissioned and was shown to have the stability required for user-mode storage ring operations.

The bunch-by-bunch transverse feedback system can also be leveraged as a powerful diagnostic tool. New data acquisition techniques have been designed to allow for the study of different instability mechanisms as well as parameters present in the equations of motion for stored particles. These techniques and the suite of results achieved are presented.

To Dr Kerrie Piper, for keeping me sane (mostly)

Acknowledgements

> "You know, completing a PhD seems similar to fixing a uterine prolapse in a cow. You spent ages pushing and heaving with no result then *whoosh* — everything falls into place and you're done."
>
> Dr Kerrie Piper BVSc (Hons)

First and foremost I thank Dr Roger Rassool and Dr Mark Boland for their supervision, inspiration and patience. Starting an accelerator physics project at a new facility was a journey for all of us and has turned out to be a fantastic learning experience.

In addition to their responsibilities as supervisors, both Roger and Mark encouraged me to participate in extra-thesis activities such as the MUPPETS science and laser shows and helping light high-school plays. My PhD experience has been unique due to the widespread abilities of my supervisors and I thank them for it. By promoting cross-training between students I have had experience in detector design, medical imaging, image processing, electronics and stage work, in addition to my training as an accelerator physicist. With their support I have visited many of the premier accelerator facilities in the world, coming away each time with a greater appreciation of the field I was involved in.

Although completion of a thesis is the goal, the people we work with are often the impetus to achieving it. To Bryn Sobott and Vivien Lee, thank you for road trips, plane trips and Skip-Bo. Without your comments, corrections and dumpling codependency this thesis would be comprised of monosyllabic statements combined with indecipherable acronyms. To Willy D, Anna Phan, Stefanie Elbracht, T'Mir Julius, Robin Wedd, Anthony Morley and all the EPP students over the last few years: thank you all for the many conversations, games of

Kolf and your patience in explaining the somewhat inscrutable world of particle physics to me.

Accelerator facilities require an extraordinary amount of effort to construct and commission and the Australian Synchrotron Light Source (ASLS) is no different. My thanks to the accelerator team at the ASLS for allowing me into your group and for your willingness to field all of my questions. The accelerator physics group at the ASLS is much smaller than other comparable facilities but the enthusiastic people in the group has lead to the ASLS leading the world as a synchrotron light source. In particular would like to thank Rohan Dowd, Eugene Tan and Greg LeBlanc for many illuminating discussions and Martin Spencer for doing the important initial work installing the feedback system. The storage ring does not run on the backs of the accelerator group alone; the operators who take care of the ring during user time provide the heart the facility. Though all of them have watched me degrade from keen physicist to beam-o-cidial maniac over a night shift, I would like to thank Joel Trewhella and Robbie Clarken in particular for their help and continued interest in my work.

The rapid commissioning of new synchrotron light facilities around the world is a testament to the amazing attitude of the accelerator community. I have had the privilege to visit and work at many of the synchrotron facilities around the world and I would like to thank the teams at MAXLAB (Lund, Sweden), SSRL (Stanford, USA), CERN (Geneva, Switzerland) and ESRF (Grenoble, France) for allowing myself and my colleagues in and making us feel at home wherever we were. In particular I'd like to thank Jeff Corbett of SSRL for his work with guiding the future of the ASLS and his amazing hospitality during our experimental runs at SLAC/SSRL.

I would also like to thank the organisers of the two major accelerator schools; CAS (CERN Accelerator School) and USPAS (US Particle Accelerator School) for gathering many of the top names in accelerator physics. The coherent dynamics course I undertook in Albuquerque with Drs Elias Métral and Giovanni Rumolo greatly assisted my understanding of this complex field.

In finishing I will say that like any successful project in the field of modern physics, this was the result of a hundred good results and a thousand frustrating ones. Without the efforts of many I would have never completed this work, let alone achieved the numerous results presented. One person needs to be pointed out as having done all the hard yards with me. Dr Kerrie Piper, my best friend of many years has stayed by my side despite the all-night machine studies and the many trips overseas. When I thought hours of research which lead nowhere was the worst way to spend a day, she would regale me with tales of performing calvings in the mud and reassembling dogs disassembled by cars. Thank you.

Contents

List of Figures

List of Tables

Outline

Synchrotron-based particle accelerators are invaluable scientific tools for studying fundamental physical properties. From large scale machines such as the Large Hadron Collider (LHC) to smaller facilities built to produce synchrotron radiation, these machines have been at the forefront on scientific endeavours around the world.

The Australian Synchrotron Light Source (ASLS) is a third-generation synchrotron light source recently constructed in Melbourne, Australia [1]. Construction of the facility began in July 2003, with the first stored beam achieved on July 14th, 2006 [2]. Making use of an injection chain consisting of a 100 MeV Linear Accelerator (LINAC) and a 3.0 GeV booster synchrotron the electrons are placed into a 216 m circumference storage ring, producing synchrotron radiation for users at experimental beamlines around the periphery. In Chapter 1, the motivation for providing a stable electron beam for synchrotron radiation production is presented and an outline of the ASLS synchrotron radiation facility is described.

The storage ring at the ASLS consists of dipole bending magnets which form a closed orbit for the electrons and an array of multipole magnets to trap and focus the electron beam. Radio Frequency (RF) acceleration cavities are used to replenish the energy lost through the emission of synchrotron radiation. Chapter 2 discusses the theory behind the acceleration and focussing of electrons in the storage ring.

Experimentalists utilising synchrotron radiation for research and development demand the stored beam meet strict stability requirements. As synchrotron-based facilities and the experimental methods mature, demands for higher X-ray flux and a smaller transverse profile increase. This in turn leads to higher stored currents, smaller beam size and destructive transverse instabilities.

This thesis is the result of a study into the diagnosis and control of transverse coupled-bunch instabilities in the ASLS storage ring. It is demonstrated that as more particles are trapped within the magnetic lattice of the storage ring, the interactions between stored bunches and the metallic environment result in the creation of coupled-bunch instabilities. These instabilities increase the transverse beam profile and cause the unwanted excursion of particles. Depending on the strength of the instability this can dramatically reduce beam lifetime and increase damage to sensitive intra-vacuum components. Chapter 3 provides the introductory theory concerning transverse coupled-bunch instabilities, drawing on results from the established literature, culminating in the definition of ring impedance which links the parameters of the electron beam to the strength of coupled-bunch instabilities.

Although some control of the instabilities can be achieved through the purely passive means discussed in Chapter 4, optimal results can only be achieved with the introduction of an active feedback system. An active feedback system provides a high damping rate by measuring the motion of unstable beam and calculating a corrective waveform. The construction and commissioning of a Bunch by Bunch Feedback (BBB) active feedback system for the ASLS storage ring is discussed in Chapter 5. In order to maximise the damping rate of the active feedback system, novel techniques were developed which allow the system to be tuned using only the feedback equipment and stored beam. Successful commissioning of the BBB system is shown with a series of long-term stability experiments.

An application of the diagnostics that the feedback system provides is the study of the creation of coupled-bunch instabilities, in particular measuring the change in instability strength versus a given ring parameter. This is of clear use when initially commissioning the system as well as diagnosing any new instabilities that arise over time. Measuring the parameters of long-term unstable beam requires a technique which can allow the beam to become unstable while preventing any beam loss. A technique called *grow/damp* was developed as part of this thesis, allowing for the measurement of both the growth rate of the instabilities and the subsequent damping rate of the feedback system. The results of the successful implementation of this technique is shown, along with a discussion of the original data acquisition methods constructed to take the data.

While the transverse feedback system is primarily used to provide a high stored current threshold for instability production it also has capabilities as a powerful diagnostic tool. The BBB system provides a full data acquisition path, from a high speed Analogue-to-Digital Converter (ADC) section to an actuation system with a Digital-to-Analogue Converter (DAC) and high-bandwidth kicker magnets. In Chapter 7 new techniques are described which extend the traditional methods of measuring ring parameters such as tune and chromaticity by utilising the high bandwidth of the BBB feedback system. A method which allows for high repetition rate single-shot measurements of the imaginary component of the ring impedance is shown, with a suite of results enabled by the unique abilities of this transverse feedback system.

The final chapter of the thesis (Chapter 8) discusses some of the future work that will be performed to extend the techniques shown in earlier chapters and presents a concise summary of the novel diagnostic methods and the new results that have been achieved.

Chapter 1

Introduction

For the last century, many areas of fundamental physics research have been driven by particle accelerators. From the earliest linear accelerators to the Large Hadron Collider (LHC) the technology used to accelerate, steer and focus charged particles has been used by generations of scientists. It has been shown that of the 141 winners of the Nobel prize in physics between 1939 and 2009, 39 (28%) were based on research made possible by contributions from accelerator physics and accelerator instrumentation [3].

As the technologies to store high intensity particle beams were advanced in response to the demands of an ever-expanding experimental user community, coupled-bunch instabilities began to limit the ability of storage ring facilities to achieve higher currents. Through electromagnetic interactions with the beam environment, strong instabilities limit the achievable stored current leading to a lower charge density for experimentalists and a reduction in scientific output for the facility.

This chapter will cover the motivation behind the commissioning of a transverse feedback system in the Australian Synchrotron Light Source (ASLS) storage ring.

1.1 Particle Accelerators

Some of the most important discoveries in basic physics have come from the study of matter by probing its properties with radiation. From Ivan Pulyui's discovery that sealed photographic film canisters became darker when exposed to vacuum discharge tubes, to modern biochemists using synchrotron radiation for protein crystallography, experiments have used radiation to probe fundamental material properties.

Initially the only available radiation sources involved natural radioactive isotopes such as ^{226}Ra, which emits a 512 keV γ-ray as part of its decay chain. Although natural sources are initially useful for scientific experiments, they are not without problems. Radioactive sources are hard to find, purify, transport and need to be adequately shielded. Advances in scientific research such as the need for high resolution, high statistics measurements led to a search for a method for producing radiation within the laboratory safely.

In 1895, William Röntgen stumbled upon the discovery of X-rays whilst conducting research using an evacuated Crookes tube (a precursor to the modern Cathode Ray Tube) which caused fluorescence on a plate, even when materials such as wood and aluminium foil were placed in between [4]. Further research into X-rays (so named purely for brevity) led to him being awarded the first Nobel Prize in Physics in 1901 in recognition of his discovery of "Röntgen Rays". Röntgen's discovery led to more fundamental studies of the nature of matter using the massless photon as a high precision probe for interactions. The ability to create X-rays in a safe and reproducible manner allowed for a wide variety of physical studies, however demand for higher X-ray fluxes quickly outstripped the abilities of the laboratory sources available.

Concurrent advances were being made in the area of particle physics research. As part of a research project into a power source for RADAR, a high power Radio Frequency (RF) voltage source was created called the *klystron* [5]. Moving away from utilising DC voltages to increase the energy of particles leads to a major advantage — the ability to accelerate a particle multiple times through the same potential. Integrating a closed loop through a static potential will always equal zero, as any energy gained will be lost as the particle approaches the same location. A potential that changes with time enables the particle to be continuously accelerated by passing multiple times through a gap. The inclusion of RF voltage sources allowed the creation of the first circular accelerators: cyclotrons [6], and betatrons [7].

All of these machines require large amounts of material to construct, and are ultimately limited in size. Both cyclotrons and betatrons require a magnet pole with a radius equal to the final bending radius of the accelerated particle,

$$B\rho = \frac{p}{e} \tag{1.1}$$

where B is the magnetic field and ρ is the bending radius of the particles with momentum p and charge e. The combination $B\rho$ is called the *magnetic rigidity* of the particle. For a constant magnetic field, the bending radius is proportional to the momentum of the particle.

In 1943 Australian physicist Mark Oliphant (independently of Vladimir Veksler and Edwin McMillan) invented a method for accelerating particles that would revolutionise the design of high energy particle physics facilities [8]. Accelerators of the time such as cyclotrons and betatrons maintain a constant magnetic field and allow the bending radius to increase with particle energy. Oliphant's realisation was that if the magnetic field was increased synchronously with particle energy the bending radius of the particles could be kept constant.

This would require the accelerator to have a magnetic field in an annulus around this orbit combined with an initial injection system of moderate energy, reducing the prohibitive costs of larger machines. After achieving the energy required, the magnets and RF systems would allow the particles to be stored in the ring for an extended period of time. Oliphant described this machine as a *synchrocyclotron* [9] and the design was used to create machines capable of higher energies than both betatrons and cyclotrons.

Currently synchrotron accelerators are the preferred method for accelerating charged particles to high energies. In particle colliders (such as the LHC) there are two counter-rotating beams of particles which are allowed to cross at specific points in the ring called *interaction points*. These interactions create new exotic particles which decay rapidly. Detectors placed at these points measure the decay products and are used to measure properties of the short-lived particles. Modern examples include the A Toroidal LHC ApparatuS (ATLAS) and Compact Muon Solenoid (CMS) experiments at the LHC as well as the BELLE experiment at KEK. Each accelerator complex is built for a different purpose and as such the detectors used vary in configuration.

Although high energy colliders were the driving force for the construction of synchrotron accelerators, many modern facilities known as *light sources* are built for the sole purpose of producing *synchrotron radiation*, a physical result of accelerating charged particles.

1.2 The Australian Synchrotron Light Source (ASLS)

The ASLS is a third generation synchrotron-based light source, situated in Melbourne, Australia [1]. Construction of the facility began in July 2003, with first light achieved on July 14, 2006 [2]. It is the largest accelerator based research facility in Australia and the only synchrotron-based accelerator in the country.

The design combines a 3 GeV storage ring with an injection chain consisting of a 100 MeV Linear Accelerator (LINAC) and a 3 GeV booster synchrotron in the configuration shown in Figure 1.1.

1.2.1 Injection Chain

Electrons are initially produced using a 90 kV cathode ray source [10]. The electrons are captured and accelerated along a 3 GHz iris-loaded LINAC, reaching 100 MeV before being transferred into the booster synchrotron. In the booster synchrotron the magnetic and electric

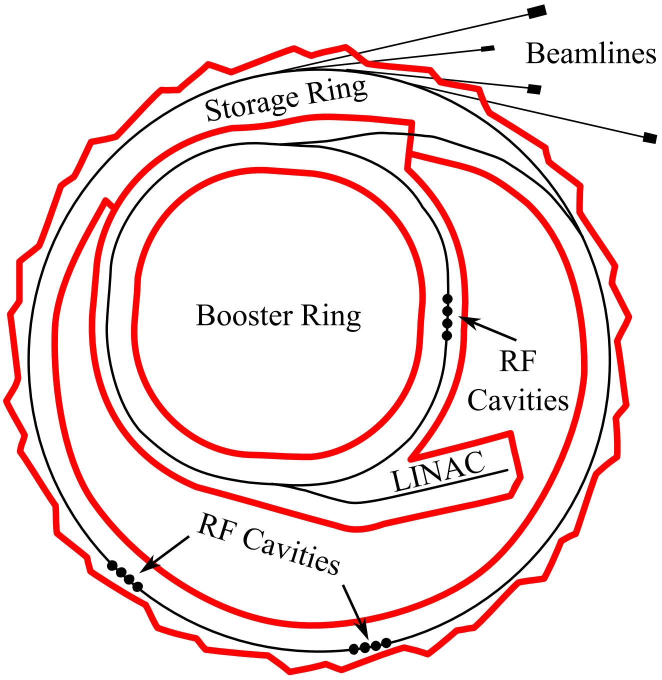

Figure 1.1: A diagram outlining the relative locations of the injection chain and storage ring at the ASLS [2] (not to scale). The red lines indicate radiation shielding walls and the black dots represent the location of RF cavities.

fields are ramped over a period of 600 ms such that the electrons reach a final energy of 3 GeV.

The accelerated electrons are subsequently transferred from the booster synchrotron using a slow bump / fast kick single turn extraction method into the storage ring [11]. Stored beam is accumulated over multiple injections at a repetition rate of 1 Hz, with a single multi-bunch injection increasing the stored current by approximately 2 mA up to a nominal storage current of 200 mA.

1.2.2 3 GeV Storage Ring

Injection into the storage ring utilises the combination of a thin horizontal septum magnet to deflect the injected beam and a set of four injection kickers to displace the stored beam at the injection point. The kicker magnets create a local bump in the stored beam, moving the stored beam phase space such that it overlays the injected beam phase space. After the current is introduced, the injection bump is reduced and the original stored beam orbit is restored.

A series of fourteen Double Bend Achromat (DBA) unit cells make up the ASLS storage ring. The basic magnet arrangement for a single cell of the storage ring lattice is shown in Figure 1.2. The DBA design matches machine parameters to allow for minimum horizontal emittance in the bending magnets [12]. Reducing emittance in the bending magnets and straight sections is important to increase X-ray flux for beamlines.

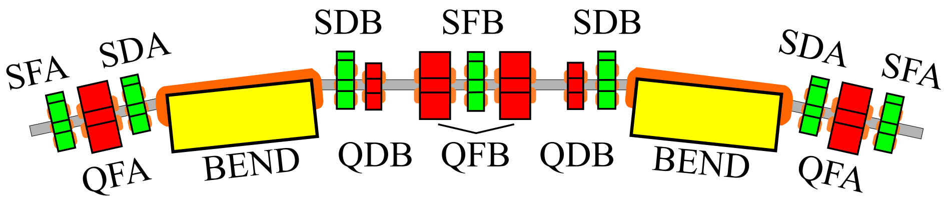

Figure 1.2: A schematic of the locations of magnets within a single DBA cell of the ASLS storage ring. Yellow magnets are combined function bending magnets, constructed to have both dipole bending and quadrupole defocussing elements. Red magnets are quadrupoles and green are sextupoles separated into the magnet families labelled. The storage ring lattice is defined by 14 of these cells, connected by straight vacuum sections for the inclusion of insertion devices.

The magnets in the storage ring maintain a constant magnetic strength and are designed for storing 3 GeV electrons. As the storage ring magnets are not altered during the injection cycle, they can be finely tuned for optimal beam stability and can trap particles for extended periods. A benefit of injecting at full energy is that it is possible to replenish lost electrons through further injections without disturbing the stored beam, apart from the construction of a local beam bump as described earlier. Some of the important storage ring parameters are shown in Table 1.1 and will be described in more detail in Chapter 2.

Table 1.1: A selection of the operating parameters of the ASLS storage ring.

Parameter	Units	Value
Energy	GeV	3.0
Nominal Current	mA	200
Circumference	m	216
Harmonic Number		360
Revolution time	ns	720.4
Revolution Frequency	MHz	1.3879

1.3 Synchrotron Radiation

1.3.1 Theory

Synchrotron radiation was first observed by Floyd Haber, a technician who helped design and operate the 70 MeV electron synchrotron at General Electric Research Laboratories in Schenectady, New York [13]. The defining structure of the accelerator that allowed the discovery of synchrotron radiation was the glass vacuum chamber in which the beam travelled. When the beam energy was increased “arcing” was spotted within the beampipe, the intensity and colour of which depended strongly on the beam energy. The arcing was visible synchrotron radiation; experimental evidence of the physical process described by Liénard. Schwinger [14] expanded the theory further, calculating the spectral nature of the radiation which peaked in the infrared / visible for the low energy rings of the time. The calculated synchrotron radiation flux produced within a bending magnet in the ASLS storage ring is presented in Figure 1.3.

Initially synchrotron radiation was a limitation to achieving higher energies, as radiation losses increase proportionally to $(\beta\gamma)^4$ where β and γ are the relativistic variables. RF acceleration gradients quickly become prohibitive for particles such as electrons which reach highly relativistic speeds at medium energies [16]. Radiation losses due to synchrotron radiation are replenished using RF cavities which take up space within the ring. For example the largest circular electron accelerator, a 27 km synchrotron situated at CERN called LEP, radiated 1.89 GeV of 90 GeV energy in synchrotron radiation per turn (2%) [17]. Replenishing this lost energy required 288 RF cavities powered by 36 klystrons [18], all of which take up valuable space within the ring while adding more points of failure.

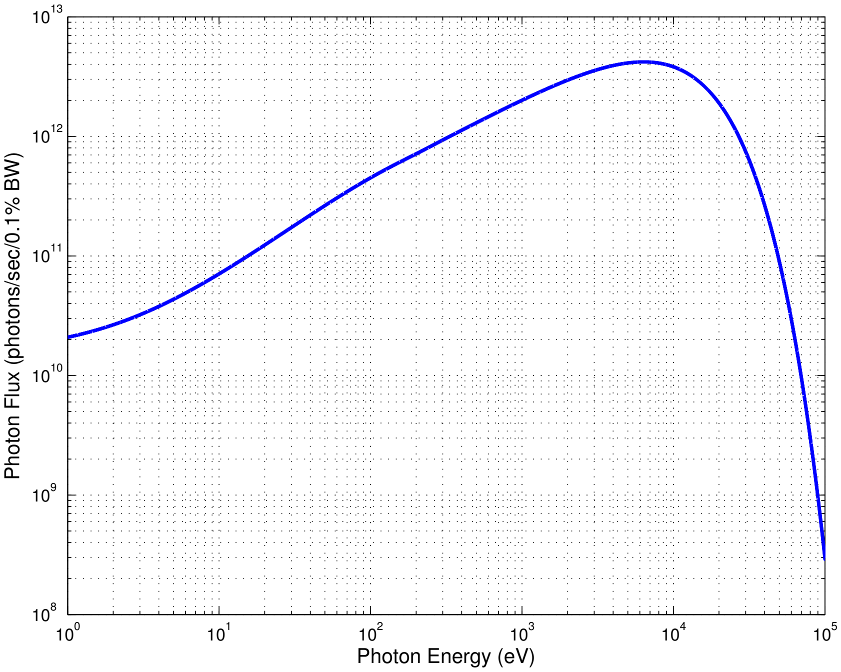

Figure 1.3: Calculated photon flux from a bending magnet at the ASLS. Data calculated using SPECTRA 8.0 [15] with the lattice simulation parameters: Energy = 3.0 GeV, $\rho = 7.29$ meters and $B = 1.37$ Tesla.

1.3.2 Diagnostic Beamlines

In contrast to being a limiting factor for large high energy rings, synchrotron radiation is a valuable resource for accelerator diagnostics and fundamental science. This section will discuss utilising synchrotron radiation for diagnostic purposes while the methods which use synchrotron radiation in broader scientific experiments will be described in Section 1.4.

Synchrotron radiation emitted from the bending beam retains many of the properties of the stored beam such as its three-dimensional profile, intensity and position and can be used to probe beam parameters. Two diagnostic beamlines have been constructed at the ASLS, the Optical Diagnostic Beamline (ODB) and the X-ray Diagnostic Beamline (XDB), and are described in detail in Reference [19]. An X-ray camera obscura setup situated on the XDB measures the transverse profile of the electron beam using the radiation from a bending magnet.

Longitudinal measurements of the electron beam are taken using equipment within ODB. Radiation emitted from a dipole bending magnet is broadband and covers the visible spectrum as well as infra-red and X-rays, as shown in Figure 1.3. The ODB uses an optical chicane to extract and route the visible part of the radiation spectrum to an optical bench located within an external hutch. A range of temporal measurement devices are housed on the optical bench, notably the Fill Pattern Monitor [20] for calculating individual bunch intensities in real time and a Bunch Purity device which uses an Avalanche Photodiode (APD) to measure the number of electrons within a bunch to high resolution [21].

Both of these beamlines will be referred to in the remainder of the thesis and provide important measurements of conditions within the ring.

1.4 Applications of Synchrotron Radiation

Modern synchrotron radiation based X-ray sources can be classed into four generations.

The first generation synchrotron radiation light sources were run parasitically from electron based particle colliders. Many scientists from diverse fields saw the advantages of using an intense flux, highly collimated X-ray source to conduct their experiments and would use the photons emitted in bending magnets of electron storage rings such as the Stanford Positron Electron Asymmetric Rings (SPEAR) at the Stanford Linear Accelerator Center (SLAC) [22].

Second generation sources were the first synchrotrons developed exclusively for X-ray based experiments, the first of which — the Synchrotron Radiation Source (SRS), was built at Daresbury Laboratory in England. Constructing facilities dedicated to producing synchrotron radiation produced an international community of scientists who have used the radiated photons to push forward the boundaries of their fields.

Third generation light sources were the first built to incorporate long straight sections between bending magnets. These long straights are used to house *insertion devices* which are long periodic arrays of magnets held close to the beam. As the beam traverses these magnetic fields they emit radiation with properties depending on the periodicity of the magnet arrangement. In a third generation light source, each bending magnet and insertion device provides a source of synchrotron radiation. All modern synchrotron based light sources currently being built are third generation sources, including the ASLS.

Fourth generation light sources are currently undergoing research and development at many facilities world-wide and involve the use of a relativistic electron source coupled with a long insertion device. Referred to as Free Electron Lasers (FELs), these devices provide a highly brilliant X-ray beam with a fine temporal structure that has proven valuable for time-sensitive experiments. They can also provide a highly coherent X-ray beam which is important for imaging techniques such as phase contrast imaging [23]. FELs are currently in operation in Germany (FLASH, Hamburg), USA (LCLS, SLAC) and currently in a testing phase at Spring-8, Japan (SCSS).

Photons from synchrotron radiation sources are used in the following ways:

Scattering: The most prevalent use of synchrotron radiation is to measure the underlying structure of a sample. A molecule of interest is formed into a crystal or another form with periodic structure; it is then placed into the path of a monochromatic X-ray beam which undergoes Bragg scattering with the sample. Detectors placed downstream measure two-dimensional intensity distributions which can be reconstructed into a three-dimensional representation of the sample.

Absorption: In this case a sample is again placed downstream in a field of monochromatic X-rays. By using gas chamber detectors to measure the photon flux before and after the sample, the absorption length of the material can be calculated. Absorption length is a function of energy, therefore as the energy of the X-rays is scanned the full absorption spectra can be taken. This enables the generation of an elemental map of the sample with the location and concentration of elements.

Fluorescence: The setup for a fluorescence experiment is similar to the absorption setup, with monochromatic X-rays incident on a target sample. A near 2π steradian detector is used to measure the fluorescence caused by the incident X-rays.

Other Such a brilliant source of X-rays is also used for a variety of other purposes, such as micro-machining, particle detector research and medical imaging/therapy.

All of the above methods have three common features:

1. Dependence on a high X-ray flux to reduce measurement times.
2. Collimation of the X-ray beam in order to measure the properties of a small part of the sample, by introducing slits into the X-ray beam until a small area is formed or focusing the X-rays using zone plates or silicon mirrors.
3. The precision beamline optics are optimised for flux throughput and any significant change in the stored beam requires retuning of the optics.

These features place stringent requirements on beam stability. Increasing the flux and reducing beam size will inevitably lead to coupled-bunch instabilities in the beam. These instabilities cause a large movement of the beam center-of-mass and reduce the X-ray flux to the beamline.

1.5 Coupled-Bunch Instabilities

Once the nominal stored current is injected into the storage ring, care must be taken to ensure it remains circulating for the beamline experiments. Charged particles require a vacuum if they are to be stored for any length of time – without a vacuum particles are quickly lost through interactions with the volume of air in the flight path. Creating a vacuum requires an infrastructure of vacuum pumps, valves and a metallic beam pipe which can withstand the forces of the pressure differential between vacuum and the environment.

The introduction of metallic components proximal to the captured charge, truncates the electric fields lines from the particles and consequently the stored particles interact with the beam pipe creating image charges which in turn create wake fields. These wake fields can couple the motion of multiple bunches, resulting in an unstable growth of particle movement called *coupled-bunch instabilities*. Coupled-bunch instabilities grow in strength at a rate proportional to the stored current. For a given ring configuration there will exist an amount of stored current where the growth rate of an instability will overcome natural damping effects. Any current injected after this threshold will cause the creation of coupled-bunch instabilities and destruction of the beam.

The transverse profile of the ASLS beam under the effects of vertical instabilities then horizontal instabilities is shown in Figure 1.4. An increase in the apparent transverse size of

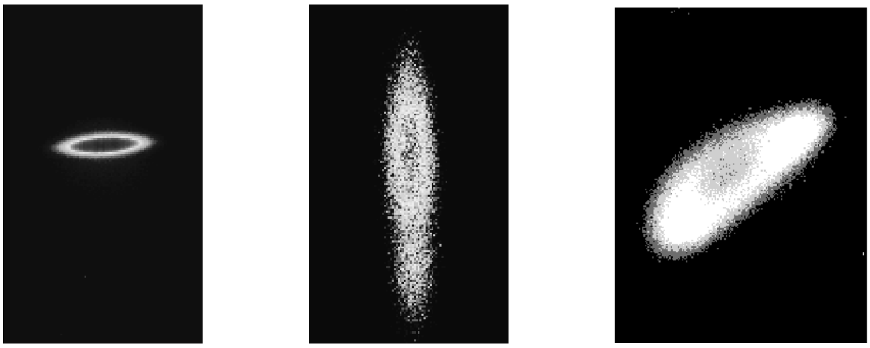

(a) Stable beam

(b) Vertical Instability

(c) Horizontal and Vertical Instability

Figure 1.4: Transverse beam profile showing the transition from stable to unstable beam. Data was taken on the XDB beamline using an uncalibrated CCD device. Initially at low stored currents the beam damps down to the profile shown in Figure 1.4a. Once the stored beam threshold is exceeded, the interactions between the particles and the environment cause coupled-bunch instability and consequently the vertical profile of the beam is enlarged (Figure 1.4b). Once the coupled-bunch threshold for the horizontal plane is reached the beam is spread out in both planes and the beamlines will see the transverse profile shown in Figure 1.4c.

the beam is an artifact of the Charge Coupled Device (CCD) camera integrating over many turns. The CCD measures the projection of the oscillating bunch center-of-mass, and is representative of what the beamline users will receive (as few beamlines can measure turn-by-turn beam movements). This will reduce the effective flux on sample and increase experimental time, reducing scientific output.

As the bunch begins to oscillate out of control it will move beyond the acceptance of the ring and will be lost, the cumulative effect of which will dramatically lower the lifetime of the ring. Particles will typically be lost at the point with the smallest transverse acceptance and will cause local heating and damage.

Therefore it is of vital importance to both the machine group and experimental users that beam instabilities are quickly diagnosed and controlled.

1.6 Conclusion

The creation of beam instabilities will affect all experimental work undertaken at the time and may damage sensitive components with localised heating. It is therefore important to both the accelerator group and the experimental users that coupled-bunch instabilities are diagnosed and controlled to prevent both damage to the machine and reduction in the X-ray flux available to beamlines.

To understand beam instabilities formation, it is important to recognize how the storage ring magnetic field traps the motion of stable beams and how the creation of wake fields begin to subvert the ability of the storage ring to store charged particles long-term. In the next chapter the physical laws which define accelerator physics will be discussed and examples of vital parameters will be taken from the ASLS storage ring.

Chapter 2

Accelerator Physics

Accelerator physics is associated primarily with the study of the creation, acceleration and behaviour of a trapped beam of particles. The coupled bunch instabilities which appear in the ASLS storage ring are characterised by the uncontrolled motion of particles normally contained within a magnetic lattice. All of the ring parameters corresponding to transverse motion are defined by the strength and placement of dipole bending magnets and higher order multipole focussing magnets. This chapter will present the physical laws that govern accelerators and introduces some accelerator formalisms that will be referred to in later chapters.

2.1 Electrodynamics

The fundamental description of an electromagnetic force acting upon a charged particle is the Lorentz Force,

$$\boldsymbol{F} = q(\boldsymbol{E} + \boldsymbol{v} \times \boldsymbol{B}), \tag{2.1}$$

where q is the charge of the particle, $\boldsymbol{v}$ is the velocity of the particle, $\boldsymbol{E}$ is the electric field and $\boldsymbol{B}$ is the magnetic field. The force on a particle from the magnetic field is always perpendicular to motion so only the electric field can change forward momentum and thus energy.

For a given velocity v and magnetic field strength B, the bending radius of a charged particle is given by [24]

$$\rho = \frac{mv}{qB} \ , \tag{2.2}$$

or,

$$\rho = \frac{p}{qB} \ , \tag{2.3}$$

where p is the momentum of the particle. This leads to a useful quantity, the *magnetic rigidity* of a particle,

$$B\rho = \frac{p}{q} \approx 3.3356p \ \text{(GeV/c)}, \tag{2.4}$$

where the last result is an approximation used when the quantities of interest are in natural units [25]. Magnetic rigidity describes how difficult it is to change the direction of a particle with a given momentum. It is what leads to higher energy accelerators requiring larger bending radii or higher strength magnetic fields*. For example, the magnetic rigidity for 3 GeV electrons is approximately 9.5 Tesla meters.

The motion of stored particles in the dipole fields is commonly referred to as the closed-orbit of the ring. As will be discussed later in this chapter, all transverse motion is a perturbation around this closed orbit.

In accelerator physics the coordinate system is based on the closed orbit of the beam as depicted in Figure 2.1. Particles are described using a six element vector, $[x, x', y, y', E, c\tau]$ where the parameters describe (in pairs) the horizontal, vertical and longitudinal dimensions of movement. The final variable $c\tau$ represents the *timing* of a particle as it goes through a fiducial location. Linkage between $c\tau$ and the energy is primarily through phase stability due to the RF cavities and this variable will not be referred to further in this thesis.

---

[*] for example, the LHC (7 TeV protons) is housed in the old Large Electron Positron Collider (LEP) tunnels (max 104.5 GeV electrons [26]) therefore the bending radius is the same, but the LHC dipoles are superconducting with a higher magnetic field.

2.2 Transverse Dynamics

2.2.1 Betatron Functions and Hill's Equation

Particle beams in synchrotrons are primarily focused through the use of quadrupole magnets, comprising of four magnetic tips alternating in polarity. Figure 2.2 shows the fields produced by a quadrupole magnet, and illustrates an important point — quadrupole magnets focus in one plane while defocussing in the other. Alternating sets of quadrupoles are needed to focus in both transverse planes, the net effect of which is that the particles oscillate in a focussed beam.

Quadrupole strength for a vertically focussing quadrupole is determined by the following equation [25]:

$$k = \frac{1}{B\rho}\frac{dB_y}{dx}, \tag{2.5}$$

where $B\rho$ is magnetic rigidity of beam and B_y is the vertical component of the magnetic field. By definition, k is positive when focussing in the vertical plane and negative when focussing in the horizontal plane.

The magnetic field strength increases linearly outwards from the center of the magnet, and symmetry considerations require that the field must be zero in the center and negative

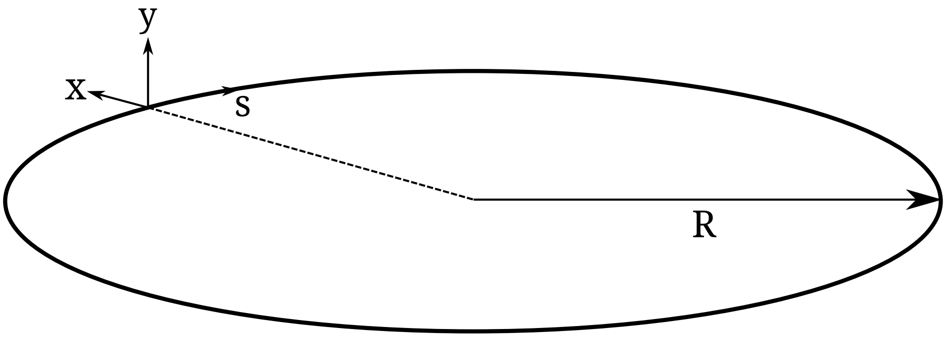

Figure 2.1: The particle coordinate system commonly used in accelerator physics. The $\boldsymbol{x}$ and $\boldsymbol{y}$ vectors form an orthogonal basis describing the transverse plane of particle movement. Not shown is the $\boldsymbol{z}$ vector which is in the direction orthogonal to both the $\boldsymbol{x}$ and $\boldsymbol{y}$ vectors. Shown instead is the $\boldsymbol{s}$ vector, which is similar to the $\boldsymbol{z}$ vector but follows the closed orbit of the ring. Increasing $\boldsymbol{s}$ moves the particle around the ring.

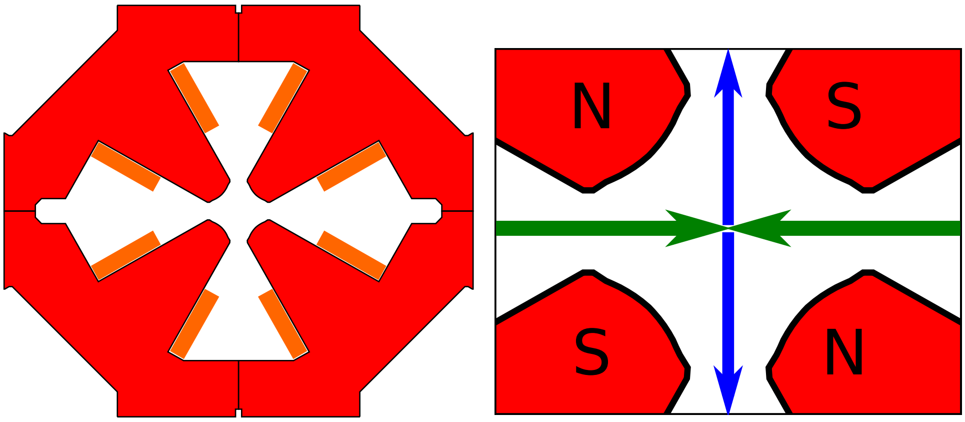

(a) Quadrupole magnet **(b)** Simplified diagram of forces within a quadrupole magnet

Figure 2.2: The magnetic field produced by an energised horizontal focussing quadrupole magnet used in the ASLS storage ring. The forces experienced by a negatively charged particle travelling away from the reader can be seen in Figure 2.2b, where the green arrows represent the horizontal forces and the blue the vertical. This configuration focusses in the horizontal while defocussing in the vertical.

either side of the vertical axis. Particles travelling through a thin quadrupole experience an angular shift of

$$dy' = \pm ky \, ds, \tag{2.6}$$

where the sign is chosen depending on the focussing plane of the quadrupole. Consequently the focussing effect is analogous to a spring with the restoring force increasing linearly with displacement. From here it can be inferred that the equations of motion should have the form of a harmonic oscillator,

$$y'' + k(s)y = 0, \tag{2.7}$$

where a dependence on the position in the ring has been introduced for focussing as the particle travels through the lattice. The focussing term is periodic, $k(s) = k(s + L)$ where L is the length of periodicity within the lattice, either the entire circumference or a single repeating cell from which the ring is built. For a more rigorous explanation of how to derive this equation from the Lorentz force and Maxwell's Equations the reader is referred to Lee [24].

A solution to this equation is known as Hill's Equation [25],

$$y = \sqrt{\beta(s)\epsilon}\cos(\phi(s) + \phi_0). \tag{2.8}$$

The solution is similar to that for a simple harmonic oscillator with the major difference being that both the amplitude (β) and the phase advance (ϕ) show a dependence on lattice position s due to the focussing elements being at discrete locations throughout the ring. Within the description of the amplitude given by Equation 2.8, there is an independent variable ϵ which relates to the width of the transverse beam distribution and will be discussed further in Section 2.3.

For Equation 2.8 to form a solution the two position-dependent variables must have the following relationship [25],

$$\phi(s) = \int \frac{ds}{\beta(s)}. \tag{2.9}$$

As the transverse position is defined according to Equation 2.8, the β variable describes an envelope of the maximum excursion of the particles captured within the focussing power of the multipole magnets.

An example calculation of these functions within the cell structure of the ASLS storage ring is shown in Figure 2.3. Vertical and horizontal betatron functions will change values in the opposite direction throughout a period due to the dual focus/defocus effects of each magnet. The combined-function bending magnets have been constructed such that they provide the majority of the horizontal defocussing quadrupole field.

2.2.2 Betatron Tunes

The vertical equations of motion of a particle can be calculated by beginning with the derivative of Equation 2.8,

$$y = \sqrt{\beta(s)\epsilon}\sin(\phi(s) + \phi_0), \tag{2.10}$$

$$y' = -\sqrt{\frac{\epsilon}{\beta(s)}}\sin(\phi(s) + \phi_0) + \left(\frac{\beta'(s)}{2}\right)\sqrt{\frac{\epsilon}{\beta(s)}}\cos(\phi(s) + \phi_0), \tag{2.11}$$

where Equation 2.9 has been used as $\phi' = \frac{1}{\beta}$. Considering a point in the lattice where $\beta' = 0$, the phase space (y, y') transcribes an ellipse with semi-axes of length $\sqrt{\beta\epsilon}$ and $\sqrt{\frac{\epsilon}{\beta}}$. As a

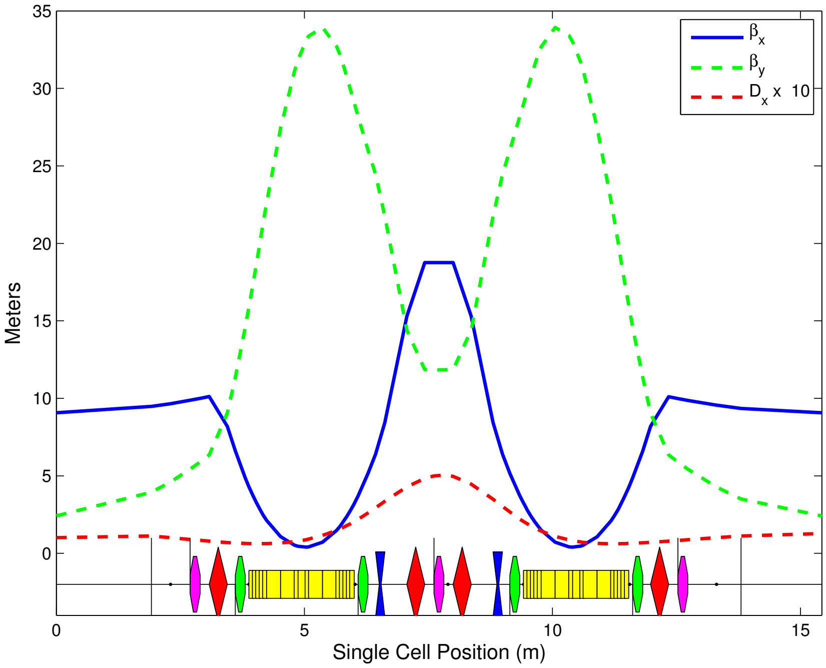

Figure 2.3: Single cell magnetic functions for a lattice with distributed dispersion in the straights calculated from a model of the ring where $(Q_x, Q_y) = (13.29, 5.216)$. The locations of the magnets within the cell are shown along the bottom axis. Note that the dispersion has been multiplied by 10 to improve readability on the same axis at the betatron functions.

particle travels through the lattice the ellipse rotates with a speed depending on the phase advance of the ring.

Consider a particle which travels from a location with an initial phase ϕ_0 around a complete circuit of the lattice. It will have experienced a phase advance of

$$\Delta\phi = \int \frac{ds}{\beta} \approx \frac{2\pi R}{\bar{\beta}}, \tag{2.12}$$

where R is the radius of curvature of the entire ring ($R \geq \rho$) and $\bar{\beta}$ is the *smooth betatron function* which assumes an equal focussing strength spread evenly around the ring. Therefore over each orbit of the ring a particle performs

$$\frac{\Delta\phi}{2\pi} = \frac{R}{\bar{\beta}_{x,y}} = Q_{x,y} \tag{2.13}$$

circuits of the phase ellipse. This number of phase ellipse orbits ($Q_{x,y}$) is known as the *tune* of the ring.

Typically the tune is split into integer and fractional components. In most cases the fractional part of the tune is the most useful as it is the only part that can be measured at a single point in the ring. At ASLS the nominal tunes are $(Q_x, Q_y) = (13.29, 5.216)$.

The choice of vertical and horizontal tunes, known as the *working point* of an accelerator, is important and is usually decided early in the design process. To prevent the creation of resonant motion within the ring due to magnet imperfections it is critical to ensure that the fractional part of tunes are not simple integer divisors (i.e. $\frac{1}{2}, \frac{1}{3}, \dots$) [24]. Magnet imperfections add a driving term to the right hand side of Equation 2.7 which can add coherently over many turns and cause the unwanted excursion of particles.

Some of the resonances that are to be avoided are

Integer resonance	$k.Q_{x,y} = n$	
Sum resonance	$k.Q_x + l.Q_y = n$	n
Difference resonance	$k.Q_x - l.Q_y = n$	

where k, l and n are integers. Resonances are described by their cause and their *order* where the order is calculated as $k + l$.

Figure 2.4 shows a plot of resonance lines and their relative locations to the nominal working point of the ASLS storage ring. Each line has a *stopgap* width which describes how the strength of the resonance changes as it is approached by the working point. If the working point of the accelerator approaches or crosses any of the resonance lines then the beam lifetime will be reduced.

2.2.3 Beam Lifetime

Electrons are placed into the storage ring from the injection chain where they are accumulated and stored. Over time the current will decay roughly exponentially as trapped particles are lost with dominant loss mechanisms changing as the beam parameters change,

$$I(t) \approx I(0) \exp(-t/\tau_l) \tag{2.14}$$

where $I(t)$ is the stored current at time t and t_l is the *lifetime* of the beam, typically measured in hours.

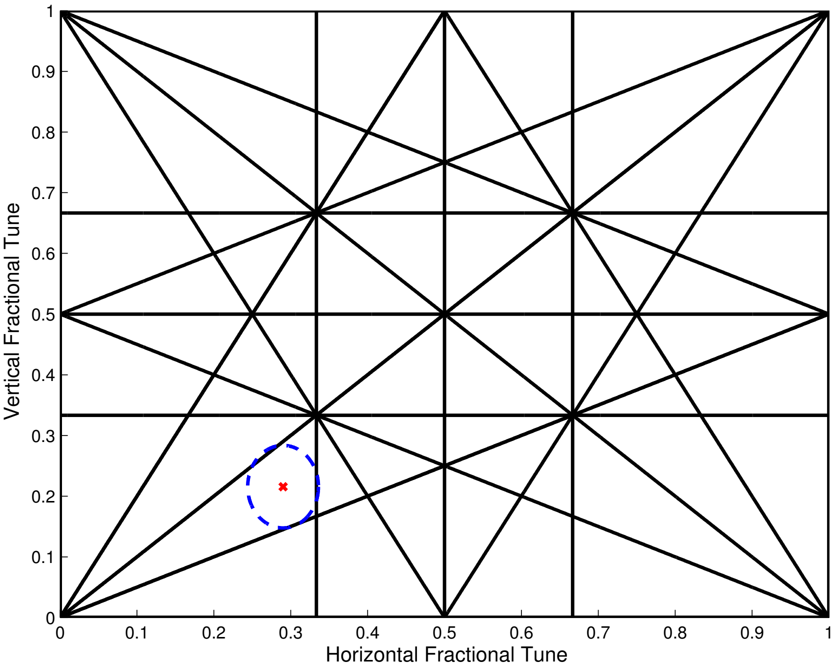

Figure 2.4: The tune resonances up to the third order, shown without changes in stopgaps. If the beam tunes approach or cross any of these lines the beam lifetime can be severely compromised. The fractional part of the nominal working tune of the ASLS storage ring $(Q_x, Q_y) = (0.29, 0.216)$ is shown with a red marker. Chromatic effects will cause a tune spread which can force the tune of specific particles near resonance lines. The blue ellipse shows the tune phase space due to a 0.1% energy spread combined with a chromaticity of $(\xi_x, \xi_y) = (3.5, 13)$.

The different mechanisms which lead to beam loss are [27, 28]:

- Elastic and inelastic scattering from residual gas nuclei.
- Elastic and inelastic scattering off gas electrons.
- Touscheck or intrabeam scattering.

For a ring with a well-conditioned vacuum system, the dominant method of particle loss is Touschek (intra-beam) scattering. This involves two electrons inelastically scattering in the transverse plane and falling outside the momentum acceptance of the ring. The particles then interact with the beampipe material through bremstrallung and are lost. Over the span of a 12 hour user beam shift the current will drop from 200 mA to ≈ 155 mA as shown in Figure 2.5.

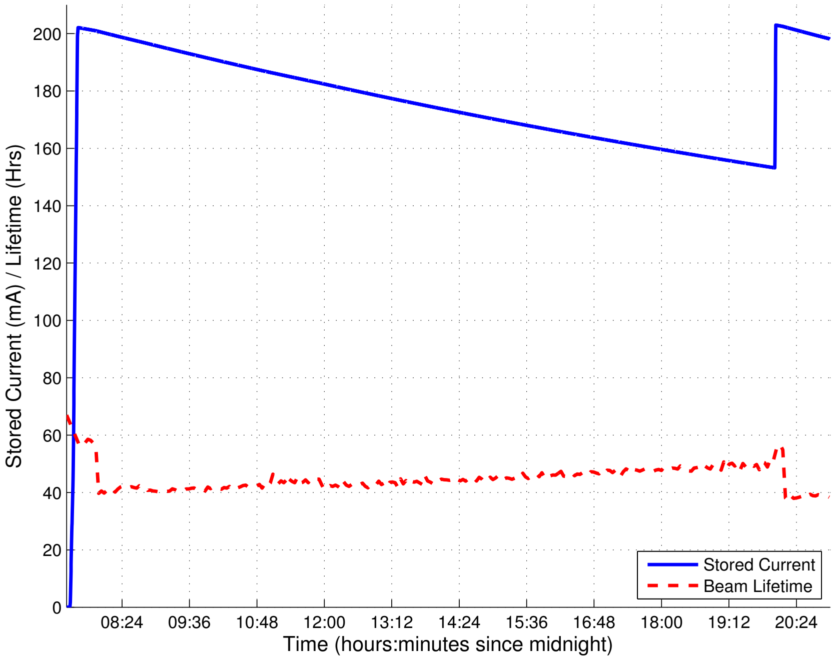

Figure 2.5: The measured current and lifetime for a 12 hour user-time shift. As this measurement was taken prior to the commissioning of the transverse feedback system, the lifetime was compromised by the high lattice chromaticity $(\xi_x, \xi_y) = (3.5, 13)$.

Lifetime can be affected by parameters of the storage ring lattice such as the acceptance of the ring, dynamic aperture and transverse coupling. An in-depth study into the mechanisms of beam loss in the ASLS storage ring is presented in Reference [29]. Synchrotron radiation experiments are dependent on the integrated flux available to beamlines which is proportional to the stored current. Consequently increasing the lifetime of the ring is directly beneficial to all synchrotron users.

2.2.4 Transverse Coupling

The equations describing the tune assume that particle motion can be decomposed into two non-interacting planes. Each particle will also travel through the major axes of the quadrupole magnets leading to uncoupled motion in the x and y planes.

Sources of coupling arise from two families of magnetic fields: solenoids and skew quadrupoles. Solenoidal fields are typically found in electron cooling rings or near interaction points in particle colliding rings. In electron storage rings the typical source of coupling is in the form of

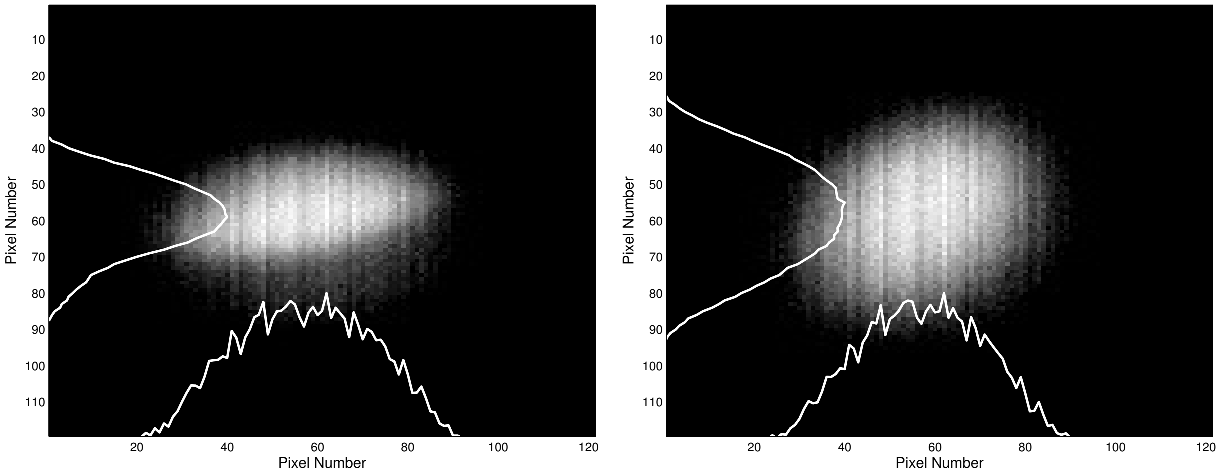

(a) Minimum Coupling (0.009%)

(b) 1% Coupling

Figure 2.6: The effect of linear coupling on the transverse beam size. Beam profile measured using a CCD installed on the XDB beamline. Shown in white are the horizontal and vertical projections of each image.

skew quadrupole fields arising from magnet field errors.

Magnet errors in positioning and roll can introduce coupling between the x and y motion of a particle. If the closed orbit does not pass through a major axis of a quadrupole, the bunch will experience both a focussing and defocussing force (one in each plane) simultaneously. This will cause amplitude coupling between the two planes, such that movement in the y plane can be observed in the x plane and vice versa.

The amount of coupling present for a given lattice is described in this thesis as the ratio between the horizontal and vertical beam sizes (more specifically the *emittances*, described in Section 2.3). The coupling is presented as a percentage with higher percentage coupling leading to larger, rounder beams. Figure 2.6 shows a comparison in beam sizes between the minimum coupling ($\approx 0.009\%$) and the user-mode coupling ($\approx 1\%$).

Manipulation of the coupling of a storage ring lattice can enable control of the vertical emittance and can also affect the beam lifetime. A heavily coupled beam becomes more round and less dense, reducing Touschek scattering and increasing the stored beam lifetime [29].

Coupling is controlled in the ASLS storage ring by 28 skew quadrupole fields which are implemented as extra windings on two sextupoles per unit cell [30]. Control of the vertical emittance through coupling has been a focus of the machine group, and this has lead to fine control over the linear coupling of the ring [31].

2.2.5 Dispersion and Chromaticity

Accelerated particles arrive at the injection point in a storage ring with a natural energy spread. Combined with the emission of synchrotron radiation this will lead to a distribution of energies within a bunch.

The closed orbit of an accelerator lattice is calculated for a particle with a given energy E_0. A particle travelling through a dipole with energy $E_0 \pm \Delta E$ has a different magnetic rigidity and so will be deflected to a different degree. This will force the particle to deviate off the closed orbit and away from the center of the quadrupoles, essentially creating a new closed orbit for these particles. In this way, the change in the energy of the particle is coupled into transverse motion. This effect is called *dispersion* and its effect on the horizontal motion of the particle is described by

$$x_D = x + D(s)\frac{\Delta p}{p}, \tag{2.15}$$

where $D(s)$ is the *dispersion function* of the lattice and x_D is the perturbed horizontal position due to the dispersion. Chromatic effects have been ignored and the betatron tune is assumed to remain constant. Figure 2.3 shows how $D_x(s)$ changes through a single cell of the storage ring.

Now having considered the coupling into the horizontal plane from the dispersive effects of dipole fields, the next magnet family to study is the quadrupole focussing magnets. Recall the equation for the focussing strength of a quadrupole, Equation 2.5. The inverse dependence on the magnetic rigidity of the particle implies that particles with different energies will experience different focussing strengths. Low energy particles possess a lower magnetic rigidity, will experience a stronger focussing force and therefore exhibit a higher betatron oscillating frequency. Introducing an energy dependence into the focussing strength of the ring $k(s)$ causes a particle with an energy of $E_0 + \Delta E$ to oscillate at a different betatron tune compared to the nominal energy particles. The change in focussing strength is given by,

$$\Delta k_x = \left[-\frac{2}{\rho} + k(s) \right] \frac{dp}{p} + O\left(\left[\frac{dp}{p} \right]^2 \right) \approx k_x \frac{dp}{p}, \tag{2.16}$$

$$\Delta k_y = -\, k(s) \frac{dp}{p} + O\left(\left[\frac{dp}{p} \right]^2 \right) \approx -k_y \frac{dp}{p}, \tag{2.17}$$

where ρ is the bending radius of the particle in the bending magnet dipole field, $K = \frac{B_1}{B\rho}$ and $B_1 = \frac{\partial B_y}{\partial x}$ [24]. From these equations it can be seen that the change in the focussing strength of the ring is linearly dependent on the energy deviation of the particle. Recalling that the tune of the ring is dependant on the focussing strength of the lattice an energy deviation will result in an alteration of the tune of off-energy particles. Stronger focussing lattices (large k) will be affected more by energy deviations then weaker focussing lattices.

This change in tune due to a change in energy is called the *chromaticity* of a lattice and is described by

$$\frac{\Delta Q}{Q} = \xi \frac{\Delta p}{p} \tag{2.18}$$

where ξ is the chromaticity and the change in tune has been normalised to the nominal lattice tune. It will be shown later how this tune spread can be utilised to provide damping against instabilities in the storage ring. As this effect occurs for both focussing and defocussing quadrupoles, chromaticity is defined for both horizontal and vertical planes. Before utilisation of the feedback system described in this thesis, the standard lattice for experimental beamline use had a normalised chromaticity of $(\xi_x, \xi_y) \approx (3.5, 13)$.

If a 0.1% standard deviation in the distribution of the energy of particles being injected into the ring is assumed, chromaticity can lead to tune spreads of approximately 0.046 in the horizontal and 0.068 in the vertical planes. This is sufficient to cause some particles to begin to interact with strong resonance lines around the working point. A storage ring without chromatic corrections will have a have a nominal tune spread due to energy spread called the *natural chromaticity.* The storage ring lattice at the ASLS has a natural chromaticity of $\xi = (-28, -27)$ [32] which should be corrected using high order multipole magnets such as sextupoles.

Before discussing how sextupoles can correct chromatic aberrations in the magnetic lattice, the form of magnetic field needed requires investigation. Equations 2.16 and 2.17 show that the focussing correction must be linearly dependent on energy deviation. The field gradient of a sextupole magnet is described by [24]

$$\frac{\Delta B_y}{B\rho} = \frac{1}{2B\rho}\frac{\partial^2 B_y}{\partial x^2}(x^2 - y^2), \tag{2.19}$$

$$\frac{\Delta B_x}{B\rho} = \frac{1}{B\rho}\frac{\partial^2 B_y}{\partial x^2}(x.y). \tag{2.20}$$

If the horizontal and vertical displacement due to dispersion (Equation 2.15) is substituted for x and y the following relationship is found [24]:

$$\frac{\Delta B_y}{B\rho} = -\left[S(s)D(s)\frac{\Delta p}{p}\right]x_D - \frac{S(s)}{2}(x_D^2 - y_D^2) - \frac{S(s)}{2}\frac{\Delta p}{p}D^2(s), \tag{2.21}$$

$$\frac{\Delta B_x}{B\rho} = -\left[S(s)D(s)\frac{\Delta p}{p}\right]y_D - S(s)x_D y_D, \tag{2.22}$$

where $S(s)$ is the effective sextupole strength,

$$S(s) = \frac{1}{B\rho}\frac{\partial^2 B_y}{\partial x^2}. \tag{2.23}$$

The first term on the right hand side of Equations 2.21 and 2.22 show a linear dependence on the energy deviation ($\frac{dp}{p}$), therefore sextupoles placed in non-zero dispersion regions ($D(s) \neq 0$) can be used to correct the chromatic aberration of a lattice.

These magnets are known as *chromatic sextupoles.* In the DBA cells that constitute the ASLS storage ring the chromatic sextupoles are situated between the dipoles, in the region of highest dispersion. Since the chromaticity needs to be corrected in both transverse planes, there are two families of chromatic sextupoles.

Care must be taken with the position of the chromatic sextupoles however, as errors in the magnetic fields can create geometric aberrations within the lattice. Sextupole magnets must be designed to provide a field strength that will correct the natural chromaticity of the ring but as discussed in Chapter 4, it is beneficial for storage rings to run at a slightly positive chromaticity to control instabilities.

2.3 Emittance, Acceptance and Dynamic Aperture

When determining the equations of motion for a particle contained in a magnetic lattice comprising of quadrupole fields, a solution is

$$x = \sqrt{\beta(s)\epsilon}\cos(\phi(s) + \phi_0), \tag{2.24}$$

where $\beta(s)$ is proportional to the envelope of the transverse particle motion around the lattice. The independent variable ϵ is proportional to the standard deviation of the transverse distribution of particles within a bunch. $\beta(s)$ is a related to lattice parameters, while ϵ is a property of the collection of particle trapped within the magnetic fields of the lattice. The particle in the beam with the largest displacement will traverse a phase ellipse described by Figure 2.7a, with semi-axis lengths of $\sqrt{\epsilon/\beta}$ and $\sqrt{\epsilon\beta}$. The area of this ellipse is $\pi\epsilon$ (mm.mrad) and ϵ is called the *emittance* of the ring. This area represents the total phase space available to the particles and is a conserved quantity for a collection of particles in a closed system, neglecting effects such as synchrotron radiation. A beam which has been stored for a time much longer than the natural damping rate of the ring can be approximated as a closed system, fulfilling phase space conservation when considered over a small number of turns [25].

The effect of emittance on experimental measurements is found through its relationship to the primary figure of merit in synchrotron light sources, *brilliance*, measured in photons per second per milliradian. Brilliance can be thought as analogous to *luminosity* in particle colliders in so far as it is a metric for light sources.

Brilliance from a bending magnet is described by

$$B = \frac{I}{\pi^2 \epsilon_x \epsilon_y}, \tag{2.25}$$

where I is the stored current and ϵ_i is the emittance in the specified plane of motion. From this description it is clear that light sources must endeavour to achieve low emittance lattices to increase the number of photons emitted per unit solid angle for a given stored current.

At any point in the ring, a stored collection of particles will have a normal distribution with a characteristic width of σ. Figure 2.7b illustrates a typical beam distribution and how σ is measured as the standard deviation. This parameter can be measured directly using

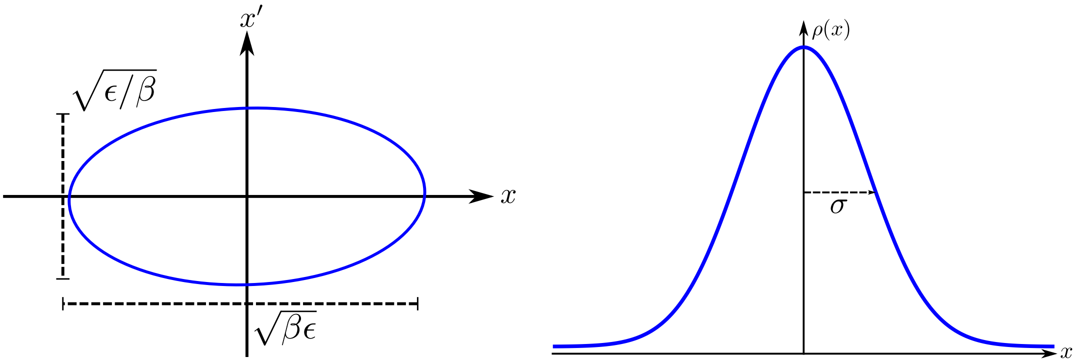

(a) An example phase ellipse for a collection of particles near a focussing quadrupole.

(b) The distribution of particles within a bunch follows a normal distribution with a standard deviation of σ.

Figure 2.7: Two representations of the phase space of a bunch of particles. Figure 2.7a represents the phase ellipse of a particle with the greatest displacement within a bunch. Each time the particle traverses this location it will have moved around this ellipse, while the ellipse itself will rotate depending on the measurement point in the ring. The particles trapped within a magnetic lattice will tend to form normal distributions of position at a given measurement point as shown in Figure 2.7b. The standard deviation of the distribution is an important parameter for calculating the emittance of a beam.

synchrotron radiation profile monitors [33] such as the monitor installed on the XDB in the ASLS storage ring. As the phase ellipse rotates according to $\phi(s)$, the value of σ will depend on the local value of $\beta(s)$ and the position of the bunch to specific focussing elements. Particles travel around an ellipse with semi-axes of $\sqrt{\epsilon/\beta}$ and $\sqrt{\epsilon\beta}$, thus σ is related to the emittance in electron storage rings by [25],

$$\epsilon = \frac{\sigma^2}{\beta}, \tag{2.26}$$

where β is the betatron function calculated at the point where σ is measured (neglecting dispersion). The *acceptance* of a ring is described as the largest excursion a particle can make before it impinges on a physical barrier in the ring. In storage rings this is first defined by the beam pipe, and then reduced as insertion devices and other in-vacuum devices are introduced. The smallest acceptance object is called the *defining aperture* of the ring and can be chosen such that the beam is preferentially lost at a given point in the ring, such as the primary collimator in the LHC [34] or a set of scrapers within an electron storage ring. These defining apertures are used to prevent damage to components sensitive to beam loss induced heating.

The physical acceptance of the ring defines the maximum available x/y phase space for particles but this maximum aperture is only achieved in an ideal machine without imperfections such as magnet errors and geometric aberrations within the lattice. Such imperfections can lead to areas within the beam pipe acceptance where particles will be preferentially lost. This reduced acceptance is called the *dynamic aperture* of the ring. Figure 2.8 shows how the phase ellipse for a particle is distorted by a third order resonance as a fraction of displacement. Distortion of the phase ellipse will eventually result in a separatrix between stable and unstable points in the ring. If the seperatrix is within the acceptance of the ring, there will be a drop in lifetime as particles move into unstable locations through quantum emission and excitation. A reduction in dynamic aperture will also reduce the injection efficiency of the ring as injected particles will have a large distribution of positions and energies before being damped through synchrotron radiation emission and will not all be within the acceptable phase space.

In the ASLS storage ring, the effect of chromaticity on the dynamic aperture manifests itself in a dramatic loss of lifetime at high chromaticities, which can be seen in Figure 2.9.

2.4 Insertion Devices

The main feature of third generation synchrotrons is the inclusion of long straight beampipe between bending sections for the inclusion of In-Vacuum Undulators (IVUs) - long sections of magnets with a periodic magnetic field. Insertion devices fall into two broad categories depending on their periodicity: *undulators* which have a longer period over their length and *wigglers* which have series of alternating magnets and a short period. Figure 2.10 shows how a particle travels through the periodic magnetic field in an insertion device.

The dipoles used in a storage ring have a fixed bending radius such that their bending angles sum to 2π. Particles with the nominal stored energy travelling through the dipole fields emit radiation in an energy spectrum according to parameters of the region such as the bending radius and magnetic field strength. Forming an integral part of the storage ring, bending magnet fields cannot be changed if the experimentalists wish to change the spectrum

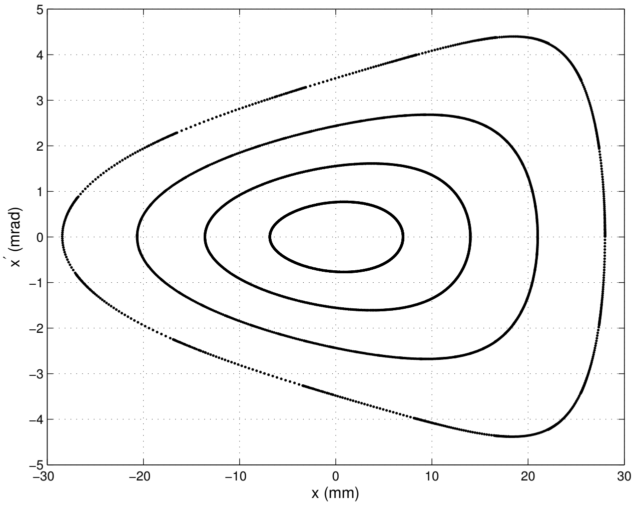

Figure 2.8: Phase space distortions due to a third order resonance. A series of particles with increasing displacements were tracked through a model of the ASLS storage ring. To accentuate the effect, the horizontal tune of the lattice was shifted to 0.3 and the effects of synchrotron radiation were neglected.

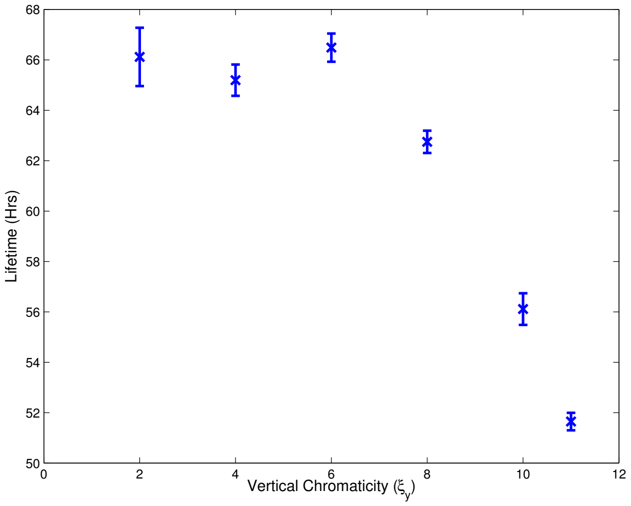

Figure 2.9: The change in lifetime versus vertical chromaticity. Data was taken with a stored current of 200 mA, no insertion devices and the transverse feedback system operational.

As the chromaticity is increased, the dynamic aperture of the lattice shrinks. Initially the dynamic aperture is larger than the acceptance so small changes in chromaticity do not have a sizable difference in the lifetime. After a chromaticity of approximately 6, the lifetime drops dramatically.

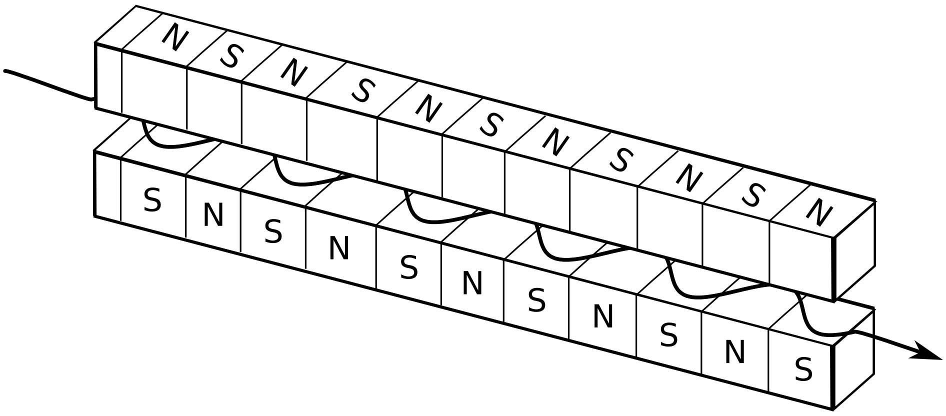

Figure 2.10: The path of a particle travelling through an insertion device. Synchrotron radiation is emitted as the particle's path is bent by the periodic dipole fields. The spectrum of the radiation is defined by the periodicity and strength of the field.

of the emitted radiation. Insertion devices are designed to minimise changes in the transverse parameters of stored electrons. Sets of correctors or quadrupoles at the entrance and exit of the insertion device are used to correct any changes in the tune or orbit of the beam. This allows the users of a beamline to alter the spectrum of energies without significantly disturbing the beam and the resultant X-rays for other users.

The transverse motion of a particle in a weak undulator field will be non-relativistic and the emitted radiation will be monochromatic at the Lorentz contracted oscillation frequency of the particle [35]. As the strength of the magnetic field increases, the transverse motion becomes more relativistic and the sinusoidal motion is distorted introducing harmonics of the fundamental frequency. At the highest end of magnetic strength, the harmonics corrupt the signal such that the output spectrum resembles that of a dipole bending magnet where the flux is multiplied by the number of periods in the magnetic field. This way, wigglers act as a series of dipole magnets, while undulators produce a lesser flux with a more monochromatic spectrum. For a more detailed study into the radiation produced by insertion devices, the reader is referred to Chapter 11 of Wiedemann [35].

As this thesis is concerned with the creation of instabilities arising in third generation light sources, the question is whether the addition of these strong periodic magnet arrangements into the lattice can lower the instability threshold of the ring. In the next chapter it will be

Table 2.1: Specifics of the three in-vacuum insertion devices installed in the ASLS storage ring.

Insertion Device	Length (m)	Minimum Height (mm)
IVU03	3	6.60
IVU05	2	6.06
IVU13	3	6.60

shown that a particular type of instability, the resistive wall instability, is sensitive to the height of the beam pipe. The undulators currently installed in the ASLS storage ring are in-vacuum devices, which means that the magnet assembly is held in the same high vacuum environment the beam travels through. This is to increase the effective magnetic field strength by bringing the undulator magnets as proximal to the beam as possible, approximately 6 mm for IVUs installed at the ASLS, dramatically reducing the effective beam pipe height from 35 mm. The minimum gaps for the IVUs present in the ASLS storage ring are shown in Table 2.1. To reduce discontinuities in the beam pipe at the IVU locations due to this change in height, *tapers* are installed to spread the change in height over a longer distance. Although these tapers reduce the gross discontinuities between taper and beam pipe, they are fixed at both ends and as such bend and warp as they move creating cavities which can induce instabilities.

Wigglers alternatively have their assembly outside the beam pipe and so do not alter the beam environment directly, though the strong dipole magnets can cause tune shifts due to the focussing effects at the edges of the dipole fringe fields. This is compensated in the ASLS storage ring using quadrupoles and a feed-forward look-up table.

The insertion devices both increase the coupled-bunch instability strengths and significantly reduce the acceptance of the ring. At the ASLS the vertical chromaticity must be increased from 2 to 13.5 in order to prevent the formation of damaging coupled-bunch instabilities. The addition of a transverse feedback system can allow for a reduction in chromaticity to the designed vertical chromaticity of 2 increasing the lifetime and the integrated flux available for users. How these instabilities are created, and the equations that govern their strength are discussed in the next chapter.

2.5 Design Parameters of the ASLS Storage Ring

The ASLS storage ring was designed by studying the effects of the physics described in this chapter. Table 2.2 shows the nominal design parameters of the ASLS storage ring. Actual operating parameters can deviate from these design values due to optimisation techniques such as lifetime scans or drifts in magnet strength.

Although the physics described in this chapter enables the creation of a magnetic lattice to trap and focus electrons for the purpose of producing synchrotron radiation, the equations assume a single macro-particle and make no reference to the metallic environment surrounding the vacuum. In the next chapter the model will be expanded to multiple bunches and the effect of the beampipe on the creation of coupled-bunch instabilities will be investigated.

Table 2.2: Operating Parameters of the Australian Synchrotron Storage Ring

Parameter	Symbol	Unit	Value	Ref
Energy	E	GeV	3.0133	[36]
Circumference	C	m	216	
Ring Radius	R	m	34.38	
Revolution Frequency	f_0	MHz	1.3880	
Harmonic Number	M		360	
Cavity Frequency	f_{rf}	MHz	499.654	
Horizontal Tune	Q_x		13.291	
Vertical Tune	Q_y		5.220	
Synchrotron Tune	Q_s		0.0105	
Nominal Stored Current	I_{max}	mA	200	
Momentum Compaction	α		0.00211	[36]
Slip Factor	η		0.0019	
Relativistic Gamma	γ		5871	
Zero Current Bunch Length	l	ps	22.3	[37]
Bending Magnet Field	B	T	1.3	[38]
Magnetic Bending Radius	ρ	m	7.29	

Chapter 3

Coherent Dynamics Theory

Coupled-bunch instabilities result in upper thresholds on achievable current when the growth rate of an instability exceeds the natural damping rate of the ring. As the instability growth rates rise proportionally with the stored current, there exists a point where the lattice no longer damps the motion of the beam and the motion will become unstable.

While the previous chapter described the physics behind the transverse motion of particles stored in an accelerator's magnetic lattice, most of the relationships used in accelerator physics are derived from single particle dynamics. These simpler equations neglect the electromagnetic fields self-generated by the beam. Wake fields are generated at any point in the ring where the electric field from beam induced image charges no longer cancel the electric field from the stored electrons. Discontinuities in the ring and finite resistivity of the beam pipe are the most common sources of wake field generation and beam instabilities. As the intensity of the beam increases, the self-generated wake fields will ultimately cause the beam to become unstable. The current at which the beam becomes unstable is called the *instability threshold* of the ring and represents the amount of stored beam where the combined growth rate of instabilities are equal to the total damping rate of the ring. Any additional current beyond the threshold will cause the beam to become unstable. Before the introduction of the active transverse feedback system described in this thesis the current threshold (at the designed chromaticity of $(\xi_x, \xi_y) = (2, 2)$) due to instability formation was 60 mA.

Measurements of the beam stability threshold relative to the lattice chromaticity without

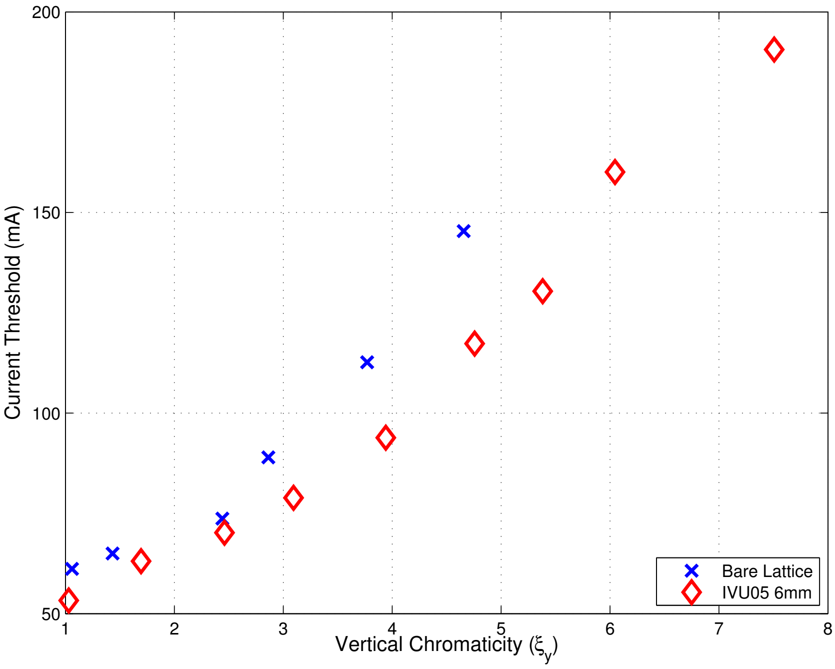

Figure 3.1: Instability thresholds for the ASLS storage ring before and after the introduction of an insertion device. The user-mode lattice in operation without active feedback relies on a chromaticity of $(\xi_x, \xi_y) = (3.5, 13)$ to raise the instability threshold with three IVUs at their minimum gaps of 6.0, 6.0 and 6.6 mm.

the influence of the active feedback system are shown in Figure 3.1. The introduction of an IVU lowers the current threshold due to an increase in the *impedance* of the ring, a measure of the electromagnetic coupling between the particles and their environment. Initially the lattice chromaticity was increased from $(\xi_x, \xi_y) = (2, 2)$ to $(\xi_x, \xi_y) = (3.5, 13)$ to compensate for the lowered current threshold. This increased chromaticity enabled the storage of the nominal 200 mA of current and caused the detrimental side-effects outlined in Section 2.2.5 including a reduction of the dynamic aperture, beam lifetime and injection efficiency.

To correctly predict the onset of instabilities the model of the particle movement within the magnetic lattice must be expanded from a single particle harmonic oscillator description to include multiple *macro-particles*. Each macro-particle represents a slice of the beam at a given longitudinal coordinate. In the case of storage rings with long bunch lengths, such as the Proton Synchrotron (PS) at CERN each bunch will have multiple macro-particles. For a ring such as the ASLS storage ring (where the bunch lengths are smaller) individual bunches will each be represented by a single macro-particle.

The science behind the creation and evolution of wake fields will not be covered in detail, rather only the specific results relevant to the data analysis in this thesis will be described. For a more in-depth treatment of the physics surrounding coherent dynamics the reader is referred to Chao [39] and Ng [40], both of which provide rigorous derivations of the properties discussed.

3.1 Betatron Tune Shifts

The particles trapped within the lattice magnetic fields oscillate in each plane of motion with a frequency called the tune ($Q_{x,y}$) dependent on the focussing strength of the lattice, $K(s)$. Under the *smooth approximation* it is assumed that the focussing strength of the ring is spread evenly along the ring's circumference which allows the longitudinal dependence to be neglected, $K(s) \rightarrow K$.

Using this approximation, the transverse betatron tunes are

$$Q_{x,y} \approx \frac{R}{\langle \beta_{x,y} \rangle} \tag{3.1}$$

where R is the radius of the ring and $\langle \beta \rangle$ is the average betatron function of the ring,

$$\langle \beta_{x,y} \rangle = \frac{\oint_C \beta_{x,y} ds}{\oint_C ds} \tag{3.2}$$

and therefore the equations of motion for the transverse plane are

$$x'' + \left(\frac{Q_x}{R} \right)^2 x = 0 \quad \text{and} \tag{3.3}$$

$$y'' + \left(\frac{Q_y}{R} \right)^2 y = 0. \tag{3.4}$$

Consider a perturbation in motion that is linear in y, in the form $F_y.y$ where F_y is the perturbing force. This introduces a driving term to the right hand side of Equation 3.4 [39],

$$y'' + \left(\frac{Q_{y0}}{R} \right)^2 y = F_y.y, \tag{3.5}$$

where the subscript 0 has been appended to Q_y to refer to the *unperturbed* or *bare* tune of the lattice i.e. the solution to the equations of motion without the driving force F_y.

The effect of the forcing term is to induce a change in the tune of the system,

$$Q_{y0}^2 \rightarrow Q_{y0}^2 - F_y R^2. \tag{3.6}$$

For a small perturbation ($F_y R^2 \ll Q_{y0}^2$) the tune shift is given by [39],

$$\Delta Q_y = Q_{y0} - Q_y = -\frac{F_y R^2}{2Q_{y0}}, \tag{3.7}$$

where the resulting tune shift ΔQ_y is complex.

To understand the importance of this result let us consider the motion described by Equations 3.3 and 3.4. As discussed in Chapter 2 the equations of motion describe a particle trapped within a harmonic potential well, leading to oscillatory solutions. One valid solution for the transverse equations of motion is

$$y(s) = A \exp\left(-i\frac{Q_y}{R}s\right), \tag{3.8}$$

where R is the ring radius and Q_y is the tune of the system including any shifts from driving terms. Since the tune shift can be complex the resulting solution will have two parts — an oscillatory exponential where the tune-shift is real and an exponential growth or decay if the tune shift is imaginary. Uncontrolled exponential growth will cause particles to be lost quickly at the beam pipe surface. It is therefore important to understand the origin of the driving terms which create tune shifts and ensure that any potentially damaging imaginary tune shifts are minimised.

Large tune shifts will arise from instabilities caused by the non-zero conductivity of the beam pipe and discontinuities in the beam environment. The source and calculation of these coupled-bunch instabilities is important during ring design and operations.

3.2 Charged Particle in an Ideal Vacuum Pipe

A stationary bunch of charged particles produces an isotropic electric field described by Gauss's law. As a bunch is accelerated the field lines contract to an opening angle of approximately $\frac{1}{\gamma}$ perpendicular to the direction of motion and when $\gamma \gg 1$ the field approximates a transverse disc travelling with the particles at relativistic velocities (see Figure 3.2) [41].

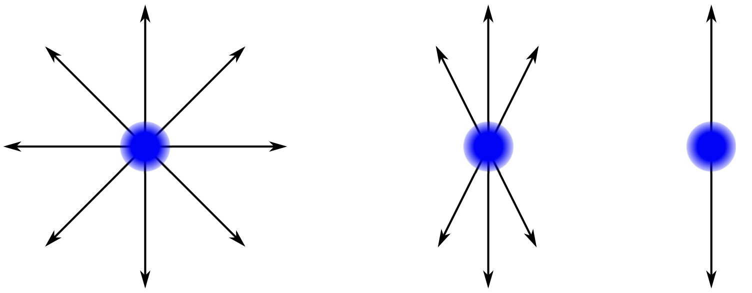

(a) $\beta = 0$ **(b)** $\beta \approx 0.1$ **(c)** $\beta \approx 1$

Figure 3.2: The electric fields from a charged particle as it increases in speed. Here $\beta = \frac{v}{c}$ and the plane of travel is horizontal.

The electric field from a particle with charge q can be calculated using Gauss's Law by drawing a pillbox with radius r and small length around the charge,

$$E_r = \frac{2q}{r}\delta(s - ct), \tag{3.9}$$

where the E_r is the magnitude of the electric field component in the radial direction $\hat{r}$, δ is a Dirac delta function and s is the longitudinal position of a particle which charge q. Applying Ampere's law to the previous equation [39] leads to

$$B_\theta = \frac{2q}{r}\delta(s - ct), \tag{3.10}$$

where $\boldsymbol{\theta}$ is the azimuth vector in the cylindrical coordinate system and B_θ is the magnitude of the magnetic field in the θ dimension. Consider a particle moving along the central axis of a *perfectly conducting* circular beam pipe — the effect of the conducting material is to truncate the field lines, creating image charges and image currents on the inner surface of the pipe. This perfect truncation only applies for a particle moving along the central axis. Consider a particle offset by a distance a from the central axis in the $\theta = 0$ direction. Using multipole moments the charge (ρ) and current density (j) can be decomposed into [39]

$$\rho = \sum_{m=0}^{\infty} \rho_m \quad \text{and} \tag{3.11}$$

$$j = \sum_{m=0}^{\infty} j_m, \tag{3.12}$$

where

$$\rho_m = \frac{I_m}{\pi a^{m+1}(1+\delta_{m0})}\delta(s-c)\delta(r-a)\cos m\theta, \tag{3.13}$$

$$j_m = c\rho_m \hat{s}, \tag{3.14}$$

and δ_{m0} is 0 when $m \neq 0$ and 1 otherwise. Equations 3.11 to 3.14 describe a ring of charge with a radius of a, where the monopole term ($m = 0$) is the total charge of the beam, I_0. Each m term is called the m^{th} *moment* of the beam [39].

When the charge is exactly on the central axis of the beam pipe the field lines are truncated and cancelled absolutely due to the boundary conditions being satisfied even though they were not explicitly used to solve the set of equations. The boundary conditions used for a perfectly conducting metallic surface are that the electric field lines are parallel to the surface normal, while the magnetic field lines are perpendicular [41]. An attempt at "simple" truncation for an offset charge fails as these conditions are not satisfied. One is therefore compelled to solve Maxwell's equations using the boundary conditions explicitly. Solving Maxwell's field equations using Equations 3.11 to 3.14 whilst imposing the correct boundary conditions results in [39]:

$$E_r = \frac{2I_m}{1+\delta_{m0}}\delta(s-ct)\cos m\theta \begin{cases} \left(\frac{1}{b^{2m}} - \frac{1}{a^{2m}}\right) r^{m-1}, & \text{if } r > a \\ \frac{1}{r^{m+1}} + \frac{r^{m-1}}{b^{2m}}, & \text{if } r < a, \end{cases} \tag{3.15}$$

$$E_\theta = \frac{2I_m}{1+\delta_{m0}}\delta(s-ct)\sin m\theta \begin{cases} -\left(\frac{1}{b^{2m}} - \frac{1}{a^{2m}}\right) r^{m-1}, & \text{if } r > a \\ \frac{1}{r^{m+1}} - \frac{r^{m-1}}{b^{2m}}, & \text{if } a < r < b, \end{cases} \tag{3.16}$$

$$B_r = -E_\theta, \tag{3.17}$$

$$B_\theta = E_r, \tag{3.18}$$

where a is the radius of the ring beam distribution and b is the radius of the beam pipe.

Two important results can be gleaned from Equations 3.15 to 3.18.

1. The longitudinal distribution enforced by $\delta(s-ct)$ causes the fields to be contained within a flat transverse disc due to the Lorentz boost of the relativistic particles.
2. The ring charge distribution (Equation 3.11) results in fields described using $\cos(m\theta)$

and $\sin(m\theta)$ which allows the different multipole moments to be decoupled and treated independently [39].

Result 1 leads to the conclusion that as the fields cannot extend forward or backwards from a relativistic particle there can be no collective instability. This is true for a particle that is

a) relativistic,

b) in a perfectly conducting pipe.

Therefore to study the instabilities that have been observed in storage rings one of these conditions must be relaxed. In a high energy electron ring (such as the ASLS storage ring[*]) the particles will always be highly relativistic, but the vacuum pipe is constructed from stainless steel and therefore is not perfectly conducting [42]. Consequently, the obvious approximation to be relaxed and studied in more detail will be that of the infinitely conductive beam pipe.

3.3 Wake Fields

Driving terms introduce complex tune shifts to the equations of motion for a focussed electron beam and can cause exponential growth of transverse amplitude. The source of these driving terms within a storage ring comes from the interaction between the trapped particles and their metallic environment. In Section 3.2 it was shown that ultra-relativistic beams in a perfectly conducting beam pipe could not produce wake fields. If the metallic environment has finite conductivity then the movement of charged particles will induce wake fields which can provide a coupling force. The magnitude of the coupling is linearly proportional to displacement and induces transverse tune shifts. As these fields lag behind the leading particle, they are referred to as *wake fields* and can be a source of the driving forces discussed in Section 3.1.

Particles within an accelerator are focussed and steered using *external* fields (typically dipole bending magnets and multipole focussing magnets) utilising the Lorentz force:

$$\boldsymbol{F}_{\text{ext}} = q(\boldsymbol{E}_{\text{ext}} + \boldsymbol{v} \times \boldsymbol{B}_{\text{ext}}). \tag{3.19}$$

When considering the path a particle will take through a magnetic lattice it is assumed that the fields exist by themselves, without the metallic infrastructure and beam pipe. If the beam

---

[*] 3.0 GeV electrons travel with a Lorentz boost of $\gamma = 5871$

pipe has finite resistivity and the particles are travelling relativistically then the image charges induced in the beam pipe will lag behind the beam leaving electromagnetic fields which can interact with any trailing particles. The forces from these fields act as a disturbance to the beam motion:

$$\boldsymbol{F}_{\text{wake}} = q(\boldsymbol{E}_{\text{wake}} + \boldsymbol{v} \times \boldsymbol{B}_{\text{wake}}), \tag{3.20}$$

where the assumption will be made that $|\boldsymbol{F}_{\text{wake}}| \ll |\boldsymbol{F}_{\text{ext}}|$, such that the effect of the wake fields can be treated as a perturbation.

Exact calculations of the wake fields for a given beam distribution and environment geometry are difficult to achieve analytically. Accurate numerical calculations can be made for certain geometries, but as many of the wake fields have high frequency components and wide bandwidth it is limited to small components. To help calculate these coherent effects on the beam, two approximations will be made [40]:

1. **Rigid-Beam Approximation** — The wake field effect is assumed to not cause the beam to move while it travels through the impedance. In terms of the equations of motion, this means that position variables do not change while calculating the effect of the impedance.

   This assumption is not self-consistent but is reasonable when considering relativistic particles.

2. **Impulse Approximation** — Following from the rigid-beam approximation, assume that the particle does not change velocity while traversing the impedance and it is only the impulse, not the force, of the wake field that is important to calculate.

$$\Delta \boldsymbol{p} = \int_{-\infty}^{\infty} dt \boldsymbol{F} = \int_{-\infty}^{\infty} dt \; q(\boldsymbol{E} + \boldsymbol{v} \times \boldsymbol{B}) \tag{3.21}$$

Maxwell's equations for particles travelling in a storage ring are

$$\nabla.\boldsymbol{E} = \frac{\rho}{\epsilon_0}, \tag{3.22}$$

$$\nabla \times \boldsymbol{B} - \frac{1}{c^2}\frac{\partial \boldsymbol{E}}{\partial t} = \mu_0 \beta c \rho \hat{\boldsymbol{s}}, \tag{3.23}$$

$$\nabla.\boldsymbol{B} = 0, \tag{3.24}$$

$$\nabla \times \boldsymbol{E} + \frac{\partial \boldsymbol{B}}{\partial t} = 0, \tag{3.25}$$

where the substitution $\boldsymbol{j} = \beta c \rho \hat{\boldsymbol{s}}$ has been performed to allow calculations with beam charge density instead of the current density [40]. In the rigid beam approximation the velocity ($v = \beta c$) is constant; this is a reasonable approximation for ultra-relativistic beams where $\beta \approx 1$.

Consider a test particle travelling a distance z *behind* a charge producing a wake field. It will experience a Lorentz force of $\boldsymbol{F}_{\text{wake}} = q(\boldsymbol{E} + \beta c \hat{\boldsymbol{s}} \times \boldsymbol{B})$ where the rigid beam approximation has been used to ensure that the test particle moves with the same velocity as the source. From the impulse approximation, the quantity of interest is the impulse on the test particle described by Equation 3.21. Using Maxwell's equations and taking the divergence and curl of the force gives [40]

$$\nabla.\boldsymbol{F}_{\text{wake}} = \frac{q\rho}{\epsilon_0 \gamma^2} - \frac{q\beta}{c}\frac{\partial E_s}{\partial t}, \tag{3.26}$$

$$\nabla \times \boldsymbol{F}_{\text{wake}} = -q\left(\frac{\partial}{\partial t} + \beta c \frac{\partial}{\partial s}\right)\boldsymbol{B}. \tag{3.27}$$

To utilise this result, take the curl of both sides of equation 3.21 and let $\nabla \times \boldsymbol{F}$ equal Equation 3.27. Algebraic manipulation yields a useful relationship,

$$\nabla \times \boldsymbol{\Delta p} = 0, \tag{3.28}$$

which is known as the Panofsky-Wenzel theorem [43]. It is important to note that no boundary conditions have been imposed and the Panofsky-Wenzel theorem is true for any geometry [40]. Equation 3.28 can be further decomposed via dot and cross products with the longitudinal vector $\hat{\boldsymbol{s}}$,

$$\nabla.(\hat{\boldsymbol{s}} \times \boldsymbol{\Delta p}) = 0, \tag{3.29}$$

$$\frac{\partial}{\partial z}\boldsymbol{\Delta p}_{\perp} = \nabla_{\perp}\boldsymbol{\Delta p_s}, \tag{3.30}$$

where $\nabla_\perp$ is the transverse gradient operator and $\boldsymbol{p}_\perp$ and $\boldsymbol{p_s}$ are the vector components of $\boldsymbol{p}$ perpendicular and parallel to $\hat{\boldsymbol{s}}$ respectively. A transverse impulse can therefore be related to a longitudinal impulse through their respective gradients. Specifically, the longitudinal gradient of the transverse impulse is equal to the transverse gradient of the longitudinal impulse. This helps to constrain the values of the different components of the impulse. An important addition to the Panofsky-Wenzel theorem comes with the assumption of an ultra-relativistic beam ($\beta \to 1$),

$$\beta \to 1 : \nabla.\boldsymbol{\Delta p}_\perp = 0. \tag{3.31}$$

If cylindrical symmetry in the beam pipe is assumed, the $\hat{\boldsymbol{s}}$ vector is a natural axis of symmetry to form the coordinate base around. The effect of non-cylindrically symmetric geometries can be rectified with a geometric correction factor [44].

Rewriting Equation 3.28 in cylindrical coordinates gives [40],

$$\frac{\partial}{\partial r}(r\Delta p_\theta) = \frac{\partial}{\partial \theta}\Delta p_\theta, \tag{3.32}$$

$$\frac{\partial}{\partial z}\Delta p_r = \frac{\partial}{\partial r}\Delta p_s, \tag{3.33}$$

$$\frac{\partial}{\partial z}\Delta p_\theta = \frac{1}{r}\frac{\partial}{\partial \theta}\Delta p_s, \tag{3.34}$$

$$\frac{\partial}{\partial r}(r\Delta p_r) = -\frac{\partial}{\partial \theta}\Delta p_\theta, \tag{3.35}$$

where Equation 3.35 utilises the ultra-relativistic assumption in Equation 3.31.

The impulse response Δp_z can then be decomposed into different azimuthal modes by letting $\Delta p_z = \cos m\theta$ where $m > 0$ [40]. The cylindrical components of the impulse then become;

$$\Delta p_s = \Delta \bar{p}_s \cos m\theta, \ \Delta p_r = \Delta \bar{p}_r \cos m\theta, \ \Delta p_\theta = \Delta \bar{p}_\theta \sin m\theta \tag{3.36}$$

where the $\bar{p}$ terms have no θ dependence. Substituting these new expressions for Δp into equations 3.32 to 3.35 result in

$$\frac{\partial}{\partial r}(r\Delta \bar{p}_\theta) = -m\Delta \bar{p}_r, \tag{3.37}$$

$$\frac{\partial}{\partial z}\Delta \bar{p}_r = \frac{\partial}{\partial r}\Delta \bar{p}_s, \tag{3.38}$$

$$\frac{\partial}{\partial z}\Delta \bar{p}_\theta = -\frac{m}{r}\Delta \bar{p}_s, \tag{3.39}$$

$$\frac{\partial}{\partial r}(r\Delta \bar{p}_r) = -m\Delta \bar{p}_\theta. \tag{3.40}$$

Consider two values for m, $m = 0$ and $m > 0$. For $m = 0$ the first and last equations require $\Delta\bar{p}_r = 0$ and $\Delta\bar{p}_\theta = 0$ to prevent singularities at $r = 0$. When $m > 0$ the above equations give

$$\frac{\partial}{\partial r}\left[r\frac{\partial}{\partial r}(r\Delta\bar{p}_r)\right] = m^2\Delta\bar{p}_r, \tag{3.41}$$

$$\Rightarrow \Delta p_r(r, \theta, z) \sim r^{m-1}\cos m\theta, \tag{3.42}$$

then the entire solution can be written as [40],

$$v\Delta p_\perp = -qQ_m W_m(z) m r^{m-1}(\hat{\boldsymbol{r}}\cos m\theta - \hat{\boldsymbol{\theta}}\sin m\theta), \tag{3.43}$$

$$v\Delta p_s = -qQ_m W'_m(z) r^m \cos m\theta, \tag{3.44}$$

for $m \geq 0$. Q_m is the electrical moment of the azimuthal mode m for the source particle. For a source particle with charge e offset by a from the central axis, $Q_m = ea^m$ [40].

The functions labelled as W are called the *wake functions* and are the only terms which rely on the boundary conditions of the system. W_m is described as the *transverse wake function* of azimuthal mode m and W'_m as the *longitudinal wake function.* The longitudinal wake field is related to the transverse wake field through the Panofsky-Wenzel theorem as the derivative of the transverse wake field.

By using Maxwell's Equations and the Impulse and Rigid Beam approximations, it is possible to reduce a large set of equations which rely on r, θ and z to simply solve for $W(z)$. The wake functions are only a function of z, the distance of the test particle *behind* the source charge. It has been implicitly assumed that $z > 0$ due to causality, with the source charge unable to affect a particle it lags.

The effect of a source charge on a test particle at position z will be affected primarily by the nature of the wake functions W_m and W'_m. As all of the calculations have been completed in the time domain the wake functions are real-valued. Transverse wake fields W_m have units of Volts/Coulomb/m^{2m-1} and the longitudinal wake fields have units of Volts/Coulomb/m^{2m} [40]. It is the strength of these wake fields that will determine the coupling between bunches and the rate of instability growth.

3.4 Impedances

As a consequence of motion in a storage ring being oscillatory, diagnostic measurements are often made in frequency space instead of time space. In a storage ring the trapped particles form a looped current described by

$$I(s,t) = \hat{\boldsymbol{I}} e^{-i\omega(t-s/v)} \tag{3.45}$$

with frequency components $f = \omega/2\pi$. This description assumes the bunches are evenly spread throughout the ring — a reasonable assumption for electron storage rings if the clearing gap[†] is much shorter than the train length.

The wake functions described earlier in time space can be transformed into frequency space using Fourier transforms. This allows time space problems, such as the need for calculating the effect on a turn-by-turn basis, to be ignored and concentrates on the overall effect that wake fields have on the oscillatory motion of the particles. Examination of each individual source of wake fields requires a model where each instability-causing component acts on a frequency range.

The impedances Z relate to their respective wake fields by

$$Z_m^{\parallel}(\omega) = \int_{-\infty}^{\infty} e^{i\omega z/v} W_m' \frac{dz}{v}, \tag{3.46}$$

$$Z_m^{\perp}(\omega) = \frac{i}{\beta} \int_{-\infty}^{\infty} e^{i\omega z/v} W_m \frac{dz}{v}, \tag{3.47}$$

where z is the trailing distance between the test particle and the source particle, ω is the angular frequency, v is the velocity of the particle and the label m represents the impedance due to the m^{th} multipole of the beam current. $Z_m^{\{\parallel,\perp\}}$ represents the frequency response of an instability and will be important in calculating the instability growth for a given beam spectrum.

[†] When storing electrons in a vacuum, positive charges from residual gas or the vacuum chamber can be drawn toward the stored bunches and are attracted to the stored charge. This can cause instabilities if the positive charges are allowed to build up. A clearing gap with no electrons is used to allow the slower, positively charged ions to recombine or be removed by the vacuum system.

Although the equations describe in general the dependence of wakefields on the charge multipole, if the beam pipe is roughly circular and the beam is aligned along the $\boldsymbol{s}$ axis, longitudinal instabilities depend only on the monopolar ($m = 0$) fields and transverse instabilities only on the dipolar ($m = 1$) fields [40]. The units for the longitudinal impedance and transverse impedance are then Ohms and Ohms/meter respectively.

Important properties of impedances can summarised as follows [40];

1. $Z_m^{\|}(-\omega) = \left[Z_m^{\|}(\omega)\right]^*$ and $Z_m^{\perp}(-\omega) = -\left[Z_m^{\perp}(\omega)\right]^*$
2. $Z_m^{\|}(\omega) = \frac{\omega}{c} Z_m^{\perp}$, assuming cylindrical geometry
3. $\mathrm{Re}\left\{Z_m^{\|}(\omega)\right\} \geq 0$ and $\mathrm{Re}\left\{Z_m^{\perp}(\omega)\right\} \geq 0$ when $\omega > 0$
4. $\int_0^\infty d\omega \mathrm{Im}\left\{Z_m^{\perp}(\omega)\right\} = 0$, and $\int_0^\infty d\omega \frac{\mathrm{Im}\left\{Z_m^{\|}(\omega)\right\}}{\omega} = 0$

The first property is a consequence of the wake fields being a real physical effect, and the second is a direct result of the Panofsky-Wenzel theorem. The third property embodies the fact that a particle can not gain energy as it passes through a beam pipe with no external electric fields, while the last property is a result of the assumption that the wake field vanishes at $z = 0$ ($W_m(0) = 0$).

In general, impedances created in real-world beam pipes can be separated into two families; (i) *resistive wall impedances* which arise from a non-zero resistance in the material used to construct the beam pipe, and (ii) *resonator-style impedances* caused by discontinuities in the ring.

3.4.1 Resistive Wall Impedance

As discussed previously, in the absence of an external environment the field lines continue to infinity. However, if a perfectly conducting metallic beam pipe is placed around the bunches the electric field lines are truncated and image charges will be created to cancel the electric field in the beam pipe. As the bunch moves through the accelerator, the image charges will travel with the bunch if the beam pipe is perfectly conducting.

If the model is taken further to include a beam pipe with non-infinite conductivity then as the bunch moves with a velocity of $v \approx c$, the image charges will lag behind and the electric field will no longer cancel exactly. The resulting non-zero electric field behind the particle can

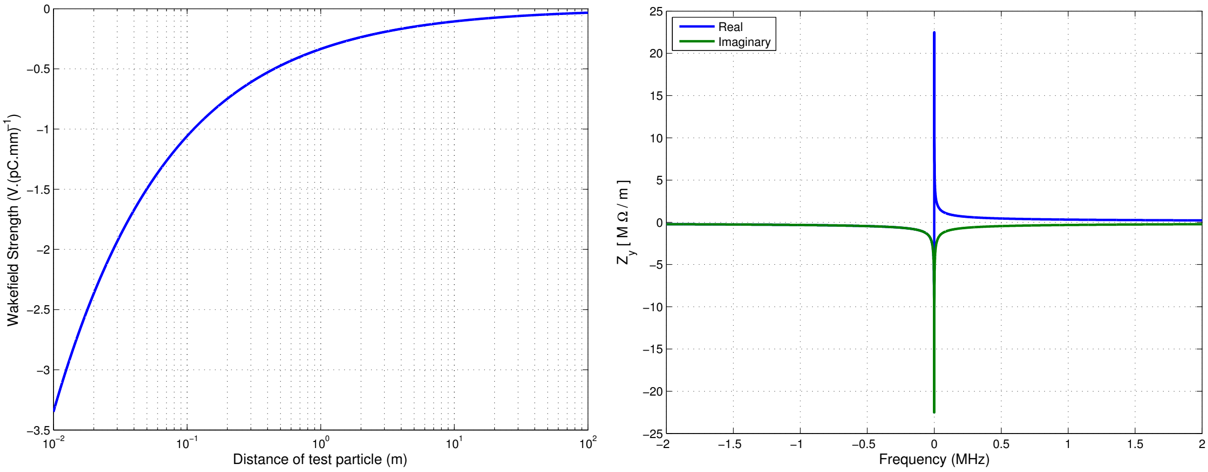

(a) Vertical resistive wall wake field

(b) Vertical resistive wall impedance

Figure 3.3: The vertical resistive wall wake field and impedance calculated for the ASLS storage ring using Equations 3.49 and 3.50. The ω^{-1} frequency dependence is visible in Figure 3.3b implying that it is strongest at low frequency coupled-bunch modes.

interact with any other bunches passing behind the originating bunch, coupling their motion.

The wake fields generated by these lagging image charges are described by [40]:

$$W_0'(z) = -\frac{c}{2\pi b}\sqrt{\frac{Z_0}{\pi\sigma}}\frac{L}{|z|^{\frac{1}{2}}} \tag{3.48}$$

$$W_1(z) = -\frac{c}{2\pi b^3}\sqrt{\frac{Z_0}{\pi\sigma}}\frac{L}{|z|^{\frac{3}{2}}} \tag{3.49}$$

and the corresponding impedances are given by

$$Z_0^{\parallel}(\omega) = \frac{\omega}{c}Z_1^{\perp}(\omega) = \frac{Z_0 c L}{2\pi(1+\mathrm{sgn}(\omega)i)bc\sqrt{\frac{\sigma Z_0 c}{2|\omega|}} - ib^2\omega} \tag{3.50}$$

where σ is the conductivity of the beam pipe material (in units of Ω^{-1}), Z_0 is the vacuum impedance, c is the speed of light, L is the length of the beam pipe and b is the half-height of the beam pipe. Calculated values for the transverse resistive wake field in the ASLS storage ring are shown in Figure 3.3a.

The transverse wake field is inversely proportional to the cube of the half-height of the beam pipe. Therefore the strength of the instability is very sensitive to any changes in the height of beam pipe, for instance collimators and IVUs. Figure 3.3b shows the ω^{-1}

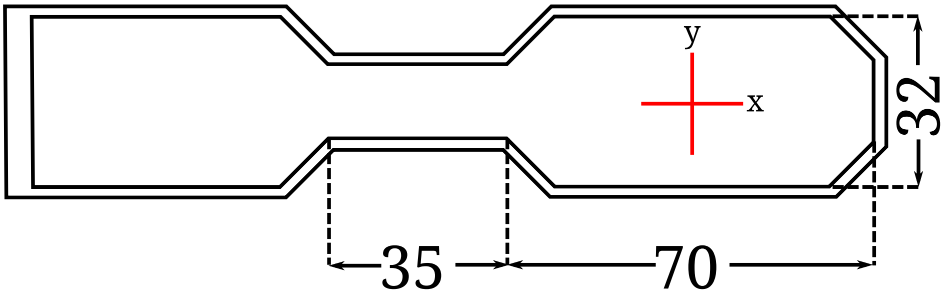

Figure 3.4: Schematic of the vacuum pipe as it passes through a quadrupole [42]. The cross represents the location of the closed orbit particle. All measurements are in millimeters.

dependence on frequency, so a symptom of resistive wall instabilities is manifested as a low frequency movement in the beam.

In modern synchrotrons the resistive wall impedance is the primary cause of unstable beam. An effort to increase the stored current while reducing beam size and beam pipe height leads to strong resistive wall wake fields. As Figure 3.4 shows, the cross-section of the beam pipe at the ASLS is not circular and the aspect ratio is such that the vertical distance (32 mm) is less than half of the horizontal distance (70 mm). Consequently, the storage ring at the ASLS has a strong resistive wall impedance in the vertical plane and a comparatively weaker one ($b^{-3} = (35/16)^{-3} \approx 1/8$) in the horizontal.

Resistive wall impedances are the major source of beam instabilities in the ASLS storage ring. Without active feedback the current threshold due to the resistive wall dominated ring impedance is 60 mA — considerably less than the nominal 200 mA operating current.

3.4.2 Resonator-style Impedance

As charged particles travel through a discontinuity within the beam pipe (for example pillbox RF cavities) the electric field can couple to the cavity, losing energy and forming a resonant wave. Any particles travelling through this resonant wave will experience a force through the wake field.

A resonant cavity can be modelled as a tuned circuit with a shunt impedance R_s, a resonant frequency ω_r and a quality factor Q. The quality factor describes how sharply peaked the frequency response is, resonators with high Q ($Q \gg 1$) are called *narrowband* and resonators with a low quality factor are called *broadband.* The general impedance of a ring can often be approximated by a sum of the resistive wall impedance and multiple resonator impedances.

The wake field from a resonator style impedance is described by

$$W_m(z) = \frac{R_s^m c\omega_r}{Q\bar{\omega_r}} e^{\alpha z/c} \sin\frac{\bar{\omega}_r z}{c}, \tag{3.51}$$

where $\bar{\omega}_r = \sqrt{|\omega_r^2 - \alpha^2|}$ and $\alpha = w_r/(2Q)$. Recalling that W_m' can be calculated from the derivative of W_m and taking the Fourier transform of the wake field, the resonator impedance can be written as:

$$Z_0^{\|}(\omega) = \frac{\omega}{c} Z_1^{\perp}(\omega) = \frac{R_s^m}{1 + iQ\left(\frac{\omega_r}{\omega} - \frac{\omega}{\omega_r}\right)}. \tag{3.52}$$

Figure 3.5 shows the wake field and impedance from both a narrowband ($Q = 100$) and broadband ($Q = 1$) resonator. Such resonators are often destructive to the beam as the available power is concentrated into a small frequency range. If the beam couples to the resonant frequency of the impedance then the motion will quickly become unstable and beam lost.

3.5 Sacherer's Equation

It was shown in Section 3.1 that a driving force such as a wake field will induce a tune shift in the beam. Tune shifts are in general complex-valued and their components cause separate effects on the beam motion — real tune shifts cause alterations in the frequency of oscillation of particles while imaginary tune shifts cause exponential movement of the center of mass of a bunch.

Assuming M equally spaced bunches with equal charge, there exist M *modes* of coupled bunch oscillation $\mu = 0, \ldots, M-1$. These modes represent a phase dependence between the movement of one bunch and the one trailing. The phase advance from one bunch to the next for each transverse coupled-bunch mode is given by

$$\Delta\phi_\mu = \frac{2\pi\mu}{M}, \tag{3.53}$$

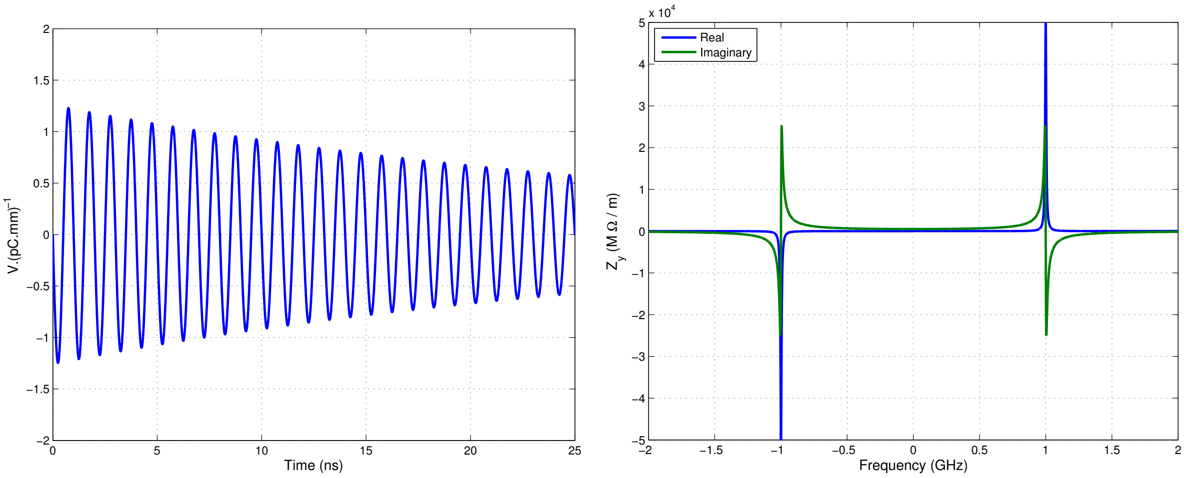

(a) High Q Resonator Wake field

(b) High Q Resonator Impedance

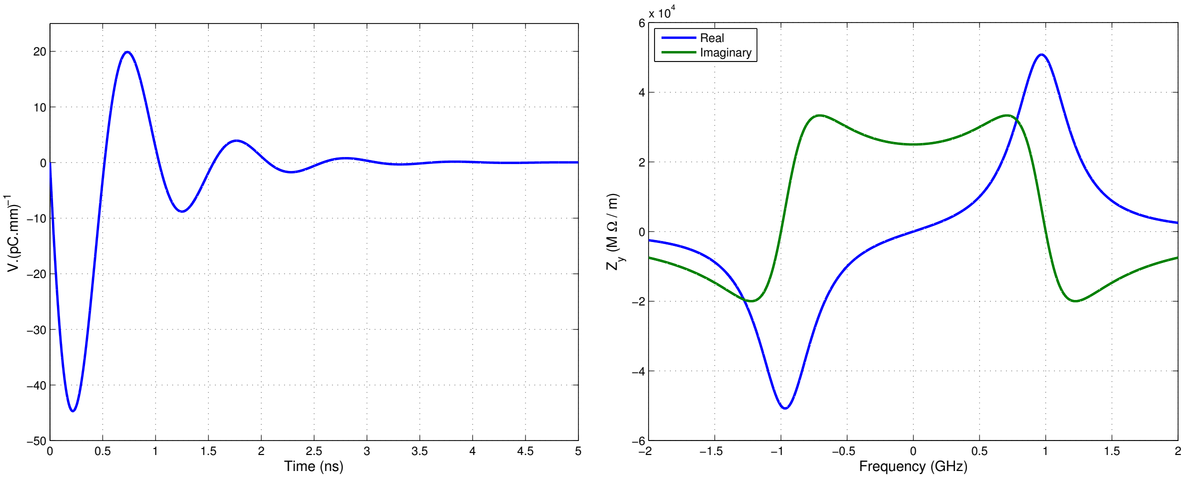

(c) Low Q Resonator Wake field

(d) Low Q Resonator Impedance

Figure 3.5: Time and frequency space descriptions of resonator-style impedances. Parameters for all plots: $R_s = 20$ MΩ, $f_r = 1$ GHz. High Q Resonator: $Q = 100$. Low Q Resonator: $Q = 2$.

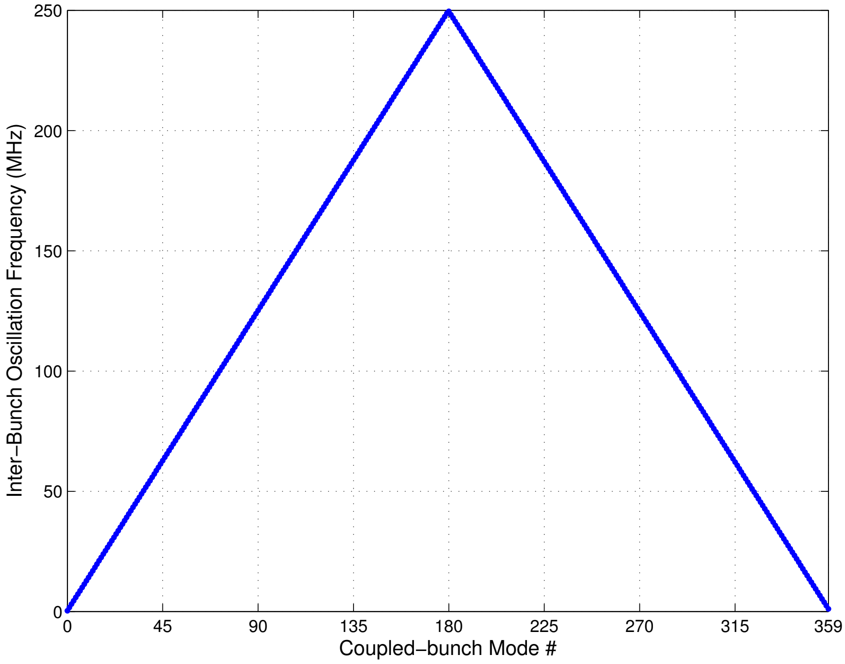

Figure 3.6: Inter-bunch oscillation frequencies for all coupled-bunch modes found in the ASLS storage ring. Mode frequencies were calculated using Equation 3.54 using the parameters listed in Table 2.2 and $f = \frac{\omega}{2\pi}$. For modes 0 → 179 the upper sidebands were calculated using $p = 0$, modes 180 → 359 were calculated using the lower sidebands and $p = 1$.

where M is 360 in the ASLS storage ring. Each of these *modes* has a characteristic frequency which appears as sidebands of the revolution harmonic:

$$\omega = (p\ \omega_{rf}) \pm (\mu + Q)\omega_0, \tag{3.54}$$

where p is an integer, Q is the fractional part of transverse tune and ω_0 is the revolution harmonic. The relationship between coupled-bunch modes and the characteristic frequencies is shown in Figure 3.6.

The shift in tune in a given ring due to the interaction of a stored beam with the coupling impedances is given by [40]

$$(\Omega - \omega_\beta - m\omega_s) = -\left(|m+1|\right)^{-1} \frac{ie\beta c^2 I_b}{2\omega_\beta E_0 L_b} \frac{\sum_q Z_1^\perp(\omega_q)\bar{\lambda}^*_{mk}(\omega_q)\lambda_{m'k'}(\omega_q)}{\sum_q \bar{\lambda}^*_{mk}(\omega_q)\lambda_{mk}(\omega_q)} \tag{3.55}$$

where:

- Ω, ω_b and ω_s are respectively the revolution, betatron tune and synchrotron tune angular frequencies.

- $\beta = \frac{v}{c}$
- $Z_1^{\perp}(\omega)$ is the transverse impedance
- m is the azimuthal mode of the beam distribution
- I_b is the stored current per bunch (assuming each bunch has the same stored current)
- E_0 is the nominal energy of the stored particles
- L_b is the bunch length
- $\omega_q = (qM + \mu)\omega_0 + \Omega$

and λ_{mk} are the eigenmodes of a matrix describing the interaction between the beam and ring impedance, which can be shown to be the $(mk)^{\text{th}}$ component of the linear beam density $\rho(\tau)$. $\bar{\lambda}_{mk}$ is the Fourier transform of λ_{mk}.

If the perturbation is small and only a single azimuthal mode will contribute then the diagonal components of λ_{mk} are the most important. Therefore by convention $k = m$ and λ_m refers to the diagonal component, λ_{mm}.

The power spectrum of the beam is approximated depending on the shape of the bunches. Single bunch instabilities at the PS accelerator at CERN have revealed that the particles possess a sine-wave like motion between the head and tail of long proton bunches, so an approximation involving sinusoidal modes was investigated. Sacherer introduced the idea of approximating the charge distribution in a ring by a linear combination of sinusoidal functions to simplify the calculation of λ_{mk} [45].

The beam density is described by a set of orthonormal functions:

$$\lambda_m(\tau) \propto \begin{cases} \cos(m+1)\pi\frac{\tau}{\tau_L} & m = 0, 2, \ldots, \\ \sin(m+1)\pi\frac{\tau}{\tau_L} & m = 1, 3, \ldots, \end{cases} \tag{3.56}$$

and the power spectrum for the modes in Equation 3.56 is approximated by

$$|\lambda_m|^2 \approx h_m(\omega) = \frac{4(m+1)^2}{\pi^2}\frac{1 + (-1)^m \cos \pi y}{(y^2 - (m+1)^2)^2} \tag{3.57}$$

where $y = \omega\tau_L/\pi$ and $\tau_L = L/v$ is the bunch length in time [40]. Figure 3.7 shows the power spectrum of the first five modes.

Using this approximation Equation 3.55 can be rewritten as

$$(\Omega - \omega_\beta - m\omega_s) = -(|m+1|)^{-1}\frac{ie\beta c^2 I_b}{2\omega_\beta E_0 L_b} Z_{\text{eff}} \tag{3.58}$$

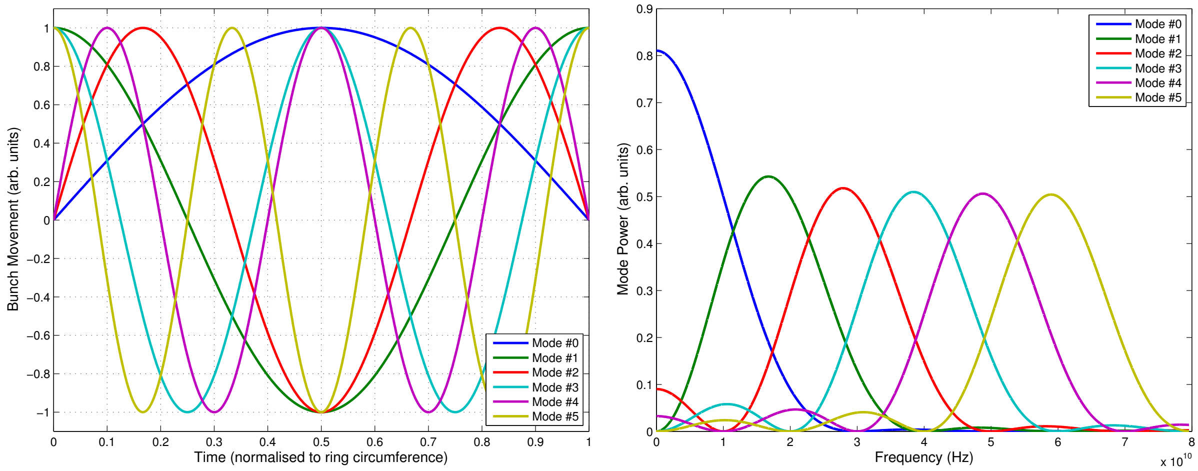

(a) Time distribution of sinusoidal modes **(b)** Power distribution of the sinusoidal modes

Figure 3.7: Sacherer's basis for an approximation of the charge distribution within a storage ring. The motion of bunches can be approximated using a sum of these functions described in Equation 3.56.

where

$$Z_{\text{eff}} = \frac{\sum_q Z_1^{\perp}(\omega_q) h_m(\omega_q)}{\sum_q h_m(\omega_q)} \tag{3.59}$$

and $\omega_q = (qM + \mu)\omega_0 + m\omega_s$. Z_{eff} describes the *effective impedance* of the ring.

The effective impedance describes how the stored beam samples the impedances of the ring. Since an imaginary tune shift gives a real growth in beam motion, it is the real part of the effective impedance that will directly instigate beam instabilities. If $\text{Re}\{Z_{\text{eff}}\} > 0$ the beam will damp while if $\text{Re}\{Z_{\text{eff}}\} < 0$ the beam will grow. Therefore, it is important to control the effective impedance such that the real part of the effective impedance will be positive for a given ring configuration. Figure 3.8 shows the overlap between power modes and impedance. As the real part of the impedance is odd and positive for $\omega > 0$, beam components at higher ω have a stabilising effect.

While still operating under the assumption that the bunches are equally spaced, the primary method for altering the beam spectrum is through chromaticity. As discussed in Chapter 2, chromaticity arises as off-momentum particles experience a different focussing strength and induce a betatron tune spread associated with the momentum spread of the

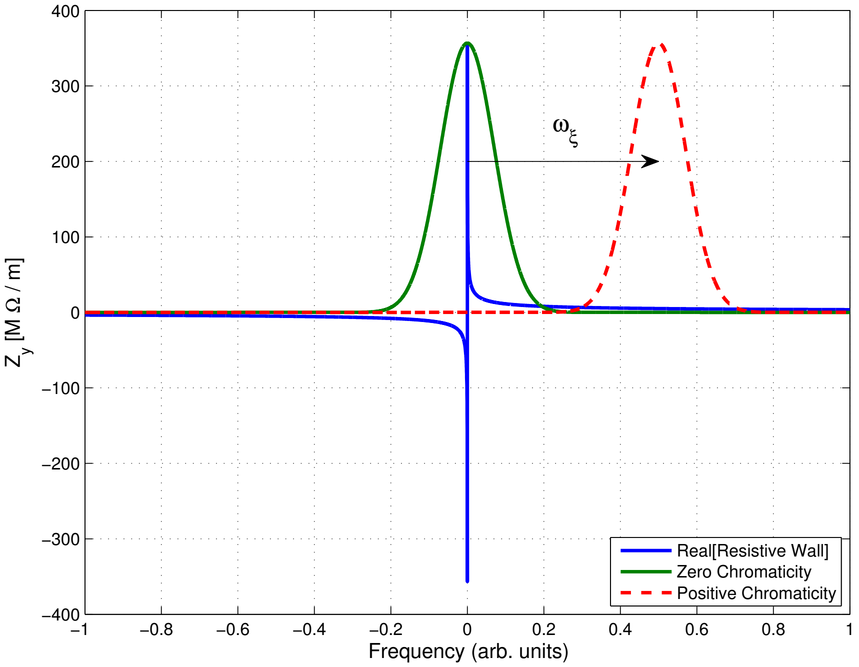

Figure 3.8: A simplified description of the effect of chromaticity on the effective impedance. By increasing the chromaticity two effects take place; the overlapping region between impedance and beam spectrum becomes smaller and the value of the overlapping area becomes positive — stabilising the instability. Only shown here is the mode #1 power spectrum, other (lower power) modes will begin to overlap with the impedance as the chromaticity is increased.

beam,

$$\Delta\omega_\beta = \xi\delta, \tag{3.60}$$

where δ is the momentum deviation of the particle. This momentum spread will result in a phase offset between particles with different momenta, which in turn leads to a frequency shift in the betatron tune frequency [40]. This betatron angular frequency shift due to chromaticity, ω_ξ, is described by

$$\omega_\xi = \frac{\xi\omega_0}{\eta}, \tag{3.61}$$

where η is the slip factor of the ring (positive for all high energy electron rings). The effect of chromaticity is therefore a shift in the frequency spectrum of the ring due to the accumulated phase shifts of off-momentum particles. To compensate, the substitution $\omega_\beta \rightarrow \omega_\beta - \omega_\xi$ is made in the beam power spectrum arguments in Equation 3.59.

The effective impedance including the influence of chromaticity becomes:

$$Z_{\text{eff}} = \frac{\sum_q Z_1^{\perp}(\omega_q) h_m(\omega_q - \omega_\xi)}{\sum_q h_m(\omega_q - \omega_\xi)}, \tag{3.62}$$

Therefore in machines for which $\eta > 0$, a higher chromaticity leads to a more stable beam by forcing the beam spectrum to sample more of the positive real part of the impedance. However, other modes may become unstable as the chromaticity is increased, as higher order modes shift to overlap the strong impedance frequencies. Figure 3.8 shows a simple example of how a mode spectrum shifts with increasing chromaticity.

Finally the growth rate of instabilities due to the coupling impedances in the ring can be calculated by combining equations 3.8, 3.55 and 3.62. If the growth of the center of mass of a bunch is described by $y \propto \exp(\frac{t}{\tau})$ then the growth rate τ can be calculated as [40]

$$\frac{1}{\tau_{m\mu}} = -\frac{1}{1+m}\frac{e\beta c^2 I_b}{2\omega_b E_0 L_b}\frac{\sum_q Re\{Z_1^{\perp}(\omega_q)\} h_m(\omega_q - \omega_\xi)}{\sum_q h_m(\omega_q - \omega_\xi)}. \tag{3.63}$$

When $\tau_{m\mu}$ is smaller than the overall damping time of the ring the beam position will grow exponentially and eventually leave the acceptance of the ring.

In the rest of the thesis methods will be discussed, both passive and active, for increasing the damping strength of the lattice and will describe a variety of techniques for measuring the impedance of the ring. Using these techniques it is possible to control the growth rate of coupled bunch instabilities and deliver stable, high current beam to users.

3.6 Measurement Conventions

Throughout this thesis reference will be made to *rates* — growth rates for unstable beams and damping rates for beams returning to stability. Growth rates are calculated by measuring the position of each bunch on every turn, extracting the mode strength over time and fitting an exponential of the form,

$$y = A\exp\left(\frac{t}{\tau}\right) + C, \tag{3.64}$$

where τ^{-1} will be the rate of growth in units of s^{-1}.

In real-world measurements, τ^{-1} is comprised of three parts:

- τ_g^{-1}: the growth rate of any instabilities present (> 0),

Table 3.1: Measured instability growth rates in the Australian Synchrotron storage ring.

	Source of Beam Movement	τ^{-1} (s^{-1})	τ (ms)
τ_g^{-1}	Resistive Wall Instability (Mode #359)	336.1	2.975
	Resonator-style Instability (Mode #228)	575.1	1.738

- τ_p^{-1}: the passive damping of the ring (< 0),
- τ_d^{-1}: the active damping of the ring (< 0).

These combine such that any measurement of the growth or damping rate of the beam τ^{-1} will be

$$\tau^{-1} = \tau_g^{-1} + \tau_p^{-1} + \tau_D^{-1}. \tag{3.65}$$

If τ^{-1} is positive then the beam is unstable and conversely when τ^{-1} is negative the beam is stable or damping back to stability. Table 3.1 shows an example of growth rates from coupled-bunch instabilities measured in the Australian Synchrotron Storage Ring. These initial instability values are derived from grow/damp measurements discussed in Chapter 6. As new measurements are discussed in each chapter this table will be appended and the values compared.

3.7 Observations of Coupled-Bunch Instabilities

In this chapter the discussion of coherent movement between bunches caused by wake fields generated as the stored beam interacts with the surroundings has been presented in a general sense. The uncontrolled growth in the transverse displacement of stored beam over time has been observed[‡] in modern storage rings and the resulting empirical observations must match the theory presented.

If the growth rate τ^{-1} (Equation 3.65) is positive, the stored bunches will become unstable and begin to oscillate with a higher amplitude. Users on experimental beam lines will observe this as a dramatic drop in the photon flux, due to the effective emittance increasing as shown

---

[‡] For an animation showing the growth in particle displacement over time due to a coupled-bunch instability at the ASLS, see `http://vimeo.com/5586591` Date Accessed: 18/10/2011

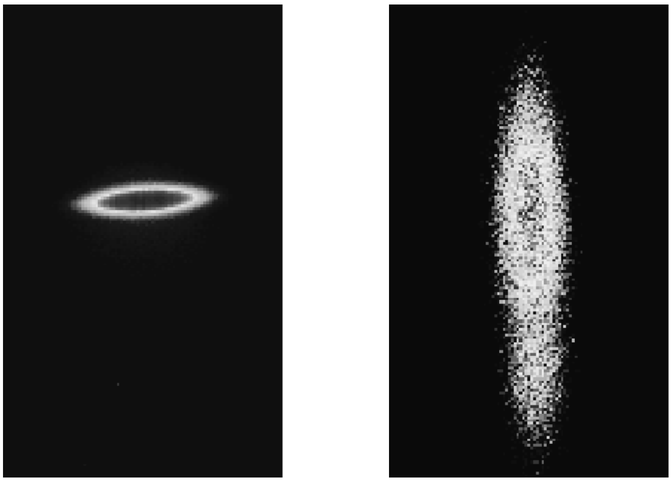

(a) Stable beam **(b)** Unstable beam

Figure 3.9: The transverse profile of a stable beam (left) and a beam under the influence of a strong resistive wall impedance (right). Data is the same as shown in Figure 1.4 and was taken using the XDB and represents the profile from a bending magnet source. A clear increase in the effective emittance of the beam can be seen, reducing the usable photon flux density for experimentalists.

in Figure 3.9.

After a short period of time the beam will be lost, usually around the defining aperture of the lattice. Figure 3.10 shows the characteristic beam loss pattern that a resistive wall instability will cause. This acute fractional beam loss has caused total beam dumps due to increased power reflection from the RF cavities to the powering klystron. Machine safety demands that any sharp changes in RF parameters instigate a shutdown of accelerating potentials and therefore a beam dump shortly afterwards. The ASLS storage ring RF cavities require approximately 25 minutes to return to operational status after beam loss. This combined with re-injecting bunches into the ring substantially reduces the available beam time for experimentalists.

In the next chapter two different methods will be presented for controlling instabilities — *passive damping* which was initially used to store 200 mA of beam and *active damping* which is more complicated but aims to provide strong damping to allow the introduction of more insertion devices in the future.

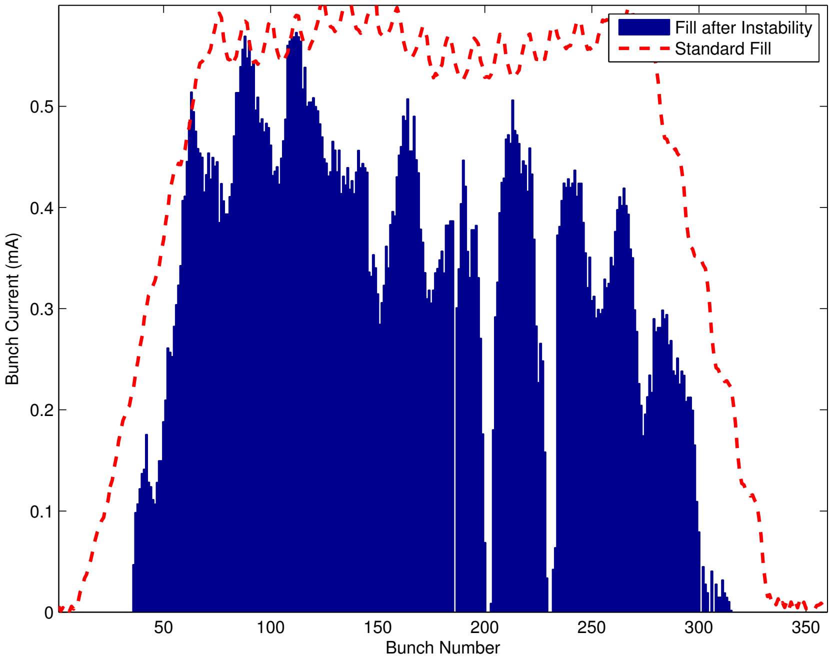

Figure 3.10: Beam loss due to resistive-wall coupled-bunch instabilities. Comparison with the standard user-fill is shown (red dashed line). With the majority of beam loss occurring in the tail of the bunch train, it is characteristic of a resistive wall instability.

Chapter 4

Controlling Coupled-bunch Instabilities

Ring impedance leads to coupled-bunch instabilities that reduce the maximum stored current. Some forms of instabilities can be controlled through passive methods such as increasing the chromaticity of the beam or using higher order multipole magnets (sextupole/octupole) to increase Landau damping, an explanation of which will be presented in this chapter. Passively damping the beam will reduce the dynamic aperture of the lattice and will be limited in controlling strong coupled-bunch instabilities.

Controlling strong coupled-bunch instabilities will require an active beam feedback system. Although such active feedback systems exist for both longitudinal and transverse coupled-bunch instabilities, this thesis will concentrate solely on transverse feedback as no longitudinal instabilities have been observed in the ASLS storage ring [46]. Active feedback operates by continuously measuring the position of all bunches within the ring and calculating a corrective waveform which will act against any unstable motion detected. This technique increases the damping rate of the ring without introducing detrimental side effects but is more difficult to successfully commission.

4.1 Passive Damping

If the instability growth rates are of the order of the natural damping of the ring lattice designers can employ various passive methods for controlling instability growth. Prior to the commissioning of the active feedback system at the ASLS, the passive damping methods which allowed for the current threshold to be raised above 200 mA involved increasing the chromaticity of the ring from $(\xi_x, \xi_y) = (2, 2)$ to $(\xi_x, \xi_y) = (3.5, 13)$. This resulted in a severe reduction in lifetime from 56 hours to 38 hours and introduced powerful non-linear fields to the injection section of the ring. This section will describe how passive damping is achieved in storage rings.

4.1.1 Preliminary Ring Design

The concept of an impedance in a storage ring which couples the motion of stored bunches was presented in Chapter 3 with a description of how a given ring design will interact with stored beam. It is vital to keep track of the impedance increase introduced by changes to the vacuum chamber – such as when new insertion devices are installed. The best way to avoid such increases in impedance is to make the vacuum transition between components in the ring as smooth as possible.

An estimate of the initial impedance of the ring must be considered in the design phase, as many decisions will become costly and time-consuming to alter in the future. A clear example of this is the decision regarding the material for the vacuum pipe.

At the ASLS, the beam pipe was constructed using 3 mm stainless steel (of type 316 LN) [42]. The advantages of stainless steel are good mechanical strength, low cost and fast penetrability by magnetic fields for fast orbit correction. Stainless steel is not a perfect conductor, which will affect the strength of resistive wall instabilities. At an increased cost, higher conductive materials can be sputtered into the inner surface of the vacuum system to reduce the resistive wall impedance [47].

Elements that introduce transitions in the ASLS storage ring include RF cavities, BPMs, in-vacuum insertion devices and in-vacuum kicker magnets. A comprehensive collection of analytic expressions for the impedance of the diverse elements of a storage ring can be found

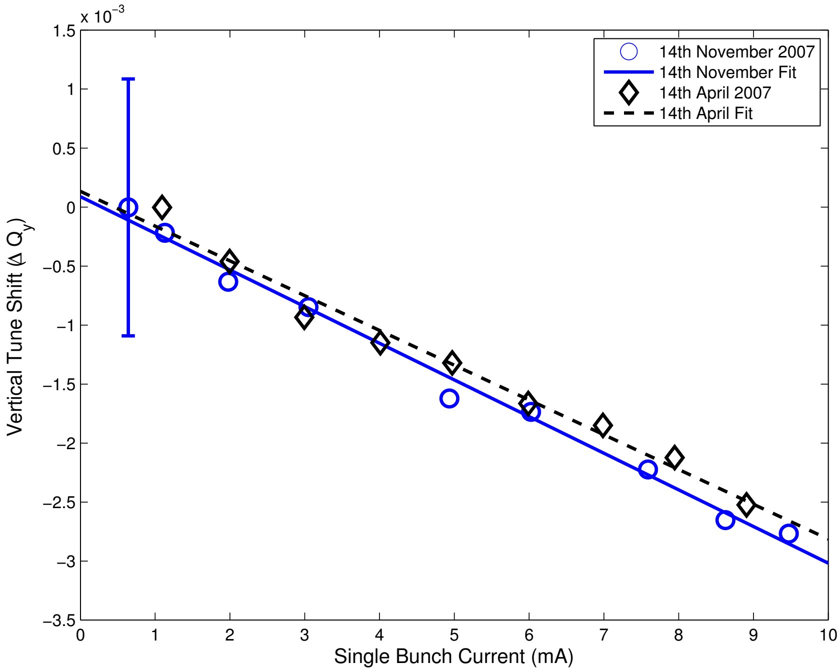

Figure 4.1: Measurements of the ring transverse ring impedance before and after the installation of an insertion device [49]. The single error bar shown in indicative of all measured points. According to Equation 3.62, as single bunch current increases the bunches will experience a tune shift proportional to the effective impedance of the ring. This technique will be described in more detail in Chapter 7. The linear fits to the tune data describe a shift in impedance from 0.85 $\mathrm{M\Omega.m^{-1}}$ to 0.92 $\mathrm{M\Omega.m^{-1}}$ due to the discontinuities introduced with the addition of an insertion device.

in Reference [48]. Typically a ring designer will start with an *impedance budget* for the lattice which is reduced for every object used to construct the ring.

Earlier measurements of the ring impedance for the ASLS storage ring show the impedance increasing with the addition of IVUs, from 0.85 $\mathrm{M\Omega.m}$ to 0.92 $\mathrm{M\Omega.m}$ as shown in Figure 4.1.

4.1.2 Alternate Fill Patterns

The wake fields which couple the motion of one bunch to a preceding bunch decay with time. Therefore if the bunches are sufficiently separated then the coupling forces will be negligible. A problem for accelerators is that most standard fill patterns maximise the number of filled bunches. This allows for rapid filling of the storage ring with multiple bunches added per injection cycle.

Other considerations must be taken into account when deciding on a fill pattern within a storage ring. From an accelerator physicist's perspective, spreading the injected charge over multiple bunches lowers the single bunch current, reducing intra-bunch scattered beam losses. There should also be a gap between the head and tail of the injected charge to allow any positive ions that have been drawn into the beam to recombine.

Instability considerations must take into account that in a circular accelerator the head of a bunch train will be subject to wake fields created by particles in the tail bunch. This can lead to a resonance condition, causing the beam to grow exponentially as the head influences the tail which in turn influences the head.

A method for reducing the strength of multi-bunch transverse coupled bunch instabilities is to increase the gap at the end of the bunch train to allow the induced voltage from the tail of the train to decay, lowering the coupling strength between two consecutive turns. Figure 4.2 shows the results of an experiment undertaken at ASLS for this thesis where the individual bunch current is maintained, but the length of the gap between head and tail is altered.

It can be seen that as the gap is decreased the resistive wall growth rate increases, which agrees well with the assumption that the instability strength is dependants on the bunch train gap due to the head and tail coupling through a decaying wake field such as the one described in Figure 3.3a and Equations 3.49.

A bunch train of 154 bunches each filled with 0.39 ± 0.02 mA was experimentally shown to be a stability threshold for the ASLS storage ring. Once the train was extended to 155 bunches, the beam would become unstable. This allowed for studies into the instabilities of the ring in a controlled fashion while the techniques described in Section 6.1 were being developed [50].

Longitudinal structure in the beam such as the fill pattern determines the beam spectrum as shown in Figure 4.3. It has been proposed that coupled-bunch instabilities can be controlled by precise construction of a fill pattern such that the beam power spectrum avoids overlap with sections of the ring impedance with a strong imaginary component [51]. Calculating this

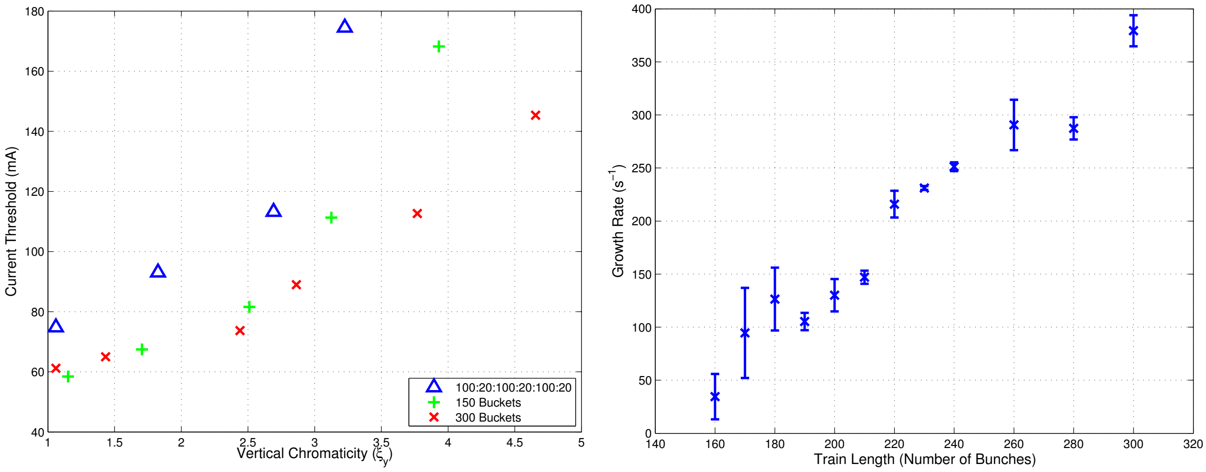

(a) Instability thresholds for different bunch train configurations

(b) Train Length versus resistive wall growth rate

Figure 4.2: Different train configurations can lead to a change in the current threshold of the ring by increasing or decreasing the growth rate of instabilities as presented in Figure 4.2a. Figure 4.2b shows the change in bunch train gap length at a lattice chromaticity of $(\xi_x, \xi_y) = (2, 2)$. The growth rate of coupled-bunch mode #359 was measured for different square fill patterns. While the length of the bunch train was extended, each individual bunch current was kept constant.

corrective fill pattern is difficult and requires a detailed knowledge of the impedance spectrum of the ring. It has not yet been attempted at the ASLS and is included here for completeness.

4.1.3 Landau Damping

Many fundamental theories in accelerator physics are understood by treating the collections of particles as a single macro-particle traversing the magnetic lattice. In reality each bunch consists of a collection of particles with finite distributions in position, energy and oscillation frequencies. A spread of frequencies within a bunch leads to a damping mechanism called *Landau damping* and is a proven method for passively damping instability growth.

Consider a particle with an oscillation frequency of ω driven by a force with an excitation frequency of Ω. This driving force is kept general at this point but could represent the oscillatory voltage of a beam-induced wake field. The equation of motion for the displacement

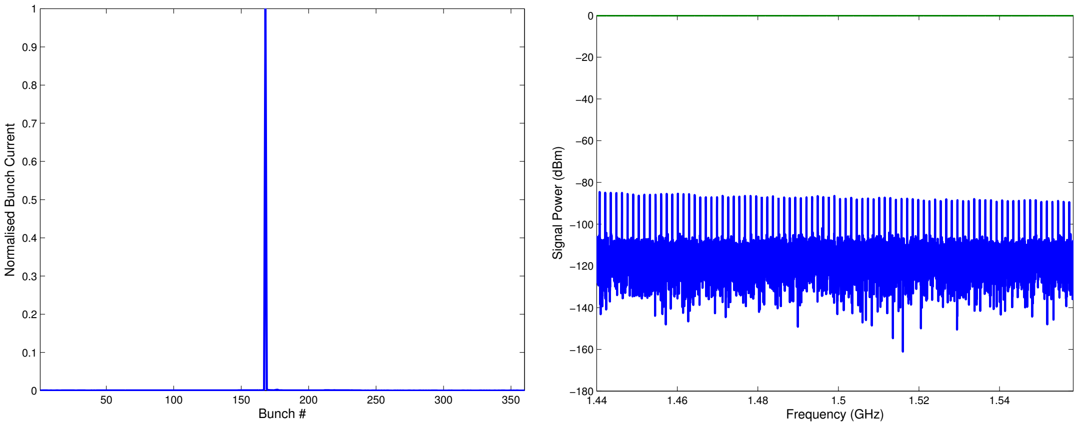

(a) Single bunch fill pattern

(b) Power spectrum from a single stored bunch. Only multiples of the revolution harmonic can be seen.

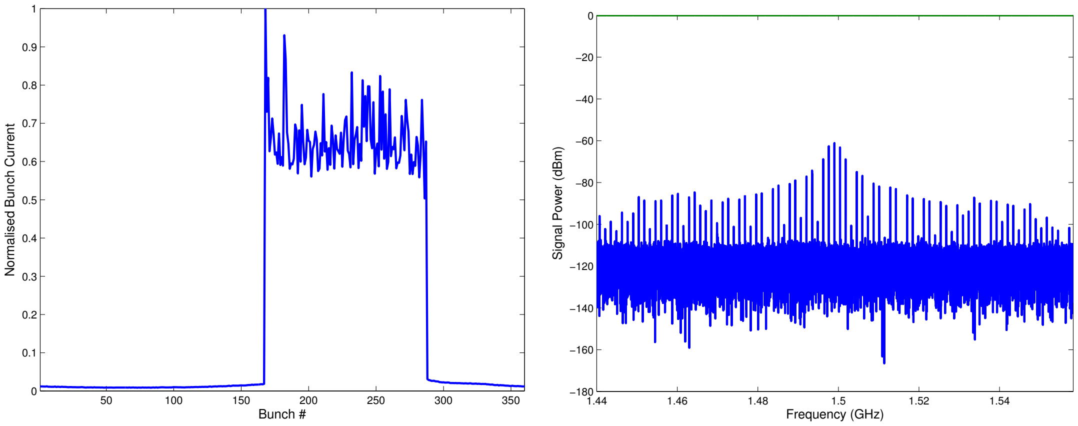

(c) 120 bunch train fill pattern

(d) Power spectrum from 120 bunch train. The spectra peaks at harmonics of the bunching frequency.

Figure 4.3: Changes in beam spectra with changes in bunch train length. As the fill pattern changes, the resulting power spectrum changes, altering how the beam couples with impedances within the ring.

$x(t)$ of a particle is [40]

$$\ddot{x}+\omega^2 x = A\cos\left(\Omega t\right). \tag{4.1}$$

The most general solution to this equation is

$$x(t) = x_0\cos(\omega t)+\dot{x_0}\frac{\sin(\omega t)}{\omega}+\frac{A}{\omega^2-\Omega^2}\left[\cos(\Omega t)-\cos(\omega t)\right], \tag{4.2}$$

where x_0 and $\dot{x_0}$ are the initial conditions of the displacement and angle of the particle respectively. The first two terms on the right hand side of Equation 4.2 describe the response of the system to a shock or impulse force. The long-term response of the system to a sinusoidal force is described by the third term and can be generalised from a single particle to a collection of particles with a distribution of oscillation frequencies by working in the center of mass of the bunch,

$$\langle x(t)\rangle = A\int\limits_{-\infty}^{\infty} d\omega\frac{\rho(\omega)}{\omega^2-\Omega^2}\left[\cos(\Omega t)-\cos(\omega t)\right], \tag{4.3}$$

where $\rho(\omega)$ is the probability distribution of oscillation frequencies, normalised such that

$$\int\limits_{-\infty}^{\infty}\rho(\omega)d\omega = 1. \tag{4.4}$$

A decision must be made on the shape of the $\rho(\omega)$. It will be assumed at this time that the probability distribution peaks at only one frequency, $\bar{\omega}$. Particles trapped in accelerator lattices tend to have strongly peaked narrow distributions so this assumption will be valid in most cases. For the sinusoidal force to excite the particles, the driving frequency must be close to the distribution peak i.e. $\Omega\approx\bar{\omega}$. Under these assumptions the expansion $\omega\approx\Omega+(\omega-\Omega)$ can be performed. Equation 4.3 can then be approximated as,

$$\langle x(t)\rangle = \frac{A}{2\bar{\omega}}\left[\cos(\Omega t)\int\limits_{-\infty}^{\infty}d\omega\rho(\omega)\frac{1-\cos((\omega-\Omega)t)}{\omega-\Omega}+\sin(\Omega t)\int\limits_{-\infty}^{\infty}d\omega\rho(\omega)\frac{\sin((\omega-\Omega)t)}{\omega-\Omega}\right]. \tag{4.5}$$

It can be seen that the sine and cosine terms have been separated, with the sinusoidal term being driven in phase and absorbing energy while the cosine term is being driven out of phase. In the approximation that the particle distribution $\rho(\omega)$ is sharply peaked about $\bar{\omega}$, Equation 4.5 becomes

$$\langle x(t)\rangle = \frac{A\sin(\bar{\omega}t)}{\bar{\omega}}\int\limits_{-\infty}^{\infty}d\omega\rho(\omega)\frac{\sin\left(\frac{1}{2}(\omega-\Omega)t\right)}{\omega-\Omega} \tag{4.6}$$

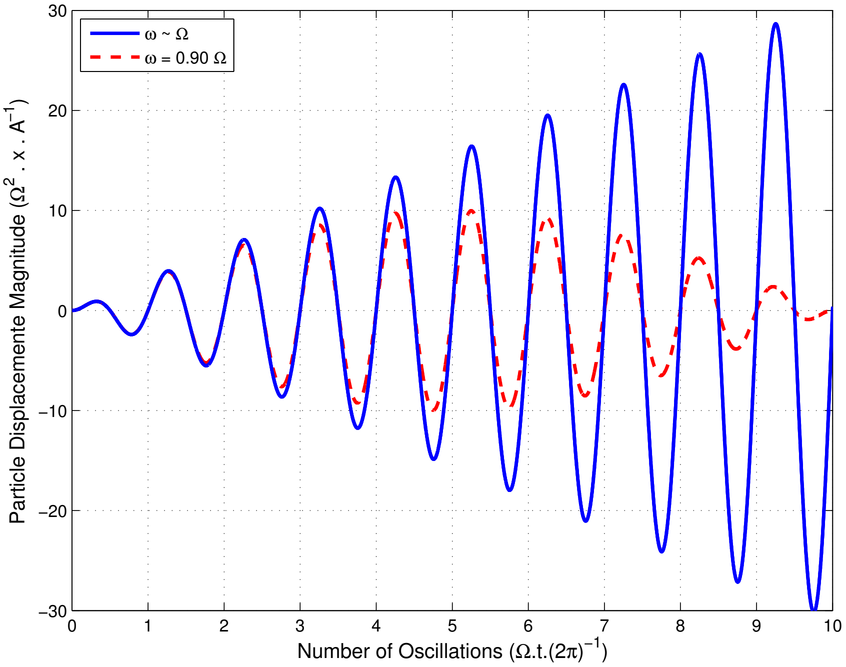

Figure 4.4: An example of Landau Damping, showing the linear position growth of a particular with natural oscillation frequencies near the forcing frequency. A particle with a natural frequency just 10% lower damps after 10 cycles [40].

where the position of the particle is driven by two terms — a fast oscillating $\sin(\bar{\omega}t)$ term and a slower envelope-like oscillation due to the $(\omega - \Omega)$ sinusoidal term. The component of the integral corresponding to a single frequency ω can be investigated by allowing $\rho(\omega)$ to be a delta function in frequency. The amplitude of the particles movement for that given frequency can be then calculated as

$$\text{Amplitude}(\omega) = \frac{A}{\bar{\omega}} \frac{\sin\left(\frac{1}{2}(\omega - \Omega)t\right)}{\omega - \Omega}. \tag{4.7}$$

Focussing on the $\sin(\frac{1}{2}(\omega - \Omega)t)$ term, the behaviour of the amplitude at different times t can be inferred. The amplitude of oscillation is zero at $t = 0$, reaches a maximum when the sine argument equals $\frac{\pi}{2}$ at $t = \frac{\pi}{(\omega - \Omega)}$, and returns to zero when the sine argument equals π at $t = \frac{2\pi}{(\omega - \Omega)}$. Particles that are driven at their oscillation frequency will continue to oscillate at higher and higher amplitudes, growing linearly in time. Excursions will eventually be stopped by the beam pipe and these few particles will be lost.

Figure 4.4 shows the displacement of a particle whose oscillation frequency is equal to the driving frequency and a particle whose oscillation frequency is 90% of the forcing frequency. Particles driven at a frequency other than their fundamental oscillation frequency will absorb energy from $t = 0$ to $t = \frac{\pi}{(\omega-\Omega)}$ after which they will start to transfer energy to particles that exhibit movement closer to the driving frequency. In this fashion all of the energy put into the system by the driving force will be transferred from the majority of the particles to the particles where $\omega = \Omega$ and these will be lost. This is the strength of Landau damping. As particles which are further away from the driving frequencies are damped through this mechanism this leads to the primary method for passively damping multi-bunch instabilities in modern synchrotrons: implementation of higher order multipole magnets to increase $\Delta\omega$.

In Chapter 2 the concept of chromaticity was discussed where each particle experiences a shift in its betatron tune due to a change in energy, specifically;

$$\frac{\Delta Q}{Q} = \xi \frac{\Delta p}{p} \tag{4.8}$$

where Q is the betatron tune, p is the momentum of the particle and ξ is the chromaticity. For a transverse instability, a higher passive damping rate can be achieved by increasing the energy spread of the particles within the ring, or by increasing the chromaticity of the lattice. Landau damping can also be strengthened by increasing the spread of synchrotron frequencies with the addition of active beam components such as Landau cavities [52].

To control coupled-bunch instabilities without the active feedback system the chromaticity of the storage ring lattice was increased from the nominal value of $(\xi_x, \xi_y) = (2, 2)$ to $(\xi_x, \xi_y) = (3.5, 13)$ in order to be stable at 200 mA of stored beam with all three IVUs at minimum gap. Future additional insertion device beamlines demand higher chromaticities to maintain stable beam. Eventually the strength of the sextupole focussing would reduce the dynamic aperture of the lattice such that any increases in Landau damping would be overcome by reduced beam lifetime and a loss of injection efficiency. In the ASLS storage ring, dynamic aperture corrections are performed using harmonic sextupoles although increasing the strength of these magnets introduces strong non-linear fields to the lattice and reduces injection efficiency.

Therefore it is inevitable that, like most other high current storage rings, the ASLS considers the use of an active feedback system to control transverse coupled-bunch instabilities and allow for the reduction of lattice chromaticities.

4.2 Active Bunch-by-Bunch Feedback

The future development of the ASLS will inevitably include more insertion devices, further eroding the impedance budget to the point where the methods described above will no longer stabilise the stored beam at 200 mA. Consequently the only solution capable of maintaining the design performance of 200 mA in the future is to implement an active feedback system.

Active damping systems provide an extra damping term for the beam, allowing control of instabilities with large growth rates. Utilising an active feedback system allows for

i) a reduction of sextupole fields,
ii) an increase in the dynamic aperture of the ring,
iii) the storage of the design current of 200 mA with an increase in beam lifetime,
iv) a damping overhead for future additions to the ring,

and provides extensive diagnostic abilities for measurement of ring parameters such as instability growth rates. The difference between *active* feedback and *passive* feedback is that damping is achieved by measuring the turn-by-turn oscillation of the beam, calculating an error signal and actuating the beam to minimize movement rather than introducing a constant damping term.

Modern synchrotron storage rings are designed for a specific function and can vary in parameters from one machine to another. Therefore the transverse active feedback systems which service these rings must also be designed specifically and this has lead to a variety of design approaches, each with advantages and disadvantages.

4.2.1 Comparison between Analogue and Digital Systems

Active damping systems can be separated into two families based on their measurement domain during operation. *Frequency domain* systems operate on a mode by mode basis, tuned to specific modes of oscillation which are the most damaging to the stability of the ring. *Time domain* systems operate on the movement of each bunch individually and by damping the motion of the beam across all modes of oscillation. The base system for active bunch-by-bunch feedback is a single Beam Position Monitor (BPM) connected to a transverse kicker separated by a phase delay of $\phi = \pi$. This setup applies a kick ($\Delta x'$) at turn $n + i$

proportional to the measured position on turn i [53],

$$\sqrt{\beta_K}\Delta x'_{K,n+i} = a\frac{x_{BPM,i}}{\sqrt{\beta_{BPM}}}, \tag{4.9}$$

where n is a positive integer, β and x are the betatron function and the horizontal position respectively. Identifying locations in the ring where the BPM and kicker satisfy the phase relationship can be difficult, so it is common to introduce a delay line such that any deviations from the optimum delay can be corrected.

Up until this point, the system can be completely constructed using analogue components and systems such as this have been successfully utilised at synchrotron facilities [54, 55]. When operating in the frequency domain, a separate system needs to be designed for each mode that requires damping. Since the number of modes is equal to the harmonic number of the ring, it is more useful for small rings with a low number of bunches. Notch filters in between the BPMs and kickers can be used to remove revolution harmonics and any offset caused by a DC shift of the beam. Removing the DC component of the beam is important to maintain dynamic range and prevent saturation of the amplifiers.

In a digital system the x and y position of the bunch is digitised using Analogue-to-Digital Converters (ADCs) and fed into a computation section. This section can comprise a PC, arrays of Digital Signal Processors (DSPs) or a Field Programmable Gate Array (FPGA). The computational section provides the filtering, and some of the delay control normally supplied by cable lengths in the analogue active feedback. Importantly, control is now provided remotely and parameters can be altered in real-time in response to changing conditions within the lattice. After the corrective signal is calculated it is fed to a Digital-to-Analogue Converter (DAC), amplifier and kicker chain to actuate the beam.

Although the digital system is more complicated than a fixed analogue method, it provides a higher degree of remote control and fine tuning of the feedback loop. Since it also requires measuring the position of each bunch every turn, it provides a range of diagnostics that will be discussed in Section 6.1 and Chapter 7. For these reasons the active transverse feedback system at the ASLS was chosen to be a digital system. The setup of the system will be described in the next chapter.

4.3 Conclusion

Coupled-bunch instabilities are a damaging phenomenon and must be controlled if a high current is to be stored within an electron storage ring. Multiple passive methods were outlined and while they can provide a solution to lower strength instabilities, they can have detrimental side-effects such as lower beam lifetimes and reductions in the dynamic aperture of the ring. The growth rates of both resistive wall and resonator style instabilities measured in the ASLS storage ring are shown in Table 4.1. Compared to the measured growth rates of instabilities within the ring, natural damping alone is not capable of controlling instabilities as the sum of damping rate and growth rate are greater than zero.

To provide adequate damping in all situations for current conditions and in the future, the active damping system should provide a damping rate an order of magnitude larger than the resistive wall growth rate. This implies that the active damping system should have a damping rate in excess of approximately 3360 s^{-1}.

Active beam feedback allows for the control of instabilities while also removing the side-effects associated with passive damping. The combined analogue/digital feedback loop also provides the capability for enhanced diagnostics as described in Chapter 7. Methods used to successfully commission the system will be presented in the next chapter and the results of a study into existing instabilities within the ring will be shown.

Table 4.1: Measured growth and damping rates in the Australian Synchrotron storage ring

	Source of Beam Movement	τ^{-1} (s^{-1})	τ (ms)
τ_g^{-1}	Resistive Wall Instability (Mode #359)	336.1	2.975
	Resonator-style Instability (Mode #228)	575.1	1.738
τ_p^{-1}	Natural Damping	−208.3	−4.801

Chapter 5

Experimental Setup

This chapter outlines the principle of operation and experimental operation of the Bunch by Bunch Feedback (BBB) system recently commissioned in the ASLS storage ring to combat strong coupled-bunch instabilities. The active transverse feedback system supplants the passive methods outlined in the previous chapter and provides a strong damping term, allowing for the continued introduction of insertion devices into the ring.

An outline of the entire transverse feedback system is shown in Figure 5.1. Due to the complex interface between the analogue measurement system and the digital signal processing commissioning the system is more difficult than the passive methods. However it ultimately provides a stronger damping term without any of the detrimental effects such as a reduction in the dynamic aperture of the beam.

An active feedback system consists of three discrete components: measurement, computational and actuation. In a typical experiment the bunch position data is taken each turn using the measurement setup, a corrective waveform is calculated in the computational section and placed onto the beam using the actuation system. Operating in the time domain, the system damps the coherent motion of the beam by damping the motion of individual bunches.

5.1 Bunch Motion Measurement

The measurement system for the ASLS BBB setup is shown in Figure 5.2. As a bunch passes the BPMs the electric fields couple capacitively and induce a voltage proportional to the

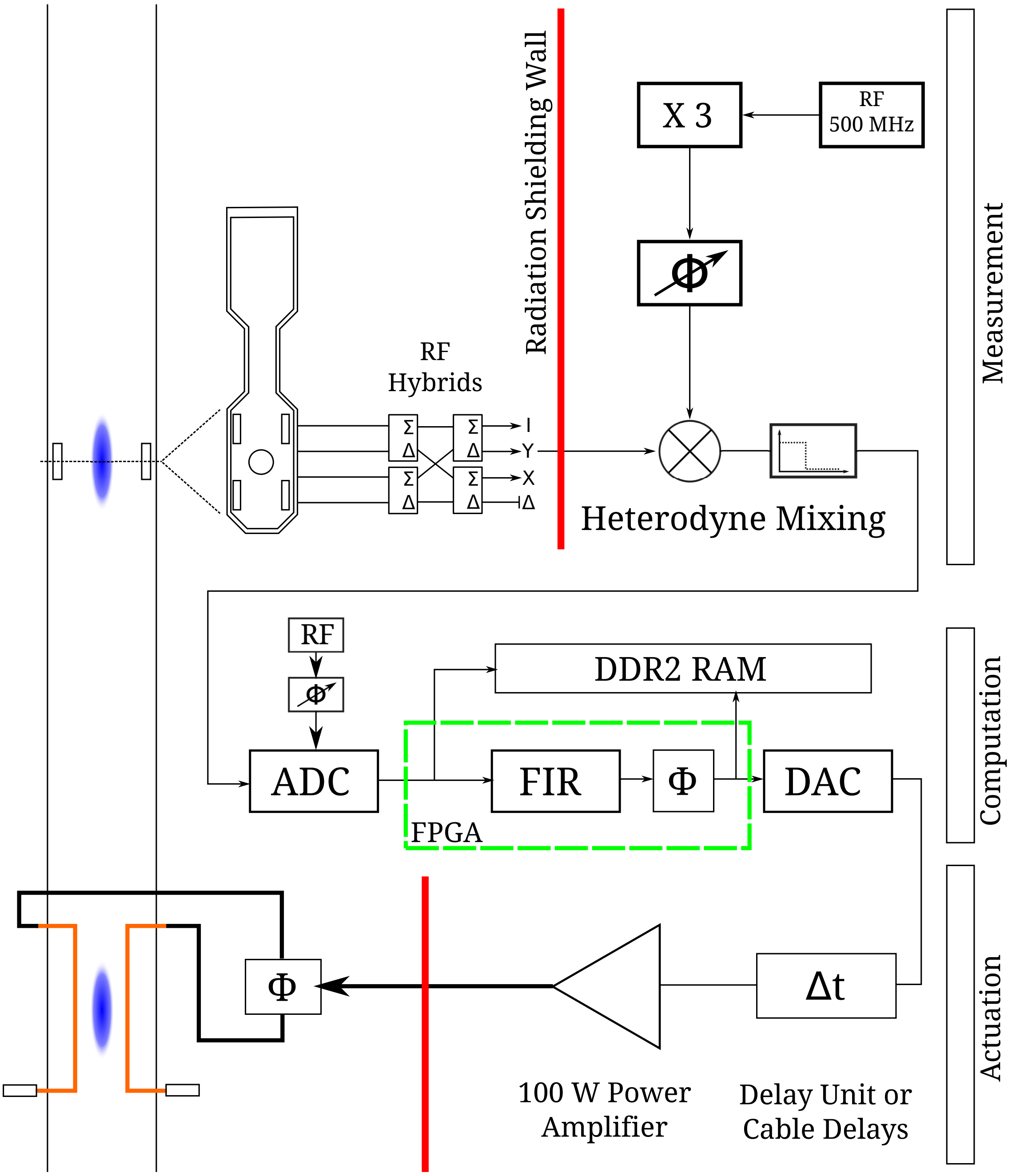

Figure 5.1: A schematic diagram of the components which make up the transverse feedback system. The system can be broken up into three broad sections: *Measurement* which determines the position of each bunch each turn, *Computation* which calculates the corrective waveform to combat any unstable oscillations and *Actuation* which applies the corrective waveform to measured bunch.

distance between BPM and the bunch. The transverse and longitudinal position of the bunch can be calculated using the sum and differences of pairs of BPMs,

$$x = (A + D) - (B + C), \tag{5.1}$$

$$y = (A + B) - (C + D), \tag{5.2}$$

$$I = (A + B + C + D), \tag{5.3}$$

where x and y are the transverse coordinates and I is the intensity of the bunch (which can be used for longitudinal feedback). A, B, C and D are four separate buttons laid out in the beam pipe as depicted in Figure 5.2. The RF arithmetic is done in analogue for the BBB system in contrast to the slower BPM system installed around the ASLS storage ring. The BPM system digitises the voltage from each button and then digitally performs the addition and subtraction which can lead to problems with quantisation error and dynamic range of the systems. To maximize bandwidth and dynamic range while reducing quantisation errors due to digitisation, x and y position calculations are achieved using analogue components such as RF hybrids.

The button style BPMs used to measure the beam position have a low spectral response at 500 MHz (see Figure 5.3) and the coaxial cabling connecting the BPMs acts as a high pass filter above 1.5 GHz — therefore sidebands of the third harmonic of the bunching frequency contain the most information available to the BBB system concerning beam motion. Many high quality inexpensive RF components are available around the 1.25 - 1.75 GHz range and the hybrids used to construct the position signal were designed to have a flat frequency response in this range. The analogue signals induced by a single high current (5 nC) bunch is shown in Figure 5.4.

Although the beam signal from the BPMs has the most power at a sideband of 1.5 GHz, the digitisation and calculation within the computational section operates at a frequency of 500 MHz. Converting the voltage pulse from the BPMs/hybrid combinations to signals which can be read by the computational section requires mixing the 1.5 GHz central frequency down to baseband. This is achieved using a common technique in RF engineering, heterodyne mixing.

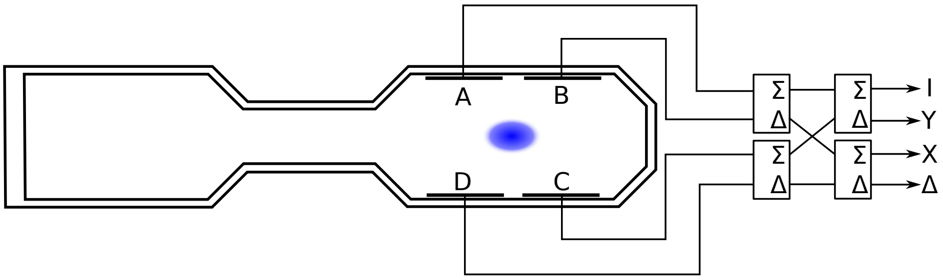

Figure 5.2: The setup used to extract x and y coordinates from a combination of BPMs using RF hybrids. Each hybrid takes two analogue inputs and outputs the sum and difference of the two input signals. By combining sum and difference, an analogue signal representing the x and y position can be constructed. For example, the analogue x position is calculated as $(A - B) + (D - C) \Rightarrow (A + D) - (B + C)$. Also reconstructed is a signal relating to the intensity of the bunch (I) and an unused signal (Δ).

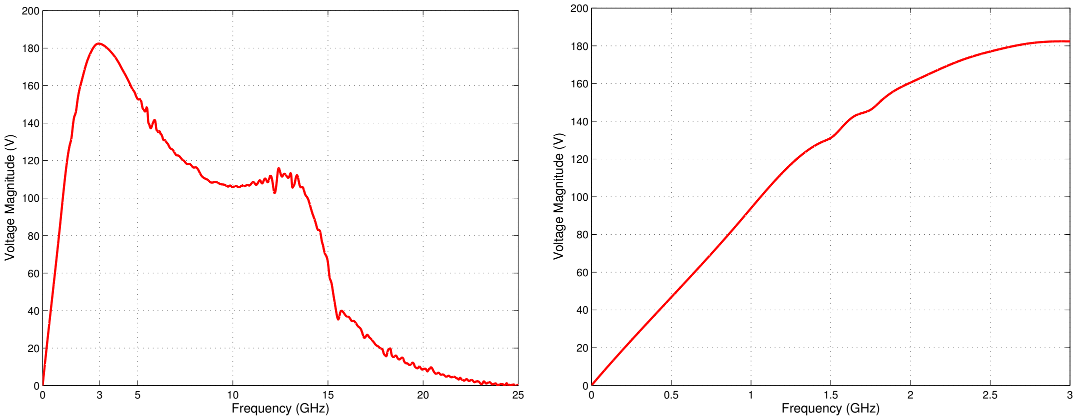

(a) The full frequency response of a BPM

(b) The frequency response, concentrating on DC to 3.0 GHz

Figure 5.3: Amplitude frequency response of a BPM to a passing 40 ps long gaussian bunch. A model of the BPM block was recreated in Microwave Studio [56] and the response to a 40 ps bunch was simulated using finite element and wake field analysis methods [57]. The response curve shown does not include cable attenuation which will act as a low pass filter, attenuating the response at frequencies higher than approximately 1.5 GHz.

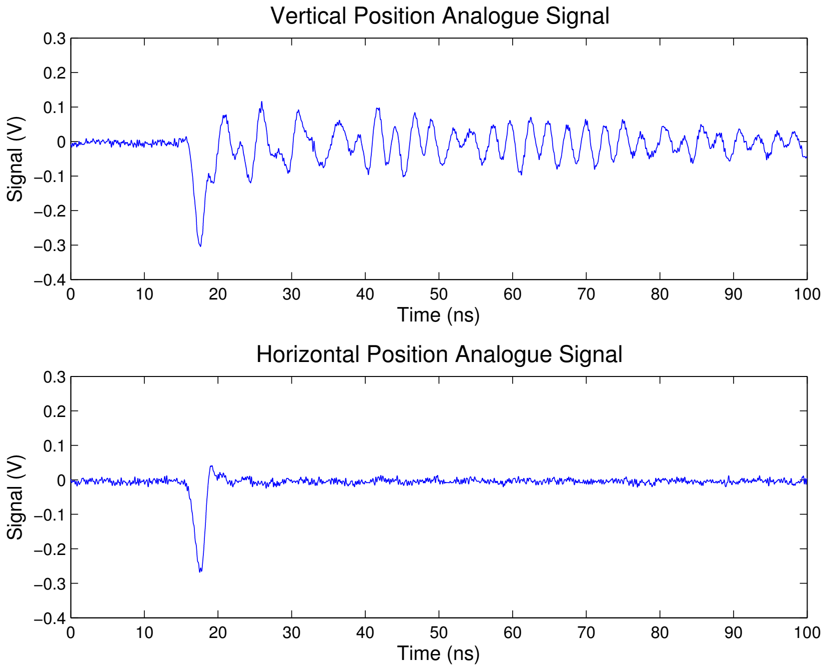

Figure 5.4: The resulting position signal from a high current (5 nC) single bunch. The large ringing in the vertical is due to a combination of the geometry of the BPMs and bandwidth limitations of the RF hybrids.

Heterodyne mixing can be described using the following trigonometric double-angle relationship:

$$\sin(A) \times \sin(B) = \frac{1}{2}\sin(A-B) + \underbrace{\frac{1}{2}\sin(A+B)}_{\text{Removed with low-pass filter}} \tag{5.4}$$

Mixing together two sinusoidal signals of different frequencies results in a signal that is the sum of two frequencies, one at $f_{\mathrm{hi}} = (A+B)$ and one at $f_{\mathrm{lo}} = (A-B)$. Applying a low pass filter post-mixing removes f_{hi} frequency leaving only the difference. This technique has been implemented for the BBB system using the system described in Figure 5.5.

Operating in the time domain and acting on the motion of single bunches, the frequency of interest for the BBB system is the tune frequency. The location of the tune sideband near 1.5 GHz is

$$f_{rf} + Q.f_0 \approx 1.500299\ \text{GHz}. \tag{5.5}$$

By mixing this signal frequency with a heterodyne frequency of 1.5 GHz the result is a combination of $f_{\mathrm{lo}} = 299$ kHz and $f_{\mathrm{hi}} = 3.0003$ GHz frequencies. Removing the high frequency

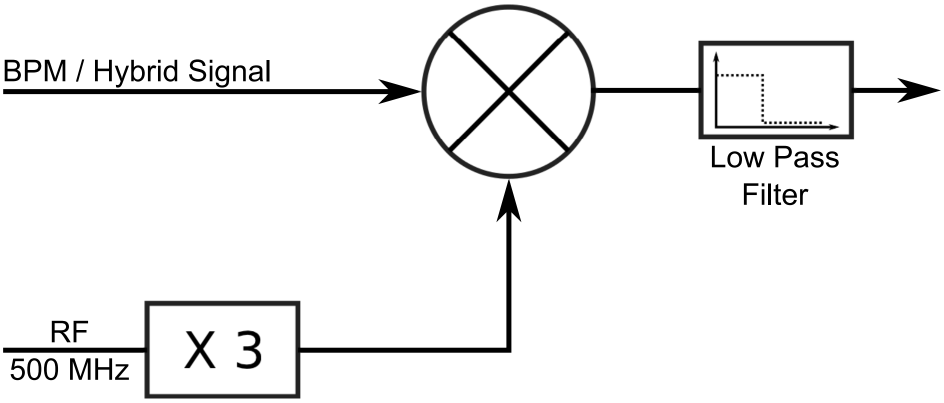

Figure 5.5: A diagram of the heterodyne down-mixing implementation. The signal is first mixed with a 1.5 GHz signal before being low pass filtered to extract the low frequency sideband. This is an electrical implementation of the trigonometric relationship described in Equation 5.4.

component with a low-pass filter, the signal corresponding to baseband (299 kHz) is within the digitisation bandwidth of the computational section.

5.2 Computational Section

Once the position of each bunch has been measured any coherent motion in the beam is extracted and used to calculate a corrective pulse. The data acquisition framework of this section of the hardware is a combination of a Libera Bunch by Bunch Feedback system with a Libera Bunch-by-Bunch Front End, both constructed by Instrumentation Technologies [58]. Input to the Libera BBB system consists of a set of four time-interleaved 14 bit, 125 MHz Analogue-to-Digital Converters (ADCs) connected to a Xilinx Virtex-II Pro FPGA [59].

Each ADC is the beginning of a data processing *chain* (4 chains in all). As the RF frequency and thus the bunching rate of the ring is approximately 500 MHz, the 125 MHz ADCs need to be interleaved such that each only measures a quarter of the bunches. By running the system at a 500 MHz clocking rate but demultiplexing the clock to the four separate chains, ADC N will only measure bunch

$$4K + N \bmod M, \tag{5.6}$$

where M is the harmonic number of the ring and K is a positive integer.

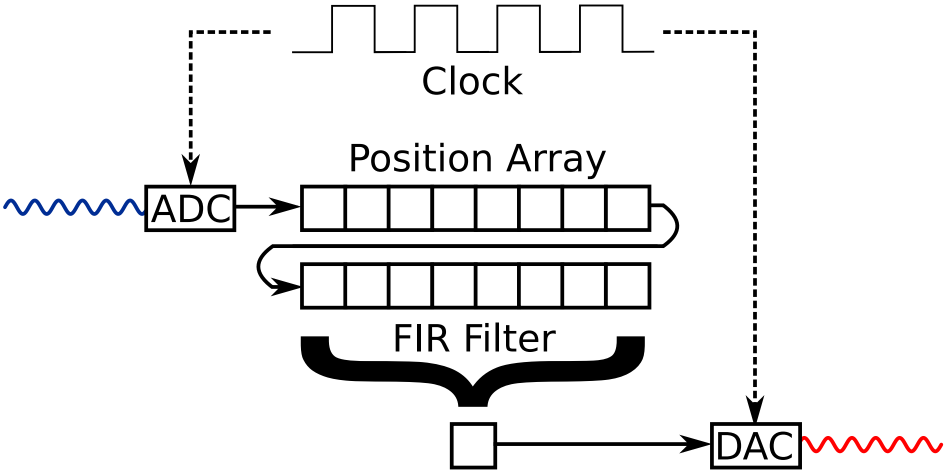

Figure 5.6: Circuit diagram of the BBB computational section. Data enters the acquisition chain through the ADCs and the position data for each bunch is placed into one of 360 sixteen element FIFO stacks. Each turn the data from the FIFO stacks is used by the FIR to calculate a corrective signal, which is then reconstructed by the DAC.

Each of the chains runs at 125 MHz and only processes data from 90 $\left(\frac{M}{4}\right)$ RF buckets. As the position of each bunch is digitised the data is placed into a bucket specific First-In First-Out (FIFO) stack. There are a total of 360 stacks divided evenly between the four data chains. Using these stacks the system accumulates information about the movement of bunches from turn to turn. After 16 turns the stack is full, and new information replaces the oldest data in the stack.

5.2.1 Finite Impulse Response (FIR) Filters

As instabilities develop, beam positions begin to deviate and therefore to combat the increase in bunch displacement over time, a corrective waveform must be quickly calculated. This is achieved by implementing an Finite Impulse Response (FIR) filter in each data acquisition chain. A FIR filter is a method of digital signal processing commonly used in embedded systems with limited resources and can be implemented rapidly in hardware using only arithmetic operations such as addition and multiplication. The FIR is a discrete time filter which convolutes a vector of N coefficients against a longer input vector.

$$X_i = \sum_{j=0}^{N} a_j x_{i-j}, \tag{5.7}$$

where x is the input vector, X is the output vector and a_j is the vector of FIR coefficients. The length of the coefficient vector (N) is referred to as the number of *taps* in a filter. An input vector may be constructed dynamically even as the coefficient vector traverses it.

Filters can be designed for a complex frequency response through a variety of methods such as *equiripple* or *frequency sampling.* Signal processing tool kits such as the one available for MATLAB [60] have a suite of functions which design FIR filters. Many of the diagnostic systems at the ASLS are controlled through MATLAB and therefore it was chosen to construct the FIR filters for the BBB feedback system.

The signal delay from an FIR filter is equal to half the number of taps multiplied by the sampling frequency (the RF frequency in this case) [61],

$$t_d(\mathrm{FIR}) = \frac{N \times f_{rf}}{2}. \tag{5.8}$$

The filter constructed for the BBB system was designed to remove any DC offset in the BPM position response caused by the BPM block not being centered on the orbit of the particles. Allowing the DC component to pass through induces a constant load on the amplifiers and does not relate to any coupled-bunch motion. Further, removing it from the waveform allows for an increase in the dynamic range of actuation. The filter must also have a high gain at the tune frequency and have a phase response to ensure that the corrective signal is out of phase by π radians where the beam is actuated.

The complex filter response, both gain and phase delay, for the standard 16 tap filter used in the ASLS BBB feedback system is presented in Figure 5.7. It can be seen that the system has a peaked response at the tune frequency and dips sharply at low frequencies to remove any residual offset in the BPM position response.

5.3 Actuation Section

Once a corrective waveform has been calculated a set of high bandwidth kicker magnets are used to correct large amplitude oscillations of bunches in the beam. A CAD diagram of both

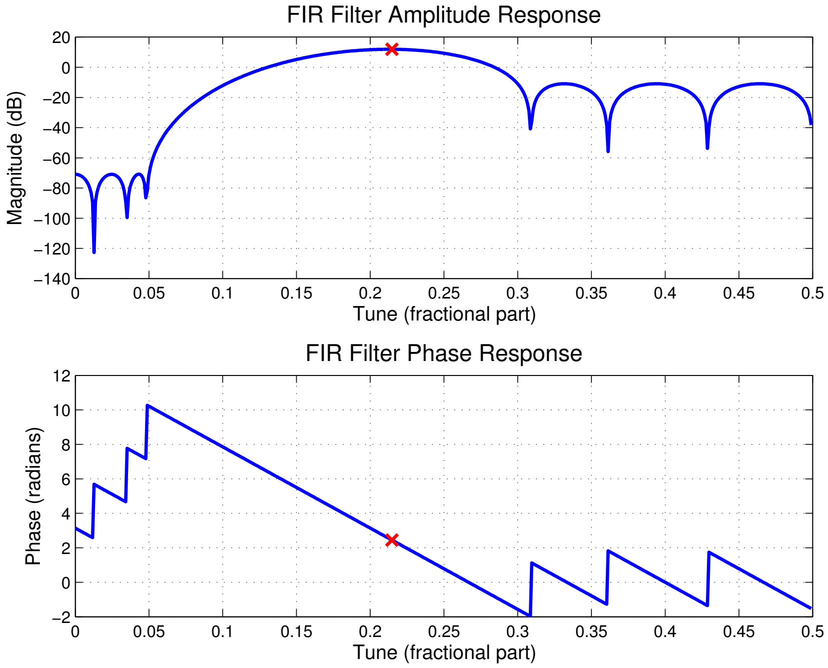

Figure 5.7: To construct a corrective pulse from the signal, the raw ADC values are passed through a FIR filter which removes the DC response from the signal and outputs a signal delaying in phase by π. All of the signal is carried by the tune frequency, shown by the marker in the above figure.

the vertical and horizontal kicker magnets is presented in Figure 5.8.

Each magnet is realised as a pair of quarter wave striplines which are driven in a differential mode by two 100 W RF amplifiers, one for each plane. A schematic of the actuation system is shown in Figure 5.9.

For the amplifiers to be suitable for BBB operations, the complex phase response of the actuation amplifier should be flat across all of the expected coupled-bunch mode frequencies. In the case of the ASLS storage ring this is from approximately 300 kHz to 250 MHz. A network analyser was used to measure the complex response of the amplifiers in the BBB system and the results are presented in Figure 5.10. Both the phase and amplitude response of the amplifiers fall within the acceptable range of ±4 dB gain and ±10° phase response.

The other important characteristic of the actuation section is the *isolation* of the signal for a given RF bucket. When a corrective pulse is calculated for a given bunch there is a requirement that the particular bunch will only experience the deflecting perturbation with

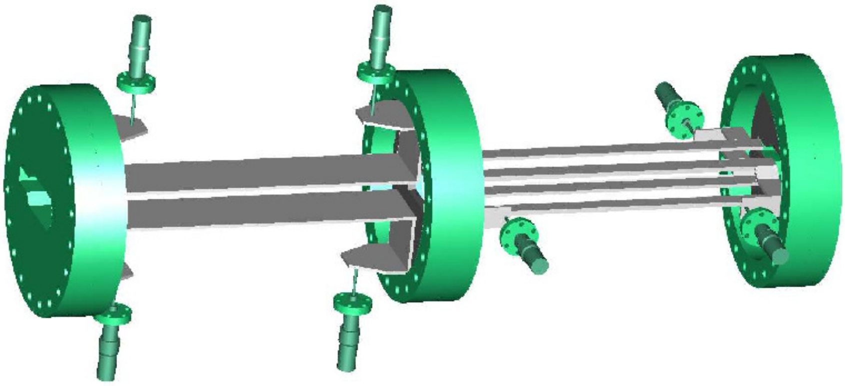

Figure 5.8: A 3D diagram of both the vertical and horizontal kicker magnets. These kicker magnets are based on the magnets utilised at DELTA [62] and are optimised for the specifications of the ASLS storage ring. Both are quarter wave stripline kickers designed to be driven with differential signals. The horizontal kicker magnet has slots cut out to prevent damage from synchrotron radiation in the horizontal plane.

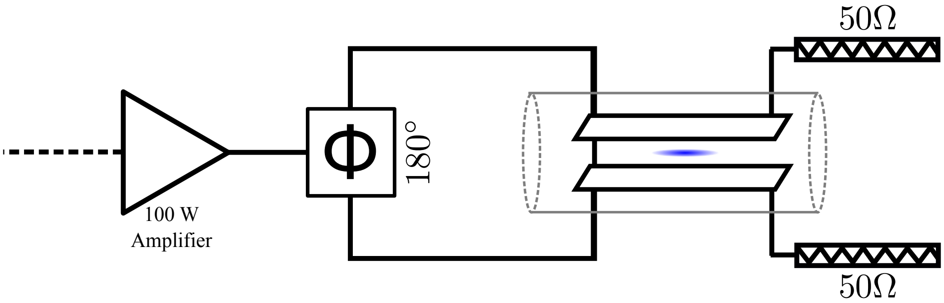

Figure 5.9: The actuation section consists of the signal from the BBB DAC, a 100 W power amplifier and a brace of quarter wave striplines. An identical setup is used for the horizontal with the exception of the design of the horizontal kicker magnet (see Figure 5.8). A corrective waveform from the BBB feedback system is amplified and passed into the storage ring through low loss cabling. The 180° splitter provides the differential signal used to drive the striplines.

Table 5.1: The coefficients used to construct the FIR filter used regularly at the ASLS. The response of this filter is shown in Figure 5.7.

#	Coeff. Value	#	Coeff. Value
0	+0.0102237	8	+0.9760704
1	−0.2366051	9	−0.4167666
2	+0.2209302	10	−0.9772611
3	+0.5351968	11	−0.1119818
4	−0.1119818	12	+0.5351968
5	−0.9772611	13	+0.2209302
6	−0.4167666	14	−0.2366051
7	+0.9760704	15	+0.0102237

no cross-talk from the signals intended for the preceding and following bunches.

Isolation is described by the ratio of voltages between the peak of the corrective pulse and voltage measured an RF period away (2.0 ns) measured in dB,

$$\text{Isolation} = -20\log_{10}\left(\frac{V_{\text{peak}}}{V_{\pm}}\right), \tag{5.9}$$

where V_{peak} is the highest voltage the pulse reaches and $V_{\pm}$ is the voltage measured 2.0 ns following (+) or leading (−) the time of the peak voltage. Figure 5.11 shows how the isolation of a signal can change after passing through the vertical feedback power amplifier.

A well tuned amplifier will exhibit a linear response at all available gains and any deviation at high gains will be the result of saturation. To maximise the dynamic range of the system, the input to the amplifier must be adequately attenuated such that at the highest amplifier gain, a full scale input signal will just reach the saturation level of the amplifier.

Figure 5.12 shows the response of the vertical power amplifier of the BBB transverse feedback system before tuning to maximise the dynamic range. Saturation can be seen between the 45 and 50 dB gain settings, where the amplified voltage begins to deviate significantly from a linear gain response. As the maximum gain of the amplifier is 54 dB and saturation is observed around 48 dB, 6 dB of input attenuation was applied at the input stage of the

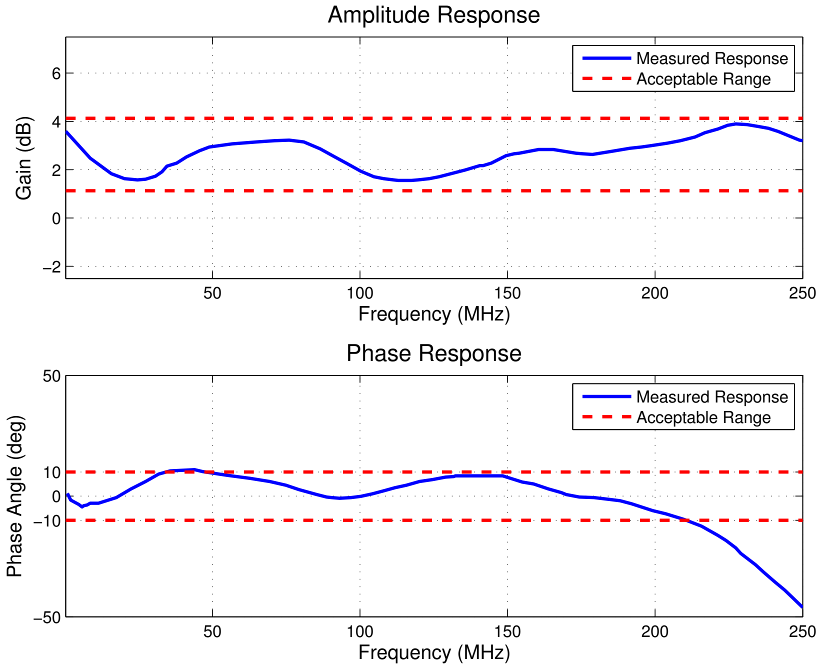

Figure 5.10: Network analyser measurement of the frequency response of the BBB actuation amplifiers. To effectively actuate the beam, the amplifier must have a known and flat complex response between 300 kHz and 250 MHz. Flat is defined in this case as falling between ±1.5 dB gain and ±10° phase response. The amplifier response satisfies the majority of the restrictions and is suitable for BBB operations.

amplifier to prevent the maximum DAC output from saturating the system. The amplifier was then left at its maximum gain without the risk of saturation during BBB feedback.

5.4 System Tuning with Beam

The analog front-end mixing phases must also be carefully selected to ensure that the signal sent from the BPMs to the FPGA is maximised. The output signal from the FPGA / DAC sent to the kickers must be delayed such that the corrective waveform calculated for a given bunch arrives at the kickers simultaneously with that bunch, albeit several turns after the measurement of that bunch motion. Finally the phase difference of the signal from the BPMs to the kickers must be π radians to generate a negative feedback system to damp the beam. The system can also be put into positive feedback mode by changing the phase difference by

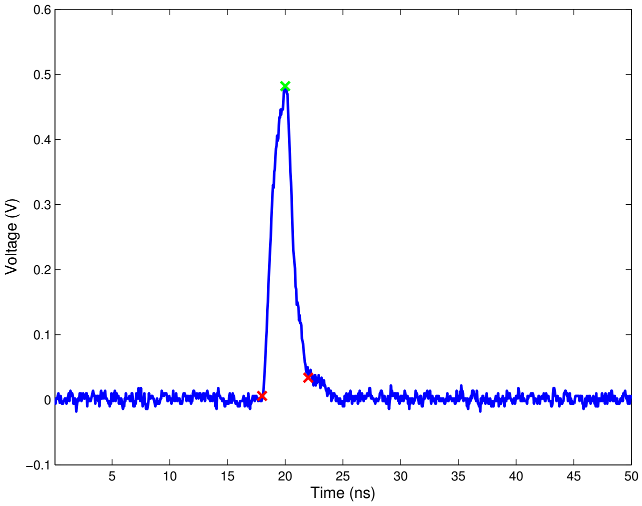

(a) Isolation measurement of a single bunch output. The test signal sent to the DAC was a 2.0 ns square wave. Measured isolation $(-,+) = (38.1\text{ dB}, 23.0\text{ dB})$.

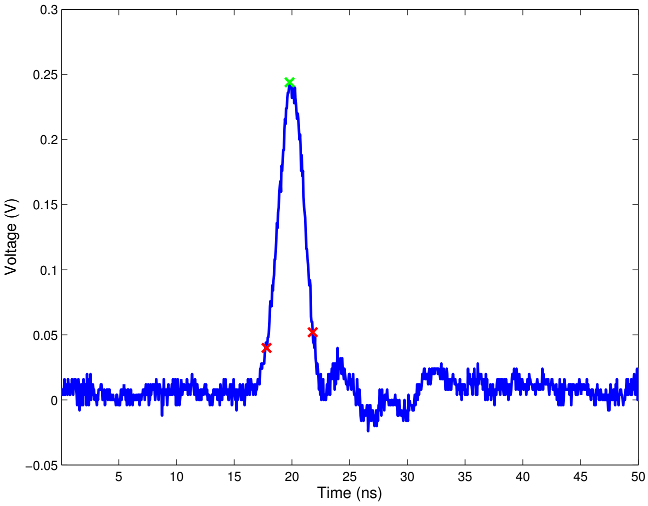

(b) Isolation measurement of the same output after passing through the power amplifier in the vertical plane. Amplifier gain was set to 45 dB. To prevent overload of the oscilloscope front end 50 dB of attenuation was added to the amplifier output. Measured isolation $(-,+) = (15.7\text{ dB}, 13.4\text{ dB})$.

Figure 5.11: Isolation measurements immediately before and after the 100 W power amplifier associated with vertical plane feedback. Figure 5.11a shows a square wave of width 2.0 ns as recreated by the BBB output DAC. The isolation was calculated using Equation 5.9, measuring the voltages leading and trailing the peak of the pulse by 2.0 ns.

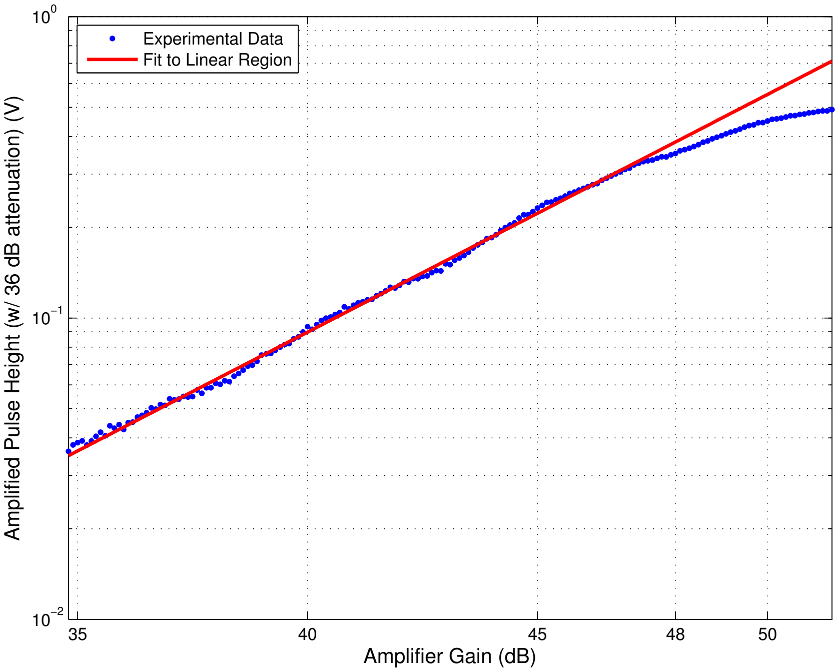

Figure 5.12: Linearity measurements of the BBB vertical actuation amplifier. The linearity was evaluated by adjusting the gain of the amplifier while monitoring the output voltage. Significant deviation from linearity can be seen from 48 dB. To maximize dynamic range, the peak gain was reduced from 54 dB to 48 dB by adding 6 dB of input attenuation.

2π for tuning purposes (as described later in this section).

A stand-alone scheme for tuning the system has been developed at the ASLS which relies only on a temporary fine resolution delay line.

5.4.1 Longitudinal Tuning

The first step is to optimise the longitudinal tuning of the system, that is to ensure the delay between the BPM signal and kicker response is equal to $N(t - \beta.c.s_{bk}^{-1})$, where t is the orbit period of the ring, $\beta = \frac{v}{c}$, s_{bk} is the ring distance from the BPMs to the kickers and N is an integer. This delay must take into account all the cable delays and internal delays in FPGA routing.

To measure the appropriate delay needed to overlap the output signals with the correct bunches the system is put into open loop mode using the following experimental setup:

1. The FIR coefficients for the plane to be measured are set to *pass-through* $(a_j = [1, 0, 0, \ldots, 0])$

so that the signal from the ADCs is passed straight to the DAC.

2. The output from the DAC is connected to a high resolution delay line prior to amplification. A temporary delay box [63] is used for tuning at the ASLS, as it allows for remote control with picosecond resolution.
3. A high bandwidth (> 1 GHz) oscilloscope [64] is connected to an upstream pickup of the BBB kickers.

With the setup outlined above, the BBB feedback kickers are used as both actuators and pickups. As the beam passes the kickers a voltage is induced onto the kickers which can be picked up by the oscilloscope. This gives a fiducial point within the RF period for when the bunch is passing through the kicker.

The feedback system is then turned on with the pass-through filter active and all variable delays are set to zero. To remove ambiguity with surrounding bunches a high purity single bunch is injected into the storage ring. As the ADCs measure a single bunch signal similar to Figure 5.4 and pass it directly to the DAC a single bunch signal will be placed onto the kicker. The voltage at the downstream pickup of the kickers will consist of both the induced signal from the beam and the signal from the feedback system. Ideally the signals would be at the same temporal location but are more likely to be offset by some Δt.

Delays are chosen such that Δt approaches zero, with delays of integer multiples of 2 nanoseconds being provided by the feedback system and the remaining delay supplied by the delay box. Once the delay has been corrected, the entire system from DAC output to amplifier input is measured using a network analyser and an equivalent length of semi-rigid cable is produced to replicate the delay.

The longitudinal tuning of the system using the preceding experimental setup was necessarily conducted early in the commissioning timeline. At this point the feedback system lacked features that would allow for a more rigorous tuning of the system. An alternative tuning method can be performed by first introducing a local beam bump in the plane to be tuned, centered around the location of the BBB BPMs. This will maximise the $\Delta\{X, Y\}$ signal for tuning measurements. Once the bump is formed, a single bunch is driven in positive feedback mode where the phase advance of the filter is shifted by π radians from the damping setting. The longitunal tuning can be completed by altering the signal delay and measuring the resulting motion of the targeted bunch and those surrounding it. When the targeted bunch movement is at a maximum while the surrounding bunches are at a minimum, the system is tuned longitudinally. This is the technique that will be used in the future if the BBB system requires retuning. Retuning will only be necessary if the timing between DAC and kicker changes, for example, if a connecting cable needs to be replaced.

Phase Tuning

One of the main advantages to the longitudinal method outlined in the previous section is that it does not require unstable beam. Tuning aspects of the feedback system using stored beam can be problematic as miscalculated phase delays can cause excitation of the beam. If the phase delay of the corrective signal is in error by π radians then the motion does not cancel but instead the beam is resonantly excited until the particles can be lost. This can be particularly frustrating as for every error in stability tuning large sections of the beam are lost, stabilising the beam. To allow tuning with stable beam, a system was developed at the ASLS using one BBB system to provide an excitation signal to drive the beam into an unstable state in a controlled manner while using the other BBB system to damp.

The output of the Libera BBB can be either controlled by the FIR filter output or it can be used as a Numerically Controlled Oscillator (NCO). The sine wave is constructed digitally within the FPGA and is called a NCO to differentiate the output from a signal derived through analogue means. The NCO can be used to output a waveform with a frequency up to 125 MHz to the DAC and can be masked such that only a subset of the bunch train will experience the NCO waveform.

As described in Chapter 3 the frequency of each unstable coupled-bunch mode of motion is a sideband of the revolution harmonic,

$$\omega_m = pM\omega_0 \pm (m+\nu)\omega_0, \tag{5.10}$$

where p is an integer, ν is the fractional tune and m is the mode of motion (from 0 to $(M-1)$).

The experimental setup is described in Figure 5.13. To tune the vertical setup, the horizontal BBB unit is set to output a frequency which corresponds to one of the coupled-

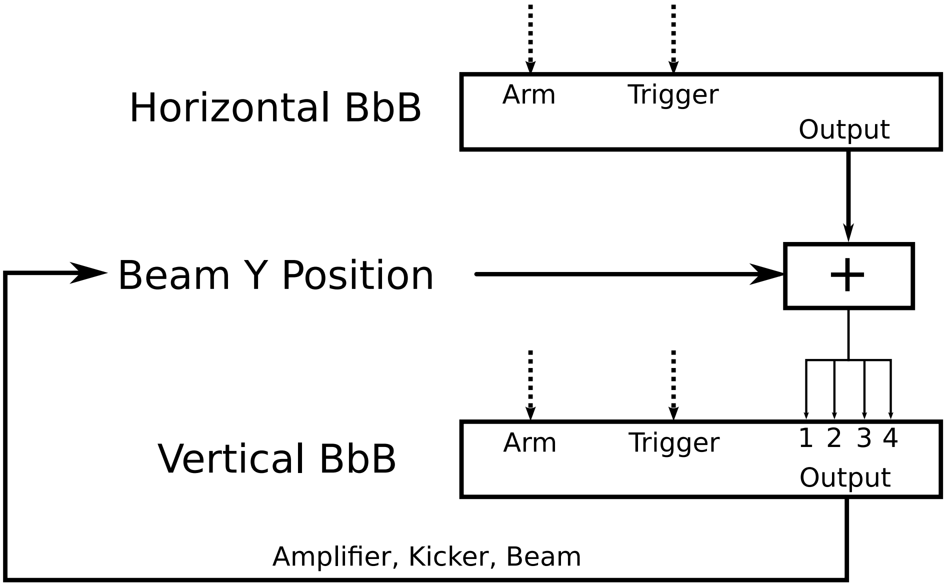

Figure 5.13: Setup for an NCO Excite/Damp measurement. The horizontal BBB unit is setup to output a sine wave signal at a coupled-bunch frequency. This signal is mixed with the BPM signal and fed into the ADCs of the vertical BBB system. A corrective output for this erroneous input causes the beam to become unstable and this signal is fed back into the vertical BBB system. Once the driving signal is removed the feedback system damps the unstable beam motion. The beginning of both the excitation signal and data acquisition is controlled by the ARM/TRIGGER inputs and the timing system (see Figure 7.11)

bunch mode frequencies using the equation above. This output signal is then mixed with the hybrid signals from the BPM. As the mixed signal is fed into the vertical BBB system, the FPGA code recognises the signal as unstable beam and tries to correct the perceived motion. This corrective signal then causes the stable beam to become unstable at which point the excitation signal is removed and the BBB system is allowed to damp the beam.

By scanning the phase angle and measuring the damping rate a relationship between the two is found as shown in Figure 5.14. The phase angle corresponding to the maximum damping rate is selected as the optimum point for BBB operations.

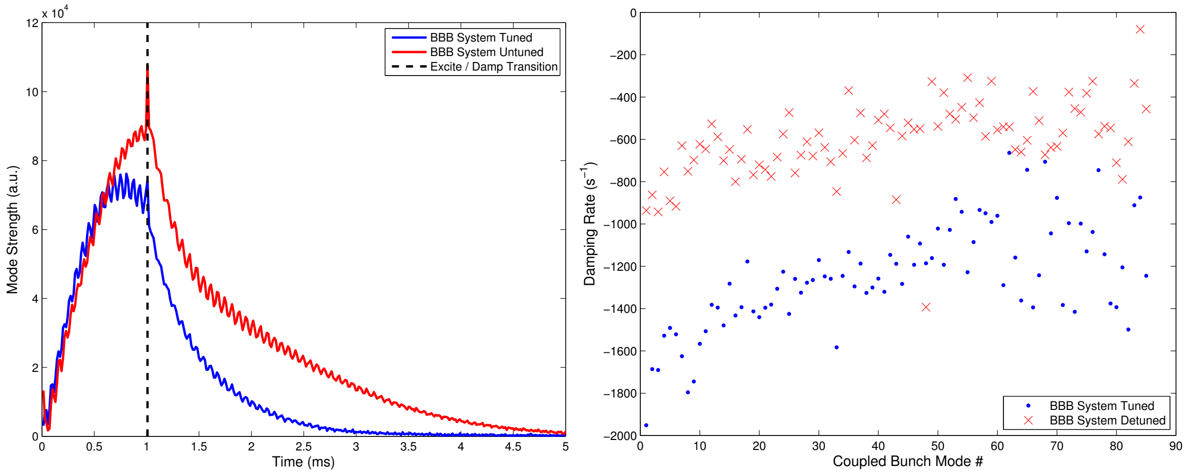

(a) NCO Excite/Damp, Mode #1

(b) Damping strength across modes 0 to 80

Figure 5.14: An example of using the NCO to excite the beam and measuring the damping rate of the ring with the BBB feedback turned on. These are measured at high chromaticity $\xi = (3, 11)$ with an initially stable beam.

5.5 Summary

Using the methods outlined in this chapter, a maximum excite/damp rate of $\tau_d^{-1} = -3511.0\,\mathrm{s}^{-1}$ was achieved. A comparison between this damping rate and the growth rates seen within the ring is shown in Table 5.2. The maximum damping for the excite/damp method is an order of magnitude larger than the ever-present resistive wall instability and significantly stronger than the growth rate for the resonator-style instabilities which occur at certain IVU heights.

This confirms that the BBB system not only provides the damping necessary to guarantee stability for the present ring configuration but will allow for the introduction of more insertion devices in the future.

In the next chapter the full commissioning of the system will be presented with real-world measurements of the damping effectiveness of the transverse feedback system. Utilising the unique characteristics of the BBB system, new techniques will be described which allow for the comparison of feedback damping rates with instability growth rates. Investigations were performed into the long-term stability of the system in preparation for user-time operations.

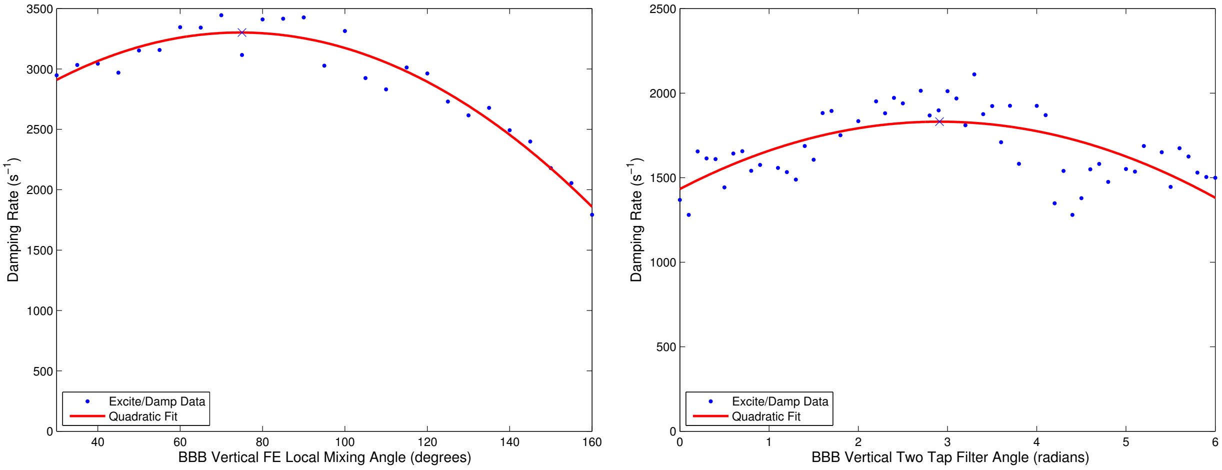

(a) Local Mixing Angle versus damping rate

(b) FIR Filter Phase versus damping rate

Figure 5.15: NCO excite/damp tuning of the both the local mixing angle used in heterodyne downmixing and the two-tap phase delay which adds an additional phase delay to the sinusoidal correction term from the DAC. In each case, the parameter was scanned and data similar to Figure 5.14a was taken. The damping strength was calculated using an exponential fit to the damping rate of mode #1.

Table 5.2: Measured growth and damping rates in the Australian Synchrotron storage ring.

	Source of Beam Movement	τ^{-1} (s^{-1})	τ (ms)
τ_g^{-1}	Resistive Wall Instability (Mode #359)	336.1	2.975
	Resonator-style Instability (Mode #228)	575.1	1.738
τ_p^{-1}	Natural Damping	−208.3	−4.801
τ_d^{-1}	Maximum Excite/Damp Result (Mode #1)	−3511.0	−0.285

Chapter 6

Commissioning of the BBB System

To successfully commission the transverse feedback system described in Chapter 5 extensive studies were conducted to prove its effectiveness over the large range of user lattice configurations. Fast, accurate measurements of instability growth and damping rates must be possible to ensure that the system is operating well below the stability threshold of the ring (where $\left|\tau_d^{-1}\right| \gg \left|\tau_g^{-1}\right|$). As the system is designed for use during user operations, tests of its long-term stability were made over the entire phase-space of insertion device heights.

Techniques designed to undertake these measurements were built upon the unique abilities of the BBB system. To observe that the system was operating below the stability threshold, the motion of the beam must be seen, damping from unstable to stable beam. Utilising high speed processing of the BBB system a suite of diagnostic techniques were designed which allowed for the measurement of both the instability growth rate and feedback system damping rate without loss of beam. Described as *grow/damp measurements*, they were a fundamental step to the successful commissioning of the BBB system.

Once the grow/damp measurements proved that the feedback system would damp instabilities within the ring, experiments were designed which would test the long-term stability of the system. As the feedback will be operational during user time it must be shown to be stable for all user-alterable lattice parameters. When left to damp the beam while IVUs were moved randomly throughout a shift, the system demonstrated stability for long periods of time.

6.1 Grow/Damp Measurements

In modern storage rings, intensity dependent coupled-bunch instabilities are the primary limitation of stored current. As discussed in Chapter 3, wake fields couple the motion of multiple bunches and introduce a driving term to Hill's Equation, leading to a complex tune shift described by Sacherer's Equation,

$$\Delta Q \Rightarrow U + iV = -(|m+1|)^{-1} \frac{ie\beta I_b}{2m_0\gamma Q_{x0}\Omega_0 L_b} \frac{\sum\limits_{k=-\infty}^{\infty} Z_x(\omega_k^x) h_{m,m}(\omega_k^x - \omega_\xi^x)}{\sum\limits_{k=-\infty}^{\infty} h_{m,m}(\omega_k^x - \omega_\xi^x)} \tag{6.1}$$

where the tune shift has been substituted for two variables U and V which represent the real and imaginary part of the tune shift respectively. Letting $Q = Q_0 + \Delta Q$ and using the exponential solution to Hill's Equation (Equation 3.8),

$$y(t) = A \exp\left(-i\frac{Q'}{R}t\right) \tag{6.2}$$

$$\Rightarrow y(t) = A \exp\left(-i\frac{(Q_0+U)}{R}t\right) . \exp\left(\frac{V}{R}t\right) \tag{6.3}$$

the solution separates into a product of oscillatory and exponential motions. From Equation 6.1 it can be seen that U depends on the imaginary part of the effective impedance while V is dependent on the real part.

It is therefore important to be able to measure the growth rate of instabilities in order to identify the strongest coupled-bunch modes. Unstable beams are difficult to work with; any lost beam needs to be replaced and may cause a total beam loss due to RF failure. A system was developed which allowed the beam instability to grow by opening the feedback loop temporarily and closing the loop before the particle moves out of the acceptance of the lattice.

6.1.1 Experimental Technique

An experimental technique for grow/damp was designed and implemented at the ASLS using custom software, designed and written for the transverse BBB system. The measurement follows several steps:

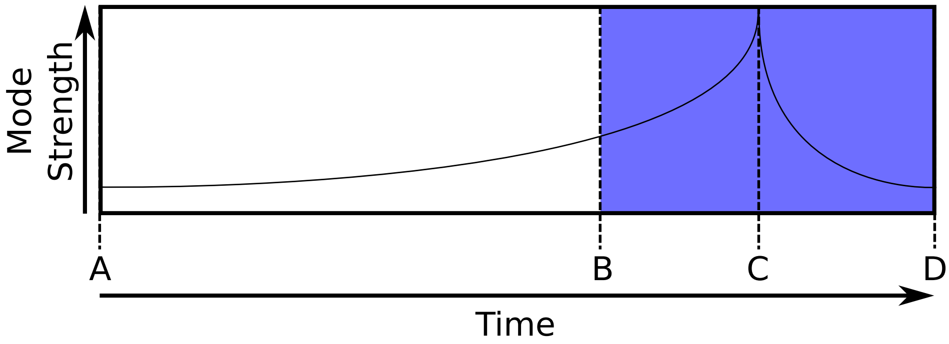

Figure 6.1: Timing diagram for a grow/damp measurement. The feedback is removed at A and after time B the data buffer begins. Feedback is restored at time C and data acquisition stops at time D. The shaded region reflects the time where data is acquired.

1. Begin with the amount of stored current above stability threshold but stabilised by the BBB system.
2. Initialise the feedback loop in an open configuration by setting the FIR coefficients to zero and the position of each bunch will begin to grow exponentially.
3. Measure the position of each bunch for a short period of time (the period will be dependent on the strength of the instability).
4. Return the feedback to closed loop configuration by restoring the FIR coefficients.
5. Measure the position of each bunch as the beam damps back to its stable position.

As these steps are completed the beam should initially be stable, grow over a specified time and then damp back to stability without any significant amount of particle loss. Figure 6.1 shows a timing diagram for a grow/damp measurement, with the unstable growth (A→C) and damping (C→D) of the system shown. Due to memory limitations within the BBB system, only a limited number of position measurements can be acquired and therefore only the shaded area in Figure 6.1 is kept for each measurement.

This grow/damp technique was not built into the available abilities of the BBB system purchased for the transverse feedback so the writing of specialised experimental control and acquisition code was necessary. The embedded single board computer which controls the FPGA is powered by an ARM processor and the local space on the machine is limited to a small amount of flash memory. To compile new software for the BBB system, it was first cross-compiled on a remote computer and made available via a Network File System (NFS) mount. This allowed for rapid prototyping and testing of new software as newly compiled ARM-based software could not be tested on the development platform due to the limited availability of the BBB hardware. Cross mounting of the local BBB system onto the remote NFS server also allowed for the acquisition and distribution of large data files without taxing the constrained local resources.

Once the data is acquired the single vector of bunch position samples versus time is reshaped into two dimensions in order to represent the motion of each bunch versus time. Figure 6.2 shows the data from a single grow/damp measurement. Although the data for each bunch is represented on the same time scale, each was measured serially at a single point in the ring. Therefore an inherent phase information loss is present which does not affect the calculation of instability growth rates.

Quantification of different instabilities requires the growth rates of all instability modes be extracted from the position data and separated for analysis. Each instability will be characterised by the modes it excites and therefore the frequency distributions present in the position data. The modes can be extracted from the position data by recognising that the movement inherent to the excitation modes have frequency components described by Equation 3.54. The frequency spectrum of a beam excited by instabilities will have peaks in its frequency spectrum at the upper and lower tune sidebands of the revolution harmonics.

An example frequency spectrum of a beam under the effect of coupled-bunch instabilities is shown in Figure 6.4. Equation 3.54 has been used to identify the tune sidebands and differentiate them from revolution harmonics. To minimise the sampling bandwidth required to reconstruct all the modal frequencies, the upper sidebands of modes $0 \rightarrow 179$ and the lower sidebands of modes $180 \rightarrow 359$ have been used. As a consequence of this frequency wrapping, both the lowest mode (0) and highest mode (359) correspond to *low* frequencies of inter-bunch oscillation. The mode frequencies peak (and wrap around) at mode 180. Twenty turns of data (7200 samples) are used in the Fast Fourier Transform (FFT) process, allowing for a clear distinction between the sideband peaks and revolution harmonics.

Figure 6.2 shows how the motion of the beam is affected by the rise of coupled-bunch instabilities, specifically resistive-wall instabilities. The absolute displacement of the bunches as well as the power of the modes grows exponentially with a strength according to the imaginary tune shift given by Sacherer's Equation.

Splitting the motion into a growth section (*feedback off*) and a damping section (*feedback on*), it is then possible to fit an exponential of the form

$$y(t) = A \exp\left(\frac{t}{\tau}\right) + C, \tag{6.4}$$

and thus extract the growth/damping rate τ^{-1}. A and C are constants of the fit.

For the system to be considered stable, a damping rate an order of magnitude faster than the related growth rate is required. Figure 6.5 show a fit to mode 359 extracted from the data shown in Figure 6.3a. In this measurement the growth rate for mode 359 was $\tau_g^{-1} = 336.1\ \mathrm{s}^{-1}$ while the damping rate was measured as $\tau_d^{-1} = -3991.1\ \mathrm{s}^{-1}$.

6.1.2 Feedback Amplifier Study

The primary motivation behind developing this technique was to study the growth of instabilities with respect to changes in the storage ring lattice. This technique was also used to tune the transverse feedback system in the early stages of commissioning before the excite/damp technique outline in Section 5.4.1 was fully realised. An example of the diagnostic capabilities of the system was the ability to check that the power amplifier actuating the beam was not saturating at high gain and distorting the corrective waveforms. A gain scan was performed across the full range of the amplifier, from 32 dB to 54 dB gain, and at each point a grow/damp measurement was acquired. An exponential increase in the damping rate of the system was observed as shown in Figure 6.6. The gain for the amplifier was therefore able to be maximised without any damaging distortion of the incoming signal.

6.1.3 Stored Current

A method for increasing the photon flux to the beamlines is to increase the stored current in the ring. Without instabilities, the current can be increased until the RF cavities are unable

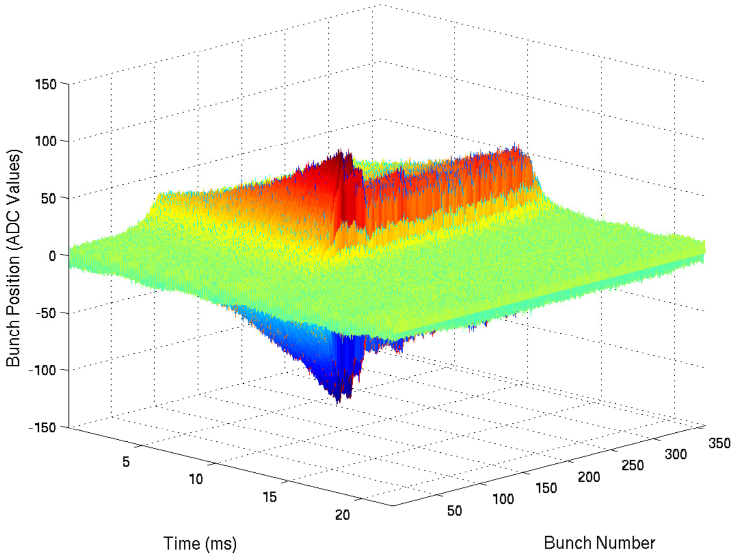

(a) The vertical displacement of all 360 bunches versus time during a grow/damp measurement.

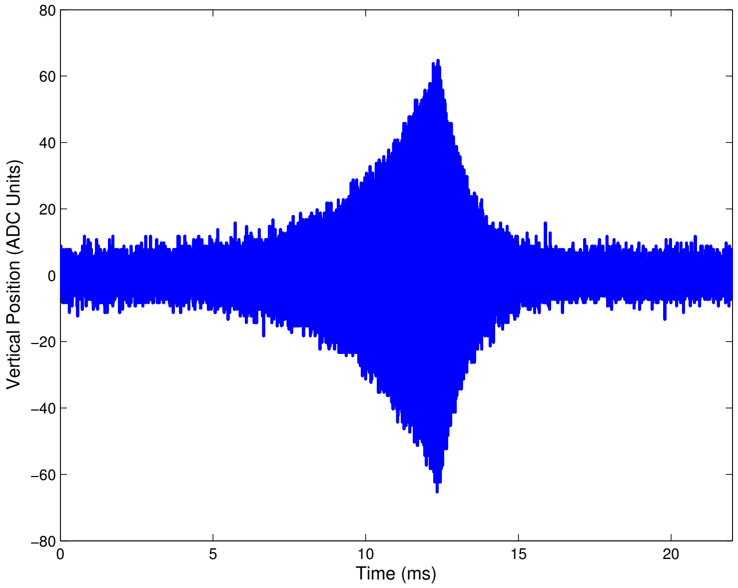

(b) Displacement of bunch #150 versus time, taking from the data shown above.

Figure 6.2: A grow/damp measurement showing the growth in the resistive wall instability over time, with no IVUs introduced to the ring. The feedback loop was closed at 12 ms with the resulting dramatic drop the mode strength and consequently beam position.

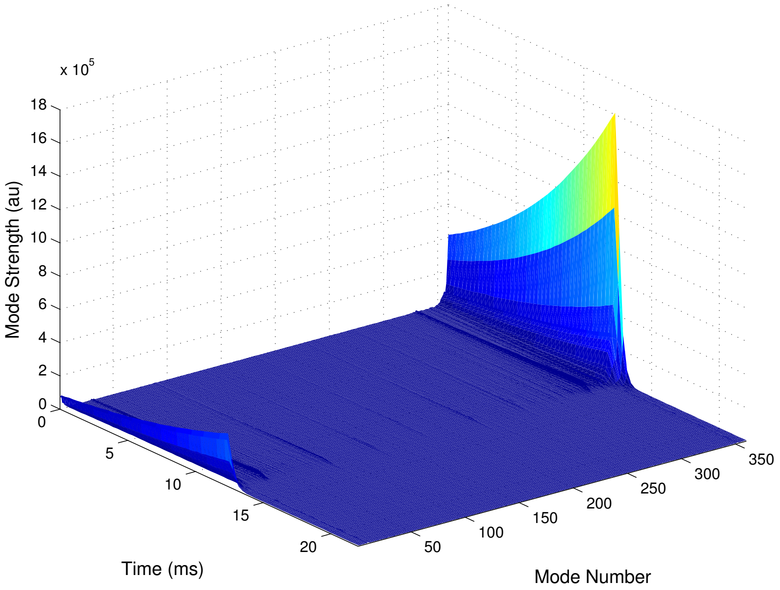

(a) Coupled-bunch mode strength versus time extracted from the data shown in the Figure 6.2a.

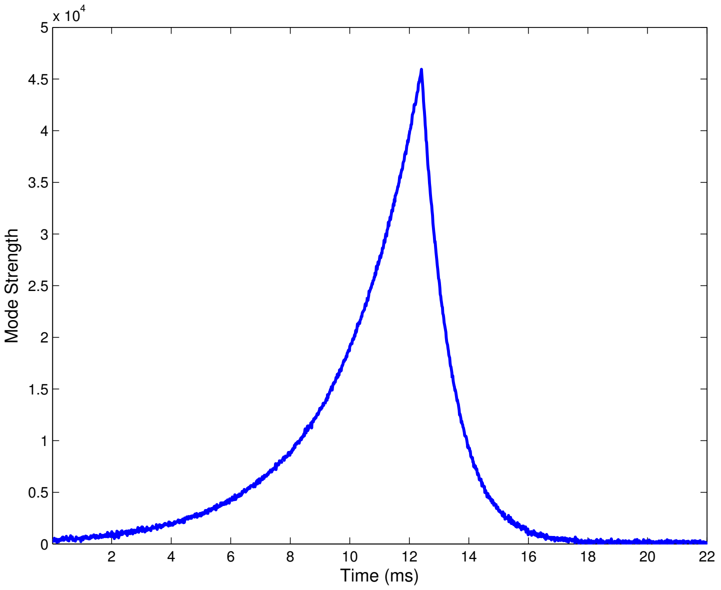

(b) Strength of coupled-bunch Mode #359 versus time.

Figure 6.3: Using the techniques discussed the coupled-bunch mode strengths were extracted from the position data presented in Figure 6.2. The presence of low frequency inter-bunch oscillations (Modes 0 → 9 and 350 → 359) imply that the motion is caused by a resistive wall instability.

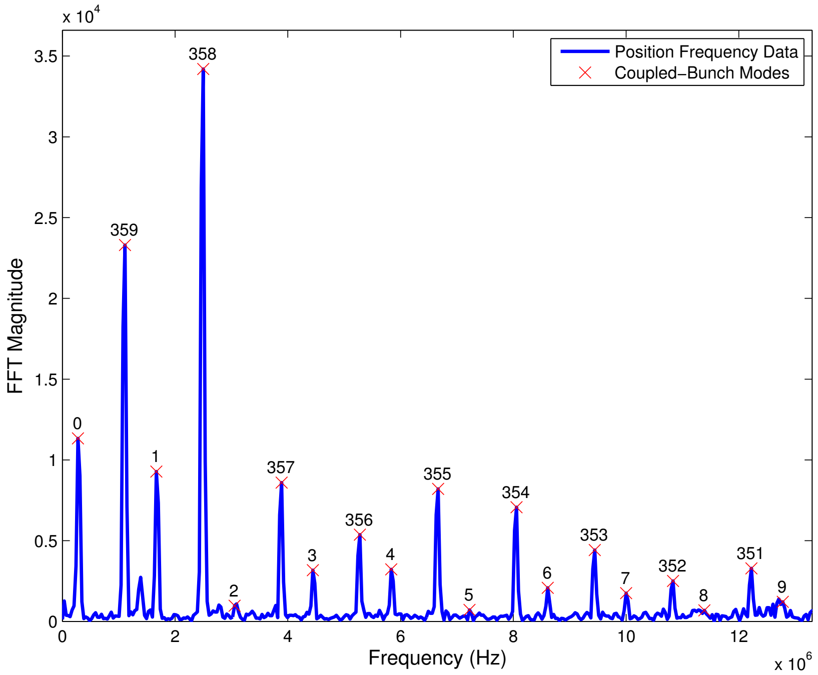

Figure 6.4: To calculate the growth rates of particular coupled-bunch modes each must be identified in the frequency spectrum of acquired position data. Twenty turns of data (7200 samples, 13.8 μs) are taken to ensure proper separation of the sidebands from the revolution harmonic. The numeric labels are located at the FFT bin corresponding to that coupled-bunch mode frequency.

to replenish the energy lost through synchrotron radiation ($\approx 240 - 250$ mA for the ASLS storage ring). Normally the storage ring is not run at these high currents as the beam line components have been designed to dissipate the heat load associated with 200 mA of stored beam.

By increasing the current, the value of I_b in Equation 6.1 increases and therefore one can see that $\Delta Q \propto I_b$. Figure 6.7 shows the linear growth rate with stored beam current as predicted by Sacherer's equation but more significantly, if the same measurement is taken with a slightly higher chromaticity, then the growth rate lowers by a constant amount.

This measurement effectively demonstrates how a change in chromaticity changes the effective impedance of the ring by altering the overlap between the beam and impedance spectra (see Figure 3.8).

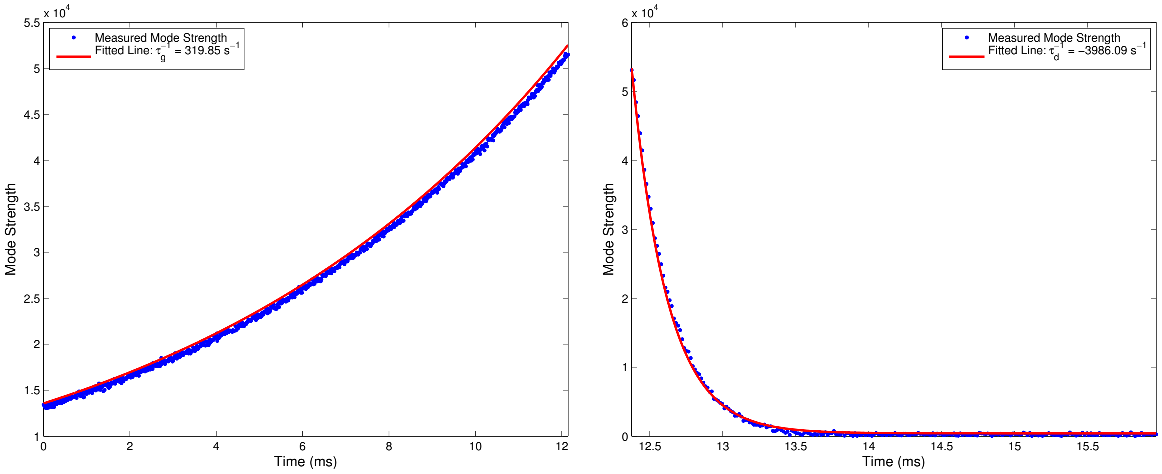

(a) Growth portion, with the feedback loop open.

(b) Damping portion, the feedback loop is closed and the instability damps.

Figure 6.5: Concentrating on only mode #359 of the data set shown in Figure 6.3a, the evolution of the mode strength is bisected into a growth section and a damping section. An exponential is fitted to each section and the growth and damping rates are extracted.

6.1.4 Insertion Devices

Although initial tests with the transverse feedback system were capable of strongly damping the dominant resistive wall instability of the bare lattice once the IVU gaps were reduced the beam would become unstable vertically at discrete IVU heights. An investigation into the modes present revealed that the two different types of IVUs present in the storage ring create instabilities with characteristic narrowband resonator-style instabilities. The three metre long insertion devices has a characteristic mode of #228 while the shorter two meter IVU has a characteristic mode of #224. A grow/damp measurement of an instability caused by the gap reduction of the insertion device IVU03 is shown in Figure 6.8.

The main candidate for the cause of these instabilities are not the IVU magnets themselves, but rather the discontinuities in the vacuum transition pieces which form when the insertion devices gaps are reduced. Discontinuities in the beam-pipe at low IVU gaps are typically compensated for by the introduction of *tapers* which are built to provide a smooth gradient between the beam pipe and the IVU surface. In the ASLS storage ring, these tapers are thin

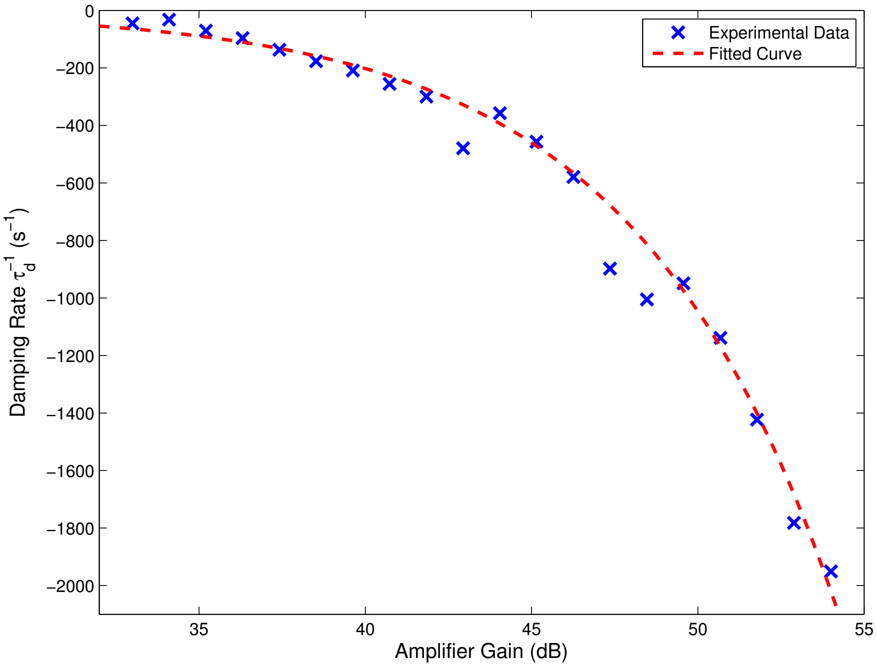

Figure 6.6: A measure of the dominant resistive wall mode damping rate as a function of amplifier gain. Saturation of the output signal can occur at high gains due to changes in the phase response of the amplifier. This would dramatically lower the damping rate of the feedback system so must be avoided. Due to the amplifier tuning outlined in Section 5.3, saturation is avoided at all gain values which can be seen in this figure.

copper sheets, fixed at one end to the IVU magnet surface and the other to the vacuum chamber providing an electrical connection for the beam-induced image currents to pass through. Tapers used in the ASLS storage ring have been observed to buckle and warp when an IVU gap is changed which may contribute to a resonator-style impedance.

It has been shown that tapers in the same configuration as the ones at ASLS are capable of producing a high frequency impedance [65], although Finite Element Method (FEM) modelling of the tapers has proved inconclusive at showing the creation of trapped modes within the standard taper configuration. These models have only been conducted at low to mid-range frequencies as FEM modelling becomes prohibitively CPU-intensive at high frequencies and high spatial resolution.

Initially these strong resonator-style instabilities prevented full commissioning of the system, since beamline experiments require that the IVUs are scanned through these gaps. High

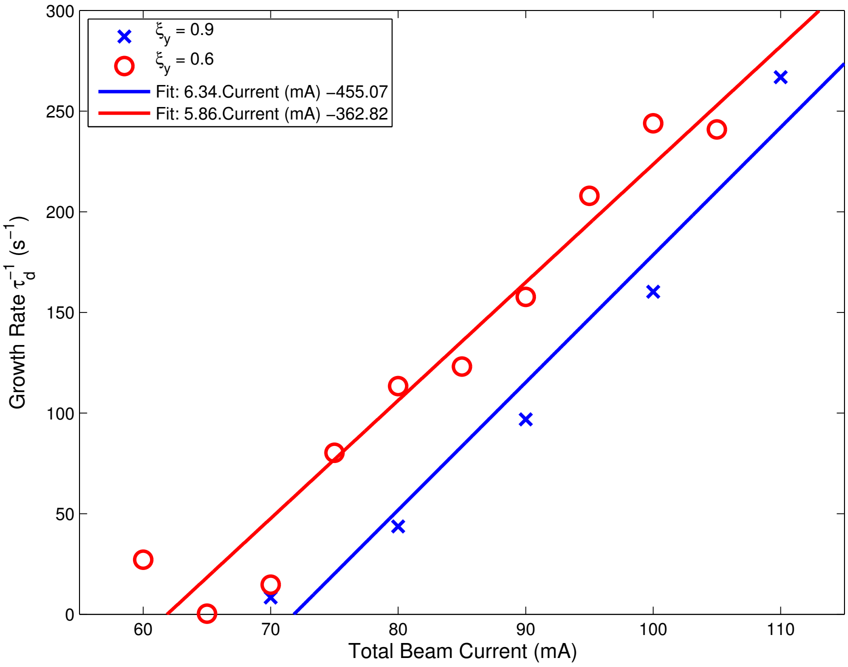

Figure 6.7: Coupled bunch instability growth rate vs stored current. It can be seen that the instability growth rate is linearly proportional to the stored current, as predicted by Equation 6.1. Altering the chromaticity of the ring shifts the beam spectrum, reducing the growth rates at all stored currents.

frequency coupled-bunch modes, such as mode #228, are especially sensitive to the phase angle of the correction waveform. It was demonstrated that while the transverse feedback was adequately tuned to damp to relatively lower frequency resistive wall instabilities the calculation of the correct phase angle was not sufficiently sensitive reducing the system's effectiveness at higher frequencies.

Re-tuning the system using the damping of the IVU instabilities as a figure of merit yielded significant advances (including the implementation of the system described in Section 5.4.1). However when the system was tuned to damp the resonator instabilities it became ineffective at damping resistive wall instabilities.

The cause for the system's apparent inability to damp higher mode instabilities was not found in the discrete components but a poor connection in the cabling between the vertical plane power amplifier and kicker magnet. This caused a high frequency ringing which would increase in the amplitude with the strength of the corrective waveform. In this fashion,

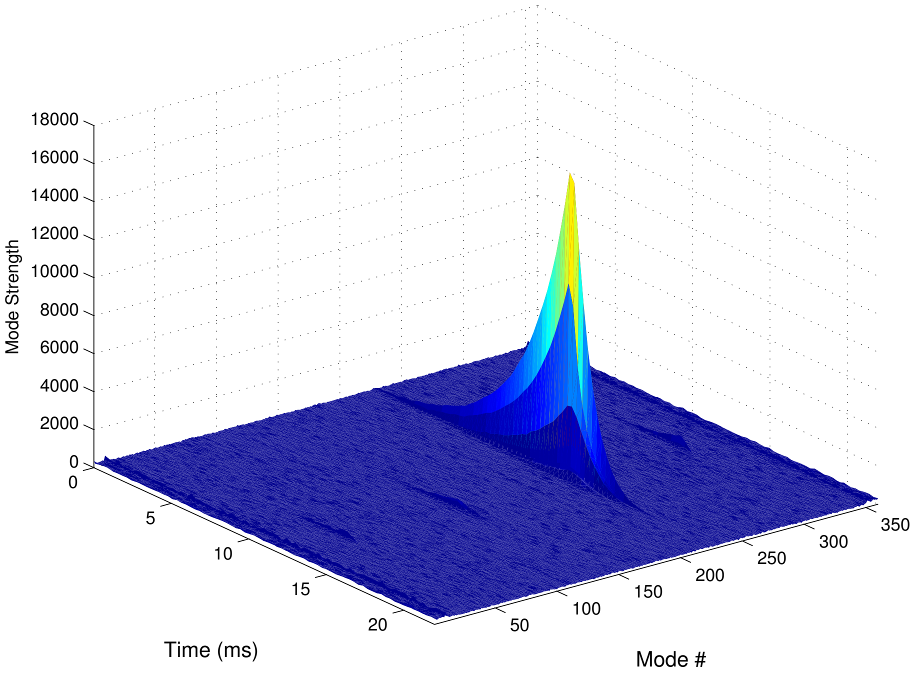

Figure 6.8: Resonator-style impedance induced when three IVUs are reduced to low heights (IVU01 at 6.06 mm height, IVU03 and IVU13 at 6.60 mm height). Mode #228 is the strongest mode with a growth rate of $366.9 \pm 9.9\ \mathrm{s}^{-1}$ measured over multiple grow/damps cycles.

the system would be simultaneously damping the resistive wall instability and exciting the higher frequency modes created by the IVUs at specific gaps. After the poor connection was corrected the transverse feedback system was able to damp the instabilities present across the IVU gap phase space.

In addition to the IVUs the storage ring is also home to wiggler-style insertion devices. As wiggler insertion devices are entirely external to the beam pipe, any change in magnet gap does not alter the metallic beam environment and should not change the impedance spectrum of the ring. The fringe fields of the dipoles within the wiggler can perturb the transverse focussing fields which will alter the tune of the lattice. As the gain of the feedback system is linked to the tune through the phase response of the FIR filter it is important that the tune is held stationary to ensure the fastest possible damping rate. In the ASLS, tune shifts due to changes in wiggler gap are corrected using a set of quadrupoles and a feed forward table for each wiggler. No significant reduction in the instability threshold has been measured with respect to changes in the wiggler gap with this feed forward table activated.

6.1.5 Transverse Coupling

Transverse coupling is the transferral of a portion of the transverse bunch motion from one plane into another, as discussed in Section 2.2. The damping rates in the horizontal and vertical planes can differ dramatically, with the horizontal plane typically damping faster due to the production of synchrotron radiation. In theory, by coupling the unstable motion from the vertical into the horizontal overall damping can be increased and the instability threshold subsequently raised [66]. The high aspect ratio of the ASLS beam pipe also implies that most damaging wake fields will be created in the vertical plane and motion coupled into the horizontal will likely not be susceptible to horizontal impedances.

A study was undertaken to investigate the effect of coupling on instability growth rates. With the skew quadrupoles inactive, the *natural coupling* of the storage ring lattice is 0.18%. Currently the lattice coupling is set to 1% using skew quadrupoles to decrease the effect of Touschek scattering on beam lifetime. In addition to the experimental user-mode 1% coupling, a series of different skew quadrupole settings have been calculated to provide a range of coupling from the experimentally determined minimal coupling of 0.0009% to 20% coupling. Using the grow/damp technique, the growth rates of vertical resistive wall instabilities were measured for the user-mode 1%, natural and minimal coupling regimes. Although it was expected that the growth rates would decrease with increased coupling, the inverse was measured. As shown in Figure 6.9, the growth rates follow the same direction as the coupling, with smaller coupling values having smaller growth rates. To further probe this result, the lattice was set to a particular transverse coupling and multiple grow/damp measurements were taken while the chromaticity was scanned. Figure 6.10 shows that even as the chromaticity is scanned, the ordering of the different coupling regimes is unchanged.

An explanation for this phenomenon lies within the shape of the instability growth of minimally coupled beam shown in Figure 6.9. Close inspection of the growth rate shows two distinct areas of growth separated by a plateau, with the instability growing, then stalling then growing again. This implies there are two regimes of growth rates for the minimally coupled beam.

Consider two of the effects that can change the growth rate of a bunch under the influence

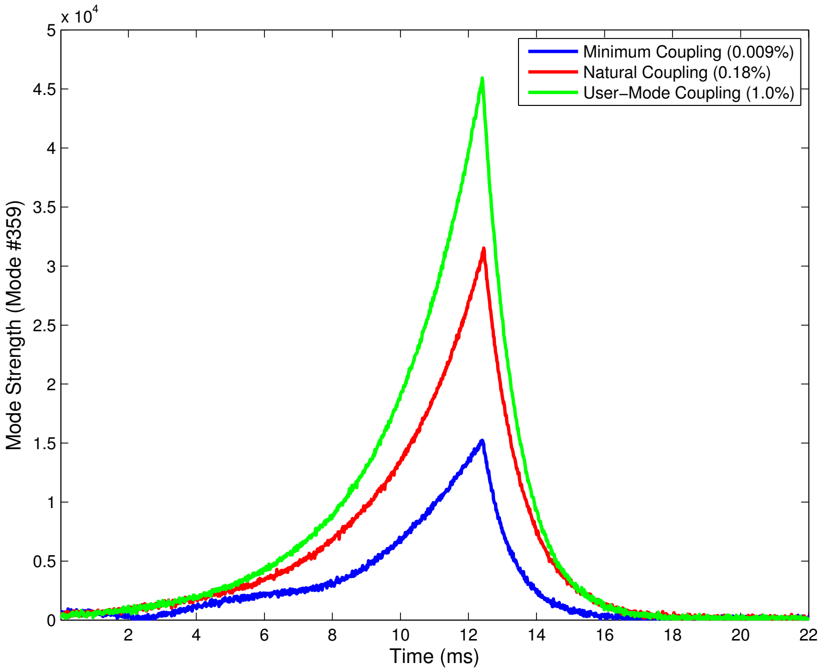

Figure 6.9: A study into the effect of coupling on impedance growth (Mode #359). Several grow/damp measurements were performed, altering only the skew quadrupole strengths. It can be seen that an increase in coupling increases the growth rate of resistive wall impedances.

of a resistive wall impedance: the extra damping from transverse coupling increasing the damping rate, and the inverse cubic dependence of the height of the beam pipe b on the resistive wall impedances (Equation 3.49). For minimally coupled beam, the vertical height of the beam is at a minimum. This implies that the vertical excursion of the beam is small and the distance from all of the particles within a bunch to the beam pipe wall is large. As the beam's size grows with increased coupling, the effective distance between the particles and the beam pipe wall shrinks. This decrease in b increases the instability growth rate beyond any benefit that increased coupling provides and could cause an increase in growth rates with an increase in coupling.

This particular argument only applies to storage rings such as the ASLS where work has been put into creating the smallest possible beam profile, combined with a high aspect ratio beam pipe. A naturally round beam, stored in a cylindrical beam pipe (such as those found in most proton sources) would not be susceptible to this effect and should benefit

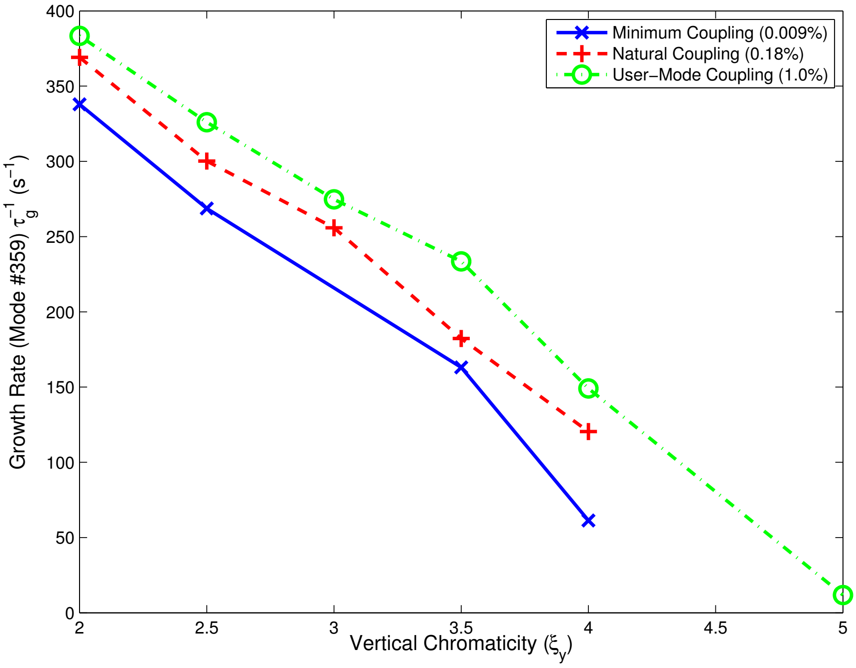

Figure 6.10: Measurement of the growth rate of the resistive wall instability (Mode #359) versus chromaticity for three different coupling regimes. The order of the growth strengths relative to coupling is the same as Figure 6.9 for all chromaticities measured.

from increased transverse coupling. In rings where horizontal BBB feedback is implemented, increased damping will be a combination of the horizontal feedback and radiative damping.

This result will require further investigation, in particular the creation of a particle tracking system which correctly accounts for coupled-bunch instability growth is needed. The software package HEADTAIL [67] was original designed to calculate trapped-ion instabilities, but is capable of calculating the growth rates of single-bunch head-tail instabilities and has been altered to work with multiple bunches [68]. This will allow for a more conclusive study into this phenomenon in the future.

Successful implementation of a grow/damp measurement system has been achieved using the transverse feedback system combined with specialised analysis code written for this task. Initially used to further tune the system, it has allowed for the measurement of both resistive wall and resonator-style impedance growth rates as well as uncovering a counter-intuitive dependence on the transverse coupling of the beam. The grow/damp technique has become an invaluable tool for diagnosing and treating coupled-bunch instabilities within the ASLS storage ring.

6.2 Long Term Stability

For the system to be considered reliable enough for user operations it must operate independently of supervision, and its stability must not be dependent on actions by the users. The only lattice element that users have direct control over is the gap of the insertion device servicing their beamline. It was therefore important to ensure that the system would be stable at all possible IVU gaps. In order to prove this, the storage ring was injected with 200 mA of stored beam, and the IVUs were set to their minimum gaps. This arrangement of 6.0 mm, 6.06 mm and 6.0 mm for IVU03, IVU05, and IVU13 respectively, should have the strongest resistive wall impedance and was shown to be stable with the BBB feedback system active. The gaps were then each set to a gap determined by a pseudo-random number generator to be between their respective minimum and 10.0 mm. Any gap height between 10 mm and the maximum of 36 mm had been observed to have no effect on the instability threshold of the ring. An occurrence of vertical instability will manifest itself as an increase in the effective vertical beam size (see Figure 1.4). By monitoring the vertical beam size at the XDB while moving the IVUs, any gaps which are not being damped can be readily observed. Figure 6.11 shows that the vertical beam size as measured on the XDB CCD does not increase at any of the IVU gaps and the system is therefore stable without the need to limit the abilities of experimental beamline IVUs.

6.3 Stored Beam Lifetime

Increases in the chromatic correction of the storage ring lattice will reduce the dynamic aperture of the ring and reduce beam lifetime. As discussed in Section 2.3 non-linear fields distort the transverse phase space available to the stored particles resulting in a seperatrix in phase space between stable and unstable motion. Particles travelling through the seperatrix into the unstable region will be lost quickly and the overall beam lifetime will be reduced.

By introducing the BBB transverse feedback system the chromaticity of the lattice can

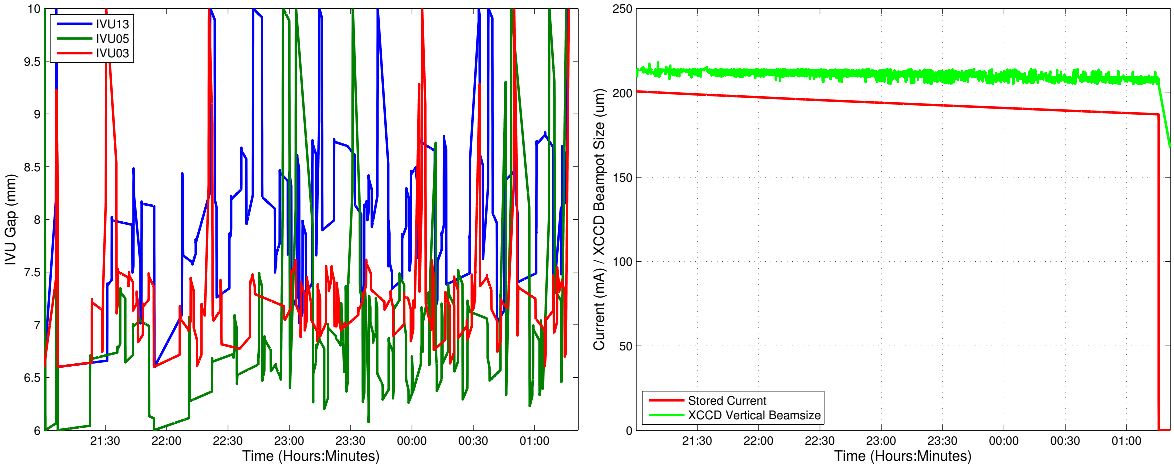

Figure 6.11: A long-term test of the bunch by bunch in a worst case setting where the IVUs are rapidly scanned through their full operating range. This experiment was designed to search for combinations of IVU gaps where the BBB system would not damp instabilities. The vertical size of the beam on the XDB CCD [69] camera was used to measure whether the beam was unstable or not. A controlled beam dump was used to end the measurement and prepare for the following user beamtime.

be reduced from $(\xi_x, \xi_y) = (3.5, 13)$ to $(\xi_x, \xi_y) = (2, 2)$. Reducing the chromaticity resulted in a 45.5% increase in beam lifetime from 38.9 hours to 56.6 hours with all insertion devices at minimum heights as shown in Table 6.1.

This will result in a larger integrated flux for experimentalists, allowing for high statistic measurements to be made in less time.

6.4 Conclusions

This chapter has shown that strong instabilities need an active stabilisation system to prevent the beam from being lost. The stability of the system was proven both with short term grow/damp measurement and long-term stability measurements. Table 6.2 shows that the feedback system fulfills the stability requirements to allow its full commissioning during experimental user runs. With a damping rate of $\tau_d^{-1} = -3264.1\ \mathrm{s}^{-1}$ the system will allow for the introduction of additional insertion devices without relying on chromatic corrections to

Table 6.1: The beam lifetime was measured at both high and low chromaticities with different insertion device gaps. It can be seen that reducing the chromaticity dramatically increases the lifetime of the beam.

Chromaticity (ξ_x, ξ_y)	I (mA)	IVU03 (mm)	IVU05 (mm)	IVU13 (mm)	Lifetime (hrs)
(3.5, 13)	200	38.0	38.0	38.0	65.5
(3.5, 13)	200	6.6	6.06	6.6	38.9
(2,2)	200	38.0	38.0	38.0	71.7
(2,2)	200	6.6	6.06	6.6	56.6

Table 6.2: Measured growth and damping rates in the Australian Synchrotron storage ring.

	Source of Beam Movement	τ^{-1} (s^{-1})	τ (ms)
τ_g^{-1}	Resistive Wall Instability (Mode #359)	336.1	2.975
	Resonator-style Instability (Mode #228)	575.1	1.738
τ_p^{-1}	Natural Damping	−208.3	−4.801
τ_d^{-1}	Maximum Excite/Damp Result (Mode #1)	−3264.1	−0.285
	Resistive Wall Damping Rate (Mode #359)	−3991.1	−0.251
	IVU Induced Resonator Damping Rate (Mode #228)	−1121.9	−0.891

the ring. Discovery of strong IVU induced resonator instabilities spurred increased precision in the tuning of the system and the BBB system is now stable at all IVU heights.

The BBB system has been successfully commissioned for the ASLS storage ring and has been shown to all transverse coupled-bunch instabilities present. In the next chapter further utilisation of the BBB system for diagnostic purposes will be discussed.

Chapter 7

Bunch-By-Bunch Ring Diagnostics and Methods

The motivation behind this chapter is to study the benefits of the ability to discern separate bunches on traditional measurement techniques. As discussed in the previous chapter, the BBB feedback system has been highly effective in the ASLS storage ring for damping coupled-bunch instabilities. Since the feedback system comprises high bandwidth ADCs coupled to a high bandwidth DAC through an FPGA stage it also has the potential as a powerful diagnostic tool. Many of the current diagnostic methods utilised at the ASLS require dedicated equipment and are therefore unable to measure properties of individual bunches, only gross parameters of the stored beam.

Initially the aim was to compare frequently used methods at the synchrotron for measuring parameters, such as the tune and chromaticity, where the BBB system provided comparable accuracy to the dedicated diagnostic systems. The advantage of the BBB system came when it was used to extend the current measurements by measuring the parameters for individual bunches in parallel or manipulating single bunches without compromising stored beam.

This chapter will describe the suite of diagnostic methods which have been developed utilising the unique properties of the transverse feedback system.

7.1 Tune and Chromaticity

Accurate knowledge of the tune and chromaticity of the lattice is integral to proper machine operation and development. Without this, uncorrected tune shifts will lead to resonances which will lower the beam lifetime as described in Chapter 2.

Traditional methods for measuring the frequency spectrum of beam movement typically involve beam excitation using a pulsed magnet. Such methods only measure the frequency spectrum of the entire bunch train and cannot separate the oscillations of individual bunches.

This section outlines a method that will measure the tune of any individual stored electron bunch with minimal disruptions of the beam using the BBB setup with an oscillatory excitation signal controlled by the BBB FPGA. Before describing the new method, it is illustrative to present some detail of the two present methods of tune measurement at the ASLS.

7.1.1 Present Methods

Kicker Magnets and Turn-by-Turn BPMs

In a stable electron beam the betatron oscillations cannot be measured using standard BPMs. Although each particle within a bunch is oscillating at the tune frequency, they do so *incoherently* with the rest of the particles within a bunch. Consequently a center-of-mass measurement of the bunch will contain no information on the movements of individual particles. To measure the tune of each bunch the component particles must be made to oscillate coherently around the closed orbit.

A traditional method for exciting the beam is to use a fast kicker magnet with an excitation pulse lasting several turns. For example the injection kickers in the ASLS storage ring impart a 4μs pulse (approximately 5 turns). This imparts a $\Delta x'$ impulse to the beam, forcing the particles into a large magnitude oscillatory motion controlled by the storage ring quadrupoles. Depending on the natural damping rate of the ring, the oscillatory motion will decay on the order of milliseconds (1000s of turns).

Effective excitation requires that the frequency spectrum of the input signal overlaps with the frequency spectrum of the beam. A fast-pulsed excitation signal that approaches a delta

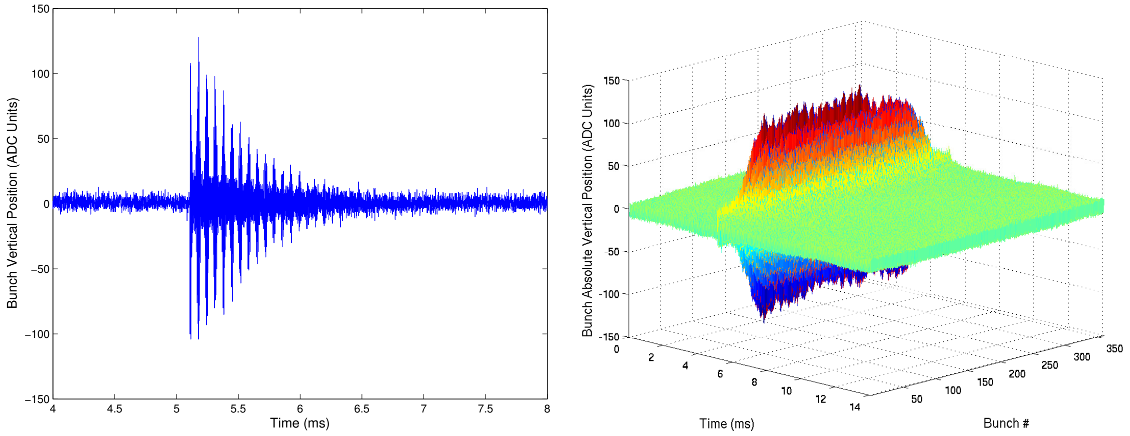

(a) The movement of a single bunch resulting from an excitation at ≈ 5.1 ms. The beating results from the high chromaticity of the lattice.

(b) Beam position evolution due to a x' perturbation at a single point in the ring.

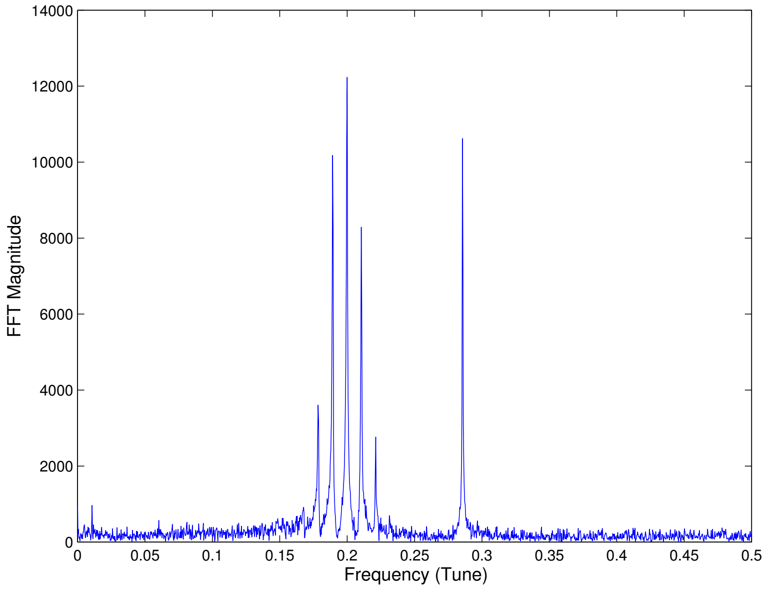

(c) Frequency spectrum of the single bunch movement reveals the frequencies of motion. The x axis has been rescaled to represent the tune at a given frequency.

Figure 7.1: A tune measurement taken with an excitation signal provided by an energised injection kicker. The lattice was such that the chromaticity was $(\xi_x, \xi_y) = (3, 11)$ and the betatron tunes were $(Q_x, Q_y) = (0.29, 0.2)$. High power sidebands are visible in the frequency spectrum due to this high vertical chromaticity. Note that the excitation is in the horizontal plane, but motion in the vertical can be measured due to the non-zero betatron coupling of the ring.

function in the time domain will have a broadband response in the frequency domain.

An example of this method of tune measurement is shown in Figure 7.1. Acquisition of turn-by-turn BPM data triggered synchronously with the kicker excitation allows for the measurement of the beam position at a single point in the lattice. Transforming the time-dependent data into frequency space using a Discrete Fourier Transform (DFT) will show a strong spectral response at the tune frequency [70]. The tune is extracted from the frequency spectrum by finding the frequency bin with the strongest response (A_i) and calculating the tune using:

$$Q = \frac{i}{N}, \tag{7.1}$$

where Q is the fractional tune (0 to 0.5), i is the index of the bin with maximum response and N is the number of position samples used to construct the DFT. Higher frequency resolution can be achieved by applying proper windowing to the data and using the values in surrounding bins in a Gaussian or parabolic fit [70].

The drawback of this method is that the broadband nature of the excitation signal requires a large amount of power to measure the response at the specific tune frequencies. High power excitations will move the beam out of the acceptance of experimental beamline optics and so can only be used when no user experiments are running.

Frequency Sweeping / Spectrum Analyzer

An alternative method for providing the coherent oscillations needed for tune measurement is to perturb the beam using a sinusoidal signal with a frequency sweep (or *chirp*) instead of an impulse.

The excitation signal can be described by [70]:

$$e(n) = \sin\left(nw_0 + \frac{\Delta\omega}{N}n^2\right) \tag{7.2}$$

where w_0 is the revolution frequency of the ring, n is the turn number and $\Delta\omega$ is the frequency step per turn. An example chirp waveform is presented in Figured 7.2. The excitation signal is stepped in frequency and the response of the beam is measured. As the exciting frequency begins to overlap with a strong frequency component of the beam motion, the beam will start to oscillate resonantly.

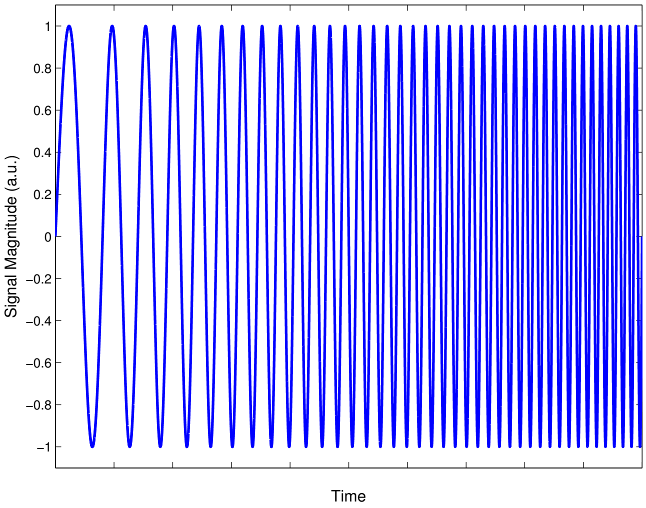

Figure 7.2: An excitation signal which is ramped evenly from one frequency to another is called a *chirp excitation*. A higher power coupling to the beam can be achieved since only the frequency components relevant to the measurement are used to excite the beam.

One major advantage of this method over the kicker based excitation is that the frequency range can be narrowed to the region of interest and the resulting signal strength is dependent on the frequency scanning rate rather than the kicker strength. Therefore the measurement device can concentrate on a particular area without disturbing the remainder of the beam.

At the ASLS this method is used for real-time tune measurements using a Spectrum Analyser (SA) with a tracking frequency generator installed [29]. The input signal to the SA is provided by a quarter wavelength stripline. To excite the beam the output sinusoidal wave is amplified to 10 W before passing through another set of vertical and horizontal striplines in serial.

After the full frequency is swept, data analysis is performed to find both the vertical and horizontal tune peaks and broadcasts the information to the control network through an Experimental Physics and Industry Control System (EPICS) process variable.

Because the system operates purely in frequency space it provides the tune for the entire bunch train and neglects any inter-bunch tune shifts. It is currently in use at the Australian Synchrotron for user-time tune measurements.

7.1.2 Single Bunch Excitation and Analysis

Since the BPM based method operates on a turn-by-turn basis and the SA operates in frequency space both methods only return a single frequency spectrum that represents the motion of all bunches. Any current or amplitude dependencies are combined in the measurement. The BBB system can measure the position of each bunch on a turn-by-turn basis, allowing a tune measurement of each individual bunch in the train.

As described in Chapter 5, part of the functionality within the FPGA of the Libera BBB system is the option to replace the standard corrective output for a bunch with a sine wave of arbitrary frequency (up to 125 MHz). This functionality can be used to produce a *chirp* signal to excite a single bunch for tune measurements similar to that described in Equation 7.2. By exciting a single bunch the rest of the beam can remain stable for users and the beam as a whole will experience minimal disturbance.

Excitation frequencies must be carefully chosen to make sure that the signal couples strongly to the beam. To ensure strong coupling, the frequency response of the BBB stripline kicker magnets must be considered [62]. Tune frequencies are present at sidebands of each revolution harmonic,

$$N.f_0 + Q_{\mathrm{x,y}}.f_0 \quad , \tag{7.3}$$

where N is an integer, f_0 is the revolution frequency and $Q_{\mathrm{x,y}}$ are the fractional tunes associated with each plane of motion. This enables excitation frequencies to be chosen at any sideband of the revolution frequency, up to the limit of the system. By altering N and measuring the effective coupling between the kicker and the beam, the response of the system can be maximised. Good results have been achieved at the ASLS using $N = 3$ and sweeping the frequencies ±10 kHz around the expected tune frequency.

An example tune measurement using the BBB measurement device is shown in Figure 7.3. In this experiment the BBB system is set up to output a chirp waveform which ramps the frequency over the expected tune space. The rest of the beam remains stable under the influence of the BBB corrective waveform while a single bunch is used to measure the tune.

By augmenting the standard technique of altering the RF frequency while measuring the tune the BBB system can also be used to measure the chromaticity of the ring. Further

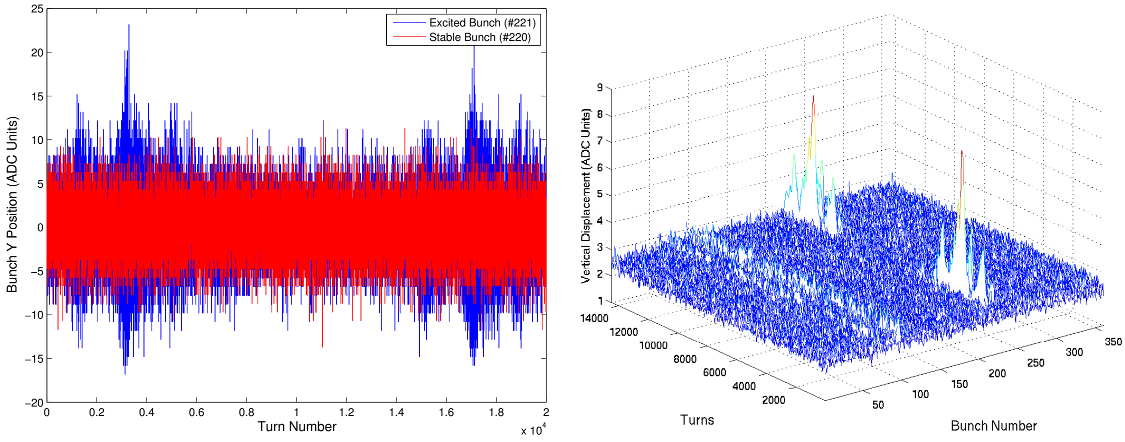

(a) A comparison of the movement of the targeted bunch (blue) to near neighbour (red). An effective isolation of the target bunch is shown.

(b) Single bunch excitation using the NCO chirp waveform. Note that only one bunch is seen to move.

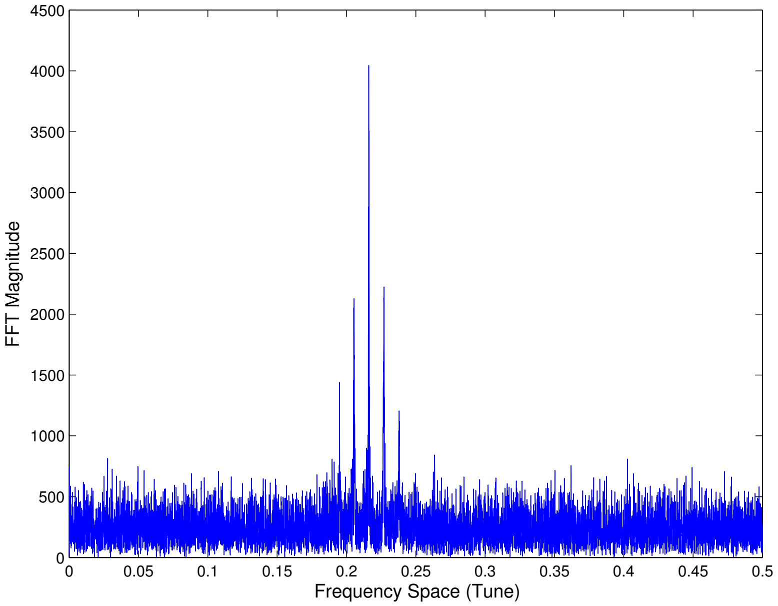

(c) The resultant frequency spectrum for the excited bunch. The main tune peak as well as synchrotron sidebands are measured. The absence of the horizontal tune is a result of the selected endpoints of the chirp waveform.

Figure 7.3: Single bunch NCO Tune Measurement. The advantages of using an NCO single bunch excitation to measure the tune of the ring are shown. Only a single bunch is excited, minimising the disturbance to users while the measurement takes place and the selection of the swept frequencies allows for a more focussed distribution of the power.

exploitation of the ability of the BBB system to measure the tune of individual bunches is discussed in Section 7.3.

7.1.3 Chromaticity Measurements

Chromaticity is defined as the change in tune with change in momentum:

$$\frac{\Delta Q}{Q} = \xi \frac{\Delta p}{p} \tag{7.4}$$

and the change in momentum is related to the RF frequency by:

$$\frac{\Delta p}{p} = \left(\frac{1}{\gamma^2} - \alpha_c \right) \frac{\Delta f}{f} = \eta \frac{\Delta f}{f} \tag{7.5}$$

where γ is the relativistic gamma, f is the RF frequency, α_c is the momentum compaction and ν is the slip factor of the ring. By altering the RF frequency in steps and measuring the tune at each step the chromaticity of the lattice can be measured. The tune measurement can be done using any of the techniques outlined above; in this example a kicker magnet is used as the tune will be shifting due to the chromaticity of the ring and the tune peaks may fall outside of the range of the chirp excitation frequencies.

An advantage the BBB system has over traditional tune measurement techniques is that it can measure the chromaticity of the lattice by measuring the tune of all stored bunches concurrently. This allows for an increase in statistics through measuring the chromaticity of all stored bunches simultaneously. How the chromaticity is calculated from a measurement of the single bunch tune shift with a change in energy is shown in Figure 7.4 where the chromaticity is extracted from the slope of the linear fit using Equation 7.5. Measurement errors can be minimised by calculating the chromaticity of each bunch and calculating the mean and standard deviation of the distribution. A measurement of the user-mode lattice chromaticity was made using this technique (see Figure 7.5) and the resulting measured chromaticity was $\xi = (2.81 \pm 0.02, 13.53 \pm 0.06)$.

Another potential use of the excitation capability is utilising the BBB system to deflect the beam to large amplitudes in a controlled manner. Using the BBB system in this way will allow for study of the non-linear portions of lattice optics and will be implemented in the future.

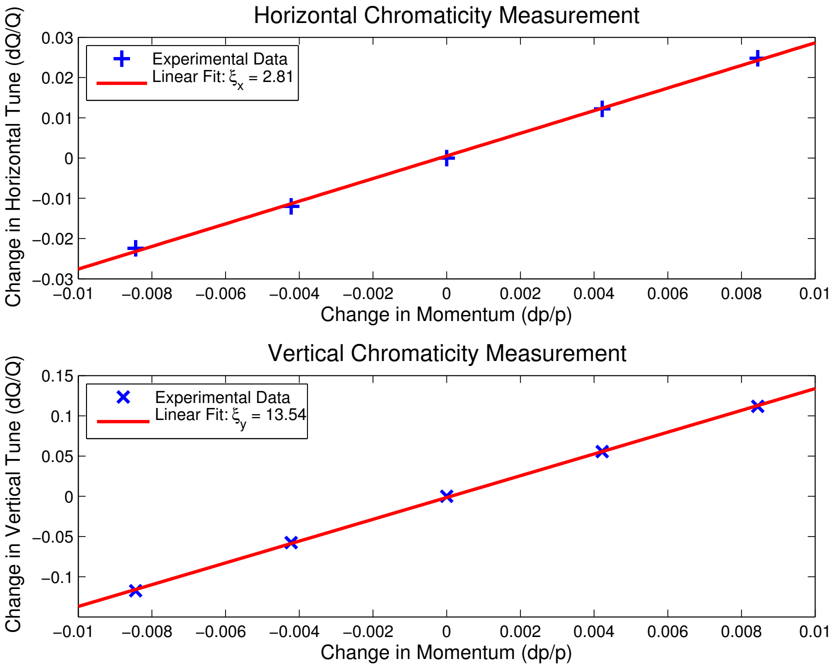

Figure 7.4: A chromaticity measurement using data from a single bunch. The tune shift versus energy change was measured and a linear fit applied to calculate the chromaticity.

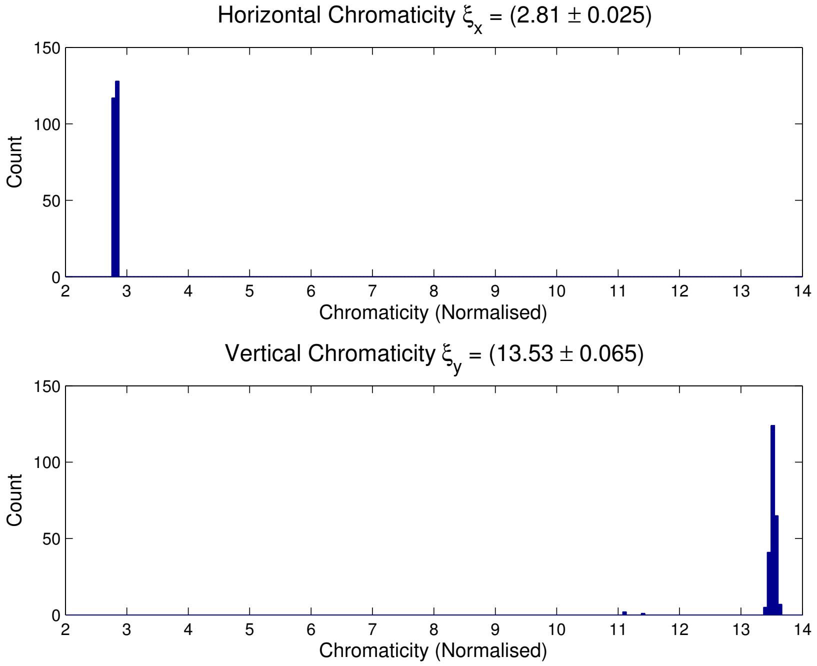

Figure 7.5: Histogram of multiple simultaneous chromaticity measurements using the BBB system. The measured chromaticity was $\xi = (2.81 \pm 0.02, 13.53 \pm 0.06)$ which matches well within the desired chromaticity of $\xi = (3, 13.5)$.

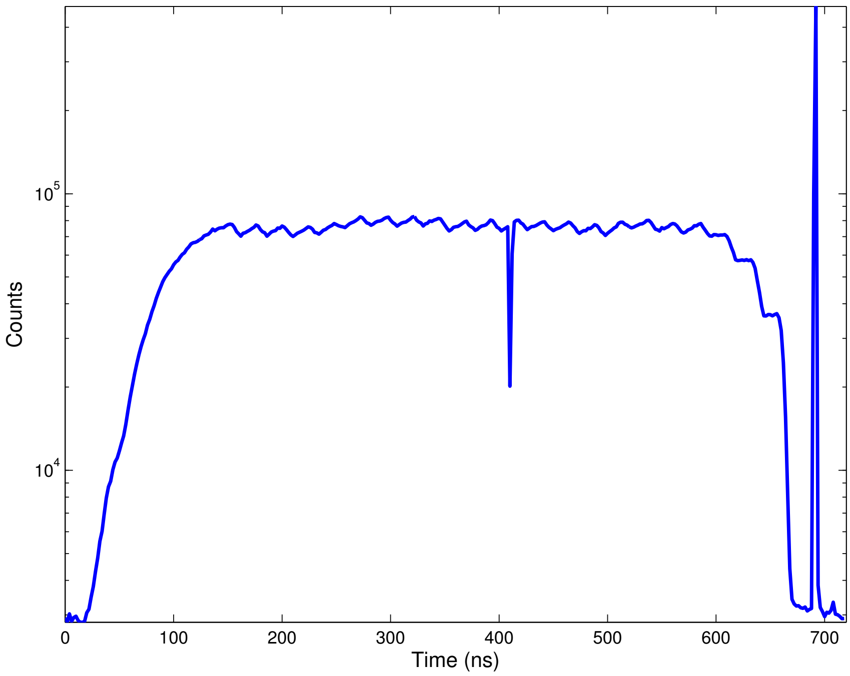

Figure 7.6: An example fill for high temporal resolution experiments. This particular fill is called a *camshaft* fill and was measured using a high dynamic-range current measurement device. A high power laser excites a change in state of the sample being observed, while the high current bunch is used to measure the state at a well-defined time using standard synchrotron measurement techniques. The dip in beam current at approximately 400 ns is due to an earlier bunch cleaning attempt.

7.2 Bunch Cleaning

Bunch cleaning is the process where an arbitrary fill pattern is created from stored beam by selectively exciting bunches beyond the acceptance of the ring and therefore removing the particles. Using this method the *purity* of a single bunch can be increased, where purity is defined as the number of electrons within one RF bucket compared to the surrounding buckets.

Figure 7.6 shows an example of a hybrid fill used for high temporal resolution measurements. An example of measurements utilising fill patterns such this are *pump/probe* measurements. A sample is excited using a laser in the period directly before the high current bunch, while the high current single bunch is used to measure properties of the sample with high temporal precision. It is important to have full knowledge and control over the fill pattern of the ring for these measurements to succeed. As every stored electron will emit X-rays as they orbit the ring, any stray electrons surrounding the single bunch will cause excitations in the sample and reduce the temporal resolution of the experiment.

Recall from Table 2.2 that the harmonic number of the ASLS storage ring is 360. Of these 360 RF buckets, a number will be populated and a number will be unpopulated depending on whether there are electrons stored within. If a bucket is intended to be unpopulated but contains a measurable number of electrons it is referred to as a *parasitic* bunch. The ratio of electrons stored in a full bucket compared to its surrounding parasitic bunches is defined as the *bunch purity*.

For high temporal resolution measurements it is important to increase the bunch purity for the single high current bunch. Bunch purities of 10^{-6} are desired to remove timing ambiguity for precision measurements. As an example, let us assume that a laser is synchronised to excite the sample 30 ns before probing the sample with X-rays emitted by the high current single bunch. If the RF bucket prior to the probe bunch has electrons stored within then any X-rays emitted will introduce a 2 ns shift in experimental assumptions and will cause ambiguity in the final result.

There are two distinct methods of injection into the storage ring: single and multi-bunch injection. Multi-bunch injection involves energising the electron gun over a relatively long time and injecting a train of electron bunches into the injection chain and accumulating them within the storage ring with a shot repetition rate of 1 Hz. Trains of 75 bunches are normally injected and the energising pulse at the electron gun can be delayed with resulting bunches overlaid to create the standard user fill. The advantages of multi-bunch fill for normal user time is that the injected current per shot is high ($\approx$2 mA) and the ring is filled from zero to 200 mA in approximately 1.5 minutes.

Conversely, single bunch mode injects a single bunch into the ring with an increase in stored current of approximately 0.2 mA per shot. This allows for a high *bunch purity* and finer control over the resulting fill pattern but dramatically increases the injection time. As a compromise, a fill such as shown in Figure 7.6 is formed with a combination of multi-bunch and single bunch injections with a reduced bunch purity. It is clear in Figure 7.6 that this filling technique introduces parasitic bunches to either side of the high current bunch.

The bunch purity can be increased after injection and maintained at a high level using a technique known as *bunch cleaning*. Bunch cleaning involves selecting two (not necessarily contiguous) sections of the ring, one to maintain and the other to eject. The RF buckets marked for ejection are excited resonantly at the tune using a fast strip-line kicker which prevents electrons from being stored. Given that the bunches will have a finite tune spread (discussed in Section 4.1.3), the excitation frequency is ramped over a range of frequencies surrounding the central tune.

Bunch cleaning can be done either in the booster synchrotron before injection [71] or in the storage ring after injection. Cleaning in the booster is often preferable as any losses are contained to the booster ring, but in the storage ring bunch purity will continue to erode over time due to electron leakage from the high current RF bucket into surrounding space . Bunch cleaning in the booster also requires dedicated equipment, while cleaning in the storage ring can utilise existing infrastructure. At the Australian Synchrotron bunch cleaning is performed in the storage ring using the BBB transverse feedback system to eject unwanted bunches while maintaining other bunches using the techniques already outlined in Chapter 5.

7.2.1 Experimental Considerations

Many synchrotron experiments with fine temporal resolution require a gap between the flat fill and a high current single bunch. Any parasitic bunches in the gap will compromise the ability of the beamline to provide accurate results. To maintain a camshaft fill, the single bunch and the flat fill must be maintained while the parasitic bunches are ejected.

To remove the parasitic bunches experience a sampled sinusoid similar to the chirp waveform described in Equation 7.2. Bunch cleaning requires the frequency to be repeatedly ramped in order to cover the full tune spread of the bunch.

Assume that the bunch selection consists of a single bunch surrounding by ejected bunches, such as the selection needed to maintain the camshaft fill in Figure 7.6. If the single bunch is stable the corrective waveform from the BBB feedback system will be negligible while

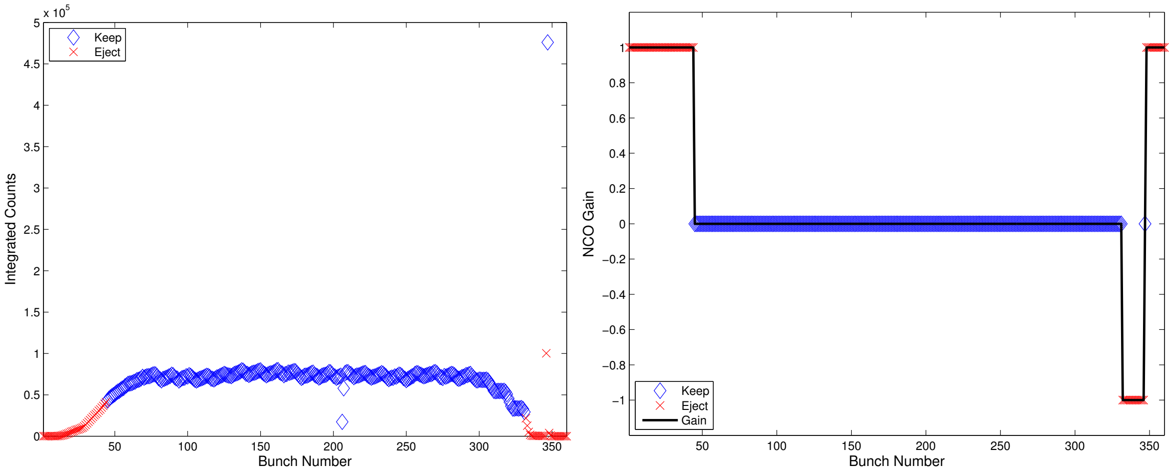

(a) Bunches to be kept and ejected

(b) Bunch cleaning mask

Figure 7.7: Derivation of a bunch cleaning mask from the selection of bunches to be kept versus bunches to be ejected.

the bunch cleaning sinusoid will have a large magnitude. This means that the sinusoid sent through the amplifier to the kickers will have a large number of high frequency components required to properly reconstruct the waveform. To reduce the required bandwidth to reconstruct the waveform, a selection method outlined in Reference [72] is used where the phase of the cleaning sinusoid is flipped either side of the bunches to be kept. This is implemented within the FPGA by changing the gain of the NCO output from +1 to −1. Figure 7.7b shows a bunch selection mask chosen using this method.

Using this mask the unwanted bunches experience the sweeping sinusoid and are resonantly excited to high amplitude, colliding with the defining aperture of the ring. At the ASLS this is set by the scrapers. As the acceptance of the ring is more restricted in the vertical plane than the horizontal plane, bunch cleaning is normally performed in the vertical.

7.2.2 Results

Initially the fill (shown in Figure 7.6) was constructed using a sliding multi-bunch injection, creating an area of 330 full and 30 empty RF buckets. The total current of the multi-bunch injection was 195 mA. After the multi-bunch injection was completed, an extra 5 mA was

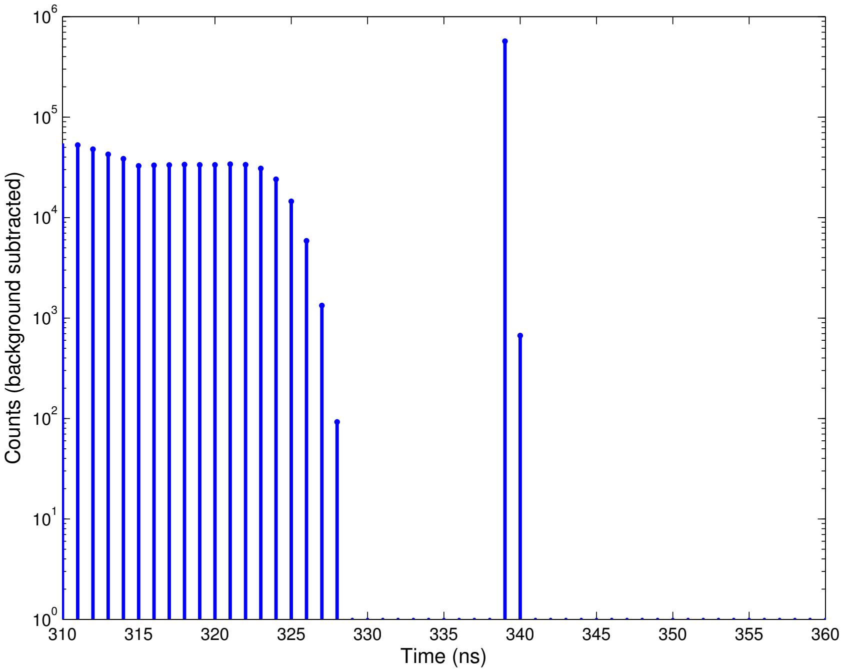

(a) Before bunch cleaning

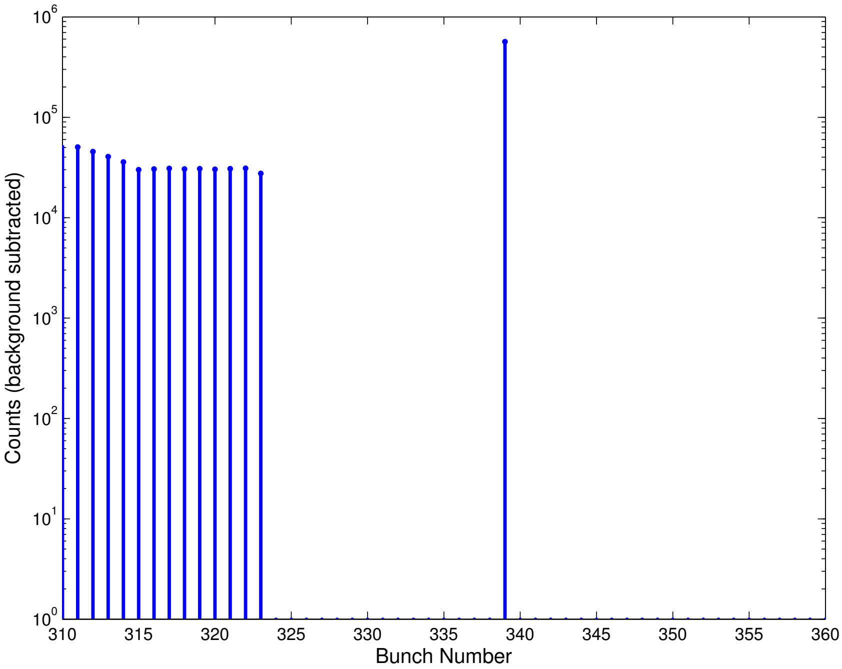

(b) After bunch cleaning

Figure 7.8: Results of a bunch cleaning experiment using the gain mask outlined in Figure 7.7. Data from the Bunch Purity Monitor has been binned into 2 ns bins for clarity. The bunch purity of the high current bunch has been increased through the ejection of surrounding parasite bunches.

injected in the middle of the 30 bunch gap using a single bunch injection.

The bunch cleaning mask was set up to keep 300 of the 330 bunches in the flat fill as well as the single high current bunch. Ejection of the other bunches was achieved with a sweeping sinusoid centered around the vertical tune frequency sideband of fourth revolution harmonic. In order to account for the tune shifts, the excitation frequency was swept over a range of 10 kHz.

To provide a known defining aperture and a controlled location for electron loss the set of scrapers installed in the storage ring were set to a height of 14 mm. This forms the defining aperture after the variation in betatron functions between the scrapers and IVUs are taken into account. Figure 7.8 shows the electron distribution before and after bunch cleaning, which achieved an increase in the bunch purity of the high current bunch from 2×10^{-4} to 3.5×10^{-6}.

Table 7.1: The bunch purity of the high current compared with a leading parasite bunch. The data for this table is that shown in Figure 7.8. The counts of each bunch (2.0 ns worth of data) are integrated after a background subtraction of 32 counts per bin [73].

	Parasite Bunch	High Current Bunch	Purity
Before	108	568659	2×10^{-4}
After	2	567990	3.5×10^{-6}

7.3 Bunch-by-Bunch Ring Impedance Measurements

In Chapter 3 the concept of a coherent tune shift was introduced, allowing for a different tune for individual bunches depending on single bunch currents. Normally it is the introduction of an imaginary tune shift that is damaging since it will induce growth or damping of the motion of a bunch, but in general the full complex valued tune shift needs to be considered. Equation 3.55 shows that an imaginary effective impedance will result in a real tune shift which can be measured using the methods outlined in Section 7.1. This will cause reductions of the beam lifetime if the tune shift moves near a strong tune resonance.

It has been shown that Equation 3.55 can, for mode $m = 0$, be expressed as [74]

$$\frac{dQ}{dI} = -\frac{e\langle\beta\rangle R}{4\sqrt{\pi}E\sigma_z}\mathrm{Im}(Z_{0,\mathrm{eff}}^{\perp}) \tag{7.6}$$

where e is the elemental charge, $\langle\beta\rangle \approx Q/R$ is the average betatron function under the smooth approximation, R is the radius of the ring, E the energy of stored particles and σ_z is the RMS bunch length in meters. $Z_{0,\mathrm{eff}}^{\perp}$ is the effective impedance of the ring, where only the mode $m = 0$ is considered.

Since the tune of the machine can be measured relatively easily, measuring the dependence of tune shift on the single bunch current enables a direct measurement of the imaginary part of the effective impedance.

The standard method for measuring tune shift as a function of current is outlined below:

1. Setup ring lattice for impedance measurement.
2. Begin injection in single bunch mode from zero current.
3. Stop periodically to measure the tune while logging the stored current.
4. If more ring parameters need to be changed then remove the stored current, change parameters and begin again.

While this is reasonable for a small number of measurements [49], if a ring parameter needs to be altered with a fine granularity then the time taken for each measurement quickly becomes prohibitive. The error rate due to the human involvement in the measurements will also cause unnecessary errors.

In order to increase the throughput of these tune-shift measurements a new method was designed which utilises the inherently high bandwidth of the BBB system. This simultaneously allows measurement of the tune-shift at multiple currents, essentially conducting a full tune-shift measurement in less than a minute without the need for re-injection of the stored beam.

The central idea for this method is to inject multiple single bunches into the storage ring each at a different current and measure the tune shifts of each individual bunch, circumventing the multiple injections necessary for the traditional method.

7.3.1 Experimental Setup

Two diagnostic functions are necessary to utilise this method of tune shift measurement: the ability to measure the stored current of each individual bunch and the ability to measure the tune shift of each bunch. The latter has been previously described in Section 7.1. In this case the injection kicker magnets will be used to provide a broadband excitation to the beam and the BBB setup will measure the tunes of the periodically spaced electron bunches.

Measuring the total current of individual bunches is a more difficult endeavour. Normally the total stored current of the ring is measured using a Direct-Current Current Transformer (DCCT). As this device is restricted to a sensitivity in frequency of the order of kilohertz [75], it is completely insensitive to bunch-induced current variations.

Higher current bunches have a lower lifetime than lower current bunches due to increased intra-particle collisions [76]. Further, the ratio of current between different bunches will change with time, preventing a prediction of the bunch currents from a known fill pattern and stored current.

The solution to the problem of measuring individual bunch currents came from an alteration to the existing BBB architecture. Figure 5.2 shows the signals from four BPMs combining to construct a vertical and horizontal position signal. The signals corresponding to the total beam current (I) and the difference of all the signals (Δ) are typically neglected in a transverse feedback system. Outputing a voltage proportional to the bunch current passing through the BPMs, the I signal is used for longitudinal feedback.

To measure the single bunches currents therefore, the longitudinal signal is down-mixed and acquired in a similar fashion to the transverse planes and down-mixed signal is connected to the horizontal BBB system in an open loop configuration. Using this setup the single bunch currents are measured with the interleaved ADC chains using code designed for acquiring data with the transverse plane signals.

Calibration

The response of the total current measurement system (BPMs, hybrids, down-mixing and ADCs) to the total current in a single bunch is non-linear. If the parameters of the data

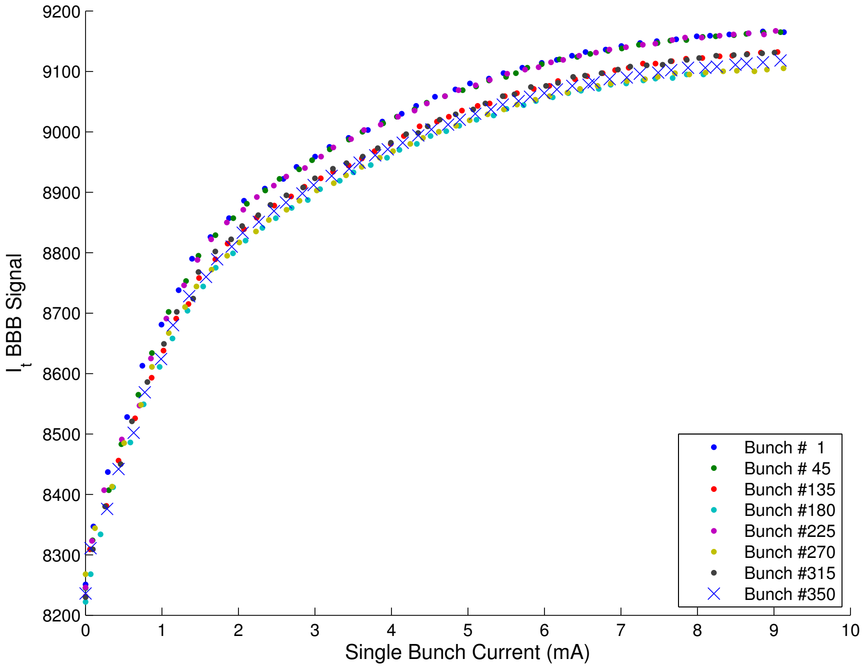

Figure 7.9: I_t calibration plots. Utilising the total current measurement from the RF hybrid (I), the BBB feedback system digitises the current of individual stored bunches. To convert raw ADC values to current, the four chains within the FPGA must be calibrated to account for gain and offset differences in the ADCs. Shown above are the calibration curves for eight bunches, showing a grouping into the four chains. The current calibration points are taken from a linear interpolation of these values.

acquisition system are not chosen carefully this will lead to a many-to-one relationship between current and measurement, preventing unambiguous knowledge of single bunch measurements. The methods of tuning the mixing angles described in Section 5.4.1 cannot be applied to the longitudinal plane since the ring is not equipped with a longitudinal kicker to excite the beam.

As the system will only operate in open loop mode during these measurements it is sufficient to maximise the signal measured at the ADCs. To achieve this, the ring is injected in single bunch mode up until the maximum current for the calibration, 10 mA for these measurements. Once the bunch is full, the mixing angle and ADC clock phases are scanned until a maximum ADC value is reached. These settings will be used for the rest of the measurements.

To calibrate the raw ADC values against current, all injected current is removed from the ring. Then, in single-bunch mode, current is injected into the ring. After each injection cycle the maximum signal from the ADCs corresponding to the injection bunch is plotted as a function of current as measured by the DCCT. For completeness this can be repeated for each ADC chain, but it will be shown later that if the injection targets are carefully chosen, only one chain needs to be calibrated. Figure 7.9 shows the resultant calibration curves for nine different bunch locations for the horizontal BBB unit. Four distinct response curves corresponding to different ADC chains are evident.

Fill Pattern

To maximise the tune shift, a fill pattern consisting of high single bunch currents is required. Shown in Figure 5.4 is the signal from a high current bunch, note that the signal persists for much longer than the bunch transit time through the BPMs. This signal ringing is due to bandwidth limitations of the RF hybrids which will lead to the signal from one bunch *leaking* into neighbouring bunches. It is therefore important to space the bunches apart with care taken to carefully avoid placing lower current bunches behind high current bunches. To this end, a pyramid fill was developed for these methods (shown in Figure 7.10a) where the strongest current bunches are surrounded by other bunches of similar size.

For the measurements presented in this section the bunches were separated by 36 RF buckets (72 ns). This allowed for 10 simultaneous measurements of the tune shift with current.

Timing

The signal for tune measurement is increased by the exciting the beam, so synchronisation between the data acquisition and the excitation signal is critical.

Timing for the BBB system is provided by the event generator which controls all of the timing signals within the Australian Synchrotron complex. Figure 7.11 shows how the timing signals are connected to the BBB system. An *event* is created which describes a particular timing signal the orbit clock (1.388 MHz) or injection trigger (1 Hz) for example. The EVG sends the event codes over multiple fibre optic connections to EVRs which are placed in proximity to systems that require the signals. Once it receives the signal, the EVR takes the

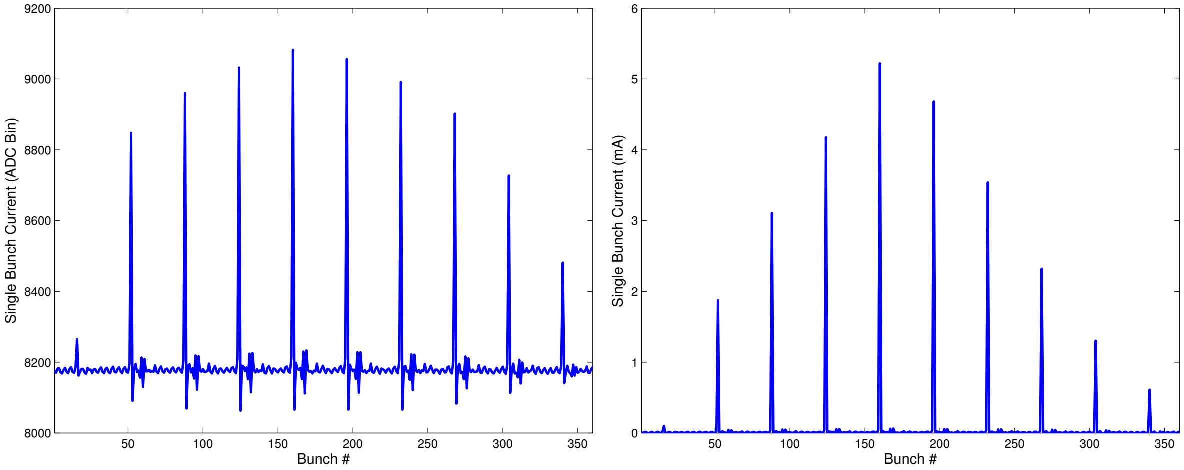

(a) Raw ADC values from the BBB system.

(b) Calibrated current values for each bunch.

Figure 7.10: A measurement of the individual stored bunch currents using the I_t output from the RF hybrids. The raw signal is measured using the BBB ADCs and then converted to current using the calibration curves seen in Figure 7.9. Induced ringing in the single bunch measurements results in unphysical currents of less than zero, therefore any negative values have been set to 0 mA.

event code and creates output signals in different forms such as TTL, CML or LVPECL.

The system clock for the BBB operates at the bunch repetition frequency, which is driven by the Master Oscillator controlling the central frequency of the RF cavities. This is converted from a sinusoidal voltage into a differential Low-voltage Positive Emitter Coupled logic (LVPECL) signal by the Libera BBB front-end, which also utilises a frequency-tripled version of the signal for local mixing of the BPM signals.

All timing connections to the BBB FPGA arrive over differential LVPECL connections. This allows for high speed trigger signals to be used with short rise times. Two signals are required to take data within the BBB system, an *arm* signal and a *trigger* signal. When a trigger signal (swapping high and low signals on the differential lines) is sent to the arm connection, the FPGA begins to place data from the ADCs into a circular buffer, rewriting old data once the memory is full. This continues until the trigger signal is sent, then the data continues to be written but once the data cycle returns to the trigger location the acquisition is completed and the data is written to a file. Approximately 22 ms of data can read from

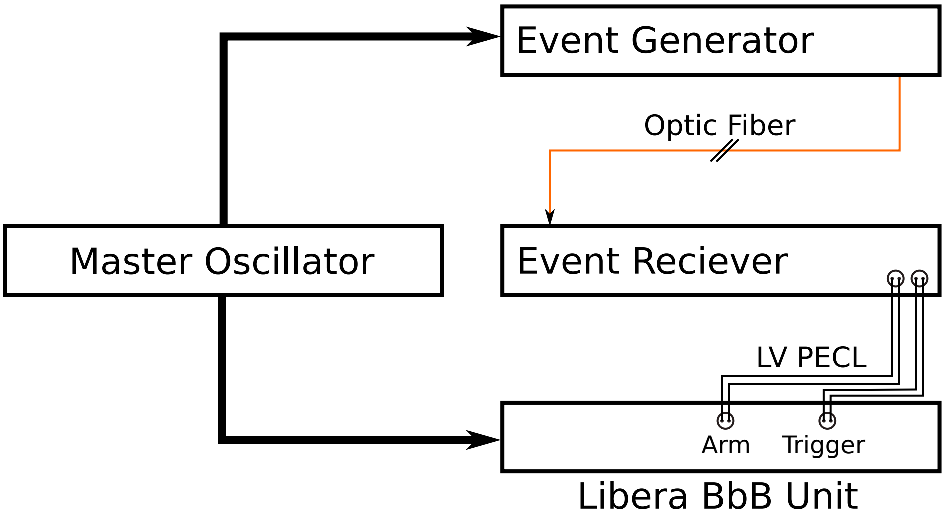

Figure 7.11: The BBB timing diagram. The timing system for beam dependent triggers at the Australian Synchrotron uses a master-slave arrangement of an EVG and EVRs. Events such as the orbit clock or 1 Hz injection trigger are created at the EVG and passed via optic fiber to the EVRs. Here the signal is converted into the necessary specification (TTL, CML, NIM) and passed to the equipment. Two signals are required by the BBB setup, an arm and trigger which are both provided by a single EVR situated nearby.

memory in a single operation and either of these signals are provided internally by the FPGA as well via external signal generators.

The injection kickers are fired once the accelerated beam from the booster arrives at the end of the Booster to Storage Ring Transfer Line (BTS) transfer line. This occurs 602.75 ms after the injection signal is used to activate the electron gun. To make sure the excitation is captured the trigger is set to precede the event by 0.5 ms, this way both the stable and excited beam should be captured.

Figure 7.12 shows an example of the beam excitation and tune measurement. A region-of-interest is placed around the excited beam and the Fourier transform is taken via an FFT. Two large peaks appear one for each of the transverse planes, in this case the leftmost peak is the vertical tune and the rightmost the horizontal. It is the position of these peaks that will change with the increase in single bunch current.

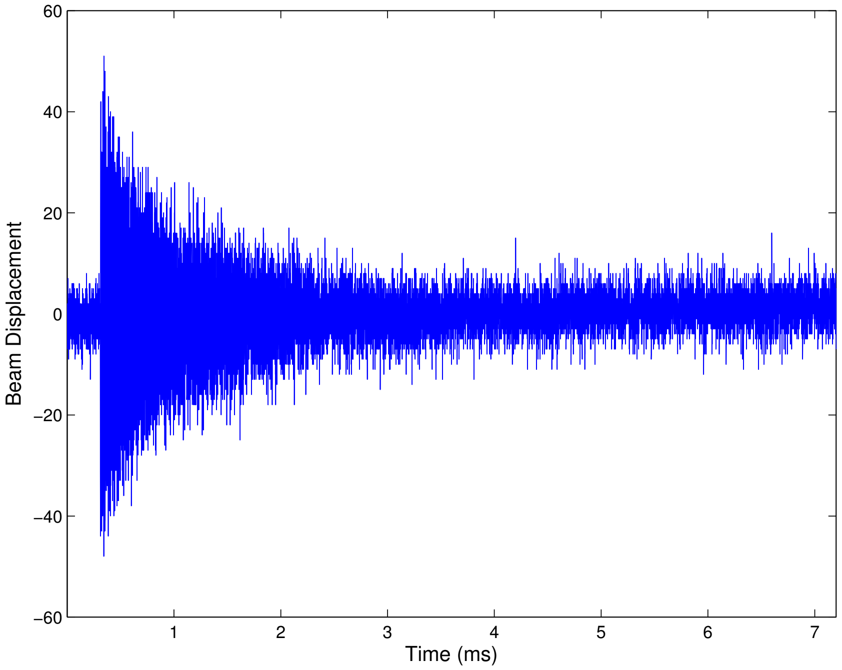

(a) Broadband beam excitation using one of the injection kicker magnets.

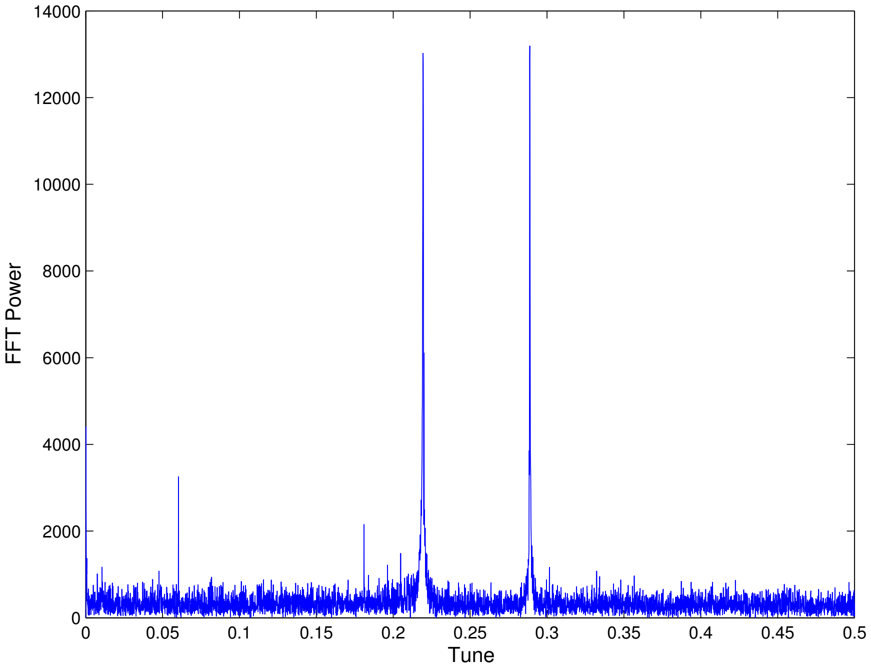

(b) The measured beam frequency spectrum of the excited bunch.

Figure 7.12: Since the goal of the impedance measurements is to measure a tune-shift a broadband excitation signal is used. The two figures above represent the motion of a single excited bunch and the resulting frequency spectrum respectively.

A frequency spectrum is calculated for each bunch and the shift in the vertical tune is extracted.

7.3.2 Results

Once the fill pattern is accumulated and the motion of the excited beam captured, the tunes are extracted for each bunch. It has been shown that the imaginary part of the effective impedance results in a real tune shift linearly proportional to the individual bunch current. From Equation 3.55, the change in tune with respect to the change in current is

$$\frac{\Delta Q}{\Delta I_b} = \frac{1}{|m+1|}\frac{e\beta c^2}{2\omega_\beta E_0 L_b}\mathrm{Im}\{Z_{\mathrm{eff}}\} \tag{7.7}$$

where Q is the tune, m is the azimuthal mode, E_0 is the nominal energy of the beam and L_b is the bunch length. The effective impedance Z_{eff} is described in equation 3.59. It is assumed here that the real part of the tune shift results in a measurable change in the frequency of motion of the particles. Since the tune shift equation has an imaginary leading coefficient, the real tune shift is proportional to the imaginary part of the effective impedance.

When the tune shifts measured for the individual bunches are plotted versus the amount of current within the bunch, the gradient of a straight line fit will be proportional to the imaginary part of the effective impedance of the ring.

Figure 7.13 shows a single measurement of the tune shift with current taken using the methods outlined in the preceding section. As described earlier, the aspect ratio of the storage ring beam pipe means that the beam is more sensitive to instabilities in the vertical plane.

The data for the measurement shown in Figure 7.13 takes approximately 10 seconds to acquire, where the bottleneck is network bandwidth between the BBB unit and the remote computer. This allows for a rapid succession of measurements to increase statistics while minimising the effect of any drift in measurement quantities.

Insertion Device Height

It has already been discussed that the resistive wall impedance is very sensitive to the half height of the ring with the impedance strength inversely proportional to the cube of the height (Equation 3.49). An increase in the machine impedance should be observable with respect to the height of the IVUs.

For this experiment the ring was filled with the fill pattern described in Figure 7.10a with

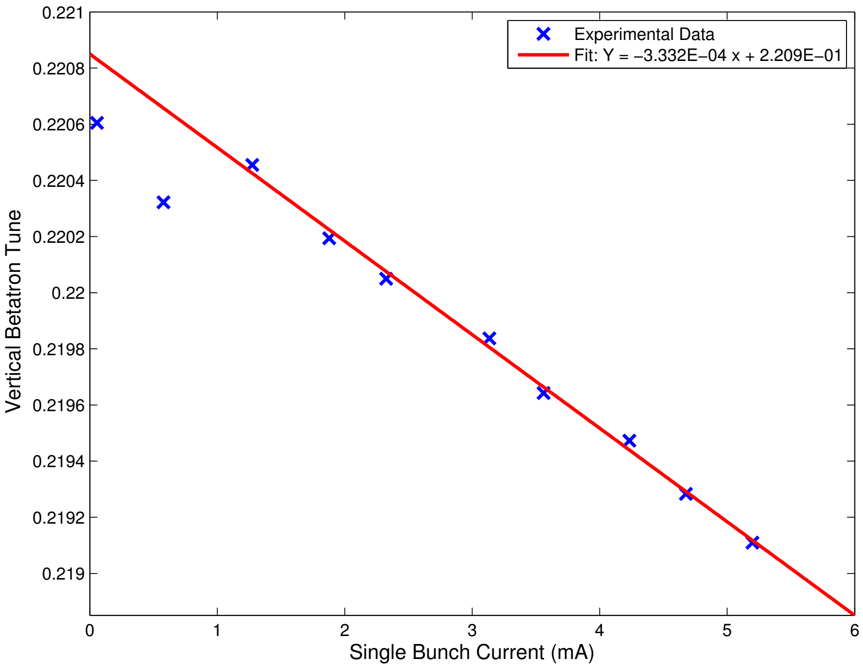

Figure 7.13: Vertical tune shift vs single bunch current. The result of a single impedance measurement. The measurement of the ring impedance is extracted from the gradient of the linear fit. The first two samples were discounted from the fit and relate to the bunches with the weakest signal being overcome by neighbouring signals.

the IVUs set to their maximum gap width of 35 mm.

Figure 7.14 shows that the total ring impedance increases as the IVU height decreases which is consistent with an increase in the resistive wall impedance of the ring.

Scraper Gap

As electrons deviate from the dynamic aperture of the ring, they will be *lost* through collisions with the beam pipe. This leads to the multi-GeV electrons interacting the material through bremsstrahlung and creating showers of X-rays at energies up to the incident energy. A proportion of these X-rays will pass through the shielding wall of the storage ring and exit onto the experimental floor. Because of this, to minimise radiation dose to experimental users, beam losses should be kept to a minimum.

Although most beam loss is unplanned, there are times when the beam must be lost in a controlled method, for instance when access to the ring is required. At these times, a set

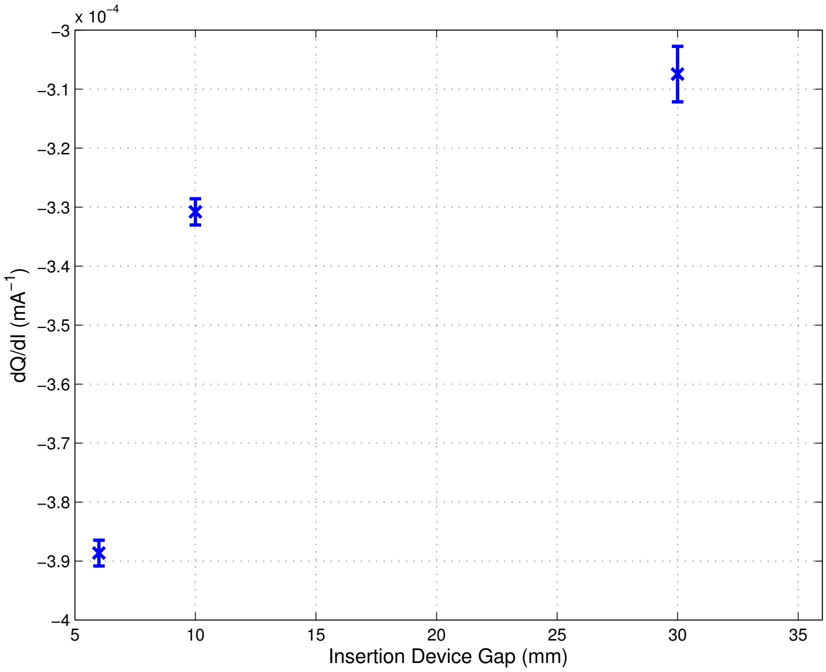

Figure 7.14: Change in Tune Versus IVU gap. The tune shift was measured as all of the IVUs gaps within the storage ring were reduced. As the IVUs are brought in, the impedance of the ring rises and the tune-shift increases.

of water-cooled metallic scrapers are slowly introduced to the outermost tail of the particle distribution. Through synchrotron radiation, particles within an electron beam spend time at high σ of the gaussian distribution. The particles with the largest deviation interact with the scrapers and are lost at a known location. This way the particle loss is controlled and can be heavily shielded against in a specific location.

It is expected that the introduction of a metallic object to the beam environment will cause a wake field to be produced. As the scrapers are thin compared to the full circumference of the ring the effect would more adequately be described by the introduction of a broadband impedance (due to the discontinuity between the beam pipe and scraper) rather than a dramatic increase in the resistive wall impedance at that point.

A clear increase in the current dependent tune shift can be seen in Figure 7.15. This measurement demonstrates the power of this more rapid technique, as the scraper height is a parameter which will effect the injection efficiency significantly and would therefore slow down the traditional method prohibitively.

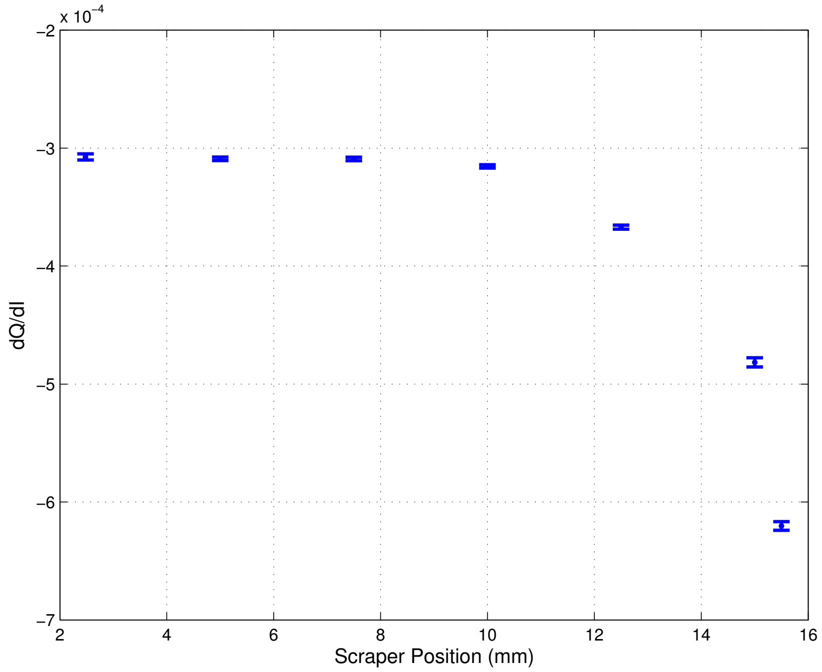

Figure 7.15: Change in tune versus scraper position. A demonstration of the power of the beam impedance measurement technique outlined. Scrapers were inserted vertically while the beam impedance was measured. A large increase the beam impedance was measured at distances greater than 10 mm, where the scrapers were close enough to interact with the beam. No significant beam losses occurred until after the scrapers were moved to 16 mm.

Betatron Coupling

Earlier it was discussed that an effect of magnetic field errors was the introduction of coupling between the betatron motion of the transverse planes. The coupling of the motion between the two planes leads to a change in the transverse profile of the beam as well as other effects both beneficial and detrimental to the beam. A series of grow/damp measurements were undertaken in Section 6.1.5 to show that increased coupling would lower the growth rate of instabilities in the storage ring. An alternate result was discovered in which increasing the coupling increased the growth rate of resistive wall instabilities (see Figure 6.10).

To verify this result with another technique, the tune shifts due to ring impedance were measured using the fast technique enabled by the BBB system. The emittance coupling was set in steps from the minimum calculated emittance of 0.009% to 20%. For each coupling setting, 10 ring impedance measurements were taken and the entire measurement run was conducted with a single injection of the fill described in Figure 7.10.

Figure 7.16 shows the results of the experiment, with the tune shift in relation to single bunch current increasing (in the negative direction) as coupling is decreased. This result shows that there is an effect on the effective impedance of the ring from the shape of the beam. In this case increasing the emittance coupling appears to decrease the real part of the effective impedance whereas prior to this the coupling would increase the imaginary part of the impedance.

This implies that increased coupling has a stabilising effect for beam which is already stable, reducing the tune shift due to the finite effective impedance of the ring. However for unstable beam increased coupling can increase the growth rate of resistive wall instabilities. Further study into this effect is currently underway at the ASLS, but the effectiveness of this tune shift measurement technique in quickly measuring multiple lattice configurations has already been proven.

7.4 Conclusions

The BBB system is a powerful combination of high-bandwidth high-resolution ADCs and FPGA computing power. A suite of diagnostics have been designed around the core of the BBB system and have been shown to be effective in measuring ring parameters such as tune and chromaticity as well as more specialised diagnostics such as ring impedance measurements.

It has been shown that the BBB system allows for the simultaneous measurements of individual bunch tunes leading to an accurate measurement of the chromaticity of the user-mode lattice: $(\xi_x, \xi_y) = (2.81 \pm 0.025, 13.53 \pm 0.065)$.

Fine control of single bunch excitation has been demonstrated using small amplitude excitations for tune measurements and high amplitude excitations for bunch cleaning. The ability of the BBB system to provide bunch cleaning will allow high-temporal resolution experiments to be performed at the ASLS.

Design and implementation of a quick ring impedance measurement system was undertaken using the BBB system and was shown to provide quick measurements of the real part

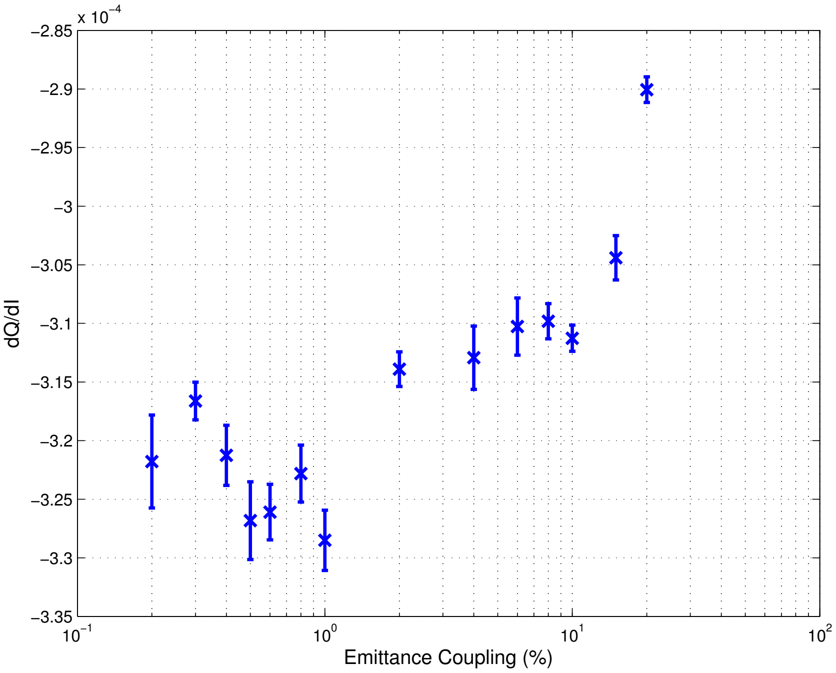

Figure 7.16: Change in impedance versus emittance coupling. The results of a study into the effect of coupling on the beam impedance. There is a clear increase as the coupling is decreased and this encouraged the grow/damp study outlined in Section 6.1.5.

of the effective impedance of the ring. It has proven to be especially suited to measurements involving rapid changes of ring parameters which may disallow re-injection into the ring, such as the introduction of scrapers and changes in the emittance coupling of the ring.

These diagnostic tools will increase the utility of the storage ring and allow for more demanding experiments to be undertaken at ASLS

Chapter 8

Conclusions and Future Work

The development of a bunch-by-bunch feedback system is a significant challenge as evidenced by the complexity of the start-of-the-art hardware and software techniques required to implement the system. This thesis has addressed many of these challenges, with particular emphasis placed on maximising the amount of current a storage ring is capable of circulating whilst avoiding the emergence of coupled bunch instabilities due to the interaction of the beam with its environment. A tangible outcome of the work contained in this thesis was the construction and commissioning of a system used to control such instabilities in the ASLS storage ring. This system will enable the installation of more insertion devices without compromising the amount of stored current and ultimately deliver a consequently higher photon flux to beamline users.

Critical to the operation of such a system is a thorough understanding of the motion of energetic electrons through the complex magnetic lattice of the storage ring. The crucial elements of the work required attention in the following areas.

- The development of a transverse feedback system
- Customised software for data acquisition
- Flexible data analysis tools
- Grow/Damp measurements of stored beam
- Bunch purity measurements and bunch cleaning

From this work, a set of novel tuning methods were devised to identify the critical aspects of beam stability and ultimately achieve the highest possible damping rate for the feedback system. As part of the tuning and proofing methods, a system for measuring the instability growth rates within the storage ring was developed. The robustness of the system was confirmed by experiment. This involved a procedure where the feedback loop was deliberately modulated, simulating a condition of significant instability. Under these conditions, grow/damp measurements verified the transverse feedback system was operating with a damping rate far beyond the growth rate of any instabilities observed within the storage ring at the ASLS. By exploiting a combination of mixing phase scans and grow/damp measurements the system was successfully commissioned in the ASLS storage ring.

8.1 The Transverse Feedback System

At the heart of the BBB is a high bandwidth transverse feedback system which has been successfully constructed and commissioned at the Australian Synchrotron, enabling storage of 200 mA at a chromaticity of $(\xi_x, \xi_y) = (2, 2)$. Prior to the installation of this system, coupled-bunch instabilities would develop in a low-chromaticity lattice configuration and effectively limit operation of the ring to 60 mA of stored current.

Novel techniques for tuning the delays and phases within the system have been created and these can be used to quickly recalibrate the system after alterations in the storage ring lattice. The techniques used for tuning the system enabled a damping rate of $\tau^{-1} = 3511$ s^{-1}, significantly stronger than the growth rate of both the resistive wall and resonator style instabilities observed within the ASLS storage ring.

8.2 Grow/Damp Measurements

To accurately measure the strength of coupled bunch instabilities within the ASLS storage ring, the instabilities must be allowed to grow without compromising the stored beam. Extensive grow/damp measurements were undertaken to examine the strength of the coupled-bunch instabilities within the ring and the effectiveness of the transverse feedback system. These measurements helped optimise the system for different ring configurations, in particular for different IVU gaps the control of which is the responsibility of the beamline scientists during experimental user times.

Growth rates for both resistive wall and resonator-style instabilities were measured within the ASLS storage ring using grow/damp methods. The strongest resistive wall growth rate (Mode #359) was measured to be $\tau_g^{-1} = 336.1$ s^{-1} while the strongest resonator-style growth rate observed was $\tau_g^{-1} = 575.1$ s^{-1}. All observed instability growth rates were well below the damping rate provided by the BBB feedback system.

8.3 Bunch Cleaning

As the sophistication of experiments evolve, more stringent demands are placed on the quality of the stored beam. One emergent area is the regime of pump-probe experiments which require extremely fine temporal resolution. These experiments demand high bunch-purity and this ideally achieved by filling a single RF bucket with a large amount of current, whilst keeping the surrounding buckets empty. However, in reality injection errors and RF bucket leakage lead to contamination where a small amount of current may be stored in adjacent buckets thereby degrading the temporal resolution. These parasitic bunches can be removed from the ring by resonant excitation to large amplitudes.

Bunch cleaning of these parasitic bunches was undertaken for the ASLS storage ring, allowing for an increase in the purity of a single high current bunch from 2×10^{-4} to 3.5×10^{-6}. The BBB system has proven able to clean bunches for an arbitrary fill pattern, enabling fine temporal resolution measurements to be undertaken in the future.

8.4 Storage Ring Diagnostic Suite

The capabilities of the transverse feedback system has also been leveraged to create a powerful diagnostic suite for measuring basic ring parameters including tune and chromaticity as well as more complicated properties such as the ring impedance. High bandwidth data acquisition allows for the separation of the motion of each bunch, while the ability to output arbitrary waveforms from the BBB system enables single bunch excitation.

Tune measurements are achieved by first exciting an arbitrary number of bunches and analysing the frequency components of the motion of each bunch over time. By measuring the tune of each filled bunch simultaneously, a large number of chromaticity measurements can be made at once. The measured tune and chromaticity compare well against the values from existing techniques.

An improved variant of the traditional single bunch ring impedance measurement has been designed and implemented using the unique capabilities of the BBB transverse feedback system. By combining the ability of the BBB system to separate the movement of individual bunches with the ability of the ASLS injection chain to construct arbitrary fill patterns, it was possible measure the complete current-dependant tune shift in a single measurement. With this new technique it is now possible to study the interactions of dynamic systems (such as scrapers or IVUs) on the effective impedance of the ring.

8.5 Future Work

Overall, the strategic combination of high bandwidth ADCs for data acquisition and DAC for beam manipulation enables the BBB feedback system to be used as a powerful diagnostic tool for accelerator physicists. This will form the basis for studies in the future; horizontal feedback and FPGA redesign.

8.5.1 Horizontal Feedback

In its current configuration, the ASLS storage ring does not suffer from coupled-bunch instabilities in the horizontal plane. However, this situation could easily change in the future if additions to the lattice reduce the instability threshold in the horizontal plane below 200 mA.

It is worth noting that there are two significant differences between the horizontal and vertical BBB feedback systems: a change in tune frequencies as shown in Table 8.1 and the addition of radiative damping due to synchrotron emission in the horizontal plane. For each of these frequencies, the local mixing phases and FIR filters must be optimised using the techniques presented in in Chapters 4 and 5.

The implementation of the horizontal feedback loop can also supplement the damping

Table 8.1: Tune frequencies for the horizontal and vertical planes. For successful BBB operations, each system must be optimised for the respective frequency.

	Fractional Tune	Tune Frequency (kHz)
Horizontal Plane	0.291	403.908
Vertical Plane	0.220	305.360

effects in the vertical plane if the beam is heavily coupled. As discussed in Section 2.2, if beam is heavily coupled motion in the vertical is transferred into the horizontal and vice-versa. This effect allows for a dual damping setup where a vertical instability experiences a corrective force from both the vertical and horizontal BBB transverse feedback systems. All of the electronics to implement horizontal plane BBB feedback have already been installed, and can be commissioned in the future.

8.5.2 FPGA Optimization

The computational center of the feedback system is an FPGA which acquires the position data and calculates a corrective waveform. An FPGA can be thought of as a large collection of logic chips where the inter-chip wiring is defined at design time and can be changed with new firmware. The versatile nature of this layout allows for high-speed digital processing, and the ability to tune for a specific computational pathway. An FPGA chip is not limited to a single digital pipeline, as different calculations can occur in disconnected sections of the chip all synchronised by a common clock signal. Disadvantages include a complicated implementation work flow, and limited floating-point number functionality.

Although the original FPGA design was constructed by the BBB supplier, functionality exists for loading alternate FPGA firmware. All of the diagnostic code presented in this thesis currently runs either locally on an ARM-based single board computer connected to the FPGA, or remotely on a general purpose CPU. Many of the mathematical steps which are conducted on the general purpose CPU could be ported to the FPGA architecture with the chance for a substantial speed increase through parallelisation. In particular, FPGA implementations of FFTs will allow for fast continuous tune measurements using the beam position as measured by the ADCs.

As discussed above, the horizontal transverse feedback system is currently not in use, so preliminary testing of the FPGA alterations could be implemented there without compromising the present ability of the ring to damp vertical instabilities.

8.6 Outlook

The BBB system has been successfully commissioned in the ASLS storage ring. With the addition of the diagnostic abilities designed and implemented as part of this thesis the ability of the accelerator physicists to understand the storage has been enhanced. In addition, future projects will further extend what has already proven to be a powerful system for damping transverse instabilities and providing diagnostic methods. By allowing for the further introduction of insertion devices and changes to the beam pipe, the BBB system will enable the ASLS facility to advance its storage ring technology in the future without concern of coupled-bunch instabilities compromising stored beam.

Appendix A

Acronyms

ADC Analogue-to-Digital Converter.

APD Avalanche Photodiode.

ASLS Australian Synchrotron Light Source.

ATLAS A Toroidal LHC ApparatuS.

BBB Bunch by Bunch Feedback.

BPM Beam Position Monitor.

BTS Booster to Storage Ring Transfer Line.

CAD Computer-Aided Design.

CCD Charge Coupled Device.

CML Current-mode Logic.

CMS Compact Muon Solenoid.

DAC Digital-to-Analogue Converter.

DBA Double Bend Achromat.

DCCT Direct-Current Current Transformer.

DELTA Dortmund ELectron Test Accelerator.

DFT Discrete Fourier Transform.

DSP Digital Signal Processor.

EPICS Experimental Physics and Industry Control System.

EVG Event Generator.

EVR Event Receiver.

FEL Free Electron Laser.

FEM Finite Element Method.

FFT Fast Fourier Transform.

FIFO First-In First-Out.

FIR Finite Impulse Response.

FLASH Free Electron LASer in Hamburg.

FPGA Field Programmable Gate Array.

IVU In-Vacuum Undulator.

LCLS Linac Coherent Light Source.

LEP Large Electron Positron Collider.

LHC Large Hadron Collider.

LINAC Linear Accelerator.

LVPECL Low-voltage Positive Emitter Coupled logic.

NCO Numerically Controlled Oscillator.

NFS Network File System.

ODB Optical Diagnostic Beamline.

PS Proton Synchrotron.

RF Radio Frequency.

RMS Root Mean Square.

SA Spectrum Analyser.

SLAC Stanford Linear Accelerator Center.

SPEAR Stanford Positron Electron Asymmetric Rings.

SRS Synchrotron Radiation Source.

TTL Transistor-Transistor Logic.

XDB X-ray Diagnostic Beamline.

Appendix B

Published Work

Journal Articles

1. V. Lee, D.J. Peake, B. Sobott, B. Schröder, Ch. Brönnimann, B. Henrich, K. Hansen, G.J. O'Keefe, G.N. Taylor, M.J. Boland, M.N. Thompson, R.P. Rassool. Imaging high energy photons with PILATUS II at the tagged photon beam at MAX-lab. *Nuclear Instruments and Methods in Physics Research A*, 603:379-383, 2009. doi:10.1016/j.nima.2009.02.024

2. D.J. Peake, M.J. Boland, G.S. LeBlanc, R.P. Rassool. Measurement of the real time fill-pattern at the Australian Synchrotron. *Nuclear Instruments and Methods in Physics Research A*, 589:143-149, 2008. doi:10.1016/j.nima.2008.01.072

Conference Proceedings

1. D.J. Peake, K.P. Wootton, R.P. Rassool, M.J. Boland, Y.-R. Tan. Operation and Storage Ring Calibration with the Transverse Bunch-by-Bunch Feedback System at the Australian Synchrotron. *IPAC 2011, San Sebastiàn, Spain.*
2. R. Dowd, M.J. Boland, G.S. LeBlanc, Y-R.E. Tan and D.J. Peake. Impedance Effects in the Australian Synchrotron Storage Ring. *IPAC 2010, Kyoto, Japan.*

3. D.J. Peake, R.P. Rassool, M.J. Boland, R. Dowd and Y.-R.E. Tan. Preliminary operational experiences of a bunch-by-bunch transverse feedback system at the Australian Synchrotron. *IPAC 2010, Kyoto, Japan.*
4. M.J. Boland, R.P. Rassool, G.S. LeBlanc, D.J. Peake, B.A. Sobott, V. Lee, A. Schubert and N. Kirby. Time Resolved Detectors and Measurements for Accelerators and Beamlines at the Australian Synchrotron. *SRI 2009, Melbourne, Australia.* doi:10.1063/1.3463174
5. D.J. Peake, R.P. Rassool, M.J. Boland and G.S. LeBlanc. Growth/Damp measurements and bunch-by-bunch diagnostics on the Australian Synchrotron storage ring. *PAC 2009, Vancouver, Canada.*
6. M.J. Boland, J. Bergstrom, G.S. LeBlanc, Y.-R. E. Tan, R. Dowd, M.J. Spencer, D.J. Peake and R.P. Rassool. Measurements using the X-ray and optical diagnostic beamlines at the Australian Synchrotron. *APAC 2007, Indore, India.*
7. M.J. Boland, G.S. LeBlanc, D.J. Peake, R.P. Rassool. Preliminary studies for top-up operations at the Australian Synchrotron. *PAC 2007, Albuquerque, New Mexico, USA.*

Available online at www.sciencedirect.com
ScienceDirect
Nuclear Instruments and Methods in Physics Research A 589 (2008) 143–149
NUCLEAR INSTRUMENTS & METHODS IN PHYSICS RESEARCH Section A
www.elsevier.com/locate/nima

Measurement of the real time fill-pattern at the Australian Synchrotron

D.J. Peake[a,*], M.J. Boland[b], G.S. LeBlanc[b], R.P. Rassool[a]

[a]School of Physics, The University of Melbourne, Melbourne, Vic. 3010, Australia
[b]Accelerator Physics Group, The Australian Synchrotron, Clayton, Vic. 3168, Australia

Received 15 October 2007; received in revised form 16 January 2008; accepted 16 January 2008
Available online 26 January 2008

Abstract

This article describes the development, commissioning and operation of a Fill-Pattern Monitor (FPM) for the Australian Synchrotron that measures the real-time intensity distribution of the electron bunches in the storage ring. Using a combination of an ultra-fast photodiode and a high-speed digitiser, real-time measurement of the fill-pattern at bunch-by-bunch resolution was achieved. The results compare very well with current methods of measuring the fill-pattern, such as a pick-up style detector. In addition, the FPM is fully integrated into the EPICS control system. The data provided by the FPM gives accurate RF bucket position and relative bunch currents over a wide range of stored beam currents, from 0.01 mA in a single bunch to 200 mA total beam current. The FPM monitors the success of an injection attempt into the storage ring and is used in a feedback loop to determine where to target the next injection. Using the FPM a beam top-up mode was successfully tested, resulting in a near constant beam current by periodic targeted injections over an 8 h shift. Results are presented for dynamically topped up real-time injection, where the beam pattern was squared using an intensity-dependent injection algorithm.

Keywords: Synchrotron; Fill-pattern; Beam diagnostics; Top-up injection

1. Introduction

The Australian Synchrotron is a third-generation light source operating at an energy of 3.0 GeV with an expected electron bunch length of 20 ps. The storage ring has a harmonic number of 360, a period of revolution of 720.5 ns, and each RF bucket has a width of 2 ns [1].

Knowledge of the fill-pattern profile of electrons in a synchrotron ring is important, especially as more sophisticated time-resolved experiments are considered. For experiments that are spatially and temporally sensitive, it is necessary to have a source with a known temporal-intensity profile in order to be able to analyse the effects of the radiation source on the results. A widely used solution for fill-pattern measurement is a pick-up type monitor, which measures the voltage induced by electron bunches as they pass through the vacuum chamber. An alternate method is to use optical synchrotron radiation and ultra-fast diodes to measure the emitted radiation intensity directly. The detector described in this paper, The Fill-Pattern Monitor (FPM), uses the latter method to measure the fill-pattern of the stored electron beam.

An accurate real-time measurement of the intensity profile allows the implementation of methods to alter the fill-pattern dynamically. These may include protocols to perform beam top-up modes, where electrons are periodically injected into the ring to compensate for losses, or the creation of custom fill patterns to meet the needs of particular beamline users. Dynamic beam top-up mode is particularly attractive as it leads to a stable beam intensity, thus preventing thermal strain on optical components as well as stabilising the experimental light available to users.

2. Experimental setup

A key feature of the Australian Synchrotron is a dedicated optical diagnostic beamline. It consists of an optical chicane, a focussing lens that forms a 1:1 primary image of the beam, and an optical bench that contains all the diagnostic instruments [2]. This facility was used to

---

*Corresponding author. Tel.: +61 3 8344 6303; fax: +61 3 9347 4783.
E-mail address: D.Peake@physics.unimelb.edu.au (D.J. Peake).

0168-9002/$ - see front matter © 2008 Elsevier B.V. All rights reserved.
doi:10.1016/j.nima.2008.01.072

align the diagnostic beam onto the small (200 μm^2) active area of a Hamamatsu G4176-03 ultra-fast MSM photodiode. This diode has a rise time of 30 ps, and is ideally suited for bunch-resolution measurements. Alignment of the incoming synchrotron radiation with the active area of the diode was achieved using an optical stage with three degrees of freedom.

Practical constraints in coupling the photodiode to the synchrotron light source limited the induced photocurrent to approximately 10 μA. Therefore a series of Minicircuits ZX60-14012L high bandwidth amplifiers was used to provide an adequate signal. High-speed digitisation of the signal was accomplished using an Acqiris DC282 8 GS/s CompactPCI card housed in a 3U CompactPCI crate. A computer embedded in the crate allowed local analysis of the data. Synchronisation with the stored electron beam was achieved by triggering the FPM acquisition-cycle with the orbit clock, which is provided by the central timing system and has a frequency equal to the orbit frequency of the stored electron beam. Configuration, control and data displays of the FPM were provided remotely through an EPICS interface. Calibration parameters, trigger delays and refresh rates could be customised for specific applications. Because EPICS is based on a distributed client/server model with TCP/IP messages created each time a variable is changed, it is unable to handle the throughput of raw data flow from the FPM. To overcome this limitation, some local preliminary processing of the data was provided by the crate processor. An overview of the experimental setup is shown in Fig. 1.

3. Results

Several measurements of the fill-pattern were made to study the performance of the FPM, and the results were compared with those using the existing method of fill-pattern measurement, the capacitive strip detector. Fig. 2 shows a comparison between fill-pattern measurements made simultaneously by the capacitive strip detector and the FPM.

3.1. Controlled loss of beam

To test the sensitivity of the FPM relative to the existing strip detector, a current of 50 mA was injected into the storage ring and a scraper was used to reduce the stored current gradually over a period of 12 min. During this process, the fill-pattern was measured simultaneously with the strip detector and the FPM. The fill-pattern measurements are shown in Fig. 3. Superior performance of the FPM is confirmed in Fig. 3(b) where at currents below 5 mA, the strip detector signal disappears into noise while the beam profile is still clearly resolved with the FPM.

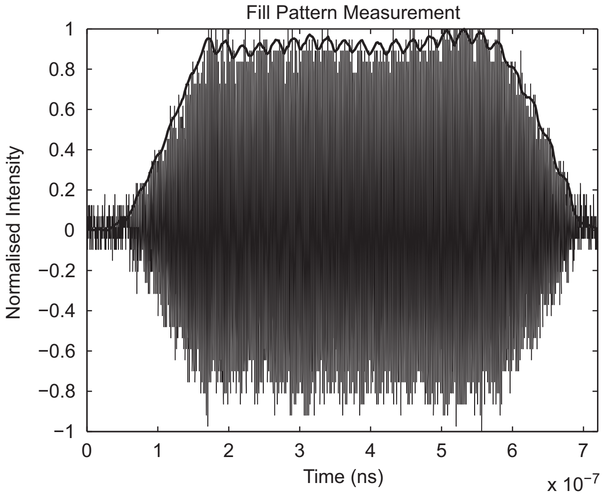

Fig. 2. Fill-pattern measurement made using the capacitive strip-detector (thin oscillating line), compared with results from the FPM (thick line).

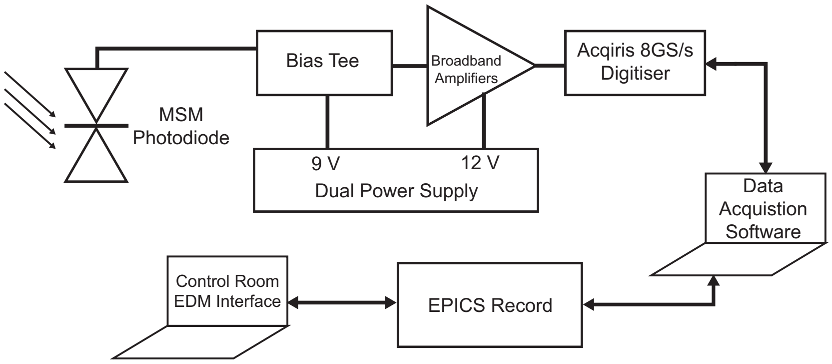

Fig. 1. Experimental setup for the measurement of the fill-pattern. Visible synchrotron radiation from the optical chicane is incident on the Metal–Silicon–Metal (MSM) Photodiode, which is biased to 9 V by the bias tee. Induced current from the incident light is amplified by 20 dB, and then digitised. The data acquisition software acquires the waveform and separates the signal into intensity values for each RF bucket, which are relayed to the control room through an EPICS interface. An EPICS interface also allows remote control of the acquisition system.

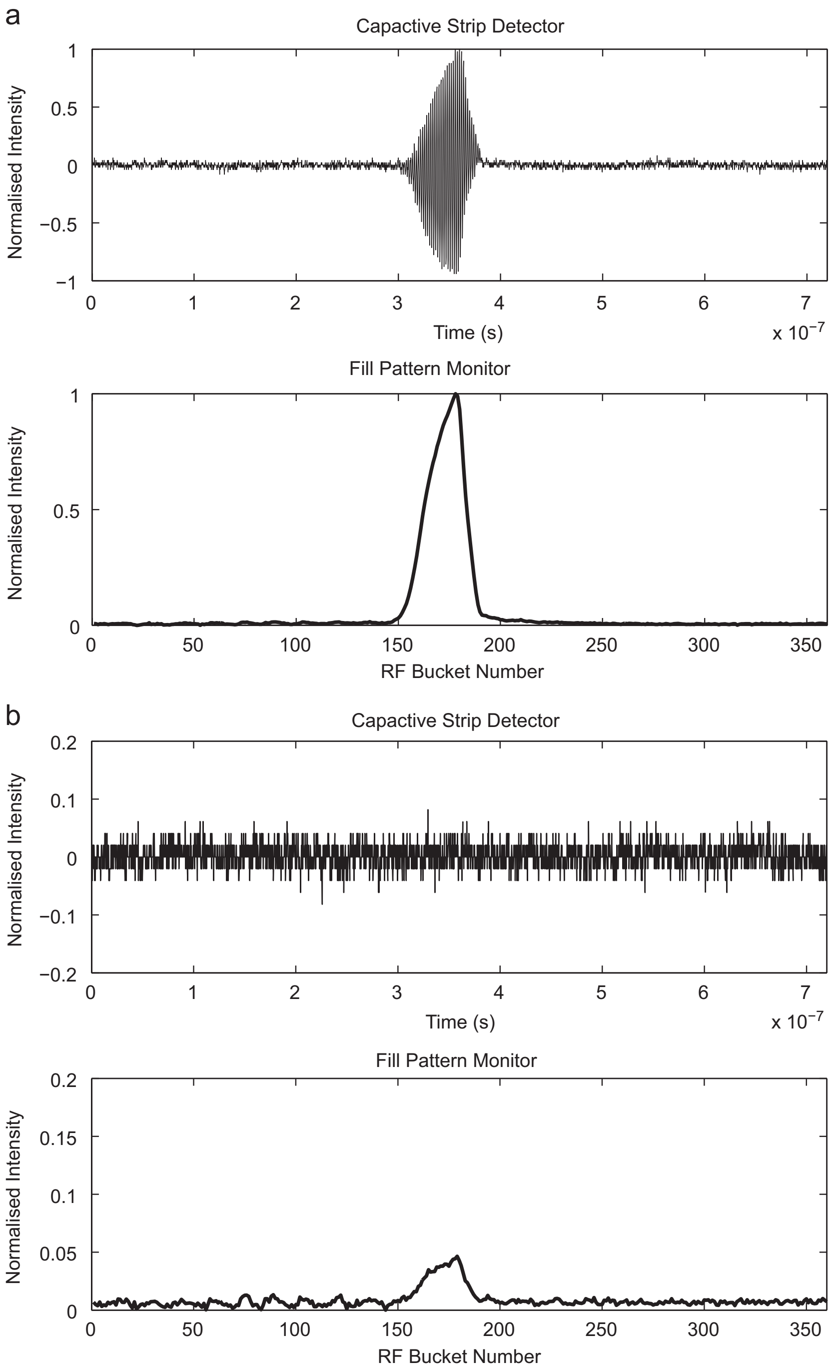

Fig. 3. Measurements of the fill-pattern during a controlled reduction of the beam intensity. The upper graph was obtained with the capacitive strip detector, and the lower graph using the FPM, (b) shows the response of both detectors at a beam intensity where the strip detector shows only noise. This low remnant fill-pattern was still measurable using the FPM.

3.2. Single-bunch injection measurements

To implement a top-up mode, the FPM must be able to measure with a high resolution the current stored in each individual bunch. A single RF bucket was filled using a single-bunch injection mode at 0.05 mA per shot, and the output from the FPM was logged. As Fig. 4(a) shows, a single shot as small as 0.05 mA could be detected by the

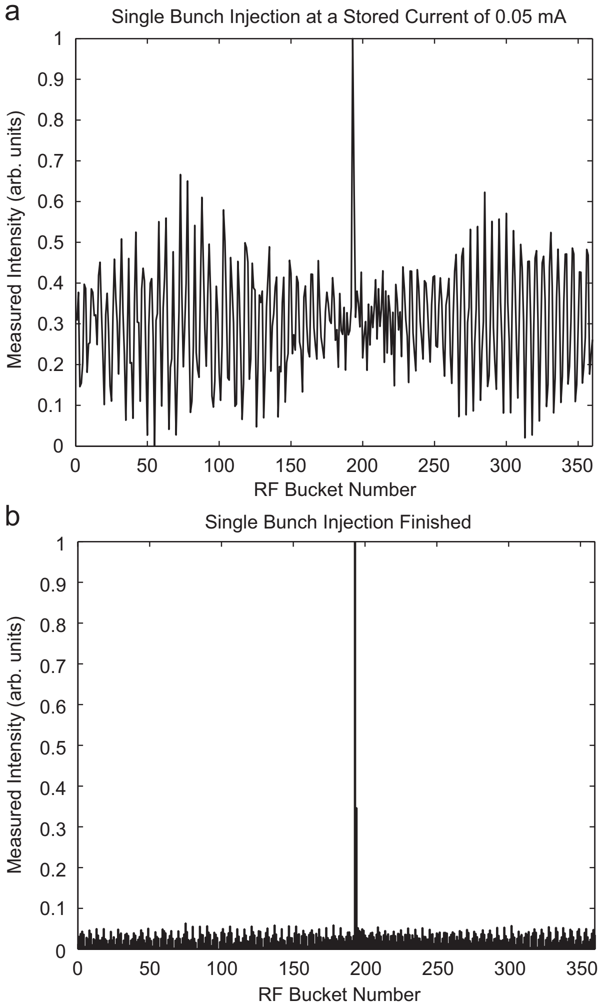

Fig. 4. Single bunch injection tests. (a) shows the first shot into the storage ring of the injection test as detected by the FPM. (b) shows the finished injection test, with all of the injected current stored in the correct RF bucket: (a) Single shot injected, (b) injection completed.

photodiode before registering in any of the presently available fill-pattern detectors. Such sensitivity will allow finer control over the selection of injection currents used in the dynamic top-up protocol.

After the single shot injection was completed, a lower intensity bunch was measured in the bucket preceding the target. To verify this signal was real, a measurement was taken on a streak camera located in the optical diagnostic hutch. The results are shown in Fig. 5; the streak camera is also measuring the lower intensity bunch. When each of the peaks are fitted to a Gaussian and integrated, they have an integrated intensity ratio of 2.9 matching the ratio between the two bunch currents measured by the FPM. The spurious bunch is a result of an error in injection phasing, which was corrected after these measurements.

3.3. *Morse code test*

Top-up operations require the system to be able to inject electrons into arbitrary RF buckets in the storage ring. To test the ability of the injection system thoroughly, a novel test was conducted to place a Morse-encoded message into the beam. Using one filled bunch for "dot" and three filled bunches for "dash", the message "ASP" was successfully placed into the stored beam, as shown in Fig. 6.

4. Top-up mode

It is expected that third-generation light sources possess a low emittance electron beam providing brilliant synchrotron radiation. Low emittance combined with a high brilliance requires a large amount of stored charge per bunch, which lowers the beam lifetime. This lower lifetime negatively affects the total photon flux during the experimental time for beamline users.

A method for compensating for the lowered beam lifetime is to periodically inject electrons into the storage ring. The real-time nature of the data provided by the FPM allows for bucket-resolution intensity targeted injections.

Top-up mode operation requires both accurate real-time data provided by the FPM as well as the ability of the Australian Synchrotron injection [3] and timing [2] systems to inject individual selected buckets in order to provide an even filling of the bunch pattern. An evenly filled beam reduces temperature fluctuations in optical components [4] by reducing medium term decay in beam loading, as well as providing users with a constant intensity radiation source for experiments. Top-up mode has been successfully tested at other light sources [5,6].

In top-up mode the FPM monitors the relative emitted light intensity of stored electrons in successive buckets in real-time. When the total stored current drops below a predetermined value, electrons are injected into the least-filled buckets. As each target bucket is filled, the next low-intensity bucket is identified for further top up. As Fig. 7 shows, during a period dedicated to top-up mode the stored current was maintained at a threshold of 100 mA using this dynamic injection targeting protocol.

A target of 3.0% stored beam stability was planned for the top-up tests. This estimate was based on a measured 2.9% standard deviation of the shot-by-shot current of the injection system. The measured beam current stability of the top-up run shown in Fig. 7 was 0.12%.

The dashed curve in Fig. 8 shows the result of an attempted pattern fill of 308 continuous filled buckets, with a gap of 52 empty buckets. This graph also demonstrates the problem with standard "pattern fill" injection: the fill-pattern is not as square as required, and the electron intensity of the filled buckets varies significantly due to an

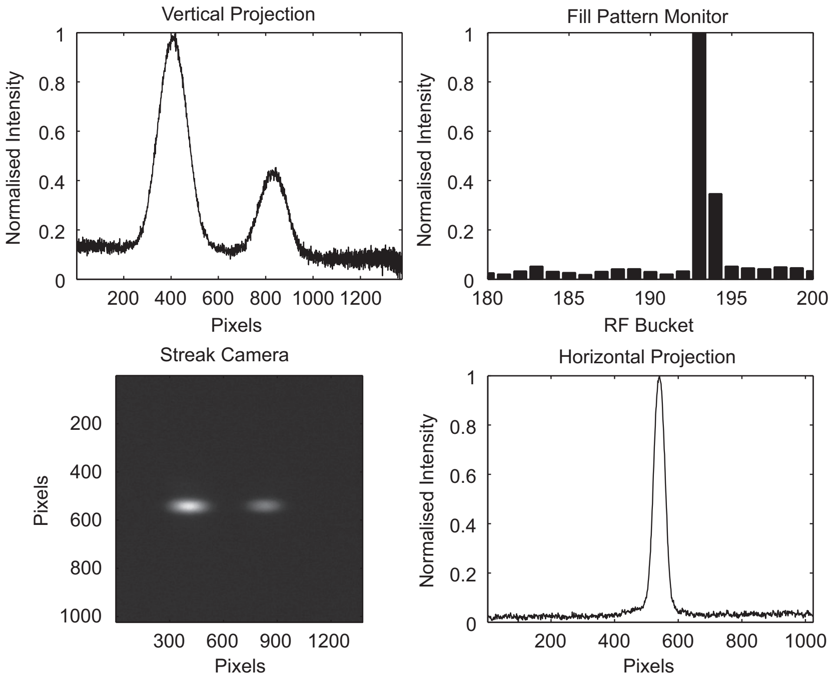

Fig. 5. A comparison between measurements from the streak camera and the FPM. The ratio between the integrated intensity of the peaks was measured to be 2.9 for both the streak camera and FPM.

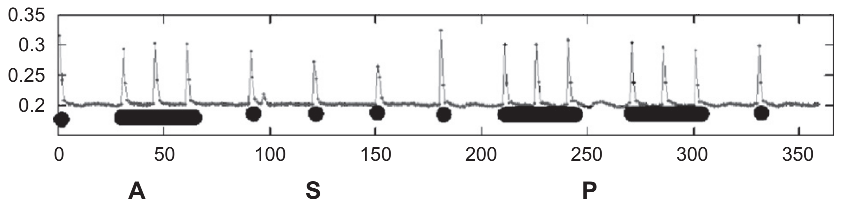

Fig. 6. “ASP” Morse code message. The morse code was used as a novel test of the injection systems ability to place current into arbitrary RF buckets.

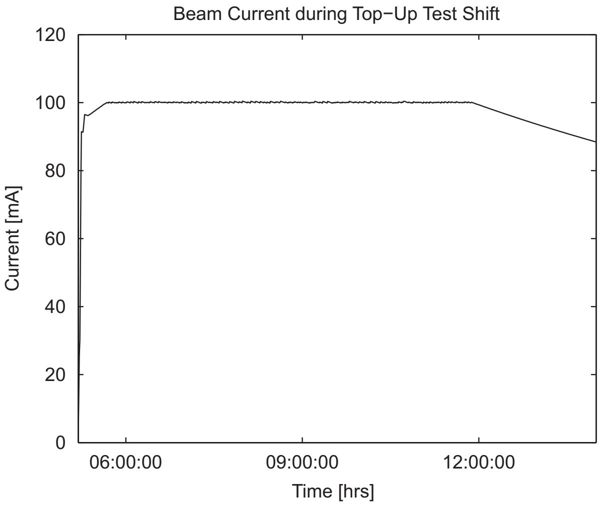

Fig. 7. The stored beam current over time during an 8 h top-up test shift. At 12:00 h, the protocol was disabled and the beam allowed to decay normally.

uneven current distribution from the electron gun. This crude pattern can be dynamically corrected using a feedback system based on data from the FPM.

As the beam current drops below a preset threshold (77.3 mA during this experiment), the injection procedure outlined above allows the fill-pattern to be corrected, and the current increased to the predetermined threshold level. A small deadband of 5 mA prevents non-stop injection. The solid curve in Fig. 8 shows the final fill-pattern after using the top-up algorithm. As the difference between filled buckets become smaller, the fill-pattern can be further squared off by altering the LINAC grid potential to reduce the injection current [7].

The standard deviation of the measured current intensity of the filled buckets, shown in Fig. 9, drops dramatically as the top-up procedure continues, showing the impact dynamic top-up has on the original fill.

One method of determining the “flatness” of a given fill-pattern is to create a histogram of the intensity values, as shown in Fig. 10. If the fill-pattern is not flat (for example

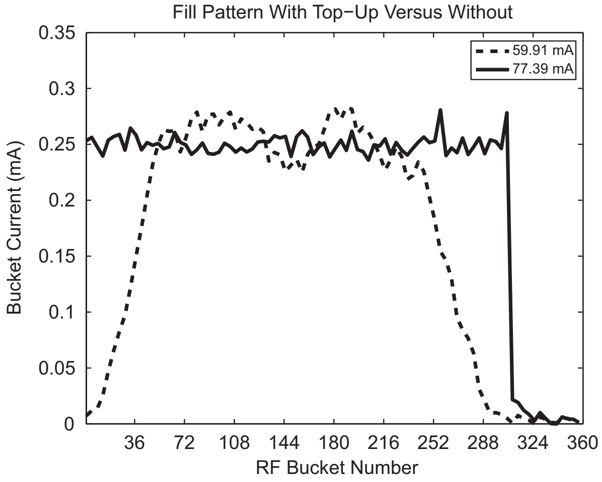

Fig. 8. Initial fill-pattern before top-up, compared with the final fill-pattern after top-up. The legend refers to total stored beam current. While the initial fill shows poor differentiation between empty (308–360) and filled buckets (0–308), after top-up the intended pattern is quite clear.

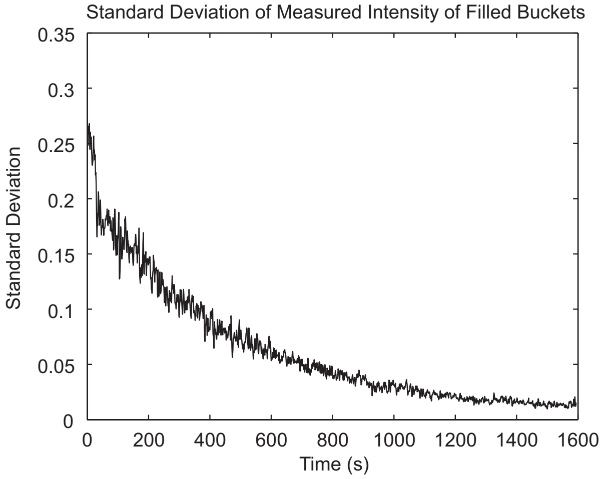

Fig. 9. The standard deviation of the measured intensity of the filled buckets versus elapsed time during top-up operations. The drop in the deviation is the result of a more even filling pattern.

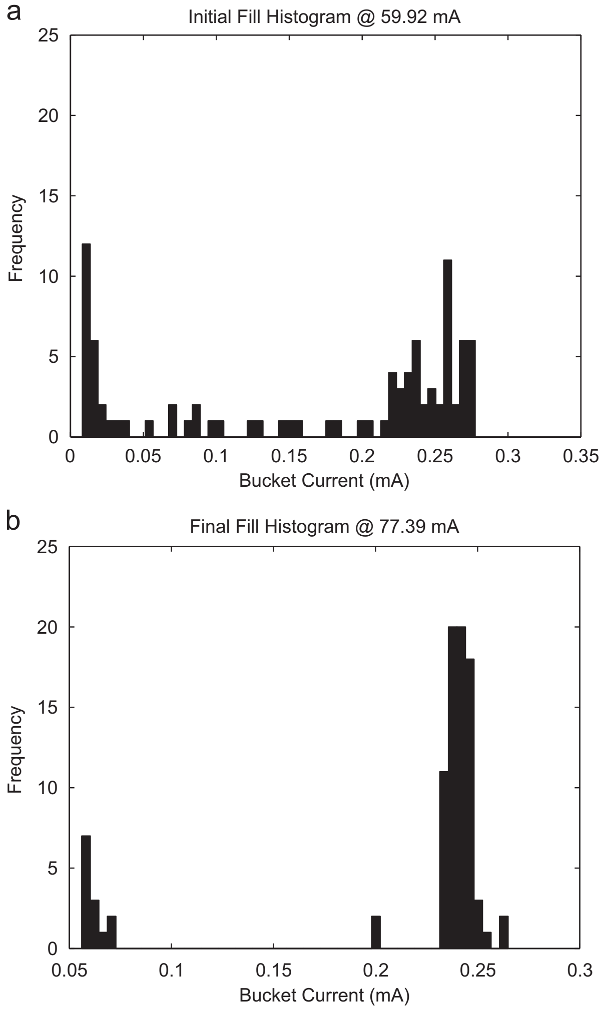

Fig. 10. Initial and final fill histograms of the bucket intensity values. The clustering of the values around two central points denotes the "ideal" current levels for both the empty and filled buckets: (a) Initial fill spectrum, (b) final fill spectrum.

the pre-top up fill-pattern shown in Fig. 8), the histogram will exhibit a continuum of intensity values ranging from empty to filled, with a shape dependant on the slope of the measured fill-pattern. As the intensity profile becomes flatter, the values will tend to converge into two groups, shown in Fig. 10(b). The standard deviation of each of the groups gives a measurement of how "flat" the intensity profile is.

Top-up mode protocol has been successfully demonstrated at the Australian Synchrotron using the real-time intensity data provided by the FPM. The FPM has proven itself to be a reliable diagnostic tool to dynamically shape and maintain the storage ring fill pattern.

5. Summary

This paper reports on the design, construction and use of a device that measures the real-time fill-pattern of the storage ring at the Australian Synchrotron. A high resolution real-time measurement of the current stored in each individual RF bucket was obtained using an ultra-fast diode combined with suitable electronics. A series of cross checked tests and complementary measurements confirmed the reliability of the system. The availability of the relative bucket intensities allowed for the implementation of an automated top-up protocol. The FPM is now well integrated in the control system software of the Australian Synchrotron [8].

References

[1] J.W. Boldeman, D. Einfeld, Nucl. Instr. and Meth. A 521 (2004) 306.

[2] M.J. Spencer, S. Banks, M.J. Boland, M. Clift, R.T. Dowd, R. Farnsworth, S. Hunt, G. LeBlanc, M. Mallis, B. Mountford, Y.E. Tan, A. Walsh, Z. Zingre, Diagnostics and timing at the Australian Synchrotron, in: Proceedings of EPAC, Edinburgh, Scotland, 2006.

[3] G.S. LeBlanc, M.J. Boland, Y.E. Tan, The Australian Synchrotron Project storage ring and injection system overview, in: Proceedings of EPAC, Lucerne, Switzerland, 2004.

[4] T.S. Ueng, K.T. Hsu, J. Chen, C.S. Chen, K.K. Lin, Top-up mode operation at SRRC, in: Proceedings of EPAC, Vienna, Austria, 2000.

[5] L. Emery, M. Borland, Top-up operation experience at the advanced photon source, in: Proceedings of PAC, New York, USA, 1999.

[6] A. Lüdeke, M. Muñoz, Top-up operation experience at the Swiss light source, in: Proceedings of EPAC, 2002.

[7] B. Kalantari, V. Schlott, T. Korhonen, Bunch pattern control in top-up mode at the Swiss light source, in: Proceedings of EPAC, Vienna, Austria, 2000.

[8] M.J. Boland, A.C. Walsh, G.S. LeBlanc, Y.E. Tan, R. Dowd, M.J. Spencer, X-Ray and optical diagnostic beamlines at the Australian Synchrotron storage ring, in: Proceedings of EPAC, Edinburgh, Scotland, 2006.

Nuclear Instruments and Methods in Physics Research A 603 (2009) 379–383

Contents lists available at ScienceDirect

Nuclear Instruments and Methods in Physics Research A

journal homepage: www.elsevier.com/locate/nima

Imaging high energy photons with PILATUS II at the tagged photon beam at MAX-lab

V. Lee [a,*], D.J. Peake [a], B. Sobott [a], B. Schröder [b], Ch. Brönnimann [c], B. Henrich [d], K. Hansen [b], G.J. O'Keefe [e,a], G.N. Taylor [a], M.J. Boland [f,a], M.N. Thompson [a], R.P. Rassool [a]

[a] *School of Physics, University of Melbourne, Parkville 3010, Australia*
[b] *MAX-lab, Lund University, Lund, Sweden*
[c] *DECTRIS Ltd., Baden, Switzerland*
[d] *Paul Scherrer Institut, 5232 Villigen PSI, Switzerland*
[e] *Centre for PET, Austin Hospital, Heidelberg, Victoria 3084, Australia*
[f] *Australian Synchrotron, Clayton, Victoria 3168, Australia*

ARTICLE INFO

Article history:
Received 17 November 2008
Received in revised form
13 February 2009
Accepted 17 February 2009
Available online 28 February 2009

Keywords:
PILATUS
MAX-lab
pixel
photon beam monitor
X-ray detector
Beam diagnostics
Photon tagging
Single photon counting
Beam profile monitor

ABSTRACT

In photonuclear experiments precise location of the photon beam relative to the experimental sample is critical. Previously used techniques such as using photographic film to identify the position, intensity and centroid of the beam is time-consuming and a faster method is required. PILATUS is a single-photon-counting pixel detector developed at the Paul Scherrer Institute (PSI), Switzerland. It is a silicon-based, two-dimensional detector with a large dynamic range and zero readout noise. Designed as an X-ray detector, its optimal quantum efficiency is between 3 and 30 keV. This paper reports measurements carried out at the MAX-lab tagged photon facility in Lund, Sweden. The beam endpoint energy of approximately 200 MeV is far above the designed optimal energy detection range of PILATUS, and provides a critical test of the use of PILATUS under high energy conditions.

The detector was placed in the photon beam and images were taken both downstream of other experiments, and in close range of a 19 mm collimator. The successful measurements demonstrate the versatility and robustness of the detector and provide an effective way of quickly and accurately monitoring beam position and profile in real time.

1. Introduction

In photonuclear experiments knowledge of beam size, intensity profile and position are important in determining the reliability of experimental results. For example if the target is not fully illuminated or if the beam's spatial intensity profile is not centred, the experimental data can be seriously compromised. Changes in beam characteristics must be known in order to make precise measurements. A beam profile monitor improves the accuracy and efficiency in data-taking during photon tagging experiments with low cross-sections.

One method of obtaining details of the photon beam such as its location or its intensity centroid is by recording an image on photographic film. However, the analysis of these pictures can be imprecise and not necessarily systemised. The process is also time consuming and disruptive to prolonged beam stability. An alternative method should be found.

Alternative systems of photon beam monitoring include blade-type monitors that analyse the photoelectric response from metal blades placed at the edges of a beam or in the beam fringes [1], and CCD-camera-based monitor systems [2]. A single-photon-counting detector system would provide an immediate visual image of the beam spot free from readout noise, provided it could operate under a high energy photon flux. This paper reports on measurements of the photon tagging beam at MAX laboratory in Lund, Sweden, using a single-photon-counting detector, the PILATUS 100K module.

2. Experimental setup

2.1. The PILATUS detector

The PILATUS detector is a single-photon-counting X-ray detector developed at the Paul Scherrer Institute for use at the Swiss Light Source. It is produced by DECTRIS in three sizes, the PILATUS 100K, the PILATUS 2M and the PILATUS 6M. For this experiment a PILATUS 100K module was used.

---

[*] Corresponding author.
E-mail address: leev@physics.unimelb.edu.au (V. Lee).

0168-9002/$ - see front matter © 2009 Elsevier B.V. All rights reserved.
doi:10.1016/j.nima.2009.02.024

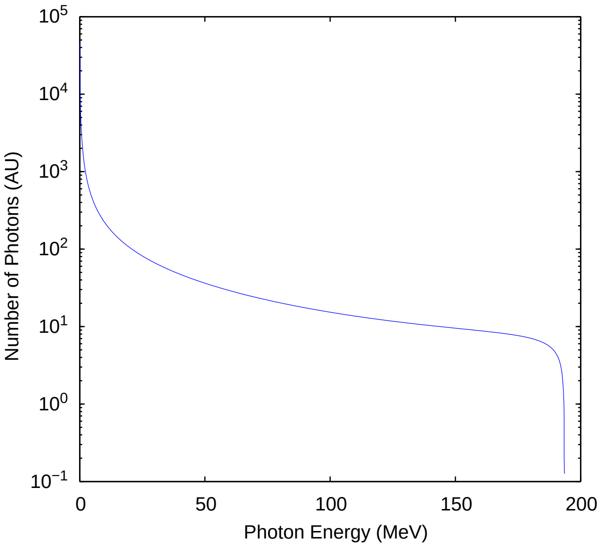

Fig. 1. Theoretical bremsstrahlung count spectrum from 194 MeV electrons incident on a 300 μm aluminium target. While only photons from 167.5 to 179.5 MeV are tagged by the magnetic spectrometer, the beam consists predominantly of photons lower than the tagged energy. This has implications for PILATUS which has optimal quantum efficiency at 3–30 keV.

The PILATUS 100K module has a sensitive area of 85.3 mm × 34.1 mm consisting of an array of 16 detector chips in an 8 × 2 array. This provides an array of 487 × 195 (94 965) pixels, each of size 172 μm × 172 μm. Connected to each pixel is a readout system consisting of a preamplifier, a pulse shaper, a comparator and a 20-bit counter, providing a 1 MHz per pixel per second count rate capability, with a ~2 ms chip-parallel readout time. The intrinsic dead time of the detector is ~10 ns the time for which the signal must remain below the threshold level in order to resolve two separate counts. The readout chips are indium bump-bonded to a 300 μm Hamamatsu silicon sensor consisting of p+ implants embedded in a high resistivity (~8 kΩ cm) n bulk. The system is reverse biased to 120 V. Physically, the entire module is 275 × 146 × 85 mm in size [3,4].

The data acquisition system for the module uses a PCI card and is controlled from a PC using TVX, PILATUS' user interface. For the experimental work carried out at MAX-lab, the PC remained in the experimental hall and was controlled through a remote VNC interface. Designed to be radiation tolerant using UMC[1] 250 nm technology, the detector incurred no detectable damage in the experiments under high energy beam flux.

2.2. MAX-lab tagged photon beam

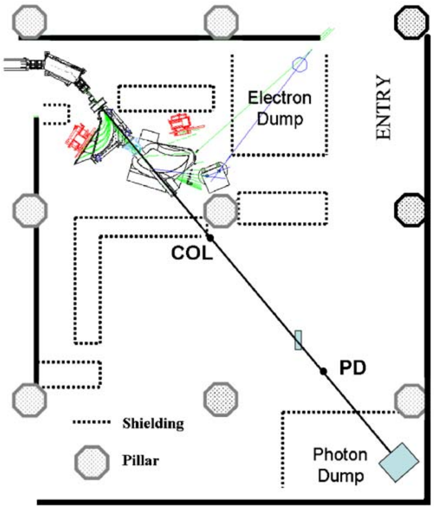

Fig. 2. Nuclear experimental hall: positions PD and COL denote the acquisition sites: photon dump and collimator.

Table 1
Experimental set up configurations.

Configuration	PILATUS position	PILATUS cover	Lead	Other
A	PD	Off	~1 cm	–[a]
B	COL	Off	None	–
C	PD	On/off	5 mm/none	–[b]
D	PD	Off	None	–

PD and COL refer to position denoted in Fig. 2. The PILATUS cover is a 2.5 mm thickness of aluminium affixed on the detector, covering the sensitive area. Measurements included insertion of lead sheets at various distances from the detector face, described in detail in main text.

[a] Pb covering left half of the sensitive area.

[b] Series of four set up configurations with and without two converters—the PILATUS cover and 5 mm of lead.

The electron source for the bremsstrahlung photon beam used in MAX-lab's nuclear hall is the MAX I storage ring operating in pulse-stretching mode. An initial 200 MeV electron pulse from a LINAC is injected into MAX I with a frequency of 10 Hz and stretched over time to maximise the duty cycle of the extracted electron beam. The electron beam is extracted from MAX I to the nuclear hall where it strikes a bremsstrahlung radiator chosen to suit the scheduled photonuclear experiments. The bremsstrahlung photons then are collimated to provide the photon beam while the electrons are magnetically swept into the electron dump [5]. The theoretical bremsstrahlung spectrum for our experiment is plotted in Fig. 1 [6].

2.3. Measurements

The PILATUS detector was set up in the nuclear experimental hall and images were taken at two detector positions as marked in Fig. 2: near the photon dump (PD), downstream of two target experiments; and 40 cm from the 19 mm beam collimator (COL). The bremsstrahlung radiator on the opposite side of the collimator was a 300 μm thickness of aluminium. Measurements involved the insertion of converters at various distances in front of the detector including different thicknesses of lead and the PILATUS protective cover, a 2.5 mm thickness of aluminium affixed to the front of the detector to cover the sensitive area. Table 1 summarises the experimental configurations for the measurements.

3. Experimental tests and results

3.1. Beam spot measurements

In order to image the beam spot, the detector was placed in Configuration A: at the PD position with 1 cm of lead inserted in

---

[1] UMC: United Microelectronics Corporation, Taiwan.

front of the detector. (Detailed in Table 1.) The lead collimator was 19 mm in diameter.

Beam spot measurements at the PD position yielded a typical beam spot size of 48.7 mm ± 3 mm FWHM. Measurements were also conducted close to the collimator using Configuration B which yielded a typical FWHM size of 29.7 ± 2 mm. These are illustrated in Fig. 3.

3.2. Imaging high-energy photons

The ability of PILATUS to image high energy photons through the production of lower energy secondaries produced in a converter was tested via the insertion of two converters between the beam and the detector module (Configuration C). These were the 2.5 mm aluminium protective cover, fixed to the front of the detector, and a 5 mm thickness of lead placed 45 cm further upstream. Between the lead and the detector was placed a steel-wire 'stencil' reading 'MAX' to provide attenuation contrast in the images (Fig. 4). The total counts per image for each converter is shown in Fig. 5. This count consists of photons and pair produced electrons and positrons. From simulation in G4beamline [8], it is estimated that 4.4% of the total count can be attributed to electrons. It can be seen that the use of only the lead converter provides the greatest enhancement of beam visible to PILATUS, followed by the aluminium cover alone. While the lead converter enhances the measured beam, the results using combined converters shows that the photons passing the lead attenuator are further attenuated by the aluminium and no significant difference from the original, unattenuated beam can be seen. Preliminary analysis of these results using attenuation coefficients supports the observed hierarchy in count rates and provides stimulus for undertaking detailed GEANT4 simulations. This will allow for the optimisation of attenuators for high energy photon imaging using PILATUS.

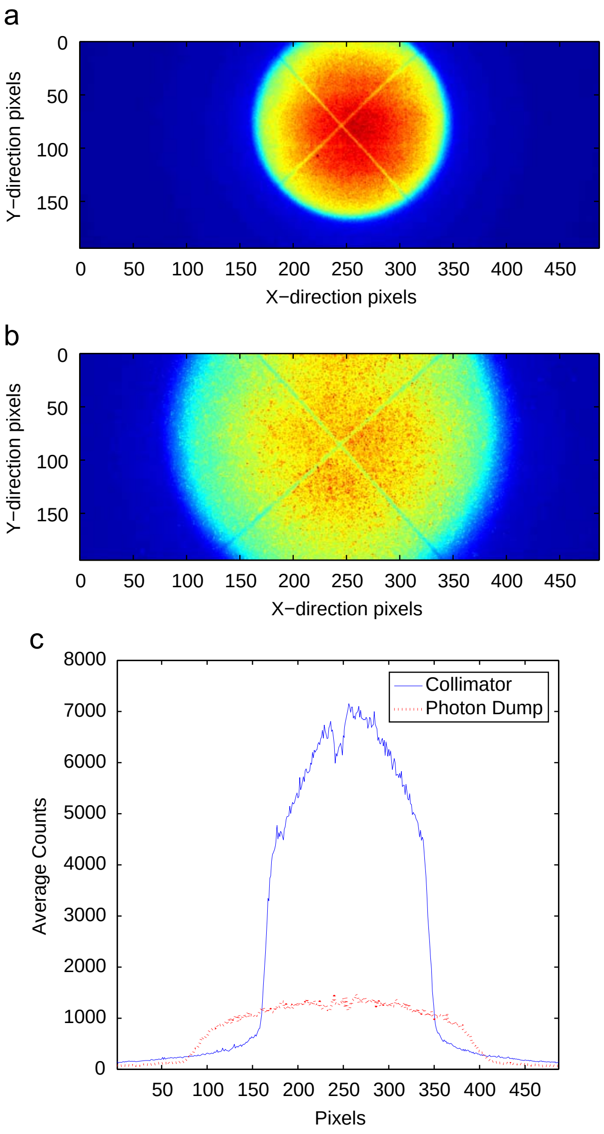

Fig. 3. Beam spot images from positions COL and PD in the experimental hall. FWHM is measured from integrated counts over a horizontal slice of 5 pixels wide. (a) Beam spot at collimator; (b) beam spot at photon dump; (c) beam spot average counts comparison.

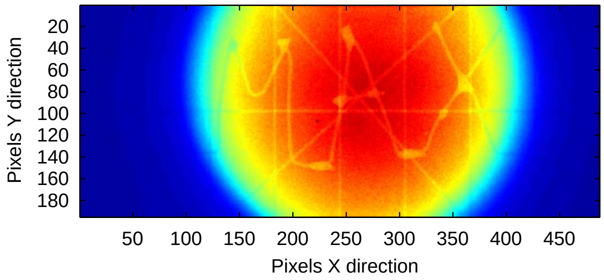

Fig. 4. Imaging the MAX stencil using Configuration C (Table 1) with aluminium cover on and without lead insert.

3.3. Temporal beam intensity profile

To obtain a temporal beam intensity profile over a typical 100 ms extraction period, the beam was imaged using Configuration D over approximately 20 000 injections, with one image taken per injection. Each of these exposures was triggered at time $(T_i + t)$ where T_i was the injection trigger pulse and t increased from 0 to 100 ms in 1 ms steps. This cycle was repeated 200 times in order to observe the beam profile over 50 min and the total photon count from each image for each step summed to form a temporal beam profile.

A tagged photon experiment running upstream provided summed data on number of events passing through their detector logic per millisecond of the 100 ms injection cycle. Their event rate is proportional to the number of photons incident on their target. Their data will be referred to as the Summed-Event Data [7].

The PILATUS temporal beam profile was then proportional to the Summed-Event Data multiplied by a constant. This constant can be seen to be dependent on ratio of detector acquisition time and focal-plane event acquisition time, provided that the acquisitions are taken simultaneously to account for changes in beam over time.

Fig. 6 compares the PILATUS-based temporal beam intensity profile with that obtained from Summed-Event Data. The profiles are in excellent agreement.

3.4. Beam alignment

In order to align the beam and test the viability of PILATUS as a real-time photon-beam monitor, the detector was placed 30 cm from the 19 mm cylindrical lead collimator and exposed to a photon beam from a 300 μm Al radiator (Configuration B). A continuous series of images of 1 s exposure time were taken and viewed. The

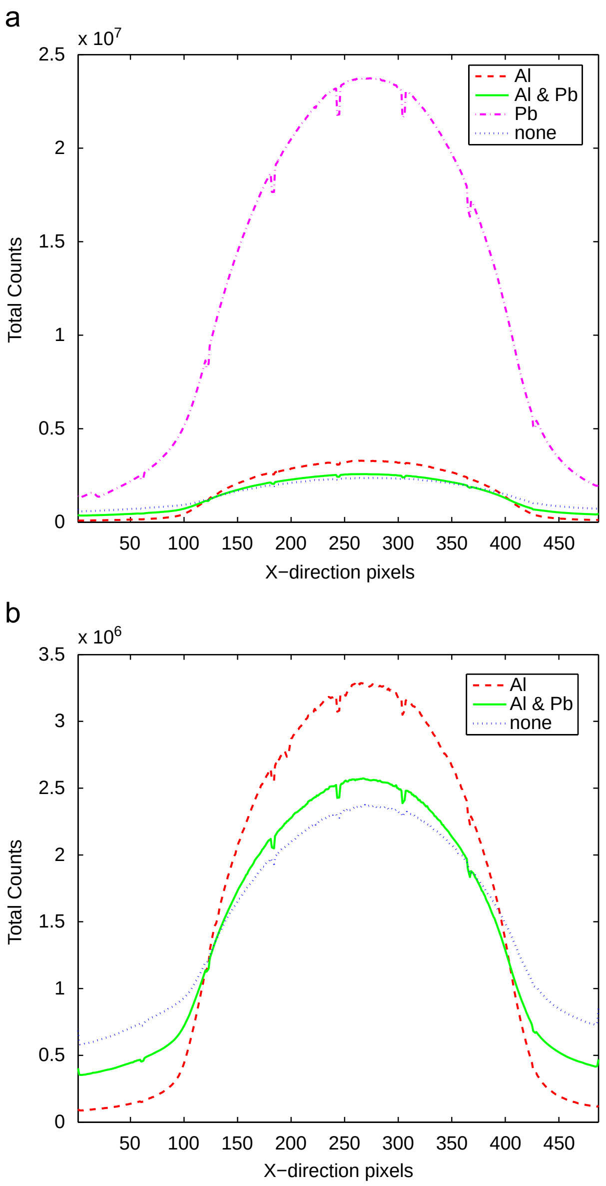

Fig. 5. Imaging with insertion of converters. Insertion of a 5 mm lead converter led to the greatest increase of photons in the PILATUS optimal energy range. Dips in the profiles are the result of string crosshairs further upstream. (a) Beam profiles through different converter configurations; (b) lower-count beam profiles from (a) replotted.

beam position was steered and the photon beam images observed in real time. Later processing of the images allowed centroid position to be plotted as a function of time. This processing would be straightforward to implement in real time. Any undesirable beam fluctuation could be identified and correlated with data-taking periods allowing, in principle, data correction to be made.

3.5. Bremsstrahlung radiators optimisation

The photon beam provided by six aluminium bremsstrahlung radiators with thicknesses of 3, 12.5, 25, 50, 150 and 300 µm was imaged. Images were taken in continuous 1 s acquisitions and the average number of photons detected averaged.

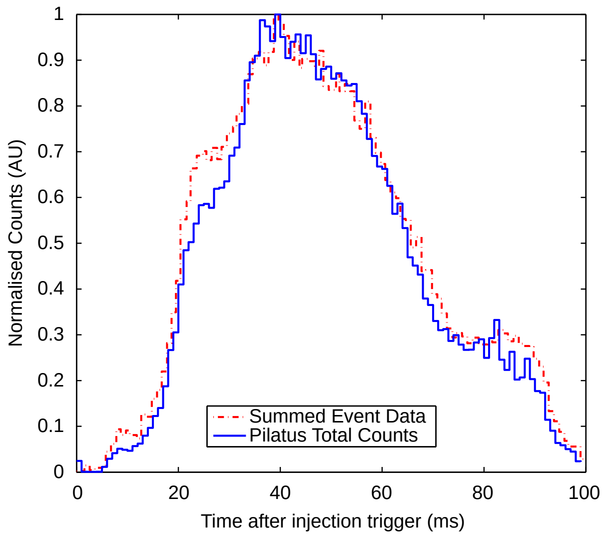

Fig. 6. Temporal beam intensity profiles from summed event data from an upstream experiment and PILATUS data. The upstream experiment plotted the sum of events accepted by their experimental set up (proportional to photon beam intensity) as a function of injection period. The PILATUS data plots total counts per 1 ms image as a function of time after injection. The profiles are in excellent agreement.

Table 2
Average counts through different thicknesses of aluminium radiator.

Al thickness (µm)	Average counts (10^6)	±
300	9.756	0.003
150	5.111	0.002
50	1.985	0.001
25	1.227	0.001
12.5	0.639	0.001

Experimental results show that a radiator of 300 µm Al yields the highest bremsstrahlung flux. This is in agreement with simulation conducted using G4beamline.

The average count intensity for each thickness is summarised in Table 2.

4. Conclusions

The measurements taken at MAX-lab demonstrate the utility of PILATUS in photon beam monitoring and diagnostics. The photon beam was successfully imaged in real time and fast visual steering was achieved. The temporal beam intensity profile obtained from PILATUS images closely matched results obtained from an existing experimental measure (Summed-Event Data from tagged photon experiment). The ability of PILATUS to image high-energy photons has been proven by obtaining images using converters and the detector's robustness was shown in its two week operation under high energy photon flux.

Acknowledgement

The authors would like to thank the Solander Program whose grant supported travel from Melbourne to Max-lab.

References

[1] H. Aoyagi, et al., Nucl. Instr. and Meth. A 467–468 (2001) 252.
[2] J. Krimmer, et al., Nucl. Instr. and Meth. A 481 (2002) 57.
[3] C. Brönnimann, et al., J. Synchrotron Radiat. 13 (2006) 120.
[4] A. Bergamaschi, et al., Experience and results from the 6 Megapixel PILATUS system, in: Proceedings of Science (Vertex 2007) 049.
[5] J. Berg, Beam monitor system for the 250 MeV photon beam at MAX-lab, MA Thesis, Lund University, Sweden, 2005.
[6] L.I. Schiff, Phys. Rev. 83 (1951) 252.
[7] L. Isaksson, et al., MAX-lab, Lund, Sweden, private communication.
[8] T.J. Roberts, et al., G4beamline Simulation program for matter dominated beamlines, in: Proceedings of the PAC07 THPAN103, Albuquerque, New Mexico, USA, 2007, p. 3968.

APAC 2007, Raja Ramanna Centre for Advanced Technology(RRCAT), Indore, India WEPMA060

MEASUREMENTS USING THE X-RAY AND OPTICAL DIAGNOSTIC BEAMLINES AT THE AUSTRALIAN SYNCHROTRON

M. J. Boland, J. Bergstrom, G. S. LeBlanc, Y.-R. E. Tan, R. Dowd and M. J. Spencer, Australian Synchrotron, Clayton, Victoria 3168, Australia.

D. J. Peake and R. P. Rassool, The University of Melbourne, Victoria 3010, Australia

Abstract

First Light has been achieved on the diagnostic beamlines at the Australian Synchrotron 3 GeV storage ring. The X-ray Diagnostic Beamline (XDB) has been used to measure the beam size, divergence and emittance, while the Optical Diagnostic Beamline (ODB) has been used the measure the bunch length and turn-by-turn stability. Both beamlines receive dipole radiation from a bend magnet and provide continuous diagnostic data to the control room. The beamlines compliment each other with the ODB providing mainly longitudinal (temporal) information, while the XDB measures predominantly transverse (spatial) information. A brief description is given of the equipment on each beamline and the commissioning results are presented.

X-RAY DIAGNOSTIC BEAMLINE

The x-ray diagnostic beamline provides mostly transverse beam information and is described in more detail in Ref [1]. Measurements made during the commissioning of the storage ring are presented here.

Image Array

A pinhole array generates 9 images of the bend magnet source point which is displayed in the control room via EPICS (see Fig. 1). The spots provide a qualitative as well as quantitative diagnostic of the status of the stored beam.

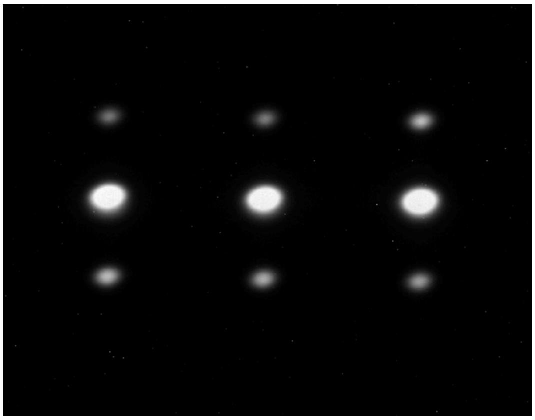

Figure 1: Array of beam spot images created by the x-ray pinhole array. The data is captured with a CCD camera viewing a YAG screen on the x-ray diagnostic beamline.

Beam Size and Emittance

The beam spot is measured from the YAG screen image and fitted with a Gaussian curve to obtain the horizontal and vertical beam sizes. The emittance was determined using the measured beam size and the beta-functions from the calibrated model that was fit using LOCO [2]. Fig. 2 shows the results of a measurement after the first correction to optics to remove beta-beating. The emittance of 17.5 nm is close to the design value of 15.8 nm for a lattice with zero dispersion in the straight sections.

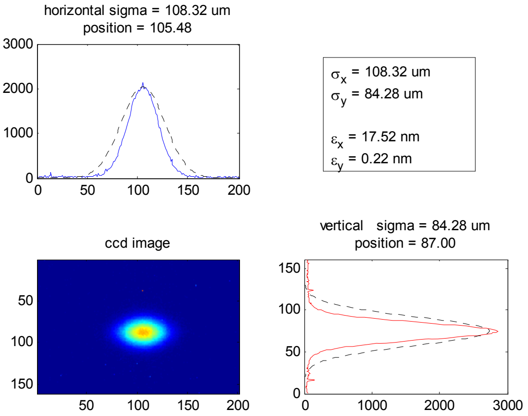

Figure 2: Emittance measurement from a single spot on the x-ray diagnostic beamline and beta-functions from a calibrated model.

Beam Stability

Using an EPICS driver to process the camera data from the Firewire CCD camera the x-ray beam centroid is monitored to track the beam stability. In order to get a good quality image the CCD integration time needs to be 50 ms or greater. With the CCD triggered at 1 Hz and a 50 ms integration time the beam stability is measured to be 2 μm rms.

Divergence

The multiple images from the pinhole array allows for divergence of the beam to be measured by fitting a Gaussian to the intensity distribution of the vertical beam spots. Fig. 3 shows the vertical profile and the Gaussian fit to the intensity distribution of the beam spot peaks.

The measurement is close to the $1/\gamma$ opening angle of 0.17 mrad.

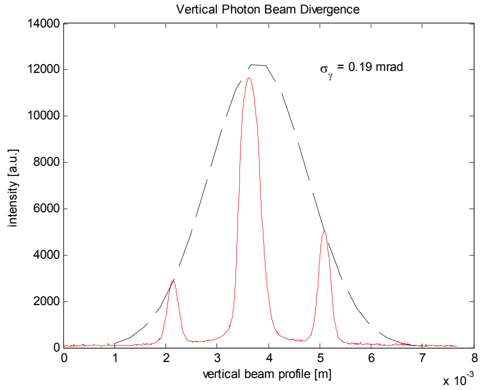

Figure 3: Vertical beam divergence measured by the x-ray pinhole array.

OPTICAL DIAGNOSTIC BEAMLINE

The optical diagnostic beamline provides mostly longitudinal beam information and is described in more detail in Ref. [1]. Results of the commissioning some of the optical instruments is presented here.

Dual Sweep Streak Camera

During the storage ring RF commissioning, the dual sweep streak camera was used to monitor the amplitude of the synchrotron oscillations while detuning the cavities. Fig. 4 shows the fast sweep on the vertical axis and the secondary sweep on the horizontal axis and the large amplitude synchrotron oscillation prior to detuning. After detuning the cavities there was no measurable amplitude modulation on the streak camera images.

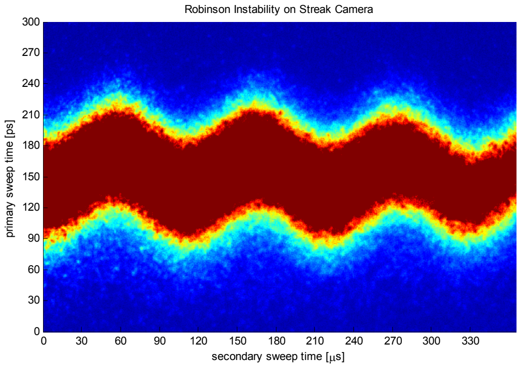

Figure 4: Dual Sweep Streak Camera image of a 9.19 kHz Robinson Instability during tuning of the storage ring RF cavities.

Beam Stability

A Position Sensitive Detector has been installed to measure the beam motion using visible light. A Hamamatsu S1300 2D photodiode connected to a C4757 controller board produces output voltages proportional to the horizontal and vertical beam position. The diode is biased by a PS2127 power supply from Oxford Electrical Products and has a stability of 1 mV RMS. The absolute position readout has not been calibrated since the beam is arbitrarily focused to as small a spot size as possible, but the frequency of the signal can be used to analyse the beam motion.

The voltage from the controller board it digitised using a Nation Instruments USB-6251 digitiser and LabView to EPICS software. Two different operational modes are used: slow and fast acquisition mode. In slow mode the systems outputs an average beam position at 1 Hz using a configurable number of samples and sample rate. This mode is used to monitor the long term stability of the beam. Using fast mode the system can output 1.4 MS/s with 16 bit resolution for up to 1.4 s to do more detailed analysis of transient beam motion.

Fig. 5 shows the beam motion during the RF commissioning when there was a large synchrotron oscillation due to the Robinson instability. The three plots of horizontal beam motion show some of the different ranges of data sampling that is possible with the system.

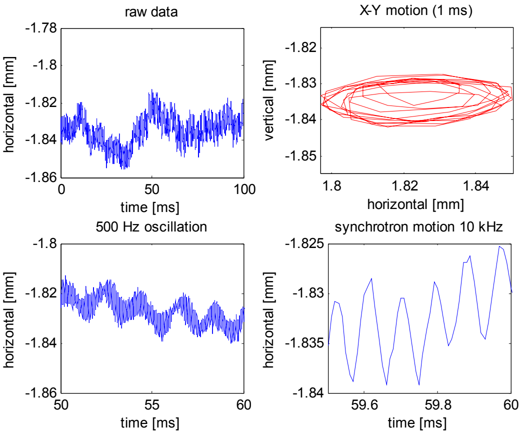

Figure 5: Beam stability measurements during RF cavity commissioning with a 2D position sensitive detector. At the maximum digitisation rate the synchrotron tune can be observed at approximately 10 kHz.

Bunch Length

During commissioning of the RF cavities, with only three of the four in operation, the storage ring was tested in single bunch mode. Using the streak camera the bunch length was measured while increasing the current in a single RF bucket. When the measurement was taken the cavities were still being conditioned and could not operate at full voltage. The theoretical bunch length at the design voltage is 22 ps, but with the commissioning settings a minimum bunch length of only 40 ps could be achieved.

Fig. 6 shows the bunch lengthening with increasing single bunch current as expected. The total current in one bunch was limited to 5 mA in this measurement as a precaution, but currents of up to 25 mA should be achievable in the future. More detailed studies will be conducted to determine the impedance of the vacuum chamber from the single bunch length, once the RF is fully operational.

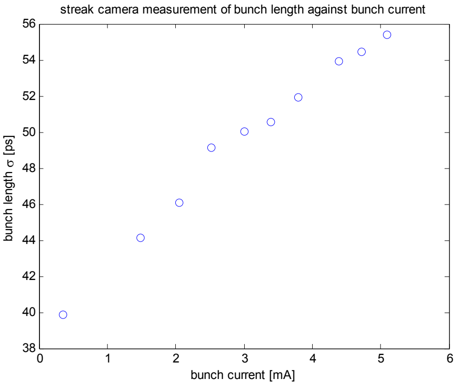

Figure 6: Bunch length measured by a streak camera for a range of single bunch currents.

Fill Pattern Monitor (FPM)

The electron bunch fill pattern in the storage ring is measured using an optical photodiode. The diode output is digitised and made available in EPICS. Fig. 7 shows a comparison between the FPM and a conventional measurement of the fill pattern using the signal from a stripline pickup on an oscilloscope. The measurements are in good agreement and the FPM is now in routine operation for controlling the filling of the storage ring.

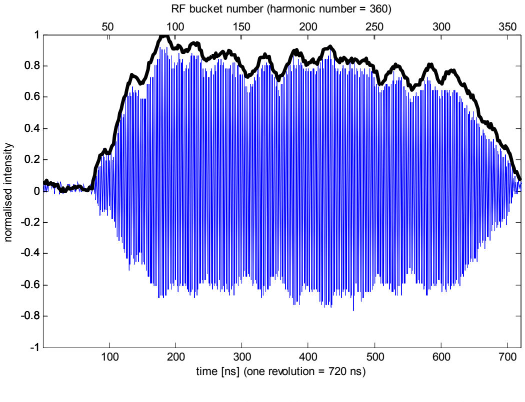

Figure 7: Comparison of the fill pattern measured on the optical monitor (thick black) and the stripline response on an oscilloscope (blue).

The system was sensitive down to less than 0.05 mA total current in the storage ring. Tests were also done with single bunch injection and the fill pattern was able to be flattened out and squared off. The fill pattern measurement was stable to less than 1 % of the maximum bunch current in an even fill, thus providing a reliable signal for injection efficiency and feedback systems. A system is under development using the FPM to provide automatic arbitrary pattern filling and can be used in a feedback loop for top up mode in the future.

SUMMARY

The diagnostic beamlines have been successfully commissioned and most of the instrumentation is now in routine operation. The x-ray diagnostic beamline has been providing stable and useful information from the first moment of stored beam in the storage ring. The optical diagnostic beamline has a powerful set of tools that have been used to tune the machine during commissioning and will be vital in the fine tuning required as we move into user operations in March 2007.

REFERENCES

[1] M. J. Boland et. al., EPAC 2006, Edinburgh, UK.
[2] J. Safranek et. al., EPAC 2002, Paris, France.

PRELIMINARY STUDIES FOR TOP-UP OPERATIONS AT THE AUSTRALIAN SYNCHROTRON

M.J. Boland, G.S. LeBlanc, Australian Synchrotron, Clayton, Victoria 3168 Australia
D.J. Peake, R.P Rassool, School of Physics, University of Melbourne, 3010, Australia

Abstract

The Australian Synchrotron is now a fully commissioned synchrotron light source providing beam for users [1]. With the facility now fully operational, the next major advancement in machine operations will be top-up mode. The advantages of running in a dynamic top-up mode are well documented by other third generation light sources (see for examples references [2, 3, 4]) ; in broad terms it leads to a better quality beam for some users, and better experimental results. An overview will be given of the top-up runs that have been conducted and the instrumentation that was used. It has been demonstrated that top-up operation is possible, however improvements in injection efficiency and beam stability during injection are required before this can become a routine mode of operation.

BACKGROUND

All contracts issued for construction of the Australian Synchrotron contained the requirement that the system delivered would not prevent top-up operation. However, there was no special requirements for the demonstration of top-up operation and it has not been specifically requested by the user community. Now that user runs are routinely conducted, it is time to look to the future possibilities of top-up operations. In order to demonstrate that top-up is feasible a machine studies run was successfully conducted but there are still improvements which need to be made before this can become a routine mode of operation.

REQUIREMENTS FOR TOP-UP

The main requirements for successful implementation of Top-Up Mode are:

- High injection efficiency,
- Low beam motion during injection,
- Good timing system and synchronization,
- Accurate diagnostic methods, especially real-time fill pattern measurements.

SQUARE-UP MODE

Experience with top-up mode at the SLS shows that it is important for beam stability to have an even fill pattern[5]. Pattern injection cannot provide the necessary fill pattern by itself. A dynamic top-up mode run after the initial fill can even out the fill pattern quickly and maintain an even pattern using periodic, intensity targeted injections. To monitor the fill pattern in real-time, a fill pattern monitor (FPM) on the optical diagnostic beamline is used[6]. The FPM provides an vector of emitted light intensities for the stored electron bunches. When the stored current is below a preset threshold, the designated “filled” RF buckets are sorted according to intensity and the bucket with the lowest measured emitted light intensity is chosen for injection. The protocol is repeated until the stored current is over the threshold. Figure 1 shows the resulting fill pattern after top-up operations. The standard deviation of the measured light intensity of the filled buckets drops dramatically when the top-up protocol is used to dynamical alter the fill pattern, as shown by Figure 2.

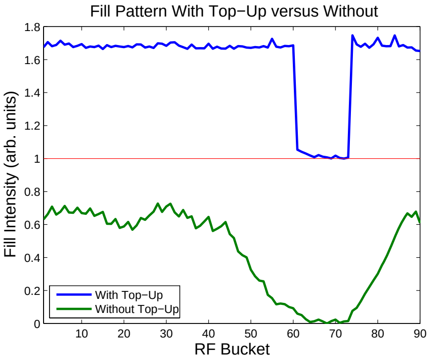

Figure 1: A sample pattern fill (lower graph), topped up and squared off using an intensity targeted injection protocol. The value of squared fill (upper graph) has been increased by 1.0 point for ease of comparison.

CAMSHAFT MODE

In camshaft mode, a single bucket in a region of empty buckets is chosen and filled to a higher current than the others (see Figure 3). Time resolved experiments can be gated using the single bucket, removing multi-bunch contributions to the experiment. Camshaft mode was successfully injected and measured using the FPM.

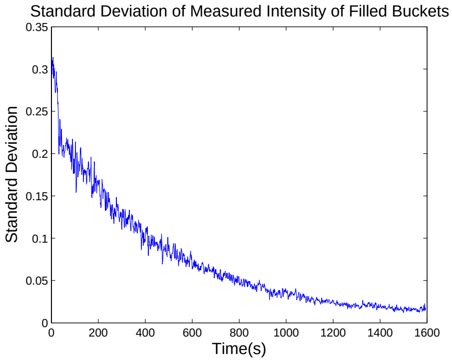

Figure 2: The standard deviation of the filled buckets over time during an intensity targeted dynamic top-up run.

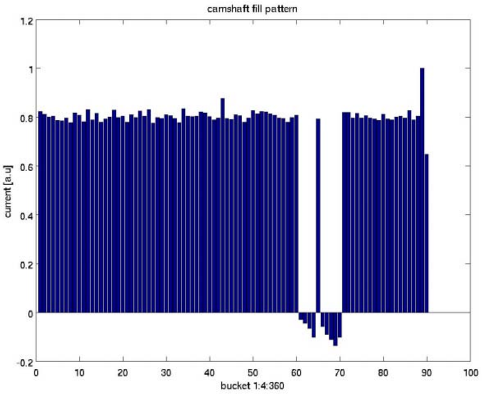

Figure 3: A successfully injected ”camshaft” fill pattern.

BUNCH PURITY

When users conduct time resolved experiments that are gated on a single high current bunch, the purity of this bunch is critical. With this in mind, a Bunch Purity Monitor (BPU) is being developed based on Reference [7]. Accurate bunch purity measurements require a diagnostic device with a high dynamic range. For the Australian Synchrotron, a Time-Correlated Single Photon Counting (TCSPC) system has been commissioned, using an avalanche photodiode (APD) and the Picoharp 300[8]. The Picoharp 300 uses a Time to Digital Converter (TDC) to measure the elapsed time between the start signal (the storage ring synchronization pulse) and the stop signal from the APD. The TDC then provides the digital timing value to address the built in histogrammer. Although this method provides a high dynamic range, in order to prevent pile-up in the measurements the synchrotron light must be heavily filtered and so the data acquisition must be taken over a time span of minutes to build up the histogram.

A preliminary bunch purity measurement has been made to test the BPU setup (see Figure 4). The acquisition time for this measurement was 10 minutes. A comparison between the BPU and the FPM is shown in Figure 5. Each of the result have been normalized to unity and the horizontal offset between the data sets have been removed. The mean absolute difference between the normalized values for the measured light intensities for each of the RF buckets is only 2.20%.

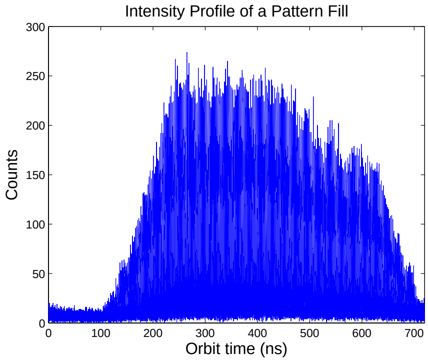

Figure 4: Stored electron beam intensity profile measured using the BPU setup.

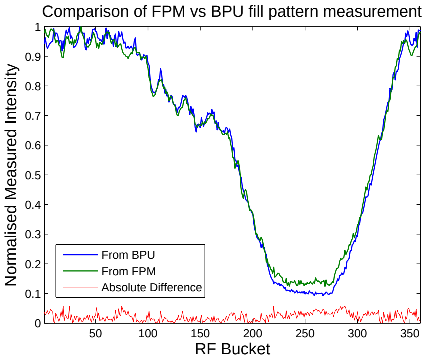

Figure 5: A comparison between the BPU and FPM on the measurement of fill pattern.

CONCLUSIONS

A dynamic Top-Up mode has been successfully designed and tested at the Australian Synchrotron. Using a real-time fill pattern measurement device, periodic targeted injections were used to square the fill. Preliminary bunch purity measurements have been undertaken using the newly commissioned bunch purity monitor and the initial results correlate well with the fill pattern monitor.

1-4244-0917-9/07/$25.00 ©2007 IEEE

REFERENCES

[1] A. Jackson, The Australian Synchrotron Project, In Proceedings of PAC2007.

[2] L. Emery *et al.*, Top-Up Operation Experience at the Advanced Photon Source, In Proceedings of PAC, 1999.

[3] B. Kalantari *et al.*, Enhancement of Top-Up Operation at the Swiss Light Source, In Proceedings of EPAC 2004.

[4] D. Robin *et al.* Plan to Upgrade the Advanced Light Source to Top-off Injection Operation, In Proceedings of EPAC 2004.

[5] B. Kalantari *et al.*, Bunch Pattern Control in Top-Up Mode at the Swiss Light Source. In Proceedings of EPAC 2004.

[6] M.J. Boland, X-ray and Optical Diagnostic Beamlines at the Australian Synchrotron Storage Ring, In Proceedings of EPAC 2006.

[7] C.A. Thomas *et al.*, Bunch Purity Measurement for Diamond, NIM A,566(2) 762766, October 2006.

[8] Picoquant, http://www.picoquant.com .

1-4244-0917-9/07/$25.00 ©2007 IEEE

GROWTH/DAMP MEASUREMENTS AND BUNCH-BY-BUNCH DIAGNOSTICS ON THE AUSTRALIAN SYNCHROTRON STORAGE RING

D. J. Peake and R. P. Rassool, University of Melbourne, 3010, Australia
M. J. Boland and G. S. LeBlanc, Australian Synchrotron, Clayton 3168, Australia

Abstract

Recently a transverse bunch-by-bunch feedback system was commissioned to combat the resistive-wall instability in the storage ring. Presently the instability is being controlled by increasing the vertical chromaticity but new diagnostic tools have been developed to characterise the instability under different machine configurations in order to tune the feedback system for future user operation. The FPGA that comes with the feedback system also provides powerful possibilities for diagnostic measurements. Results will be presented for growth/damp measurements to quantitatively characterise instability growth rates and bunch-by-bunch diagnostics such as tune.

INTRODUCTION

The Australian Synchrotron storage ring now has 3 IVU IDs of approximately 6 mm minimum gap installed, which has reduced the beam current threshold for resistive wall instabilities in the vertical plane to below the maximum user beam current of 200 mA. The instability has been charaterised in Ref. [2, 3] and Figure 1 shows the vertical beam blow up effect measured on the x-ray diagnostic beamline. The instability is presently being controlled during user operations by increasing the vertical chromaticity to 11.

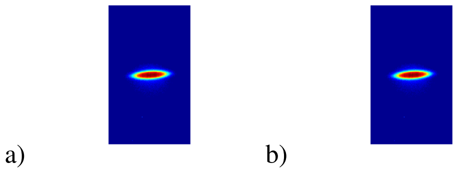

Figure 1: X-ray beam spot with vertical feedback in a) open and b) closed loop.

A transverse bunch-by-bunch feedback system (BBB) was designed and commissioned for the Australian Synchrotron electron storage ring, the details of which have been reported previously [1]. Figure 1 shows the x-ray beamspot succesfully damped vertically once the loop was closed on the BBB after phasing and timing the frontend, FIR filters and kicker amplifiers. This result shows the system works in principle, however the commissioning phase did not include charaterising the system and tuning it for user operation. Since the hardware commissioning, diagnostic software has been developed to monitor the beam which will enabled the characterisation and optimisation the system for stable user operation. The initial results of system characterisation with beam are presented here.

EXPERIMENTAL SETUP

Storage Ring Fill Pattern

The storage ring was set to a chromaticity of $\xi_x = 3$ and $\xi_y = 0.6$ and using the fill pattern feedback injection [4] a square fill pattern was injected. The instability threshold current was gradually approached using two methods: i) keeping a fixed bunch current and increasing the number of bunches, and ii) keeping the number of bunches fixed and increasing the bunch current. Using this technique the instability threshold could be reached in a controlled and reproducible way. It was found experimentally that by filling 155 of the 360 RF buckets with 0.39 (± 0.02 mA or 5% bunch current variation) the instability would blow the beam up vertically without losing beam (see Figure 1). By sitting right at the threshold it was possible to test the BBB feedback by adjusting many parameters. With 154 buckets filled there were no signs of the instability but while injecting the $155\mathrm{th}$ the instability developed. When the BBB feedback was in closed loop and a parameter change removed the damping, sometimes bucket 155 alone was kicked out of the ring.

Growth/Damp Measurement

Growth/Damp measurements were performed once the BBB was in closed loop mode by turning off and then back on the FIR filters as shown in the schematic in Figure 2.

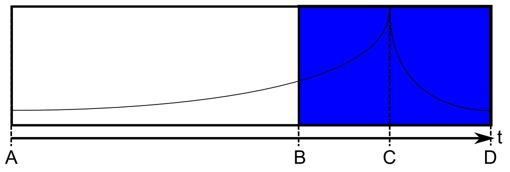

Figure 2: The timing graph for the grow damp measurements. A: Stop feedback, B: Start Data Acquisition, C: Restore feedback, D: Readout DAQ buffer.

The delay time between turing the filters off and on was adjusted to achieve a large peak in the ADC measuring the bunch position. The instability could not grow too large so the that beam could be damped within the maximum acquisition time of the FPGA (22 ms). A typical growth/damp data set is shown in Figure .

Using this technology the final phase adjustment on the filter before the DAC output was tuned to maximise the

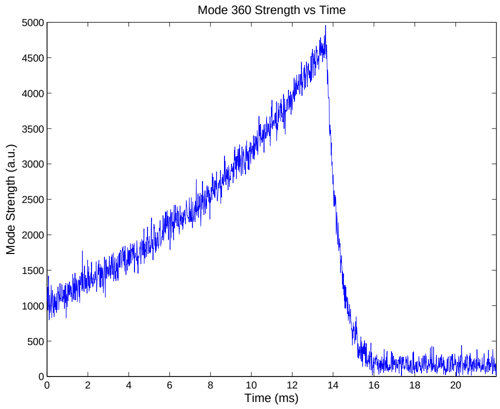

Figure 3: An example growth and damping cycle of mode 360.

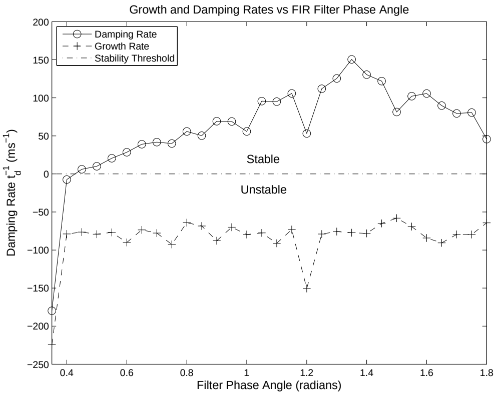

Figure 4: Mode 360 damping rate versus the Finite Impulse Response Filter Angle. It is important that the final corrective pulse placed onto the beam by the kickers is a sinusoid phase shifted by π radians from the beam motion at the kickers.

damping rate. Figure 4 shows the phase angle scan and measured growth and damp rates. As expected the growth rate remained constant as the nature of the instability did not change, however the damping rate varied as the feedback was moved in and out of phase.

A test of the kicker amplifier performance was also conducted to see if the system was saturating. The damp rate was measured while the gain was varied from the minimum to the maximum value. As shown in Figure 5 the damping rate increased smoothly right to the maximum gain, indicating there was no saturation in the system.

Current Dependence

The growth rate of the instability was mapped out with increasing current at two different settings of the vertical chromaticity. Figure 6 shows that the growth rate increases with bunch current and decreases with higher chromaticity settings. This type of data will be used to predict the condition under which the BBB system can stabilise the beam for user runs.

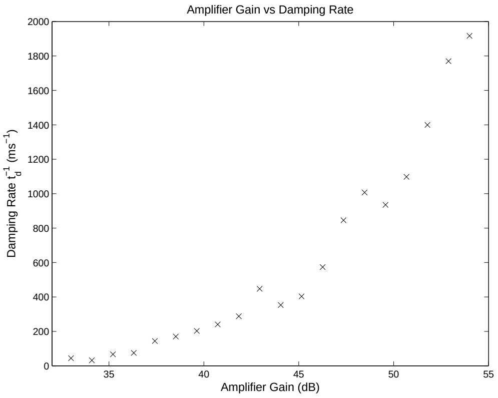

Figure 5: Mode 360 Damping Rate vs Amplifier Gain. The total beam current is 80 mA, evenly filled into 155/360 buckets.

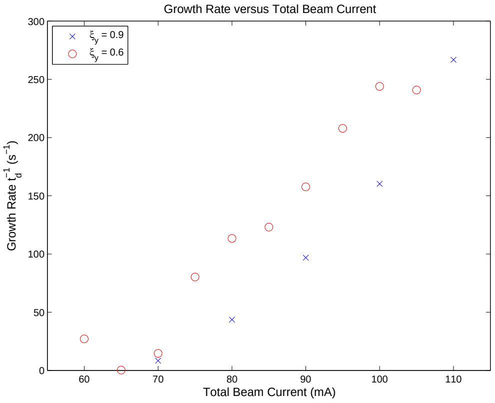

Figure 6: Mode 360 growth rate versus current, for vertical chromaticities of 0.9 and 0.6.

Mode Analysis

Coupled bunch instabilities are characterised by a coherent movement between the bunches, usually coupled through a wake field. Each bunch still oscillates at the tune frequency, but there is a phase difference between bunches given by:

$$\Delta\Phi = m\frac{2\pi}{M} \tag{1}$$

where M is the number of bunches, and m is the mode number. In the frequency realm, these phase differences can be measured as sidebands of the revolution frequency.

$$\omega = p\,\omega_{rf} \pm (m + \nu)\omega_0 \tag{2}$$

where p is an integer, ω_{rf} is the frequency of the storage ring RF cavities, m is the mode number, ν is the tune and w_0 is the revolution frequency.

By taking an FFT across the bunch dimension (length M) the modal growth can be plotted versus time. The modal damping rate is especially important as it can highlight problems in the tuning of the feedback system. A slight mistune in the placement of the corrective kicker pulse onto the beam may not be seen in low order modes, since the phase change between two bunches will be quite small (as shown in Equation 1). Higher order modes are more sensitive to the damping signal phase changes, as the phase change between bunches will approach 180° so a pulse intended to damp bunch N will excite bunch $N + 1$.

The measured mode strengths are shown in Figure for both open and closed loop, demonstrating that the BBB system is effectively suppressing the modes excited by the vertical instability.

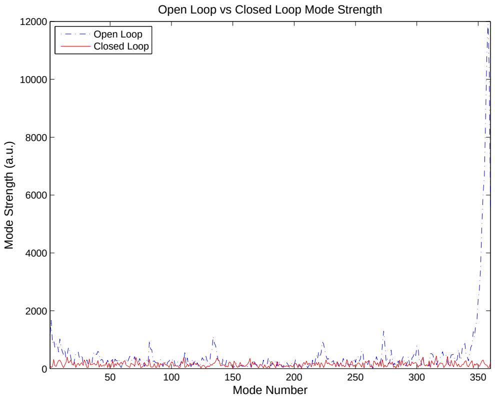

Figure 7: Open loop versus closed loop mode strength.

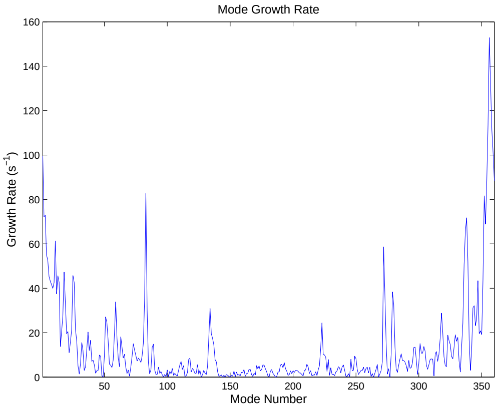

Figure 8: The median growth rate for each mode, taken from 30 grow/damp measurements.

A growth rate (τ_G^{-1}) of 109 ms^{-1} was measured for mode 360 which corresponds to a growth time of 9.2 ms. Vertical radiative damping has been calculated to be 4.82 ms based on a model of the ring lattice.

BEAM DIAGNOSTICS

By taking an FFT along the time access of each bunch a spectrum like the one shown in Figure 9 is obtained which allows for a tune measurement of each bunch individually. At the moment, growdamp measurements are used to provide the necessary amplitude in the position space to measure the tune, but in the future single bunch excitation of a stable beam could be used to provide continuous tune measurements.

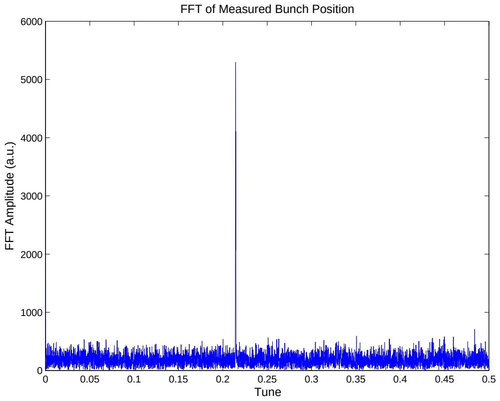

Figure 9: Single bunch FFT measurement during a grow/damp measurement. The peak shown is at the storage ring vertical tune of 0.2147.

CONCLUSION

Diagnostics to tune and optimise the transverse Bunch-By-Bunch feedback system have been developed for the Australian Synchrotron storage ring. Initially they have been used to perform growth/damp measurements in order to characterise observed vertical resistive-wall instability. Studies of beam parameters such as tune and mode dependant instability growth rates have been performed. These techniques will be used to bring the feedback system in to stable operation for user runs in the future.

REFERENCES

[1] M. J. Spencer, G. Leblanc and K. Zingre, Design and Commissioning of a Bunch by Bunch Feedback System for The Australian Synchrotron, Proc. EPAC, 2008.

[2] R. Dowd, M. Boland, G. LeBlanc, M. Spencer, E. Tan, J. Byrd and F. Sannibale, Measurements of impedance and beam instabilities at the Australian Synchrotron, Proc. PAC, 3859-3861, 2007.

[3] R. Dowd, M.J. Boland, G.S. LeBlanc, M.J. Spencer, Y.-R.E. Tan, Single Bunch Studies at the Australian Synchrotron, Proc. EPAC, 2008.

[4] D. J. Peake, M. J. Boland, G. S. LeBlanc, R. P. Rassool, Measurement of the real time fill-pattern at the Australian Synchrotron, NIM-A, 589, 143-149, 2008.

Time Resolved Detectors and Measurements for Accelerators and Beamlines at the Australian Synchrotron

M. J. Boland*,†, R. P. Rassool†, G. S. LeBlanc*, D.J. Peake†, B.A. Sobott†, V. Lee†,
A. Schubert† and N. Kirby*

**The Australian Synchrotron, Clayton, Victoria 3168, Australia*
†School of Physics, The University of Melbourne, Parkville, Victoria 3010, Australia

Abstract.
Time resolved experiments require precision timing equipment and careful configuration of the machine and the beamline. The Australian Synchrotron has a state of the art timing system that allows flexible, real-time control of the machine and beamline timing parameters to target specific electron bunches. Results from a proof-of-principle measurement with a pulsed laser and a streak camera on the optical diagnostic beamline will be presented. The timing system was also used to fast trigger the PILATUS detector on an x-ray beamline to measure the fill pattern dependent effects of the detector. PILATUS was able to coarsely measure the fill pattern in the storage ring which implies that fill pattern intensity variations need to be corrected for when using the detector in this mode.

Keywords: Australian Synchrotron, time-resolved measurements, PILATUS, x-ray detectors, pump-probe measurement, fill-pattern
PACS: 29.20.dk, 07.85.Qe, 07.85.Fv

INTRODUCTION

At the present suite of beamlines at the Australian Synchrotron, only the Accelerator Physics Optical Diagnostic Beamline (ODB) on 7BM1 performs time resolved measurements. In collaboration with the Experimental Particle Physics Group at The University of Melbourne and the SAX/WAX beamline at the Australian Synchrotron, some proof-of-principle measurements have been conducted to test the readiness of the machine and the beamlines for time resolved experiments. New measurements were successfully made on the ODB and SAX/WAX beamlines that demonstrate the timing accuracy and detector gating abilities of these beamlines. The ODB measurement in the visible spectrum demonstrated the timing of a pulsed laser with a single bunch in the storage ring, a technique which could be used on an x-ray beamline for a pump-probe type measurement. The PILATUS II measurements used 10 keV x-rays from the SAX/WAX beamline to test the performance of the fast gating mode and its sensitivity to certain bunch fill patterns in the storage ring.

ODB MEASUREMENTS

For the ODB measurements, a camshaft fill pattern was injected into the storage ring with a 2 mA single bunch in the gap. The fill pattern control is descried in Ref. [1]. The ODB has an *Event Receiver* [2] (EVR) VME module which is synchronised with the accelerator timing system. A 500 MHz reconstructed RF signal from the EVR was used as in input to a streak camera synchroscan unit and phased so the odd and even bunches were combined (See long streak in the top of Fig. 1). 1 Hz signals from the EVR were then used to trigger both a pulsed laser and the secondary sweep unit on the streak camera. The delay on the laser trigger was adjusted so the laser pulse (bottom right stripe in Fig. 1) appeared just prior to the camshaft single bunch (top right stripe in Fig. 1). The streak camera has a 2 ps timing resolution and the laser pulse has a 3 ps timing jitter.

This configuration of the storage ring and the ODB timing demonstrates that in principle an x-ray beamline could use this technique on a sample, instead of the streak camera, and make pump-probe type measurements.

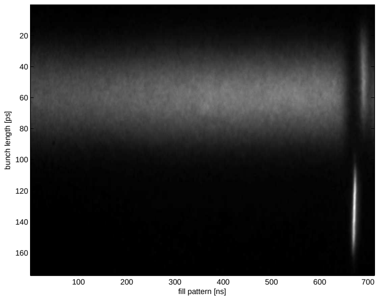

FIGURE 1. Laser pulse synchronised with a single bunch in camshaft fill pattern in the storage ring captured with a streak camera at the Optical Diagnostic Beamline.

SAX/WAX MEASUREMENTS

PILATUS Fast Timing

The PILATUS detector is a single photon counting hybrid pixel detector designed for use at X-ray energies of 3-30 keV, with a quantum efficiency of 99% at 8 keV. It has a readout time of 2.7 ms and a framing rate of 300 Hz. Detailed descriptions of the PILATUS detector systems can be found in [3].

Fill Pattern Tests

Standard Fill Pattern

The storage ring at the Australian Synchrotron has a harmonic number of 360, a revolution period of 720.5 ns and RF buckets of 2 ns wide [4]. In standard operation 330 sequential buckets out of 360 buckets are filled to a stored current of 200 mA. This decays to approximately 160 mA over a 12 hour period after which re-injection occurs. The fill pattern is monitored using the Fill Pattern Monitor which is based on acquisition of signal from visible synchrotron radiation incident on an ultra-fast MSM photodiode [1].

The PILATUS 100K detector was placed in a focused 10 keV beam on the SAX/WAX beamline. The incident flux was moderated using slits and aluminium attenuators. A storage ring orbit clock (SROC) signal that is synchronised with the electron bunch train was supplied the from by the EVR on the SAX/WAX beamline. Using the EVR the SROC was divided by 10 to derive a 139 kHz gating trigger for the PILATUS detector. The width and delay relative to the bunch train were again controlled using the EVR module.

The EVR internal 125 MHz clock provides for delays and pulse widths to the trigger in 8 ns steps. The gate to PILATUS was adjusted from $16-48$ ns in width and $0-2000$ ns in delay time to scan across the fill pattern in photon counting mode. Figure 2 shows the integrated counts at gate each delay for four different gate widths and each scan does a good job of reproducing the known fill pattern as measured on the ODB (right plot in Fig. 2). The storage ring orbit period is 720.5 ns, so almost three periods of the longitudinal x-ray profile are captured.

The results in Figure 2 are based on standard detector operation settings – medium gain ($V_{\mathrm{rf}} = -0.2$ V). The gain was lowered ($V_{\mathrm{rf}} = -0.3$ V) to reduce pulse length, resulting in faster signal acquisition. The measured intensities are compared to the fill pattern as obtained from the FPM (See right plot in Figure 2). A reduction in total count intensity between fast and standard settings can be seen and this is due to a constant discriminator setting. The fast setting results show a narrower waveform, and a greater peak to valley ratio (≈10% improvement) for the fluctuation at 550 ns - 700 ns as shown by the FPM. Importantly, the results for faster settings show troughs reaching zero counts where the storage ring buckets were empty.

The fill pattern was then modified from standard fill pattern to a squared fill (See References [1, 5] for more detail on fill patterns), filling 80 out of the total 360 available buckets. Figure 4 shows the PILATUS results and the fill pattern as acquired from the FPM; they compare favourably. The reduction in intensity for the PILATUS results for the 80 bunch fill can be attributed to a reduction in beam current. The two FPM results have been normalised and their relative intensities can not be directly compared- they are shown on the same plot for ease.

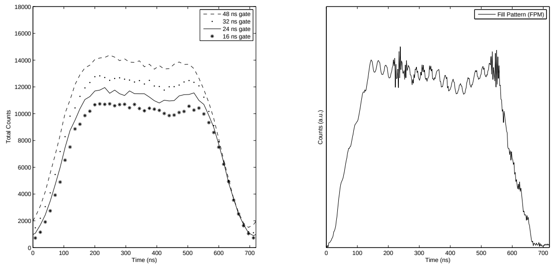

FIGURE 2. Integrated Counts vs Time (8 ns bins). The detector's active counting time was controlled by a gate from the event receiver of fixed widths: 48 ns, 32 ns, 24 ns and 16 ns. As expected, the total integrated counts per image rises with gate width.

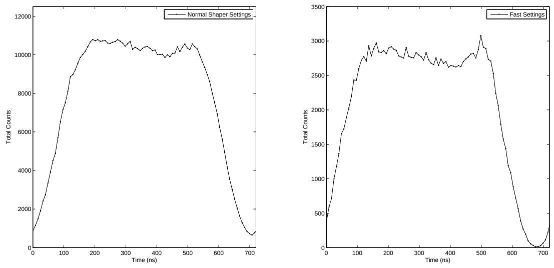

FIGURE 3. Comparison of shaping time settings: normal and fast shaping.

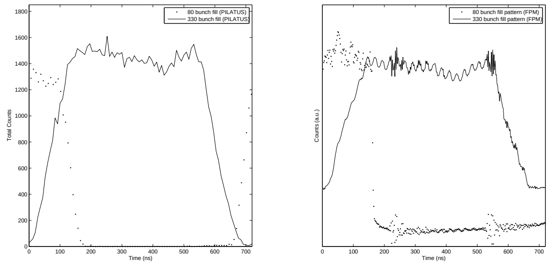

FIGURE 4. Standard Fill and 80 Bunch Fill for PILATUS and from the Fill Pattern Monitor (FPM).

Novel Fill

The fill pattern was further modified to contain a single bunch in bucket 221, 80 bunches plus one bunch. Measurements with 80 bunches + 3 bunches (in buckets 220, 221 and 222) were also performed. The results are compared in Figure 5. It can be seen that in the PILATUS measurements, the three bunch pattern is distinguished from the one bunch pattern by greater measured counts, even though they can not resolve a single bunch.

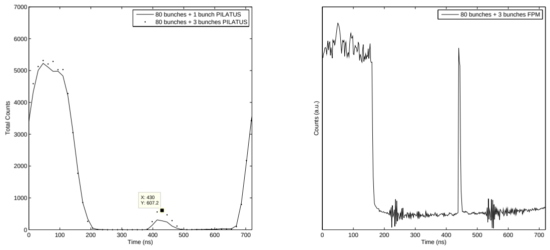

FIGURE 5. 80 bunches plus 1 bunch and 80 bunches plus 3 bunches. The 80 plus 3 bunches data has been normalised to match the 80 bunch region of the 80 plus 1 data.

Single Bunch Fill

Finally a 5 single-bunch fill pattern was used for measurements. Data sets were taken for gate widths of 16 ns and 40 ns. A run was also conducted with an increasing gate width (no delay) from 0 – 1432 ns. Results are shown in Figure 6. The 16 ns gate width data shows peaks with smaller Full Width Half Maximum as expected (≈64 ns versus ≈88 ns), as well as troughs which approach zero counts, closer to the known fill pattern. The 40 ns gate width data shows more counts in each frame as expected due to the longer active counting period.

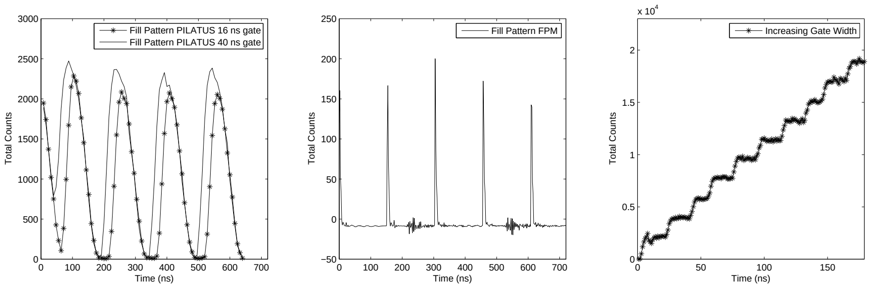

FIGURE 6. Five single bunch fill. Single bunches injected into buckets: 1, 77 153, 229 and 305. The third plot shows the intensity profile when widening the gate from 0 ns to 1432 ns. As expected, the counts increase with time, plateauing as it falls off each bunch in the temporal profile. Note that the third plot shows results over two orbits.

CONCLUSIONS

The proof-of-principle experiments conducted on the visible ODB and x-ray SAX/WAX beamlines demonstrate the ability to conduct time resolved measurements at the Australian Synchrotron. The ODB measurements demonstrate the ability to configure the accelerator to perform pump-probe type experiments, while the PILATUS measurements reveal the time structure of the storage ring fill pattern needs to be accounted for when in fast trigger mode.

REFERENCES

1. D. J. Peake et. al., *Nucl. Instrum. Meth. A* **589**:2 143-149 (2008).
2. Micro-Research Finland Oy, `http://www.mrf.fi`.
3. Ch. Broennimann et. al., *Journal of Synch. Rad.* **13** 120-130 (2006).
4. J.W. Boldeman and D. Einfield, *Nucl. Instrum. Meth. A* **521** 306-317 (2004).
5. M. J. Boland et. al., *Preliminary studies for top-up operations at the Australian Synchrotron*, Proc. PAC Particle Accelerator Conference, ISBN 1-4244-0917-9, pp. 3856-3858 (2007).

PRELIMINARY OPERATIONAL EXPERIENCES OF A BUNCH-BY-BUNCH TRANSVERSE FEEDBACK SYSTEM AT THE AUSTRALIAN SYNCHROTRON

D.J. Peake, R.P. Rassool, The University of Melbourne, Victoria, Australia
M.J. Boland, R. Dowd, Y.-R. E. Tan, Australian Synchrotron, Clayton, Victoria, Australia

Abstract

The Australian Synchrotron storage ring has a high resistive wall impedance in the vertical plane. Presently the instability from this impedance is being controlled by increasing the vertical chromaticity. However new in-vacuum insertion devices that significantly increase the ring impedance will demand chromatic corrections beyond the capabilities of the sextupole magnets. A transverse bunch-by-bunch (BBB) feedback system has been commissioned to combat the vertical instability and provide beam diagnostics. A high frequency narrow band mode that could not be damped was initially encountered with IVUs at specific gaps preventing the system from being implemented during user beam. Study into the lattice has lead to a configuration of the sextupoles that can be used for user operations.

INTRODUCTION

The Australian Synchrotron (AS) is a 3rd generation light source situated in Melbourne, Australia. An overview of the design can be found in Reference [1]. The storage ring is 216 m in circumference and operates at an RF frequency of 500 MHz. There are currently 9 operational beamlines with three of these relying on small-gap in-vacuum undulators (IVU). The introduction of more insertion devices will increase the impedance of the ring and so a plan has been made to increase the damping capabilities of the ring with an active feedback system.

TRANSVERSE BUNCH-BY-BUNCH FEEDBACK

In modern third-generation synchrotron storage rings coupled-bunch instabilities can place a limitation on the maximum stored current. As the stored current approaches this threshold, the growth rate of the instability overcomes the natural damping of the ring and the beam will increase in effective emmittance. Figure 1 shows how dramatic this effect can be on the beam. Normally this is controlled by increasing the chromaticity of the lattice such that the effective impedance of the ring is reduced. The effectiveness of this approach is limited by the available strength of sextupole magnets and the growth rate of the instabilities.

At the Australian Synchrotron the standard user lattice operates at a chromaticity of $[\xi_x, \xi_y] = [3, 11]$ in order to store our nominal current of 200 mA with a full range of insertion device gaps.

With more insertion devices planned for the ring, the instabilities may grow beyond our ability to control them purely using sextupole magnets. Another approach is available to add additional damping to the ring in the form of an active bunch-by-bunch feedback system.

An active feedback system has been designed and commissioned at the Australian Synchrotron to combat coupled-bunch instabilities, and has been described in detail in Reference [2]. It consists of a set of button-style Beam Position Monitors (BPMs) connected to a set of RF hybrids to provide an X and Y coordinate for each bunch. After passing through an ITech Libera analogue front end, a set of ADCs are used to sample the beam position over time and an FPGA calculates a corrective signal using a Finite Impulse Response filter (FIR). The signal is then fed into a DAC and placed onto the beam using a set of differential stripline kickers. The digital functionality (ADC, FPGA and DAC) is provided by an ITech Libera Bunch-By-Bunch system, running a combination of ITech and in-house developed code.

In this way we have both the pickup and actuator built into a closed loop system where an increase in the movement of a bunch causes the increase in the strength of the corrective waveform.

Initially the system was successful in damping the resistive wall instabilities that would prevent storage of the nominal 200 mA of current even without the IVUs inserted. Storage of 200 mA without IVUs was successfully completed at a chromaticity of [2,2]. Efforts to control the instabilities with the IVUs in was hampered by the discov-

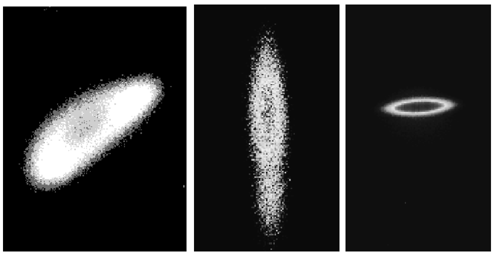

(a) Both horizontal and vertical instabilities (b) Vertical instability (c) Stable Beam

Figure 1: Some examples of the effect a coupled bunch instability can have on the transverse profile of the beam, as measured by the X-ray Diagnostic Beamline (XDB). From left to right the plots show: a) BBB off b) horizontal BBB active and c) both BBB systems active.

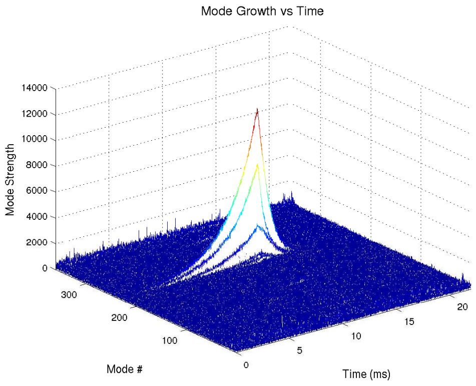

Figure 2: A grow/damp measurement showing the strong growth rate of a resonator centered about mode 228 (of 360). This instabilities shows up only at discrete low IVU gaps (6.8 mm for example).

ery of a strong narrow-band resonator impedance at discrete low IVU gaps (6.8 mm for example). The resonator would appear and disappear with a movement of 100 μm and is believed to be caused by the flexible IVU tapers providing the transition between the beampipe and the copper wakeshields. Initial FEM analysis of the tapers has not shown any resonant modes but further study into this is planned.

Figure 2 shows the growth of the resonator at mode 228 (of 360) which is far stronger than the resistive wall instability growth rates (described in more detail in [3]).

Horizontal tune sidebands had been measured in the vertical data during the resonator growths, so the horizontal BBB system was comissioned as well, as initially the focus had been on vertical instabilities. It was also discovered that lowering the harmonic sextupole strength with the chromatic sextupole strength reduced the growth rate of the resonator instability.

The system now has been shown to be effective at increasing the effective damping of the lattice, allowing operations at a reduced chromaticity of $[\xi_x, \xi_y] = [4, 2]$, at all IVU gaps.

USER OPERATIONS

Long-term Test

If the BBB feedback system is going to be used during user beamtime then it must be shown to be stable over a long time period. During a machine studies period, a low chromaticity lattice was used to test the BBB system for stability. The beam was injected to 150 mA and allowed to decay over an 8 hour period. Figure 3 shows the result of the test.

Successful operation of the BBB system allowed for in increase in both vertical and horizontal dynamic aperture, though the IVUs impose a smaller physical aperture in the vertical. In spite of this, the increase in horizontal dynamic aperture allowed for a 10% (40 to 44 hrs) increase in lifetime with IVUs at minimum gaps (IVU03/IVU13 at 6.60 mm and IVU05 at 6.06 mm). With no step losses or increased loss of the beam, the system is stable for an extended period of time. Studies need to be conducted with realistic movement of insertion devices similar to standard experimental settings, but the IVUs have been scanned at all gaps independently with no instabilities seen.

Bunch Cleaning

Many light sources worldwide are becoming increasingly interested in controlling the bunch purity of their fill patterns, with a long bunch train for regular experiments and a single high current “camshaft” bunch for pump-probe measurements. It is important to maintain a high bunch purity in order to prevent parasite bunches producing X-rays which interact with the sample before the pump measurement. At the Australian Synchrotron, the injection system is capable of targeting single buckets during injection [4], but a variety of conditions during injection can lead to a higher than desired electron population in neighbouring buckets.

A technique known as bunch cleaning [5] can be employed to force unwanted bunches to exit the beampipe while keeping the bunches needed for experiments. Using software designed for the FPGA within the BBB system, the unwanted bunches are excited at a harmonic of the vertical tune frequency while the wanted bunches receive the standard corrective waveform. The motion of the excited bunches is increased beyond the acceptance of the ring and they are lost. To increase the speed of loss, a set of vertical scrapers are brought to within ±2mm of stable beam.

Figure 4 shows the evolution of the fill pattern as the bunch cleaning signal is used to keep bunch number 40 to 350 and the single bunch at position 359. A high dynamic range device modelled after the bunch purity device con-

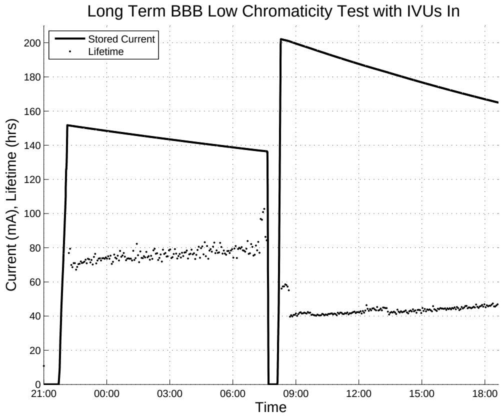

Figure 3: The results of a long term test of the BBB feedback system. Machine studies shifted to user time at 08:00.

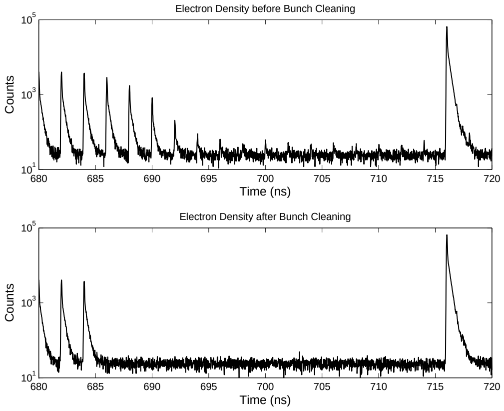

Figure 4: The effect of bunch cleaning on electron density. A high dynamic range detection system, the Bunch Purity Monitor, was used to measure statistical distribution of electrons in the ring.

	Parasite Bunch	Main Bunch	Purity
Before	108	568659	2×10^{-4}
After	2	567990	3.5×10^{-6}

Table 1: Change in integrated counts for the main bunch and parasite bunch during bunch cleaning. Data taken directly from Figure 4 after a background subtraction of 32 counts per histogram bin.

structed at Diamond [6] called the Bunch Purity Monitor was used to measure the distribution of electrons within the ring. The initial fill was injected using a "pattern fill" with a long bunch train from the injection chain. This leads to the parasitic bunches seen between the regular fill and single bunch. Parasitic bunches such as these will produce synchrotron radiation at times not intended for the experiment.

Initial results with bunch cleaning (shown in Figure 4 and Table 1) show promising results, with the purity for a high-current single bunch increasing from 2×10^{-4} to 3.5×10^{-6}.

Harmonic Sextupole Scan

In order to control the chromaticity within the ring, the AS lattice has two families of chromatic sextupoles (SDB and SFB). Increasing the strength of the chromatic sextupoles reduces the dynamic aperture of the ring, so to recover some of the aperture two families of harmonic sextupoles are used (SDA and SFA).

To optimize settings, the SDA and SFA families were scanned in strength and the lifetime of each lattice measured. A single bunch of 10 mA was injected into the ring to maximise DCCT response, allowing for a more accurate lifetime measurement.

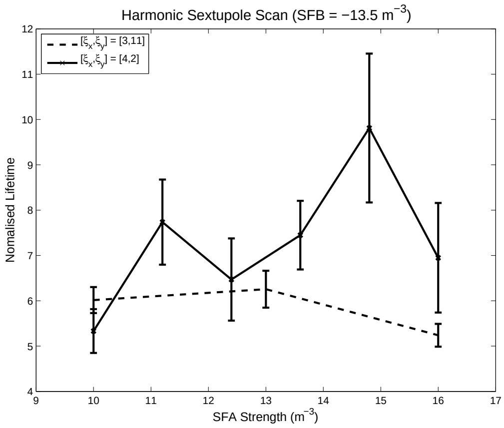

Figure 5: A scan of harmonic sextupole strengths versus lifetime. The scan was done with the chromaticity set to $[\xi_x, \xi_y] = [4, 2]$ and a 10 mA single bunch. The increase in lifetime from 6.2 hours to 9.8 hours is due to an increase in dynamic aperture.

Figure 5 shows that careful selection of sextupole strengths allow for an increase in lifetime from 6.2 hours to 9.8 hours for a single 10 mA bunch at low chromaticity.

CONCLUSION AND FURTHER WORK

The bunch-by-bunch transverse feedback system for the Australian Synchrotron storage ring has been successfully commissioned. It has increased the damping of the ring, allowing a reduction in chromaticity from $[\xi_x, \xi_y] = [3, 11]$ to $[\xi_x, \xi_y] = [4, 2]$. The increase in dynamic aperture allowed for a 10% increase in lifetime from 40 to 44 hours at regular user fill with all of the insertion devices at minimum gap.

Further work needs to be done to implement these results during experimental user time. Long term stability tests involving a more realistic movement of insertion devices as well as implementation user time online beam diagnostics are planned.

REFERENCES

[1] J.W. Boldeman, D. Einfeld, Nucl. Instr. and Meth. A **521**, 2004.

[2] M.J. Spencer, *et. al.* "Design and Commissioning of a Bunch by Bunch Feedback System for the Australian Synchrotron", *EPAC08, Genoa, Italy.*

[3] D.J. Peake, *et. al.* "Growth/Damp Measurements and Bunch-By-Bunch Diagnostics On The Australian Storage Ring", *PAC09, Vancouver, Canada.*

[4] S.W. Friis-Nielsenm *et. al.* "Commissioning Results From The Injection System For The Australian Synchrotron Project", *EPAC06, Edinburgh, Scotland.*

[5] J.M. Vogt, *et. al.* "Bunch Cleaning at the Canadian Light Source", *PAC09, Vancouver, Canada.*

[6] C. Thomas, *et. al.*, Nucl. Instr. and Meth. A **566**, 2006

Proceedings of IPAC'10, Kyoto, Japan TUPD026

IMPEDANCE EFFECTS IN THE AUSTRALIAN SYNCHROTRON STORAGE RING

Rohan Dowd, Mark James Boland, Gregory Scott LeBlanc, Yaw-Ren Eugene Tan
(ASCo, Clayton, Australia)
David J. Peake (The University of Melbourne, Melbourne, Australia)

Abstract

The Australian Synchrotron storage ring must maintain a stable electron beam for user operations. The impedance characteristics of the storage ring can give rise to instabilities that adversely affect the beam quality and need to be well understood. Collective effects driven by the resistive wall impedance are particularly relevant at the Australian synchrotron and their strengths are enhanced by small gap insertion devices, such as IVUs. This study will explore the impedance issues identified in the Australian Synchrotron storage ring and current mitigation techniques.

INTRODUCTION

The Australian Synchrotron (AS) is a 3rd generation light source facility located in Melbourne, Australia. Commissioning was conducted in 2006, with beamline operations commencing in April 2007. The 3 GeV storage ring is 216 metres in circumference and can store a beam of up to 200 mA current. A design overview can be found in [1]. The Australian Synchrotron currently has nine operational beamlines. Of these nine beamlines, six use insertion devices (IDs), with three of these devices being In-Vacuum Undulators (IVUs). Both kinds of insertion devices require specialised vacuum chambers and their inclusion has an effect on the impedance of the storage ring. Careful attention will need to be paid to these effects as more insertion devices are added to the storage ring for future beamlines.

SOURCES OF IMPEDANCE

The dominant source of impedance leading to beam instabilities at the Australian synchrotron is the resistive wall effect. Other sources of impedance include vacuum chamber transitions, BPMs and injection elements, however these sources are minor contributors to the total impedance. The standard vacuum chamber used in the storage ring is stainless steel with a typical full height of 32 mm and width of 70 mm. The three standard insertion devices use an elliptical aluminium chamber of 11 mm full height. There are two 3 metre IVUs which close to a gap of 6.6 mm and one 1 meter IVU that closes to 6 mm. While all three IVUs have a thin copper inner layer to minimise resistive wall impedance, their small vertical gap still produces a significant transverse impedance. The longitudinal and transverse impedances from the resistive wall effect are given by [2]

$$\frac{Z_{\parallel}}{n} = \frac{Z_0(1-i)\delta}{2b}\left(\frac{L}{2\pi R}\right)F_0\left(\frac{a}{b}\right) \tag{1}$$

$$\frac{Z_{\perp}}{n} = \frac{Z_0 L(1-i)\delta}{2\pi b^3}F_{1x,y}\left(\frac{a}{b}\right) \tag{2}$$

where $\delta = \sqrt{2/\omega\mu\sigma}$ is the skin depth, L is the chamber length, b is the chamber half height, σ is the chamber resistivity, F_0 and $F_{1x,y}$ are geometry shape factors. F_0 is equal to 1, $F_{1x} = 0.411$ and $F_{1y} = 0.822$ for our chamber geometry

LONGITUDINAL INSTABILITIES

Bunch lengthening due to longitudinal impedance in the AS storage ring has been studied in depth in [4]. Since this study the damaged IVU has been repaired and re-installed. Streak camera measurements were repeated and an inductance of 70 nH was extracted from the bunch lengthening fits, corresponding to a Z/n of 0.6 Ω.

We currently see no longitudinal instabilities on the beam. We have not been able to observe the onset of the microwave instability in single bunches of up to 10 mA. We do not fill bunches to above 10 mA as a precaution against induction of high voltages on BPM and other RF pickups in the storage ring, although this limitation may be revisited in the future.

TRANSVERSE INSTABILITIES

The vertical impedance of our vacuum chamber, assuming the standard chamber geometry for the whole storage ring is given by equation 2 as

$$Z_y = 0.94(1-i)\frac{1}{\sqrt{n}}\mathrm{M\Omega m^{-1}} \tag{3}$$

Using this value for the impedance we can calculate a growth rate for the vertical resistive wall instability. By setting this growth rate equal to the vertical radiation damping rate of 4.8 ms, an estimate of the threshold current for the onset of the instability can be obtained. The effective vertical impedance here is estimated for n_b equally spaced bunches as

$$\begin{aligned} Z_{eff} &= \sum_{p=-\infty}^{\infty} e^{-(\omega_{pn}\sigma_B)^2} Re|Z_y(\omega_{pm})| \qquad (4)\\ Z_{eff} &= 1.201\mathrm{M\Omega m^{-1}} \end{aligned}$$

with $\omega_{pn} = \omega_0[pn_b+n+Q]$ and $n_b = 360$ (even fill). Using this to calculate the current threshold (for a zero chromaticity lattice) we obtain

$$\begin{aligned} \frac{1}{\tau} &= \frac{1}{2}f_0\frac{I}{E} < B > Z_{eff} \qquad (5)\\ I_{\mathrm{th}} &= 50.3\,\mathrm{mA} \end{aligned}$$

The threshold current calculated here has neglected chromaticity effects, however we can see that the value of 50 mA agrees very well with the observed onset of vertical instabilities for a 360 bucket fill at low chromaticity, as shown in figure 2. The horizontal instability has a much higher threshold at 229 mA, as the horizontal resistive wall impedance is half of the vertical and the average beta functions and horizontal damping times are both lower.

The resistive wall impedance of the insertion devices is calculated as $0.21\,\mathrm{M\Omega m^{-1}}$ for the 2 m long, 6 mm gap device device, and $0.46\,\mathrm{M\Omega m^{-1}}$ for both of the 3 m long, 6.6 mm gap device devices (when they are at minimum gap). Adding this to the storage ring impedance, we obtain a new transverse impedance of $1.54\,\mathrm{M\Omega m^{-1}}$ when the devices are all at minimum gap. The effect of this increased impedance is also clear in Figure 2 as reduced thresholds for when the IVUs are at minimum gap.

Tune shift with current

The transverse impedance will cause a current dependant tune shift in the beam. The tune of a single bunch was measured at various currents up to 10 mA. A clear negative shift in the vertical tune was observed, with no clear signal in the horizontal tune.

Measurements were taken with IVUs at maximum and minimum gap, with the results shown in Figure 1. The tune shift slope, $d\nu/dI$, was found to be 0.256 and 0.336 for IVUs at maximum and minimum gap respectively. The frequency shift from transverse impedance is given by [3]:

$$\Delta\omega = \frac{-i}{2Q\omega_0\sigma_z}\frac{e\beta}{\gamma m_0}Z_{eff}I \qquad (6)$$

Using equation 6 we find the effective vertical impedance for the ring as 1.13 $\mathrm{M}\Omega m^{-1}$ with IVUs open and 1.487 $\mathrm{M}\Omega m^{-1}$ with all IVUs closed. These results are in good agreement with the calculated resistive wall impedances shown above.

Increased Chromaticity operation

The effective transverse impedance is determined by the overlap integral of the bunch power spectrum, $h(\omega)$, and the impedance spectrum. The presence of chromaticity in the lattice will introduce a frequency shift in the bunch spectrum, thus altering the effective impedance.

$$Z_{eff}(\omega_\xi) = \frac{\int_{-\infty}^{+\infty} h(\omega-\omega_\xi)Z(\omega)\,d\omega}{\int_{-\infty}^{+\infty} h(\omega-\omega_\xi)\,d\omega} \qquad (7)$$

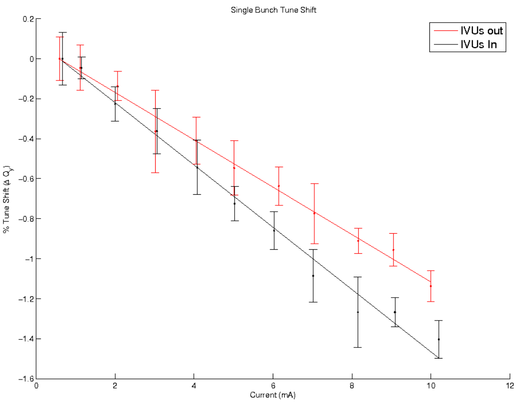

Figure 1: Single bunch tune shift vs. bunch current. Measurement was taken with IVUs wound out (red) and all IVUs wound in to minimum gap (black). Initial Vertical tune is 5.216

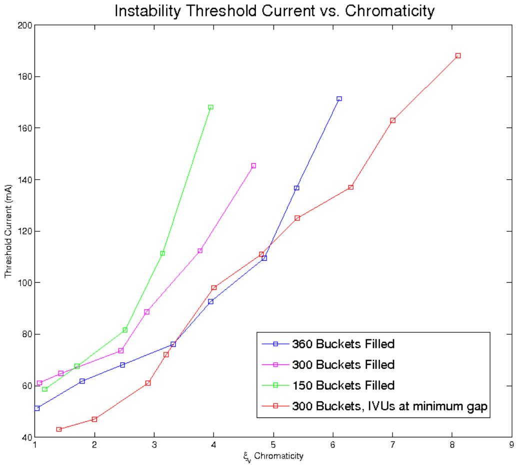

Figure 2: Measured onset of Vertical instability for different fill patterns and vertical chromaticity.

For the resistive wall impedance, applying positive chromaticity has the effect of reducing the effective impedance and therefore raising the instability threshold. Figure 2 shows measurements of the observed onset of vertical instability at different vertical chromaticity and fill pattern. The measurement of the instability onset is difficult due to the difficulty in defining precisely at what point the beam is unstable, but the trends are quite clear. We can see that the shorter the bunch train, the higher the instability thresholds. We also see the effect of the small gap IVUs on the transverse impedance, with a very high chromaticity needed to stabilise the full 200 mA beam with these devices closed. The storage ring is currently set to a chromaticity of 3 in the horizontal and 11 in the vertical to control the resistive wall instabilities for user operations. The harmonic sextupoles have been adjusted to regain dynamic aperture at such high chromaticity. While this has been successful so far we are near the limit of our sextupole magnet's strength and will require an active feedback system if more IVUs are installed in the future.

Transverse Feedback

A transverse Bunch-by-bunch feedback system has been designed and is currently being commissioned at the Australian synchrotron [6]. The system has been able to damp the resistive wall instabilities quite well but has had some difficulties due to the IVUs. When the IVUs are near their minimum gap, there is often the sudden emergence of a high frequency coupled bunch instability, at mode number 228. While this seems to imply a resonance in the IVU chamber, 3D electromagnetic simulations of the IVU chamber geometry have so far not been able to determine a source of the resonance.

COUPLING EFFECTS

Growth Rate vs Coupling

A series of coupling settings have been devised at the Australian Synchrotron [5], allowing the emittance coupling ratio to be finely controlled. During testing of the grow/damp measurements [7] of the feedback system we noticed that the instability growth rates would change depending on coupling. While conventional wisdom says that a higher beam transverse coupling should reduce the growth rate of the vertical instabilities by allowing extra damping in the horizontal plane, we see the opposite effect. As coupling is increased, the growth rate seems to increase. Figure 3 shows the vertical instability growth rates vs chromaticity for three different coupling settings. The growth rate shown is for the strongest resistive wall mode and is consistently higher at the higher coupling settings.

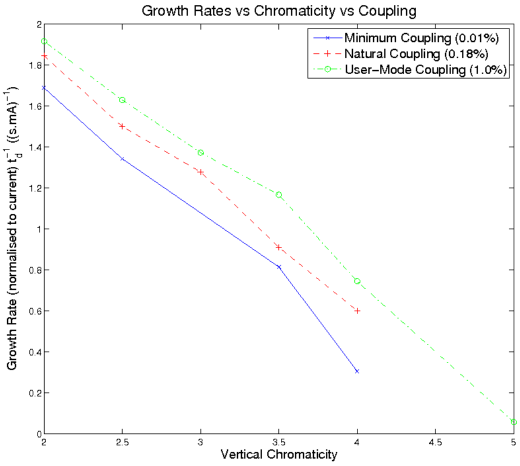

Figure 3: Normalised growth rates for vertical coupled bunch instability at different chromaticity. Measurements were taken at three different coupling settings.

Tune shift vs Coupling

To further investigate this effect a series of single bunch vertical tune shift measurements were taken at various emittance coupling settings. The results are shown in Table 1 and show a clear increase of the tune shift with higher coupling. Combined with the growth rate results, this seems to indicate that the effective impedance is increased by having a larger emittance coupling. It is not yet known what exactly is causing this and it is hoped further study will reveal the underlying effect.

Table 1: Current dependant tune shifts vs. coupling

Coupling (%)	**Tuneshift (dν/dI)**
0.01	-0.2465 ± 0.020
0.18	-0.2452 ± 0.022
0.3	-0.2594 ± 0.016
0.5	-0.2579 ± 0.024
0.8	-0.2681 ± 0.021
1.0	-0.2745 ± 0.032
20	-0.2922 ± 0.018

CONCLUSIONS

Studies of the impedance of the Australian synchrotron storage ring show that the dominant source of impedance driven instability is the resistive wall effect. Measurements of both the onset of instabilities and beam tune shifts point to a total machine impedance that is very close in magnitude to the expected resistive wall impedance. An interesting connection between emittance coupling and effective impedance has been observed in both tune shift and growth rate measurements and needs to be studied further.

REFERENCES

[1] J. Boldeman, D. Einfeld, Nucl. Intr. and Meth., A **521**, 2004, pg. 306

[2] R. Gluckstern, J. Zeijts,"Coupling impedance of beam pipes of general cross section " B. Zotter, Phys. Rev. E, **47** (1993) 1

[3] F.J. Sacherer, "Transverse Bunched Beam Instabilities - Theory", Proceedings of the 9th International Conference on High Energy Accelerators, Stanford, p347, 1974.

[4] R. Dowd, et al., "Single Bunch Studies at the Australian Synchrotron", EPAC'08, Genoa, Italy, June 2008.

[5] R. Dowd, et al., "Emittance Coupling Control at the Australian Synchrotron", PAC'09, Vancouver, Canada, May 2009.

[6] D.J. Peake, et al., "Preliminary Operational Experiences of a Bunch-By-Bunch Transverse Feedback System at the Australian Synchrotron", These Proceedings.

[7] D.J. Peake, et al., "Growth/Damp Measurements and Bunch-By-Bunch Diagnostics on the Australian Synchrotron", PAC'09, Vancouver, Canada, May 2009.

OPERATION AND STORAGE RING CALIBRATION WITH THE TRANSVERSE BUNCH-BY-BUNCH FEEDBACK SYSTEM AT THE AUSTRALIAN SYNCHROTRON

D. J. Peake, K.P. Wootton, R.P. Rassool, University of Melbourne, VIC, Australia,
M.J. Boland, Y.-R. Tan, Australian Synchrotron, Clayton, VIC, Australia.

Abstract

The first operational experience with the transverse bunch-by-bunch feedback system for the storage ring shows a doubling of the lifetime and the ability to damp instabilities caused by IVU gap changes. The system was also used to calibrate the ring by doing simultaneous measurements on several single bunches with different bunch currents.

INTRODUCTION

Results from the transverse bunch-by-bunch feedback system commissioning, diagnostic tools, bunch cleaning and beam lifetime improvements have been reported previously [1–3]. Here we report on the operational results from using the system under user beam conditions. There were two main goals for the operational setup; i) damping the high order mode instabilities induced by the the IVUs at specific gaps; and ii) reducing the chromaticity in order to increase the beam lifetime. Experimentally the two goals could not be simultaneously optimised, so a compromise was reached that nonetheless resulted in an increased lifetime and a stable beam for all IVU gaps.

IVU INDUCED INSTABILITIES

IVU Gaps and Instability Modes

At very narrow ranges of IVU gaps high order mode instabilities are induced in the storage ring. The harmonic number of the storage ring is 360, so the possible coupled bunch modes are $m = 0 - 359$. Table 1 list some basic properties of the IVUs and the unstable gaps and modes that are present.

Table 1: ASLS IVU parameters and instabilities at low chromaticity $\xi_x = 3, \xi_y = 3$.

ID	Min. Gap [mm]	Unstable [mm]	Modes
IVU3	6.6	6.8, 7.1	197, 227
IVU5	6.0	6.2, 6.5, 10	197, 224, 227
IVU13	6.6	6.6, 7.7	197

The instabilities are present for $\pm 50\ \mu$m variation of the gaps and the gaps at which they occur have changed over the past few years.

Phase Tuning with Grow/Damp Measurements

The technique of allowing an instability mode to grow for a few ms and then damping it again by briefly opening and closing the loop was used to optimise the kick phase. Fig. 1 shows the damping time variation with a change in the final two tap filter of DAC signal that gets sent to the stripline kicker. The higher order mode 224 is very sensitive to the kick phase and the optimal phase varies for each mode. A compromise was reached between optimal phase for the higher order modes and the resistive wall low modes.

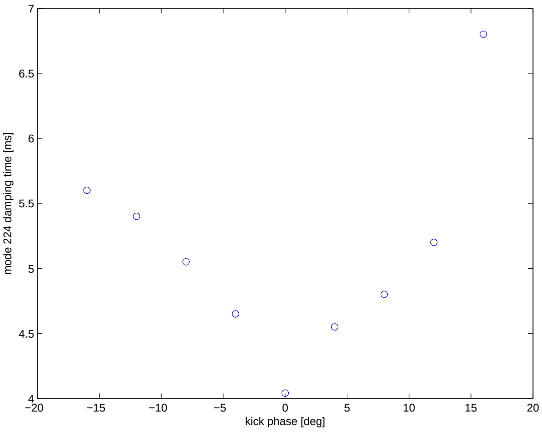

Figure 1: Damping time vs kick phase for mode 224 with IVU5 closed.

This technique was used at each of the observed instability modes and the an indication of the typical growth and damping times of the modes is presented in Table 2. One of the limitations of the system is the optimal phase for damping a mode is not necessarily the same phase for each mode. The main reason for this is believed to the be the strong frequency dependent phase shift of the kicker amplifier at low frequency.

Table 2: Coupled bunch instability grow/damp times.

Mode	Growth Time [ms]	Damping Time [ms]
197	7.5	20
224	25	4
227	3.5	6.5
359	5	1

SEXTUPOLE OPTIMISATION

The original work on optimising the lattice with the harmonic sextupoles is described in Ref. [4] and includes the details of the lattice. Since that study IVUs that induce beam instabilities have been added to the ring and thus the optimisation criteria have changed due to practical experience with the ring.

Motivation

There are a number of competing parameters that need to be considered for the optimisation of the sextupoles:

- lowering the chromaticity;
- damping all coupled bunch instabilities;
- improving the lifetime;

The chromaticity was increased after the IVUs went into the storage ring to counter the coupled bunch instabilities during user beam but the subsequent spread of the tune peaks into synchrotron side bands interfered with machine studies. Using the BBB feedback system the chromaticity can be lowered and the tune synchrotron sidebands reduced, making it easier to excite the beam as more power can be absorbed by the beam at the main tune peak. Fig. 2 shows the vertical tune spread decrease with lower vertical chromaticity.

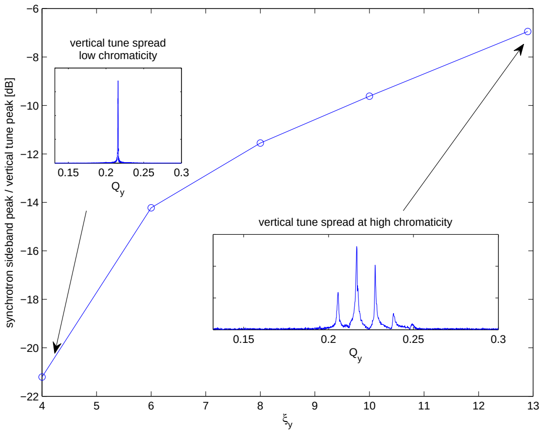

Figure 2: Tune spread vs vertical chromaticity.

In the future this improvement is planned to be exploited to put the system into positive feedback for a short time to excite the beam to large amplitudes and then measure the tune shifts with amplitude.

Lifetime Optimisation

From a user beamline point of view the lifetime is probably the most critical parameter that can be improved with the bunch-by-bunch feedback system. For a given working point the harmonic sextupoles (SFA, SDA) can be adjusted to control the tune shifts with amplitude and momentum. The initial figure of merit for the harmonic sextupole scanning before the IVUs were installed was the restoration of the dynamic aperture lost at high chromaticities. This aim was achieved with the harmonic sextupoles approximately equal and opposite in sign and at high strength.

Table 3 shows the normal user beam at high chromaticity with the IVUs at minimum gap has a lifetime of 28 hr. With the bunch-by-bunch system the chromaticity can be lowered and all instabilities damped if the harmonic sextupoles are at low strength. However the lifetime can be further improved, in fact doubled that of the present user mode, if the harmonic sextupoles are unbalanced. At high harmonic sextupole strengths the growth rate of coupled bunch instabilities is also higher. This experimental lifetime results are not in agreement with earlier modelling which indicated that the best lifetime is achieved with balanced harmonic sextupoles [4].

Table 3: Beam lifetime with IVUs at minimum gaps.

ξ_x, ξ_y	**SFA,SDA [1/m^3]**	**Lifetime [hr]**
3.5,12.9	34,-33	28
2,3.5	12,-12	42
2,3.5	30,-24	56

RESULTS

User Mode Test Shift

In order to fully test the feedback system the IVU gaps were scanned at random time intervals to the gaps that are set by users to test the beam stability under normal operations. Fig. 3 shows the IVU gaps for one much test shift and Fig. 4 shows that no current was lost due to exciting an instability with the IVU gap changes the beam was stable and did not blow up in the vertical plane.

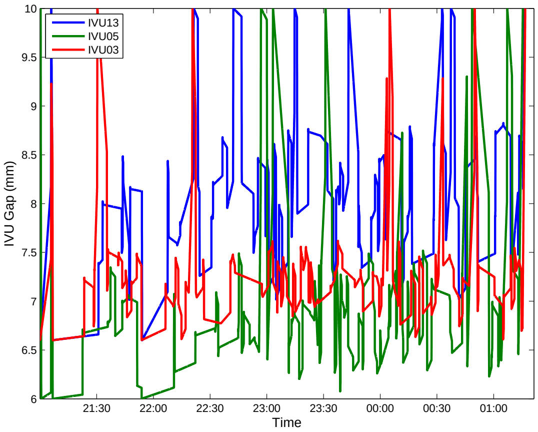

Figure 3: Test of transverse bunch-by-bunch feedback system with varying IVU gaps.

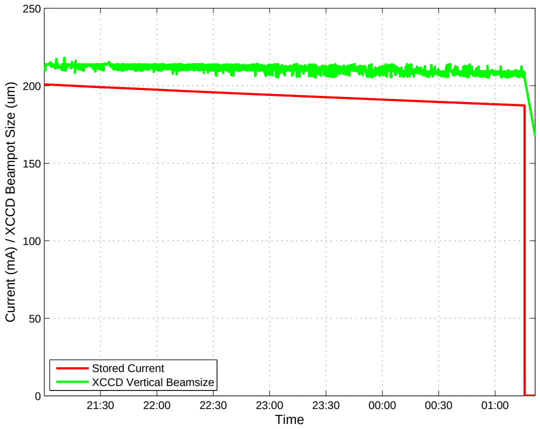

Figure 4: Beam current and vertical beam size during IVU gap scanning.

LATTICE CALIBRATION

Storage Ring Impedance

As part of testing the diagnostic capability some single bunch excitation studies were performed. One such measurement was on a sparsely filled ring with ten single bunches, each with a different bunch current, which were excited and the response measure with the feedback system. The imaginary part of the ring impedance can then be deduced from the change in tune with respect to the change in current, given by

$$\frac{\Delta Q}{\Delta I_b} = \frac{1}{|m+1|}\frac{e\beta c^2}{2\omega_\beta E_0 L_b}\text{Im}\{Z_{eff}\}, \qquad (1)$$

where Q is the tune, m is the azimuthal mode, E_0 is the nominal energy of the beam and L_b is the bunch length and Z_{eff} is the effective impedance.

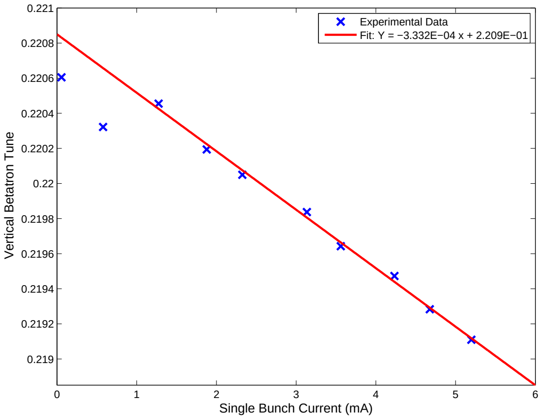

Figure 5: Single shot tune shift with bunch current measurement.

These measurements have been regularly made to keep a close account of the impedance budget of the storage ring (see Ref. [5]), in particular before and after the installation of insertion device chambers and in vacuum IDs. This new technique will simplify and improve the accuracy of these impedance measurements.

CONCLUSION

The transverse bunch-by-bunch feedback system was finely tuned to damp all the higher order modes induced by varying the IVU gaps during user beam. A compromise was reached in the setting of the harmonic sextupoles that increased the growth rate of instabilities but also resulted in a doubling of the beam lifetime at low chromaticity and with all IVUs at minimum gaps. Future plans are to use the excite/damp capabilities of the system to calibrate the nonlinear dynamics and reconcile a discrepancy with the harmonic sextupole modelling. A novel technique for rapidly deducing the ring impedance was also demonstrated.

REFERENCES

[1] M. J. Spencer, G. Leblanc and K. Zingre, “Design and Commissioning of a Bunch by Bunch Feedback System for The Australian Synchrotron” Proceedings of EPAC08, Genova 2008, THPC136, p. 3306, `http://www.JACoW.org`.

[2] D. Peake, R. Rassool, M. Boland and G. LeBlanc, “Growth/Damp Measurements and Bunch-by-Bunch Diagnostics on the Australian Synchrotron Storage Ring”, Proceeding of PAC09, Vancouver 2009, TH6REP066, p. 4105, `http://www.JACoW.org`.

[3] D. J. Peake, R. P. Rassool, M. J. Boland, R. Dowd and Y.-R. Tan, “Preliminary Operational Experiences of a Bunch-by-bunch Transverse Feedback System at the Australian Synchrotron”, Proceedings of IPAC10, Kyoto 2010, WEPEB027, p. 2743, `http://www.JACoW.org`.

[4] E. Y. R. Tan, M. J. Boland and G. LeBlanc, “Applying Frequency Map Analysis to the Australian Synchrotron Storage Ring” , Proceedings of PAC05, Knoxville 2005, p. 407, `http://www.JACoW.org`.

[5] R. Dowd, M. Boland, G. LeBlanc, M. Spencer, and Y.-R. Tan, “Single Bunch Studies at the Australian Synchrotron”, Proceedings of EPAC08, TUPC010, Genova 2008, p. 1062, `http://www.JACoW.org`.

Bibliography

[1] J. Boldeman and D. Einfeld. The physics design of the Australian Synchrotron storage ring. *Nuclear Instruments and Methods in Physics Research A*, 521:306–317, November 2004. doi:10.1016/j.nima.2003.11.191.

[2] G. LeBlanc. Status of the Australian Synchrotron Project. In *Proceedings of APAC'07, Indore, India*. 2007.

[3] E. Haussecker and A. Chao. Influence of Accelerator Science of Physics Research. *ICFA Beam Dynamics Newsletter*, 53:11–24, December 2010. URL `http://www-bd.fnal.gov/icfabd/Newsletter53.pdf`.

[4] W. Röntgen. On a New Kind of Rays. *Nature*, 53:274–276, January 1896. doi:10.1038/053274b0.

[5] R. H. Varian and S. F. Varian. A High Frequency Oscillator and Amplifier. *Journal of Applied Physics*, 10(5):321–327, January 1939. doi:10.1063/1.1707311.

[6] E. O. Lawrence and D. Cooksey. The Production of High Speed Light Ions Without the use of High Voltages. *Physical Review*, 40:19–35, April 1932. doi:10.1103/PhysRev.40.19.

[7] D. Kerst. Acceleration of Electrons by Magnetic Induction. *Physical Review*, 58:841, November 1941. doi:10.1103/PhysRev.60.47.

[8] E. M. McMillan. The Synchrotron—A Proposed High Energy Particle Accelerator. *Physical Review*, 68(5-6):143–144, Sep 1945. doi:10.1103/PhysRev.68.143.

[9] J. Rotblat. Obituary: Mark Oliphant (1901-2000). *Nature*, 407:468, 2000. doi:10.1038/35035202.

[10] E. Meier, R. Dowd and G. LeBlanc. Characterization of the Australian Synchrotron Linac. *Nuclear Instruments and Methods A*, 589:157–166, 2008. doi:10.1016/j.nima.2008.02.009.

[11] S. W. Friis-Nielsen, H. Bach, F. Bødker *et al.* Comissioning Results from the Injection System for the Australian Synchrotron Project. In *Proceedings of EPAC'06, Edinburgh, Scotland*. 2006.

[12] S. Y. Lee. Emittance optimization in three- and multiple-bend achromats. *Physical Review E*, 54:1940–1944, 1996. doi:10.1103/PhysRevE.54.1940.

[13] H. C. Pollock. The Discovery of Synchrotron Radiation. *American Journal Of Physics*, 51(3):278–280, 1983. doi:10.1119/1.13289.

[14] J. Schwinger. On the Classical Radiation of Accelerated Electrons. *Physical Review*, 75(12):1912–1925, June 1949. doi:10.1103/PhysRev.75.1912.

[15] T. Tanaka and H. Kitamura. http://radiant.harima.riken.go.jp/spectra/. Date Retrieved - 02/08/2010. URL `http://radiant.harima.riken.go.jp/spectra/index.html`.

[16] D. Iwenenko and I. Pomeranchuk. On The Maximal Energy Obtainable in a Betatron. *Physical Review Letters*, 65(11 & 12):343, June 1944.

[17] F. Barbarin, F. Iselin and J. Jowett. Particle Dynamics in LEP at Very High Energy. In *Proceedings of EPAC 94, London, United Kingdom*. 1994.

[18] P. Brown, O. Brunner, A. Butterworth *et al.* Ultimate Performance of the LEP RF System. In *Proceedings of PAC'01, Chicago, USA*. 2001.

[19] M. Boland, J. Bergstrom, G. LeBlanc *et al.* Measurements Using The X-Ray and Optical Diagnostic Beamlines at the Australian Synchrotron. In *Proceedings of EPAC'06, Edinburgh, UK*. 2006.

[20] D. Peake, M. Boland, G. LeBlanc *et al.* Measurement of the real time fill-pattern at the Australian Synchrotron. *Nuclear Instruments and Methods in Physics Research A*, 589:143, 2008. doi:10.1016/j.nima.2008.01.072.

[21] C. Thomas, G. Rehm, H. Owen *et al.* Bunch purity measurement for Diamond. *Nuclear Instruments and Methods in Physics Research A*, 566:762–766, 2006. doi:10.1016/j.nima.2006.07.059.

[22] H. Winick. The Stanford Synchrotron Radiation Project. Technical Report SLAC-PUB-1439, SLAC, Stanford, California, June 1974. URL `http://www.slac.stanford.edu/cgi-wrap/getdoc/slac-pub-1439.pdf`.

[23] A. Snigirev, I. Snigireva, V. Kohn *et al.* On the possibilities of x-ray phase contrast microimaging by coherent high-energy synchrotron radiation. *Review of Scientific Instruments*, 66:5486–5492, 1995.

[24] S. Lee. *Accelerator Physics.* World Scientific, second edition, 2004.

[25] E. Wilson. *An Introduction To Particle Accelerators.* Oxford University Press, 2001.

[26] G. Arduini, R. Assmann, R. Bailey *et al.* Electron-Positron Collisions at 209 GeV in LEP. In *Proceedings of PAC'01, Chicago, USA*. 2001. doi:10.1109/PAC.2001.987514.

[27] S. Kahn. Study of the BESSY II Beam Lifetime. In *Proceedings of PAC'99, New York, New York, USA*. 1999.

[28] E. Huttel, I. Birkel, A.-S. Müller *et al.* Studies of Beam Lifetime Effects at ANKA. In *Proceedings of Particle Accelerator Conference '03, Portland, Oregon, USA*. 2003.

[29] M. Spencer, M. Boland, R. Dowd *et al.* Tune and Lifetime Studies at the Australian Synchrotron. In *Proceedings of APAC'07, Indore, India*. 2007.

[30] R. Dowd, M. Boland, G. LeBlanc *et al.* Emittance Coupling Control at the Australian Synchrotron. In *Proceedings of PAC'09, Vancouver, BC, Canada*. 2009.

[31] R. Dowd, M. Boland, G. LeBlanc *et al.* Achievement of ultralow emittance coupling in the Australian Synchrotron storage ring. *Phys. Rev. ST Accel. Beams*, 14(1):012804, Jan 2011. doi:10.1103/PhysRevSTAB.14.012804.

[32] G. LeBlanc, M. Boland and Y.-R. Tan. The Australian Synchrotron Project Storage Ring and Injection System Overview. In *Proceedings of EPAC'04, Lucerne, Switzerland.* 2004.

[33] E. Bravin. Transverse beam profiles. In *CERN Accelerator School: Beam Diagnostics.* 2008.

[34] R. Assmann, O. Aberle, M. Brugger *et al.* Designing and Building a Collimation System for the High-Intensity LHC Beam. In *Proceedings of PAC'03, Portland, Oregon, USA.* 2003.

[35] H. Wiedemann. *Particle Accelerator Physics II.* Springer, 1998.

[36] H. Panopoulous. *Energy Calibration of the Australian Synchrotron using Resonant Depolarization.* Master's thesis, School of Physics, The University of Melbourne, 2010.

[37] R. Dowd, G. LeBlanc and K. Zingre. Commissioning and operation of the 500 MHz storage ring RF system for the Australian synchrotron. *Nuclear Instruments and Methods A*, 592(3):224 – 229, 2008. doi:10.1016/j.nima.2008.04.037.

[38] E. Huttel, J. Tanabe, A. Jackson *et al.* The Storage Ring Magnets of the Australian Synchrotron. In *Proceedings of EPAC'04, Lucerne, Switzerland.* 2004. URL `http://accelconf.web.cern.ch/AccelConf/e04/PAPERS/WEPKF030.PDF`.

[39] A. W. Chao. *Physics of Collective Instabilities in High Energy Accelerators.* John Wiley & Sons, Inc., 1993.

[40] K. Ng. *Physics of Intensity Dependent Beam Instabilities.* World Scientific, 2006.

[41] J. D. Jackson. *Classical electrodynamics.* John Wiley & Sons, Inc., 3rd edition, 1998.

[42] E. Huttel, B. Barg, A. Jackson *et al.* The Vacuum System of the Australian Synchrotron. In *Proceedings of EPAC'04, Lucerne, Switzerland.* 2004.

[43] W. K. H. Panofsky and W. A. Wenzel. Some Considerations Concerning the Transverse Deflection of Charged Particles in Radio-Frequency Fields. *Review of Scientific Instruments*, 11:967, 1956. doi:10.1063/1.1715427.

[44] A. Chao, S. Heifets and B. Zotter. Tune shifts of bunch trains due to resistive vacuum chambers without circular symmetry. *Physical Review Special Topics - Accelerators and Beams*, 5:111001, 2002. doi:10.1103/PhysRevSTAB.5.111001.

[45] F. Sacherer. Methods For Computing Bunched-Beam Instabilities. Technical Report CERN/SI-BR/72-5, CERN, Geneva, Geneva, September 1972. URL `http://cdsweb.cern.ch/record/322545`.

[46] R. Dowd, M. J. Boland, G. S. LeBlanc *et al.* Impedance and Beam Stability Study at the Australian Synchrotron. In *Proceedings of EPAC'06, Edinburgh, Scotland.* 2006.

[47] L. Wang, K. L. F. Bane, T. Raubenheimer *et al.* Resistive-Wall Instability In The Damping Rings of the ILC. In *Proceedings of EPAC'06, Edinburgh, Scotland.* 2006.

[48] K. Ng and K. Bane. Explicit Expressions of Impedances and Wake Functions. In A. Chao and M. Tigner, editors, *Handbook of Accelerator Physics and Engineering*, pages 229–236. World Scientific, 3rd edition, 2006.

[49] R. Dowd, M. Boland, G. LeBlanc *et al.* Single Bunch Studies At The Australian Synchrotron. In *Proceedings of EPAC'08, Genoa, Italy.* 2008. URL `http://accelconf.web.cern.ch/accelconf/e08/papers/tupc010.pdf`.

[50] D. Peake, R. Rassool, M. Boland *et al.* Growth/Damp Measurements and Bunch-by-Bunch Diagnostics on the Australian Synchrotron Storage Ring. In *Proceedings of PAC'09, Vancouver, BC, Canada.* 2009.

[51] S. Prabhakar, J. Fox and D. Teytelman. Curing Coupled-Bunch Instabilities with Uneven Fills. *Physical Review Letters*, 86(10):2022–2025, March 2001. doi:10.1103/PhysRevLett.86.2022.

[52] M. Georgsson, A. Andersson and M. Eriksson. Landau Cavities at MAX II. *Nuclear Instruments and Methods A*, 416:465–474, 1998. doi:10.1016/S0168-9002(98)00667-6.

[53] J. T. Rogers. Feedback Systems for Coupled Bunch Instabilities. In A. W. Chao and M. Tigner, editors, *Handbook of Accelerator Physics and Engineering*. World Scientific, 2006.

[54] W. Barry, J. Byrd, J. Corlett *et al.* Commissioning of the ALS Transverse Coupled-Bunch Feedback System. In *Proceedings of PAC'95, Dallas, Texas, USA*. 1995.

[55] J.-L. Pellegrin. Beam Feedback Electronics For The SPEAR Storage Ring. *Nuclear Instruments and Methods*, 108(2):365–373, April 1973. doi:10.1016/0029-554X(73)90614-9.

[56] CST Microwave Studio. Date Retrieved: 18/10/2011. URL `http://www.cst.com/Content/Products/MWS/Overview.aspx`.

[57] R. Dowd. Personal communication, March 2011.

[58] Instrumentation Technologies. Date Retrieved: 10/06/2010. URL `http://www.i-tech.si/`.

[59] Instrumentation Technologies. *Libera Bunch-By-Bunch User Manual v1.80.*

[60] MATLAB. *version 7.9.0.529 (R2009b).* The MathWorks Inc., Natick, Massachusetts, 2009. URL `http://www.mathworks.com/products/matlab/`.

[61] L. Tan. *Digital Signal Processing.* Academic Press, 2007.

[62] G. Blokesch, M. Negrazus and K. Wille. A slotted-pipe kicker for high-current storage rings. *Nuclear Instruments and Methods in Physics Research Section A*, 338(2-3):151 – 155, 1994. ISSN 0168-9002. doi:10.1016/0168-9002(94)91308-0.

[63] Colby Instruments PDL-100A Specifications. Date Retrieved: 18/10/2011. URL `http://www.colbyinstruments.com/prod_pdl100a.html`.

[64] Tektronix TDS7000 Series Datasheet. Date Retrieved: 18/10/2011. URL `http://www2.tek.com/cmswpt/psdetails.lotr?ct=PS&cs=psu&ci=13469&lc=EN`.

[65] G. Stupakov and B. Podobedov. High-frequency impedance of small-angle tapers and collimators. *Physcial Review Special Topics - Accelerators and Beams*, 13:104401, 2010. doi:10.1103/PhysRevSTAB.13.104401.

[66] R. Cappi, E. Métral and D. Möhl. Control of Coherent Instabilities by Linear Coupling. Technical Report CERN-PS-2001-010-AE, CERN, Geneva, April 2001.

[67] G. Rumolo and F. Zimmermann. Practical User Guide for HEADTAIL. Technical Report CERN-SL-Note-2002-036 AP, CERN, 2002. URL `http://cdsweb.cern.ch/record/702717/files/sl-note-2002-036.pdf`.

[68] G. Rumolo and E. Métral. Multi-bunch Simulations With HEADTAIL. In *Proceedings of PAC'09, Vancouver, BC, Canada.* 2009.

[69] M. Boland, A. Walsh, G. LeBlanc *et al.* X-Ray and Optical Diagnostic Beamlines At The Australian Synchrotron Storage Ring. In *Proceedings of EPAC'06, Edinburgh, Scotland.* 2006.

[70] R. Steinhagen. Tune and Chromaticity Diagnostics. In *CERN Accelerator School: Beam Diagnostics.* 2008.

[71] E. Plouviez and N. Michel. Cleaning of Parasitic Bunches in the ESRF Booster Synchrotron For Time Structure Modes of Operation. In *Proceedings of EPAC'04, Lucerne, Switzerland.* 2004.

[72] J. M. Vogt, J. C. Bergstrom, S. Hu *et al.* Bunch Cleaning at the Canadian Light Source. In *Proceedings of PAC'09, Vancouver, Canada.* 2009.

[73] D. Peake, R. Rassool, M. Boland *et al.* Preliminary Operational Experiences of a Bunch-by-Bunch Transverse Feedback System at the Australian Synchrotron. In *Proceedings of IPAC'10, Kyoto, Japan.* 2010.

[74] F. Sacherer. Transverse Bunched Beam Instabilities - Theory. In *The 9th International Conference on High Energy Accelerators, 1974*, pages 347–351. 1974.

[75] J.-C. Denard. Beam current monitors. In *CERN Accelerator School: Beam Diagnostics*. 2008.

[76] M. Spencer, M. Boland, R. Dowd *et al.* Lifetime Contribution Measurements at the Australian Synchrotron. In *Proceedings of PAC'07, Albuquerque, New Mexico, USA*. 2007.